Surface deformation mechanisms in laser smoothing and micromachining of optical glasses

Surface deformation mechanisms in laser smoothing and micromachining of optical glasses

Krystian Lukasz Wlodarczyk

Submitted for the degree of Doctor of Philosophy

Heriot-Watt University

School of Engineering and Physical Sciences

April 2011

Abstract

The thesis addresses important issues in laser processing of optical glasses, such as fused silica (HPFS®7980 Corning), Borofloat®33, and some selected lead-silicate glasses, when treated by a CO_2 laser beam at a 10.6 µm wavelength, using beam diameters of either 1 mm or 50 µm. The investigations were carried out in the melting and vaporization regimes to study laser-induced surface deformations and stresses, and laser smoothing of fused silica etched structures. Novel applications for CO_2 laser polishing have been found and some preliminary results are presented.

With regard to the surface deformations and stresses, it has been discovered that fused silica behaves differently than other glasses. Deformations in fused silica are observed to be in the form of shallow depressions, as a result of glass densification driven by a fictive temperature increase. These deformations are completely removed by annealing. In raster scanning, the depressions merge to generate surface stress in the range of 10 - 30 MPa, which is largely reduced by annealing. In contrast, CO_2 laser radiation of Borofloat®33 produces surface bumps, now driven by both the fictive temperature and an irreversible Marangoni effect. In this case, the bumps are only partially removed by annealing. However, laser machining and polishing conditions for non-cracking treatment of Borofloat®33 have been successfully established, now opening the possibility of using the CO_2 laser-based processes for manufacturing micro-optical components. Lead-silicate glasses were found to have strong bumping and complex Marangoni shaping, limiting the prospects for CO_2 laser machining of micro-optics.

Application of CO_2 laser smoothing for surface relaxation of binary gratings and multi-level etched structures has shown that sharp step edges can be relaxed over a distance from submicron to about 30 µm. An optical method based on analysis of light scatter from binary gratings provides an excellent calibration method for CO_2 laser polishing. The submicron resolution in smoothing may be applied for fine relaxation of diffractive optics and nanostructures fabricated in fused silica. On the other hand, large scale relaxation of the etched steps provides a promising result to be used for the fabrication of micro-optics, as a viable alternative to the thermal reflow process.

A pioneering approach for the rapid prototyping of silica toroidal mirrors has given a high ratio of principle radii of curvature, successfully applied in mode-selective resonator configurations to improve the laser beam quality of planar waveguide lasers.

Acknowledgements

I am afraid that there are no appropriate words which would express my grateful thanks to the people mentioned below although the English vocabulary is so rich. Nevertheless, I will try to do it since these people truly deserve it …

Firstly, I would like to thank my supervisors, Professor Howard Baker and Professor Denis Hall, for giving me the opportunity to work within the Lasers and Photonics Applications group at Heriot-Watt University. I incredibly appreciate their support, professional guidance, constructive meetings, and well treatment. Special thanks must go also to Dr Roy McBride, Managing Director of PowerPhotonic Ltd. (my industrial sponsor), for helping me to solve some scientific problems described in this thesis and providing me financial support. Finally, I pay special tribute to Professor Krzysztof Abramski for giving me his support and trust. Thanks to him my adventure in Scotland became real.

I would like to thank all of my colleagues from the Lasers and Photonics Applications group for their support, enthusiasm, and collaboration. In particular, my thanks go to those who I have worked most closely with: Ms. Natalia Trela, Dr Enrique Mendez, Dr Ian Thomson, Dr Aaron McKay, Dr Fernando Monjardin, Mr. Victor Valles-Gomez, and Mr. Alberto Campos Zatarain.

I also thank my officemates and flatmates for their support, friendship, and making my spare time very enjoyable. Special thanks go to Ms. Nadia Kotova, Mr. Nicolas Bastien, Mr. Jens Apel, and again Ms. Natalia Trela.

Finally, special thanks must go to my mom Anna, sister Asia, and my “little” nephew Bartek. I am extremely grateful for their unwavering love, motivation, and support given me throughout the whole period of my studies.

Thank you!

Dziękuję!

Table of Contents

List of Variables

d	thickness, m
d_c	thickness of a compressive stressed layer, m
d_m	diameter of bumps, m
	diameter of the melt pool, m
d_s	thickness of a tensile stressed layer, m
g	laser energy introduced as a volumetric heating source, J
h	depth of the molten layer of glass, m
k	thermal conductivity, W/(m·K)
	extinction coefficient, -
l	length, m
m	mass, kg
n	refractive index, -
t	time flow of the molten layer of glass, s
u	speed, m/s
w	radius of laser beam, m
	width, m

A	surface area, m^2
	pre-exponential factor in the Arrhenius equation, -
	constant applied to the Vogel-Fulcher-Tammann equation, -
	initial step height of a binary grating, m
B	activation energy, J/mole
	constant applied to the Vogel-Fulcher-Tammann equation, -
C	scale factor, -
C_1, C_2	principle curvatures, 1/m
C_p	specific heat, J/(kg·K)
CTE	linear coefficient of thermal expansion, ppm/K
D	depth of a ditch, m
D_{EF}	effective depth of the glass which undergoes densification, m
F	laser fluence, J/m^2
E	Young's modulus, Pa
G	shear modulus, Pa
H	height of a bump, m
I_{ax}	axial irradiance, kW/cm^2
N	number of laser scans, -
P_{av}	average laser power, W
ΔP	pressure difference across the interface between two fluids, Pa
	laser power fluctuations, W
PD	laser pulse duration, µs
R	reflectivity, %
	gas constant, R ≈ 8.314 J/(mol·K)
R_1, R_2	principal radii of curvature, m
$R_{C/sec}$	maximum rate of cooling, ºC/s

RD	relaxation distance, m
T_A	annealing point, °C
T_F	fictive temperature, °C
T_G	transition point, °C
T_M	melting point, °C
T_0	initial temperature, °C
T_S	softening point, °C
T_{ST}	strain point, °C
T_T	transformation range, °C
V	relative change in the glass volume, m^2
α	absorption coefficient, 1/m
	mark-to-space ratio of a binary grating, -
β	volumetric coefficient of thermal expansion, ppm/K
Δx	raster pitch, m
γ	shear strain, -
	surface tension, J/m^2
ε	tensile or compressive strain, -
η	viscosity, Pa·s
θ	angle between the principle curvature vector and the X-axis, deg
κ	thermal diffusivity, m^2/s
λ	laser wavelength, m
	spatial period of undulation, m
Λ	spatial period of a binary grating, m
ν	Poisson's ratio, -
ρ	density, kg/m^3

σ	tensile or compressive stress, Pa
σ_{ac}	acceptable stress at the mid-plane of glass, Pa
τ	shear stress, Pa
	laser pulse duration, s

List of Publications

Journal publications

K. L. Wlodarczyk, E. Mendez, H. J. Baker, R. McBride, D. R. Hall, *'Laser smoothing of binary gratings and multi-level etched structures in fused silica'*, Applied Optics **49**, 1997-2005 (2010).

Publications in preparation

K. L. Wlodarczyk, H. J. Baker, *'CO_2 laser fabrication of toroidal mirrors for planar waveguide laser applications'*. – to be published in Applied Optics

K. L. Wlodarczyk, H. J. Baker, *'Investigation of surface deformations induced by CO_2 laser polishing of fused silica and Borofloat®33'*. – to be published in Journal of Applied Physics.

Conference contributions

K. L. Wlodarczyk, H. J. Baker, D. R. Hall, *'Laser fabrication of 1D micro-optical components by localized vaporization and bumping'*, Poster presented at the CLEO/QELS 2010, San Jose, USA (2010).

I. J. Thomson, H. J. Baker, K. L. Wlodarczyk, N. Trela, D. R. Hall; *'400W Yb:YAG planar waveguide laser using novel unstable resonators'*; in Procedings of SPIE vol. **7578**, Photonics West Conference, San Francisco, USA (2010).

K. L. Wlodarczyk, I. J. Thomson, H. J. Baker, D. R. Hall, *'Mode-selective toroidal mirrors for unstable resonator planar waveguide and thin slab solid-state lasers'*, Poster presented at the CLEO/Europe and EQEC Conference, Munich, Germany (2009).

K. L. Wlodarczyk, A. C. Zatarain, H. J. Baker, D. R. Hall, *'CO_2 laser micromachining of glass, LTCC and nanocarbon films'*, Poster presented at the James Watt Institute (JWI) Conference, Edinburgh, UK (2009)

K. L. Wlodarczyk, E. Mendez, H. J. Baker, M. R. Taghizadeh, R. McBride, D. R. Hall, *'Micro-optical fabrication based on laser smoothing of etched structures'*, Talk presented at the Optical Fabrication and Testing (OF&T) Conference, Rochester, NY, USA (2008).

K. L. Wlodarczyk, E. Mendez, H. J. Baker, G. Muyo, M. R. Taghizadeh, D. R. Hall, *'New applications of laser smoothing in diffractive optics and optical surface forming'*, Poster presented at the Supporting Manufacturing Innovation (SMI) Conference, Edinburgh, UK (2008).

K. L. Wlodarczyk, E. Mendez, H. J. Baker, J. F. Monjardin, K. M. Nowak, R. McBride, D. R. Hall, *'Fabrication of novel micro-optics for applications in manufacturing'*, Poster presented at the Scottish Manufacturing Institute (SMI) Conference, Edinburgh, UK (2007).

E. Mendez, K. L. Wlodarczyk, K. M. Nowak, H. J. Baker, R. McBride, D. R. Hall, *'CO_2 laser micro-smoothing of silica'*, Poster presented at the Scottish Manufacturing Institute (SMI) Conference, Edinburgh, UK (2007)

Chapter 1
Introduction

1.1 Opening words

This thesis is in the area of laser processing of glasses for optical applications. Within this work, CO_2 laser-induced deformations produced on the surface of fused silica, Borofloat®33, and some selected lead-silicate glasses, when treated by approximately 1 mm and 50 µm diameter laser beams, are investigated in detail. Further development of a CO_2 laser polishing technique [1-4], which is currently used for the fabrication of free-form silica micro-optical components, is carried out. Finally, searching of new possible applications for CO_2 laser polishing is also undertaken by the author.

The research has been carried out within the Lasers and Photonics Applications (LPA) group at Heriot-Watt University, under the auspices of the Heriot-Watt Innovative Manufacturing Research Centre (HW-IMRC). The work described in this thesis has been partially funded by PowerPhotonic Ltd., an industrial partner involved in the research activities carried out by HW-IMRC. This company specializes in manufacturing of micro-optical components to the customer's specifications.

1.2 Historical background

For the last 10 years, researchers of the LPA group have studied CO_2 laser beam interactions with fused silica surfaces. Within this time period, they have developed

a unique laser-based technique that enables the fabrication of customized refractive micro-optical components, such as phase corrective plates for high power diode laser (HPDL) bars and stacks [5, 6] and flat-top beam shapers for laser beam transformation in fibre laser applications [7].

Nowadays, HPDLs in the form of bars and stacks are extensively used for pumping both high power solid-state and fibre lasers as well as for direct material processing. Although HPDLs clearly surpass other laser sources in terms of efficiency, compactness, and lifetime, they suffer from poor beam quality which is caused by beam positioning errors (commonly named the 'smile' effect) and wavefront aberrations [6]. Generally, the smile effect and the aberrations result from the practical imperfections in manufacturing and mechanical mounting of the bars as well as from a fast-axis collimation (FAC) lens [8], which is typically mounted to the chip in order to reduce high beam divergence along the fast (X) axis, as can be seen in Figure 1.1.

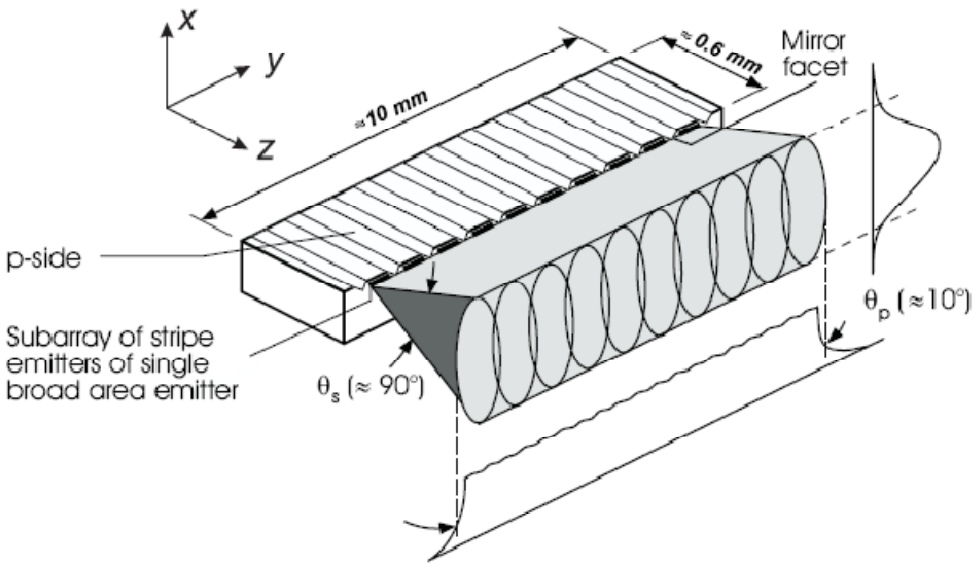

Figure 1.1: Illustration of a single diode laser bar, published in [8].

To restore the intrinsic radiance (brightness) of commercially-available diode laser bars and stacks, a novel beam corrective technique has been developed within the LPA group. Generally, this technique involves three stages. At the first stage, the smile effect and FAC errors along each bar, as clearly seen in Figure 1.2 (a), are measured using a wavefront sensing procedure developed in-house [5]. Measurements are carried

out for the stack operating at full laser power. Once the measurement is finished, the output data are processed and a net-shape surface for the phase plate for compensating the smile effect and aberrations is obtained. Physically, the phase plate is manufactured by laser ablation of a fused silica blank. Since a laser-cut surface is characterized by relatively high roughness, the machined structure is required to be polished. For this purpose, a CO_2 laser polishing process – the subject of this thesis – is employed. Once the phase plate surface is smoothed, the component is AR-coated for the required wavelength, and then is mounted to the heat sink. The evidence of effectiveness of the correction process applied for a single bar of a 440 W HPDL stack (OptoPower Corp., US) is shown in Figure 1.2 (b).

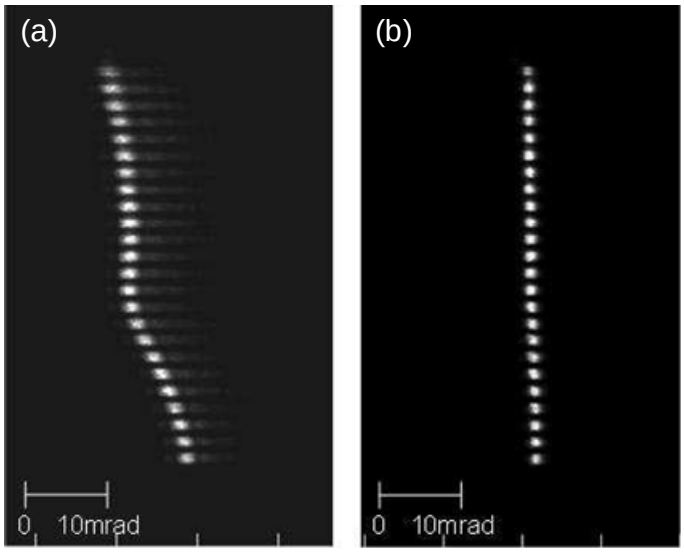

Figure 1.2: Slow-axis image, fast-axis far-field of a single diode bar in the stack: (a) as delivered by manufacturer, and (b) when a corrective phase plate is applied. Published already in [5].

As mentioned above, the fabrication process of corrective phase plates for HPDLs utilizes a CO_2 laser polishing process. Generally, this completely thermal process performed on a glass surface relies on the generation of a thin layer of melt pool, which flows under the action of surface tension forces, so that small surface defects and roughness can be effectively reduced, and even removed [1].

The pioneering work within the LPA group on CO_2 laser beam interactions with fused silica was carried out by G. Markillie [9]. Based on his research, a potential

window for CO_2 laser processing of fused silica was established. The first group member working on CO_2 laser polishing was K. Nowak, who characterized the CO_2 laser polishing process performing with a small diameter laser beam (less than 1 mm) as a fourth-order low-pass filter in the Fourier domain (see Section 4.2 for more details). Based on this concept, at present, it is possible to determine the laser smoothing conditions at which the surface roughness represented by high spatial frequencies is significantly reduced, whilst the overall shape of the polished structure represented by low spatial frequencies is minimally disturbed [3]. Finally, it is necessary to mention E. Mendez, whose research was focused on damage repair of fused silica optics using a moving laser beam [10]. Within this study, he developed a theoretical viscous flow model based on the Navier-Stokes equations for describing CO_2 laser polishing of fused silica surfaces. In addition, he made an initial assessment of the capability of CO_2 laser polishing for smoothing sharp step edges in the binary etched structures. The research in this field is continued and extended in Chapter 4 of this thesis.

In conclusion, it should be noted that CO_2 laser polishing is not only limited to the fabrication of free-form micro-optical components, as covered above. Based on the scientific literature, this process has also found use in the enhancement of surface damage resistance in fused silica optics [11-13], in laser polishing of conventional glasses [14] and optical fibre ends [15, 16], as well as in localized repairing of damage in fused silica optics [1, 2]. Due to the fact that so many applications exploit CO_2 laser polishing, it is obvious that advanced research in this field must be continued.

1.3 Motivation

The international interest of many researchers in use of CO_2 laser polishing for micro-optical manufacturing [3-7] and surface improvement [1, 2, 11-16] has resulted in the need for further development of this excellent technique. At present, however, this completely thermal process is restricted only to fused silica surfaces. The motivation of the research carried out in this thesis is to expand the CO_2 laser polishing technique to new optical materials. Successful CO_2 laser processing of non-silica glasses without material cracking may be a groundbreaking approach in the fabrication of free-form micro-optical components with diverse properties (e.g. refractive index and thermal expansion coefficient). In the future, this achievement may lead, for instance, to the

miniaturization of micro-opto-electromechanical devices (MOEMS) as well as highly-integrated laser systems. Searching for new possible applications of CO_2 laser polishing is also an appropriate motivation for writing this thesis. For instance, preliminary results on CO_2 laser smoothing of binary gratings [10] suggest that the polishing may also be applied for the fabrication of micro-optical components using the concept of thermal reflow [17]. Finally, CO_2 laser polishing requires further investigation in terms of laser-induced surface deformations and stresses. Since this process is used for many applications, as mentioned above, the knowledge concerning the deformations and stress is highly desirable. For instance, this knowledge may lead to the improvement in surface finishing of state-of-the-art micro-optics, i.e., corrective phase plates and beam-shapers.

1.4 Objectives of this thesis

The objectives of this thesis are listed as follows:

- Investigation of surface deformations in fused silica (HPFS®7980 Corning), when treated by a moving CO_2 laser beam, in order to determine the extent of distortions produced by CO_2 laser polishing.
- Evaluation of the magnitude of the CO_2 laser-induced stresses that have occurred in the surface of fused silica plates (HPFS®7980 Corning).
- Study of the capability of CO_2 laser polishing for the relaxation of sharp step edges of etched silica structures, in order to convert this digital optic into a continuous surface.
- Demonstration of CO_2 laser polishing as a method for the fabrication of sub-millimetre-wide toroidal mirrors for some selected planar waveguide applications.
- Investigation of CO_2 laser machinability of Borofloat®33 and some selected lead-silicate (high-refractive-index) glasses, in order to extend the range of applications for the CO_2 laser-based fabrication process. CO_2 laser treatment of glass, when preheated to high temperature, is also the aim of the research.

1.5 Thesis structure

This dissertation is organized into nine chapters plus an appendix for Chapter 7. This chapter describes the motivation and main objectives of this thesis. Chapter 2 contains the background information necessary for the understanding of the experiments and results described in the subsequent chapters of this thesis. Hardware used in the thesis experiments and a general experimental protocol is presented in Chapter 3. The experiments are described in Chapters 4 to 8. In Chapter 4, binary and multi-level etched structures are treated by a moving CO_2 laser beam in order to determine the extent of the surface relaxation of sharp step edges that occurred in these structures. Based on these results, a novel approach for characterizing the CO_2 laser smoothing effect has been developed. In Chapter 5, the CO_2 laser-induced deformations produced on the surface of both fused silica and Borofloat®33 glass, when treated by a moving laser beam, are investigated in detail. In this chapter, some interesting findings in terms of the fictive temperature and the Marangoni effect have been uncovered. In addition, for the first time to the author's knowledge, an operational CO_2 laser polishing window for Borofloat®33 has been determined. Chapter 6, in turn, describes a novel approach (based on CO_2 laser polishing) for the fabrication of toroidal mirrors with a high ratio of the two principle radii of curvature. As will be shown in this chapter, these mirrors may be successfully applied in some mode-selective resonator configurations to improve the laser beam quality of a high-power planar waveguide laser. Chapter 7 is focused on the investigation of stresses induced by CO_2 laser polishing, suggesting that stress is anisotropic in the laser-treated fused silica plates. Chapter 8, in turn, provides pioneering results with regard to CO_2 laser micro-machining of Borofloat®33 and some selected lead-silicate glasses, showing characteristic features occurred at the surface of each glass, when irradiated by a single laser pulse, using an axial irradiance between 25 and 600 kW/cm^2 and laser pulse duration in the range of 25 - 100 µs. Finally, Chapter 9 concludes the work covered in this thesis and discusses future work related to the subjects covered in each experimental chapter.

Chapter 2
Fundamentals of laser processing of glass

2.1 Introduction

This chapter includes background information that is necessary for the understanding of results presented in this thesis. The structure of this chapter is as follows. Section 2.2 explains the nature of glasses and shows the formation mechanism of the amorphous structure in these materials. A discussion on chemical composition of different types of glasses, such as fused silica, borosilicate glass, soda-lime silicate glass and lead-silicate glass, is provided in Section 2.3. A specific chemical composition of these glasses results in diversity of their physical properties, e.g., refractive index, thermal expansion coefficient, and softening point. This means that each type of glass may react to laser irradiation differently at specific wavelengths, laser powers, and pulse durations. The physical properties of glasses which are important from the point of view of processing with a CO_2 laser are discussed in detail in Section 2.4. The thermal, optical, and mechanical properties of different glasses are collated in this section. This section also provides a detailed discussion on the modification of the fictive temperature and the viscosity of glass by laser irradiation. In Section 2.5, special attention is paid to selected issues related with the phase transition in glasses caused by rapid heating and cooling during CO_2 laser processing. Problems such as crystallization of glass, devitrification of fused silica, the generation of surface deformations, thermal stresses and fractures in glass due to laser irradiation, and stress removal by annealing, are also

discussed here. Section 2.6 includes a review of laser-based machining techniques for the fabrication of micro-structures and micro-optical components in glass. This section puts special emphasis on CO_2 laser micro-machining, indicating the advantages and disadvantages of this process in comparison to other laser-based machining techniques.

2.2 Glass as an amorphous solid

Glass is defined as a solid product of fusion of a material which has been cooled from the liquid state to that of a rigid body without crystallization. This means there is a lack of long range periodicity in the molecular structure of glass. The formation of the glassy state can be described in terms of the following specific volume vs. temperature diagram, as shown in Figure 2.1.

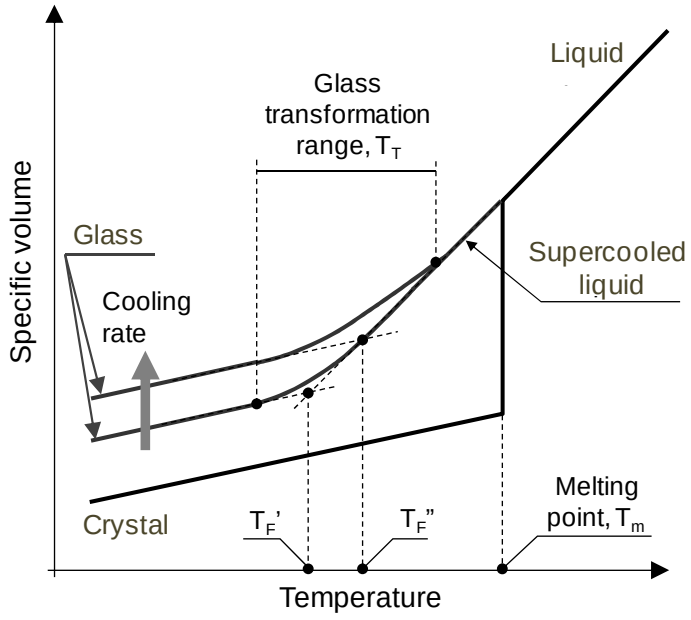

Figure 2.1: Specific volume as a function of temperature during the state transformation of glass.

The specific volume of a molten glassy material (liquid) decreases steadily as the melt is cooling down. If the rate of cooling is sufficiently low, the process of crystallization may occur, forming a long-range periodic arrangement in the glass network. Crystallization is characterized by a rapid decrease of specific volume at the melting point, $T_{M,}$ and soon after a steady contraction of the solid with decreasing temperature. The specific volume is defined as the volume occupied by unit mass of a material. It is equal to the reciprocal of the material density.

If the cooling rate is higher than the rate of nucleation and crystal growth, it is possible for the liquid to be cooled below the melting point without crystallization. This state of matter is called supercooled liquid. The structure of a supercooled liquid at a molecular level continues to rearrange as the temperature decreases. There is no abrupt decrease in the specific volume as occurs with crystals. As the liquid is cooled further, the viscosity increases and the displacement of atoms become more difficult. The specific volume then begins to deviate from the equilibrium line, following a curve of gradually decreasing slope, as shown in Figure 2.1. When the viscosity of glass is sufficiently high ($\eta > 10^{12}$ Pa·s), the liquid becomes a frozen amorphous solid. Further cooling of the solid glass continues to shrink the material, steadily reducing its specific volume. The final value of specific volume of the glass at low temperature is strongly dependent on the cooling rate used. Normally, the specific volume increases for higher cooling rates.

The temperature region where the specific volume has nonlinear behaviour is called the glass transformation range, T_T. This transformation range varies, depending on the cooling rate. By extrapolation of the glass and supercooled liquid lines in Figure 2.1, it is possible to define the point at which these two lines are intersected. This point is called the fictive temperature of the glass, T_F. This characteristic temperature is strongly dependent on the cooling rate and is generally higher when the molten glass is cooled faster. As will be discussed in Section 2.4.5, the fictive temperature has an influence on the physical properties of the glass. Many material properties, such as refractive index, density or thermal stress resistance, are changed as fictive temperature increases.

2.3 Chemical composition of glasses

The main ingredient of most glasses is silica (SiO_2) which is commonly found in nature as quartz sand. The tetrahedral structure of this oxide allows both forming glass on its own and provides a base for other mixed-oxide glasses. A pure silica glass is known for exhibiting the highest melting point, the smallest thermal expansion, and good chemical durability in comparison to other glasses. By adding a mixture of sodium oxide (NaO_2), calcium oxide (CaO), magnesium oxide (MgO), aluminium oxide (Al_2O_3), boron trioxide (B_2O_3), or lead oxide (PbO) to pure silica, it is possible to produce glasses with

higher refractive index, lower melting point, modified viscosity, good chemical resistance, etc.

To date, there are hundreds of different glasses on the market that are used in our daily life. Since many of them have a similar chemical composition, one can classify them into four major groups: pure fused silica, soda-lime-silica glasses, borosilicate glasses, and lead-silicate glasses. The main features of each glass group, e.g., chemical composition and physical properties, are described in following two subsections.

2.3.1 Fused silica

Fused silica has very high melting temperature (T_m > 1700°C), and when melted has a high viscosity ($\eta \sim 10^6$ Pa·s) [18]. Since the viscosity of fused silica cannot be significantly reduced by simply increasing the temperature, this glass is very difficult to produce by conventional glass-melting techniques. Several methods, such as electrical fusion, flame fusion, arc-melting, flame hydrolysis of $SiCl_4$, and chemical vapour deposition (CVD), have been used to fabricate silica glasses with high purity (SiO_2 > 99.9%) [19].

Depending on the manufacturing method used and the impurities present in raw quartz, silica glass has significant differences in its structure that result in variations in its material properties. The electrical fusion technique, for example, utilizes a large carbon rod to heat up the surrounding quartz sand by passing an electric current of 1000 – 2000 A through the rod. This causes, however, only partial amorphisation of the quartz since it is non-uniformly melted. The flame method gives more complete fusion, making the glass structure more random. This method, however, introduces additional impurities that break up the continuity of the network. The highest purity silica glass is obtained by using CVD in which volatile silicon compounds are oxidized at high temperatures. This technique is expensive and unprofitable for mass production of fused silica plates; however, it is extensively used for fabrication of optical fibre preforms where an extremely high purity of SiO_2 is desired.

Silica glasses are generally classified into four categories, according to their synthesis process [20]. Type I silica glasses are produced from natural quartz by electrical fusion under vacuum or within an inert gas atmosphere. They contain a few ppm OH ions but relatively high concentration of metallic impurities, such as Al or Na.

Type II silica glasses are produced from quartz crystal powders by flame fusion. Metallic impurities in theses glasses are less than in Type I silica glasses, but the atmosphere of hydrogen-oxygen flames causes an OH content of about 150 - 400 ppm. Types III and IV silica glasses are synthetic vitreous silica produced by hydrolysis of $SiCl_4$. They are practically free from metallic impurities. Type III silica glasses contain a high amount of OH ions, in order of 1000 ppm, and about 100 ppm of chlorine. Type IV silica glasses contain a small amount of OH content, less than 1 ppm, and approximately 200 ppm of chloride [20, 21]. The impurity content of three fused silica samples provided by different manufacturers is compared in Table 2.1.

Table 2.1: Comparison of three samples of fused silica provided by different manufacturers [21].

Glass name	HPFS®7980	Suprasil®W	Puropsil®A
Manufacturer	Corning	Heraeus	Saint Gobin Quartz
Type (category)	III	IV	I
Manufacture method	flame hydrolysis	flame hydrolysis	electric fusion
Origin material	$SiCl_4$	$SiCl_4$	natural quartz
Impurity of OH ions	900 ppm	0.4 ppm	20 ppm
Other impurity	Cl (unknown ppm)	200ppm Cl	metallic (Al or Na)
Density [g/cm^3]	2.201	2.204	2.003

The OH content plays significant role in determining the thermo-mechanical properties of fused silica. For instance, fused silica with the low OH content has a viscosity of $\eta = 10^{13}$ Pa·s at 1400°C, whilst the viscosity of high OH content silica at the same temperature is only 10^{11} Pa·s [22]. Such a difference in the glass viscosity at constant temperature means that CO_2 laser processing of silica from various manufacturers may need to be performed at different laser irradiation conditions.

The experiments described in Chapters from 4 to 7 were carried out on high-purity synthetic fused silica samples (HPFS®7980 Corning) produced by flame hydrolysis. They belonged to type III silica glasses. The samples were provided by Valley Design Corp. (US).

2.3.2 Silicon-oxide based glasses

As indicated in Table 2.1, samples of fused silica produced by different method or from different raw materials have different impurities, and hence some small changes in their physical properties. In order to obtain more significant changes in the properties of glass, many other inorganic oxides (called network modifiers and intermediates) are added to the SiO_2 network during the glass-making process. Network modifiers disrupt the continuity of the former structure, whereas intermediates either join the network or occupy holes in the network. The list of common network modifiers and intermediates with their characteristics is presented in Table 2.2.

Table 2.2: Common network modifiers and intermediates added to the SiO_2 network former and their influence on properties, according to [19].

Oxide	Function and its effect on SiO_2 network former
NaO_2	*Network modifier*. Reduces softening point and durability. Raises thermal expansion and ionic conductivity.
K_2O	*Network modifier*. Similar to Na_2O but larger K^+ ion less mobile.
LiO_2	*Network modifier*. Similar to Na_2O but smaller Li^+ ion more mobile. Promotes devitrification, i.e., the process of crystallization in a formerly crystal-free glass.
CaO	*Network modifier*. Inhibits mobility of alkali ions, hence increases resistivity and durability of alkali glasses.
MgO	*Network modifier*. As CaO.
ZnO	*Network modifier*. As CaO.
Al_2O_3	*Intermediate*. Strongly suppresses devitrification. Increases viscosity and therefore makes melting and refining more difficult.

Apart from network modifiers and intermediates, one can distinguish other inorganic oxides that readily join with silica oxide, forming a glass with varied properties. For instance, an oxide mixture of boron and silica reduces the viscosity of glass liquid without producing adverse changes in thermal expansion and durability, whereas lead oxide is widely used to raise the refractive index and dielectric constant of

a glass. A wide variety of oxides that can be mixed with the SiO_2 former network means that the glass market is filled up by hundreds of glasses with different chemical and physical properties. Depending on the glass composition, however, each silica-based glass can be allocated to one of three major groups:

Soda-lime-silica glasses

Soda-lime-silica glasses are basically mixtures of silica (70 – 74 %), sodium oxide (12 – 16 %) and calcium oxide (5 – 11 %). This group of glasses is widely used in the form of bottles, jars, and window panes. Coloured glass can be made by adding other chemicals. The soda-lime-silica glasses have excellent internal glass quality, high transmission in the visible spectrum, and good resistance to chemical attack from aqueous solutions. The drawback of these glasses is low durability to high temperatures and sudden thermal changes.

Borosilicate glasses

These glasses are made mainly of silica (70 – 80%) and boron trioxide (7 – 13%) with small amounts of aluminium oxide and the alkalis, such as sodium and potassium oxides. These glasses have relatively low alkali content and consequently have good chemical durability and thermal shock resistance. They are widely used in the chemical industry for laboratory glassware, for domestic ovenware, for various high intensity lighting applications, and as glass fibres for textile and plastic reinforcement.

Lead-silicate glasses

The main compositions of lead-silicate glasses are lead oxide (20 – 65%) and pure silica (30 – 60%). They also contain small amounts of the alkalis, i.e., potassium and sodium oxides. These glasses have a high chemical durability and high refractive index. They are commonly used in art, for decorative glass objects, in electronics, for glass-to-metal seals in the bases of electric lamps and electronic valves, and also in optics, for production of lenses and optical fibres. Glass with high lead oxide content (~ 65%) is also used for radiation shielding because of lead's ability to absorb gamma and other forms of harmful radiation.

In this thesis, an investigation of an influence of CO_2 laser irradiation upon the surface morphology of both borosilicate and lead-silicate glasses was carried out. In experiments described in Chapter 8, samples of Borofloat®33 from the borosilicate glass family and samples of LAFN7®, SF57®, and N-SF66® from the flint lead-silicate glass group were used. All these glasses were manufactured by Schott AG in Germany.

2.4 Physical properties of glass materials

The most important physical properties of glass materials which are relevant to the processes involved in CO_2 laser treatment are discussed in this section. A review of the thermal, optical, and mechanical properties given here provides the basic knowledge which is required to facilitate understanding of both the observed phenomena and the results described in the following chapters.

2.4.1 Thermal properties

CO_2 laser treatment of glass is a thermal process in which laser pulses with duration greater than 1 µs generate high temperatures on the glass surface. Thus, the thermal properties of glass, such as the coefficient of thermal expansion (*CTE*), thermal conductivity (k), specific heat (C_p), and thermal diffusivity (κ) must be known because their values tell us how a particular material reacts to an incident laser beam. For instance, Xiao *et al* have shown that only glasses with a low coefficient of thermal expansion can be laser polished at room temperature without cracking [23].

The thermal properties of glass are divided into two major groups: structure sensitive and structure insensitive. The thermal properties which are structure sensitive depend on occasional irregularities which occur in the quasi-ordered arrangement of atoms. These irregularities in the structure of a glass may be introduced by some impurities, but also by the thermal rearrangement of atoms or molecules as the temperature of the glass increases. Structure insensitive properties are those which are resistant to changes in micro- or macro-structure. They are related mainly to the local short-range interactions between atoms or molecules in the glass. This means that the value of a structure insensitive property for a glass is much the same as that for a crystal of the similar composition [19].

Thermal conductivity

An example of the structure sensitive property is the thermal conductivity, k, which indicates the ability of glass to conduct heat. This parameter is defined as the quantity of heat flux, dQ/dt, transmitted normally through a plate of particular area, A, when a certain temperature gradient, dT/dx, exists over the material. Then, thermal conductivity is given by:

$$k = \frac{1}{A} \cdot \frac{dQ}{dt} \cdot \frac{dx}{dT} \tag{2.1}$$

For non-metallic solids (e.g. crystals and glasses) the heat transfer by conduction is realised mainly by phonons, i.e., quasi-particles characterized by the quantization of the modes of thermal vibrations of the glass lattice. Due to an irregular arrangement of atoms (molecules) in glasses phonons transmitted through the structure are scattered, so that the thermal conductivity of glasses is lower in comparison to crystals of the same composition [24].

The thermal conductivity of fused silica in the temperature range from 27°C to 1827°C has been measured by Wray and Connolly [25]. Good approximations of their experimental results are given by two linear equations. In the temperature range from 27°C to 795°C, the thermal conductivity in *W/m·K* units is given by:

$$k(T) = 1.120 \cdot 10^{-3}\, T + 1.285 \tag{2.2}$$

whereas for temperatures between 795°C and 1827°C,

$$k(T) = 1.177 \cdot 10^{-4}\, T + 2.082. \tag{2.3}$$

The thermal conductivity of Borofloat®33 glass can be also described using a linear equation, but the available data only exist for the range of temperatures from 20°C to 160°C [26]. In this case, the thermal conductivity as a function of temperature is given by:

$$k(T) = 0.846 \cdot 10^{-3}\, T + 1.117 \tag{2.4}$$

Coefficient of thermal expansion

Another example of the structure sensitive parameter is the coefficient of thermal expansion. This thermal property defines a change in the size of a solid when the

material is subjected to the temperature change. The volumetric coefficient of thermal expansion, β, is defined as:

$$\beta = \frac{1}{V} \cdot \left(\frac{\partial V}{\partial T}\right)_{P=const} \tag{2.5}$$

where V is the volume of a solid, and $\partial V/\partial T$ is the rate of the volume change with temperature at constant pressure P. Since glass is an isotropic material, it is more common to use the linear coefficient of thermal expansion, *CTE*, which is three times smaller than β.

Thermal expansion of glass originates from the non-harmonic vibrations of its atoms [27]. These vibrations occur in a substance at any temperature above 0 K. As the temperature of a glass increases, the amplitude of vibrations also increases. Because forces between atoms are asymmetrical (the repulsive forces are larger than the attractive forces for the same amplitude of atomic vibrations), this means that glass expands as its temperature is increased [19]. An exception is fused silica glass which has negative *CTE* at temperatures below -80°C. This unusual behaviour may be related to the very open structure of the glass network and the consequent predominance of vibrational modes involving displacement of the silicon and oxygen ions transverse to the bond direction [19]. At room temperature and above, fused silica has a very low thermal expansion coefficient, in comparison to quartz or to other glasses. The linear *CTE* of this glass was shown to be about 0.6 ppm/K over a wide temperature range from 20ºC to 1400ºC [28]. Such a low *CTE* is advantageous from the point of view of CO_2 laser micro-machining of fused silica.

Specific heat capacity

The third important thermal property of glass materials is the specific heat capacity, C_p, often shortened to the specific heat. This parameter determines the heat energy, Q, which is required to increase temperature of a material that has a mass, m, by a certain temperature interval, ΔT. The specific heat is defined as follows:

$$C_P = \frac{Q}{m \cdot \Delta T} \tag{2.6}$$

The specific heat is a thermal property which is structure insensitive. This means that the specific heat for glass is similar in value to the specific heat for a crystal of the same composition.

Figure 2.2 shows the change in the specific heat as a function of temperature for Borofloat®33 glass [26] and fused silica [29]. Data are available for temperatures up to the transition point for Borofloat®33 (T_g = 525ºC) and slightly above the softening point for fused silica (T_S = 1600ºC). According to [29], the specific heat for fused silica, C_p, can be described by a 5th order polynomial function, given as follows:

$$C_P(T) = 9.9048 \cdot 10^{-14}\, T^5 - 8.0867 \cdot 10^{-10}\, T^4 + 2.5806 \cdot 10^{-6}\, T^3 - 0.0041\, T^2 + 3.3688\, T + 35.9360 \quad (2.7)$$

Equation (2.7) is valid for a temperature range from 273 K to 1973 K. The values of C_p are expressed in the J/(kg·K) units.

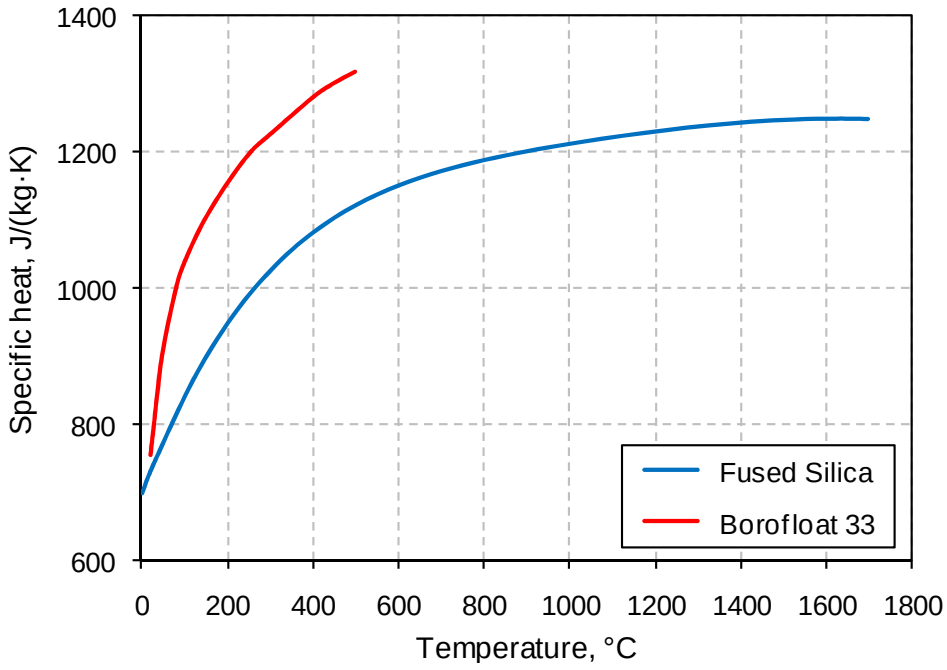

Figure 2.2: Specific heat capacity of fused silica and Borofloat®33 as a function of temperature. Data taken from [26, 29].

Thermal diffusivity

In situations in which the temperature of a material changes with time, it is necessary to use a thermal property called a thermal diffusivity (κ). This parameter is related to the thermal conductivity (k), density (ρ), and specific heat capacity (C_P) as follows:

$$\kappa = \frac{k}{\rho \cdot C_P} \tag{2.8}$$

The thermal diffusivity is used to describe the propagation rate of the thermal front in glass under transient thermal conditions. Generally, materials with high thermal diffusivity are able to adjust their temperature rapidly to that of their surroundings, because they conduct heat quickly in comparison to their thermal bulk.

Table 2.3 shows a list of thermal properties of the glasses used in the experiments described in this thesis. Values of the thermal conductivity and the specific heat capacity for fused silica and Borofloat®33 are given both at room temperature and at the highest temperatures for which data are available.

Table 2.3: Comparison of thermal properties of selected glasses at room temperature. The values of some thermal properties for fused silica and Borofloat®33 are also given for higher temperatures.

Glass	*CTE* [ppm/K]	k [W/m·K]	C_P [J/kg·K]
Silica (HPFS Corning 7980) [30]	0.6	1.31	770
		2.30@1830ºC	1250@1630ºC
Borosilicate (Borofloat®33) [26]	3.2	1.20	830
		1.31@160ºC	1320@500ºC
Lead-silicate (SF57) [31]	9.2	0.62	360
Lead silicate (N-SF66) [31]	6.8	0.80	540
Lead-silicate (LAFN7) [31]	6.4	0.77	-
Soda-lime-silica (Float Glass) [32]	8.4	0.90	860

2.4.2 Optical properties

The optical properties of solids are not directly dependent on the form or even existence of long-range order in the structural network, but rather on the nature and local arrangement of the constituent atoms or ions [19]. Thus, the optical properties of glasses are similar to those of crystals of the same chemical composition.

Absorption coefficient

When light propagates through glass, its intensity, *I(x)*, decreases exponentially along the optical path, *x*, according to the Lambert-Beer law:

$$I(x) = I_0 \exp(-\alpha\, x) \tag{2.9}$$

The rate of the intensity decay depends on the absorption (attenuation) coefficient, α, of the glass.

Most oxide glasses absorb little light in the wavelength range from visible to near infrared of up to 3.5 µm. This means that these glasses have a high transmittance in this spectrum band, usually greater than 80 percent. In the ultraviolet (UV) and infrared (IR) spectral regions beyond 3.5 µm, the absorption coefficient significantly increases and the light may be efficiently coupled into the material. The absorption of light by glass in the UV spectrum range is dominated by electronic excitation of molecules, while in the IR it is dominated by molecular vibrations [33]. Strong optical absorption by glasses in the UV and IR regions of the spectrum opens the possibility for machining of these materials using appropriate lasers. A more detailed discussion of processing of glasses using different types of lasers is provided in Section 2.6.

Extinction coefficient

The absorption coefficient is related to an extinction coefficient of glass, *k*, which is the imaginary part of the complex index of refraction, $n' = n + ik$. The extinction coefficient determines the strength of material absorption and is strongly dependent on wavelength [34]. The relationship between the absorption coefficient, α, and the extinction coefficient, *k*, is:

$$\alpha = \frac{4\pi \cdot k}{\lambda}. \tag{2.10}$$

Absorption depth

In many cases, it is more convenient to use the term "absorption depth", which is defined as the inverse of the absorption coefficient. The absorption depth determines the distance into the glass at which the incident light decreases by a factor of *1/e* of its original intensity.

Reflectivity

Another important optical property of glasses is the reflectivity (*R*). This parameter determines the fraction of the incident radiation which is reflected from a glass surface. The reflectivity of glass is dependent on the real part (*n*) and the imaginary part (*k*) of the complex refractive index, as follows:

$$R = \frac{(n-1)^2 + k^2}{(n+1)^2 + k^2} \tag{2.11}$$

Figure 2.3 shows both the absorption depth and the reflectivity of commercial fused quartz Vitreosil® in the IR wavelength range from 7 µm to 14 µm. The two curves have been generated using equations (2.10) and (2.11) with optical constants, *n* and *k*, taken from Table 1 in [35].

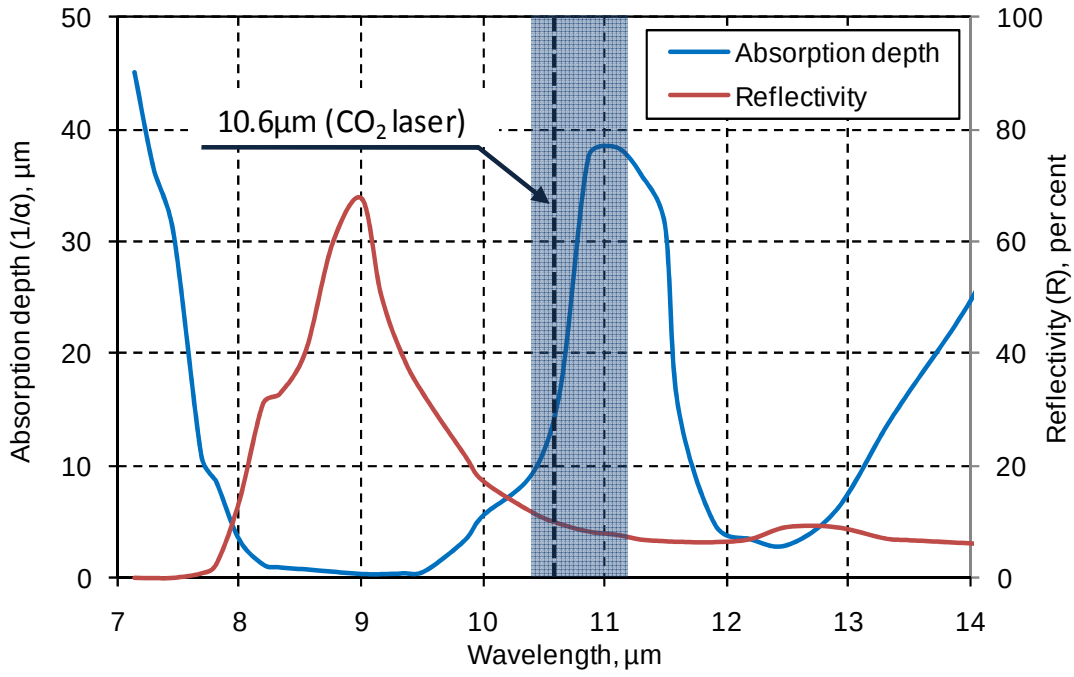

Figure 2.3: Absorption depth (1/α) and reflectivity, *R*, of an electrically fused quartz Vitreosil® sample as a function of wavelength, based on data from [35].

In the IR spectrum shown in Figure 2.3, the absorption depth is less than 40 µm, so that the light absorption by the glass is very strong. The reflectivity of this glass is below 20 percent for most wavelengths, apart from the band between 8 µm and 10 µm in which the reflectivity is higher, reaching more than 70 percent at 9 µm. The band of high reflectivity at 9 µm wavelength is attributed to the bond-stretching vibration between the Si and O atoms in a Si-O-Si linkage [19]. The peak of high reflectivity at 9 µm wavelength is typical for all silicon-based glasses.

The wavelength band between 10.4 µm and 11.2 µm has been specially shaded in Figure 2.3 because it corresponds to the operating spectrum of CO_2 planar waveguide lasers. In this wavelength band, the absorption depth of glass varies from 10 µm to ~ 40 µm, whereas the reflectivity is approximately 10 percent. The large variation of absorption depth means that CO_2 lasers used for glass machining may require wavelength stabilization because any fluctuations of the laser wavelength during the process will cause changes in the absorption depth and consequently produce a different rate of glass removal.

Finally, all optical properties of glasses are temperature dependent. For instance, McLachlan and Meyer showed that the extinction coefficient of high-purity fused silica and 96% silica Vycor® samples increases substantially with temperature in a linear manner [34]. Based on this knowledge, the extinction coefficient as function of temperature can be simply given by the linear least square fitting function $k(T) = A \cdot T + B$. The list of A and B coefficients which describe the temperature dependence of the extinction coefficient of high-purity fused silica for three wavelengths of 10.26 µm, 10.55 µm, and 10.59 µm is given in Table 2.4. The measurement of the extinction coefficient was performed for a number of about 30 µm-thick samples using temperatures of up to 1800ºC and wavelengths in the range from 9.6 µm to 10.6 µm [34]. A 40 W continuous wave CO_2 laser source was used to generate the high temperatures at specified wavelengths.

Table 2.4: Temperature dependence of the extinction coefficient of high-purity fused silica expressed by the linear least squares fitting function $k(T) = A \cdot T + B$ for given temperature range and laser wavelength, according to [34].

Wavelength, µm	A	B	Temperature range, °C
10.26	$16.67 \cdot 10^{-5}$	$3.41 \cdot 10^{-2}$	25-1200
10.55	$11.04 \cdot 10^{-5}$	$1.82 \cdot 10^{-2}$	25-1600
10.59	$10.10 \cdot 10^{-5}$	$1.82 \cdot 10^{-2}$	25-1800

From the results provided by McLachlan and Meyer, we can also calculate the change of the absorption depth of fused silica as a function of temperature for a specific wavelength using equation (2.10). As shown in Figure 2.4, the absorption depth of fused silica varies significantly with temperature and laser wavelength used. For wavelengths of 10.55µm and 10.59 µm, the absorption depth decreases non-linearly from 40 µm at room temperature to 4 µm at 1800ºC, whereas changes in the absorption depth from 21 - 3 µm in the temperature range of 20 - 1200ºC are observed for the 10.26 µm wavelength. Since the absorption depth of high-purity fused silica does not exceed 45 µm, this means that CO_2 laser machining of this glass is dominated by surface heating without significant absorption of the light into the bulk material.

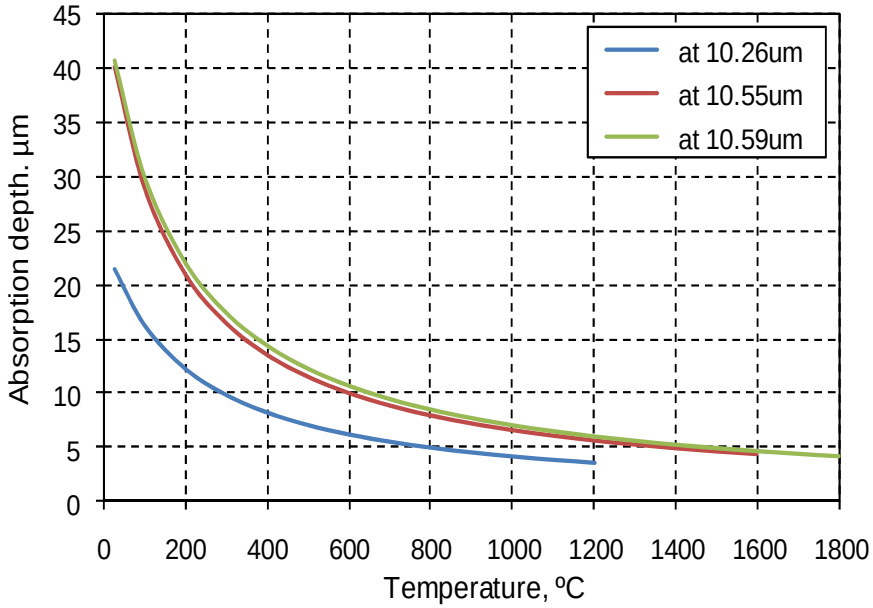

Figure 2.4: Absorption depth of fused silica as a function of temperature at three different wavelengths: 10.26 µm, 10.55 µm, and 10.59 µm, based on data from [34].

2.4.3 Mechanical properties

Glasses at temperatures below the transition point, T_G, become solids and exhibit a brittle-elastic behaviour. This means that deformations in glasses are proportional to applied stress, σ, according to Hooke's law:

$$\varepsilon = \frac{\sigma}{E} \tag{2.12}$$

Generally, the deformations are represented by the tensile strain, ε, which causes an elongation of the material, Δl, per its unit length, l. The quantity, E, is called the Young's modulus and is a characteristic constant of the individual glass. The Young's moduli of the glasses studied in this thesis are listed in Table 2.5.

In glasses, the deformations caused by the stress in one direction usually produce a deformation of the material along the other axis. The ratio of a lateral strain to the longitudinal strain is described by a parameter called Poisson's ratio, v. In glasses this parameter varies from 0.17 to approximately 0.30.

Table 2.5: Mechanical properties of selected glasses at room temperature, based on data from [26, 30, 31].

Glass	Young's modulus, GPa	Poisson's ratio, -
HPFS 7980 Corning	73	0.170
Borofloat®33	64	0.200
LAFN7	80	0.280
N-SF66	95	0.259
SF57	54	0.248

Another mechanical property of glasses is the shear modulus, G, which describes the material's response to a shearing strain, i.e., a strain which acts parallel to the surface of the glass opposed to a normal stress. Similar to the Young's modulus, the shear modulus is defined as the ratio of the shear stress, τ, to the shear strain, γ. For fused silica, the Shear modulus is equal to 30.6 GPa [30].

The mechanical properties *E*, *G*, and *v* are characteristic for the specific type of glass because they are dependent on the chemical composition [19]. For instance, fused silica containing only SiO_2 molecules exhibits relatively high Young's modulus and the lowest Poisson's ratio of all available optical glasses. Young's modulus is the highest for flint glasses containing lanthanum, as shown in Table 2.5.

2.4.4 Glass viscosity

The viscosity, η, is a quantity that describes an internal resistance of a substance to flow when either shearing or tensile stresses are applied. The viscosity plays a significant role in glass making [36], and is also very important in the processing of glasses using CO_2 lasers [9]. It determines parameters such as the melting conditions, annealing temperature, crystallization rate, and maximum temperatures of use. The SI unit of viscosity is Pa·s but the CGS unit Poise is also widely in use. The correlation between these two units is 1 Pa·s = 10 Poise.

The viscosity of glasses is strongly temperature dependent. It varies from non-measurable levels of more than 10^{14} Pa·s at room temperature to less than 10^{2} Pa·s at temperatures above the point when glass starts to evaporate. For a wide range of temperatures above the transformation range, T_T, the viscosity of many glasses can be described by the Arrhenius equation:

$$\eta(T) = A\, exp\left(\frac{B}{R \cdot T}\right) \tag{2.13}$$

where *A* is called a pre-exponential factor, *B* is the activation energy in J/mole, *R* is the gas constant, and *T* is temperature in Kelvin units.

An example of glass which has a viscosity-temperature relation that can be fitted to the Arrhenius equation is fused silica. In the temperature range from 1273 to 1673 K, the viscosity of silica in Pa·s units is given by [37]:

$$\eta(T) = 3.8 \cdot 10^{-14}\, exp\left(\frac{712000}{R \cdot T}\right) \tag{2.14}$$

whilst the viscosity in a temperature range from 1465 to 2755 K is expressed as [38]:

$$\eta(T) = 5.8 \cdot 10^{-8}\, exp\left(\frac{515400}{R \cdot T}\right) \tag{2.15}$$

According to Doremus [39], who provided critical assessment of experimental data on the viscosity of silica from the literature, equations (2.14) and (2.15) describe the most reliable viscosity change of silica over a wide temperature range.

An accurate model of glass viscosity has been developed recently. This model is relevant to commercial applications by using a global statistical approach and is based on a viscosity database of more than 2200 glass compositions available in the SciGlass information system [40]. The viscosity curve that results from the model can be described by a three-parameter equation, the so-called Vogel-Fulcher-Tammann (VFT) equation:

$$\log_{10}\eta(T) = A + \frac{B}{T - T_0} \tag{2.16}$$

where *A*, *B*, and T_0 are temperature-independent constants. Table 2.6 contains a list of values of *A*, *B*, and T_0 constants applied to the VFT equation which describes the viscosity-temperature relation of borosilicate [41], soda-lime-silica [42], and lead-silica glasses [43].

Table 2.6: The list of *A*, *B*, and T_0 coefficient values which describe the viscosity in Pa·s units as a function of temperature in common glasses.

Glass	*A*	*B*	T_0 [°C]	Reference
Borosilicate	-2.560	4852	192.5	[41]
Soda-lime-silica	-2.729	4560	240.8	[42]
Lead-silica	-2.621	4255	152.1	[43]

Figure 2.5 shows four curves which represent the viscosity change as a function of temperature for fused silica, borosilicate, soda-lime silica, and lead-silica glass. The curves were obtained from the Arrhenius equation (2.15) for fused silica, and based on the VFT coefficients from Table 2.6 for other glasses.

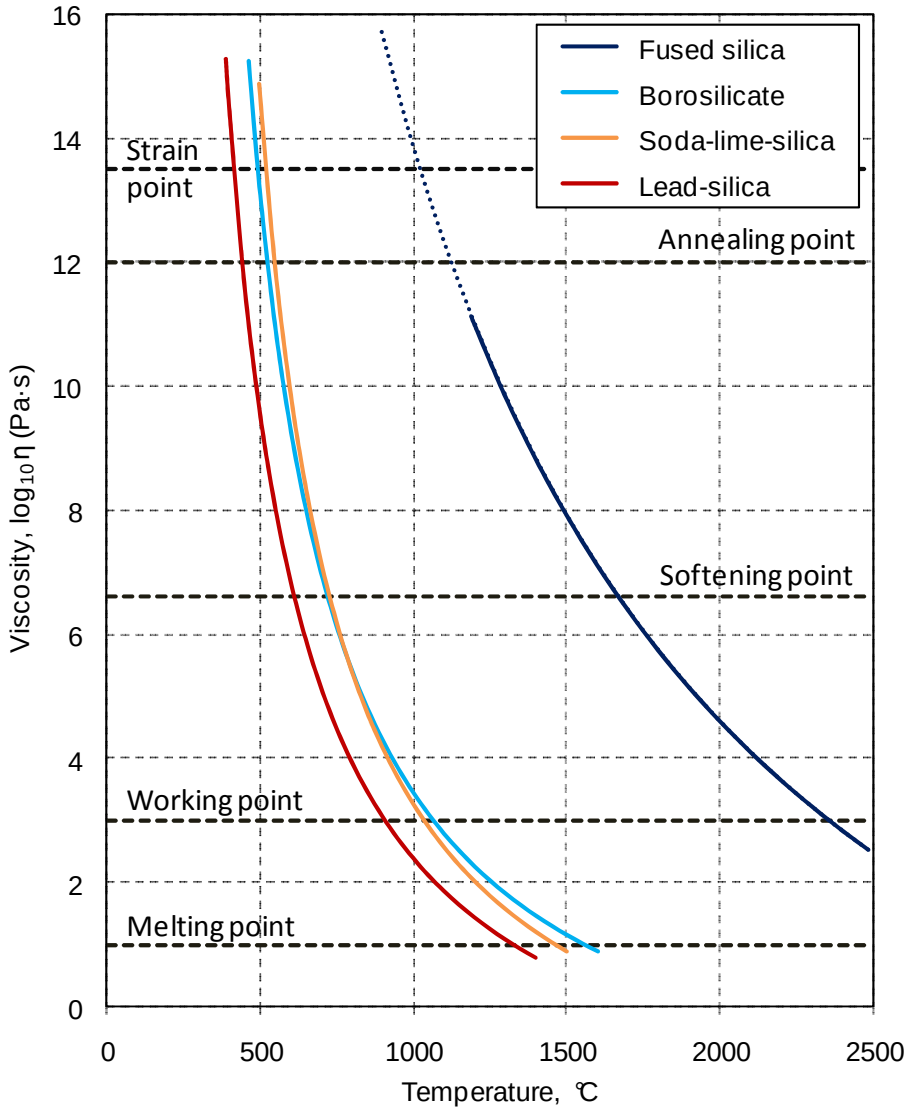

Figure 2.5: The viscosity-temperature relation in common glasses. Curves were plotted based on data from [38, 41-43].

Generally, there are a number of named temperature regions assigned to glasses in which certain melt properties are identified. From the lowest to the highest temperature, these regions are as follow:

a) The **strain point** at viscosity of $10^{13.5}$ Pa·s, is the highest temperature from which glass can be rapidly cooled without introducing serious internal stresses. A glass is kept at this point for a several hours to substantially relieve internal stresses.

b) The **annealing point** at viscosity of 10^{12} Pa·s, where any internal stresses in glass are relieved within a few minutes.

c) The **softening point** at viscosity of $10^{6.6}$ Pa·s, where glass deforms under its own weight. The glass is still considered as a solid.
d) The **working point** at viscosity of 10^{3} Pa·s, where the glass is sufficiently soft for shaping (blowing, pressing) in a glass forming process
e) The **melting point** at viscosity of 10^{1} Pa·s.

Comparing the curves in Figure 2.5, one can notice that the viscosity-temperature relation of silica is much different from those for other glasses because all characteristic points are obtained at temperatures which are at least twice as high. This means that fused silica, especially with a low concentration of OH ions [22, 37], is difficult to shape because the working point is close to a temperature of about 2800°C at which a significant volatilisation of silica at atmospheric pressure takes place.

The internal stresses in glasses are relieved faster for lower viscosity. The time required to relax the glass is determined by the relaxation time. This quantity is defined as the time at which stresses fall to 1/e of their initial value if the strain is kept constant. In general, the relaxation time in glass is equal to the ratio of viscosity to the Young modulus [44]. This means that internal stresses in the glass are relieved more slowly when the viscosity is higher. For viscosities above the strain point the relaxation time is practically infinite.

2.4.5 Fictive temperature

The term of fictive temperature was first time proposed by Tool [45] who suggested that glass, which is cooled through the transformation range (see Figure 2.1), has an identical frozen-in structure as to that of its melt at some equilibrium temperature. The temperature at which the liquid structure is frozen into the glassy state is called the fictive temperature [21]. Depending on the cooling rate of glass in the transformation range, the glass network undergoes either faster or slower structural change and therefore the material may have different fictive temperature values. Glass cooled rapidly usually has higher a fictive temperature than the same glass cooled more slowly. The value of fictive temperature may vary from the strain point to the softening point for a particular glass [46]. Normally, commercial glasses have fictive temperatures between the strain point and the annealing point because they are cooled slowly in the manufacturing process (during annealing). However, the value of fictive temperature

of glass can be increased if the material is re-heated above the annealing point and then is cooled down with a high cooling rate, as happens for example in some laser machining processes.

The change of fictive temperature affects many of physical properties of glass. Fictive temperature dependent properties include: refractive index, density, hardness, viscosity, and specific volume (as shown in Figure 2.1). The effect of the fictive temperature depends on whether glass is normal or anomalous.

A classic example of an anomalous glass is fused silica. This glass exhibits increasing density [21, 47-51], refractive index [20, 52], hardness [53], and Young's modulus [54] with increasing fictive temperature. According to Shelby's measurements [47], the density of fused silica increases by ~ 5 ppm/°C in the fictive temperature range from 1000°C to 1600°C, whilst the refractive index change in the similar fictive temperature range is ~ 1 ppm/°C [52].

Most silicate glasses such as soda-lime-silica, lead-alkali-silica and alumina-silicate glasses, are classified as normal [55]. This means that most of their properties exhibit the opposite trend to those in fused silica as the fictive temperature is increased [56]. The exceptions, however, are the viscosity and the mechanical strength. For both normal and anomalous glasses, the viscosity decreases [37] and the mechanical strength increases [57] with increasing fictive temperature.

From the point of view of CO_2 laser micro-machining of glasses, the influence of fictive temperature changes on the glass properties have enormous significance for structural modifications during laser processing. As mentioned previously in this section, the fictive temperature of the manufactured glass has a value between the strain point and the annealing point. In the case of CO_2 laser micromachining, the glass is repetitively heated up to temperatures above the annealing point and cooled down to room temperature with the rate as high as 10^4°C/s [58], and thus the fictive temperature of the glass is increased. This means that the properties of glass after laser irradiation, such as refractive index or density, are different to those before laser firing [59]. A partial restoration of the original properties of such glasses can be obtained by an annealing of laser-irradiated samples. More information on the annealing process is given in Section 2.5.5.

2.5 Issues related to phase transition in glasses during laser processing

When a laser beam is coupled into the surface of a glass substrate, the material may undergo phase transitions between solid, liquid and gaseous states of aggregation, depending on the temperature and pressure generated by the incident beam. The transformation of the glass state may then lead to changes in its structure and physical properties. This section outlines some important aspects related to phase transitions occurring in glasses when they are undergoing heat treatment, typically in the form of laser beam irradiation.

2.5.1 Crystallization

Crystallization is a localized process which starts from nuclei. Crystal nuclei start to form when the glass is heated to some temperature within the transformation range. Further temperature increase causes that the rate of nucleation is increased to some maximum at a specific temperature depending on the glass composition, and then decay to zero at the melting point. Nucleation can occur homogeneously (i.e. randomly without preferential sites in the material) or heterogeneously (i.e. at preferred sites such as surfaces, grain boundaries, and second-phase particles). In glass, heterogeneous nucleation dominates because of the presence of defects and impurities in the structure.

Nuclei in the molten glass initiate the crystallization process. Below the melting point, the glass structure is thermodynamically unstable and therefore shows a tendency towards crystallization. The rate of crystal growth is determined by the probability of formation of stable crystal nuclei. The highest rate of crystallization takes place within the transformation range. Below this range, the crystallization process is less intensive and here it is caused by the presence of alien nucleation centres, such as metal ions, interface boundaries or dust.

The rate of crystal growth is also determined by the cooling rate of the particular glass composite. For instance, substances like SiO_2 start to crystallize when the cooling rate is less than 1°C/hour, while for metallic melts cooling rates as fast as 10^{12}°C/s may start this process [60]. This fact has important implications in CO_2 laser processing of fused silica. A lack of crystallization is observed in this glass because the cooling rate during laser machining is significantly faster than the rate of crystallization of SiO_2.

Most commercial glasses have a tendency to crystallize mainly at the surface due to the dominant heterogeneous nucleation resulting from structural defects, grain boundaries and any impurities adhered to the surface. From the point of view of fabrication of micro-optical components, this effect is destructive because it leads to an increase in the light scatter, making the glass opaque.

2.5.2 Devitrification of fused silica

The process in which a glassy texture of a material is converted into a crystalline texture below its fusion point is called devitrification. In the case of fused silica, devitrification takes place at temperatures above 1200°C, but may also happen below 1000°C if some impurities are present in the glass. At room temperature, the devitrification rate in silica is practically zero [61]. However, the rate may be significantly increased if the material is in direct contact with the human skin which contains alkali metal elements, such as sodium, potassium, and other impurities. To overcome this problem, glass should be washed in pure deionised or distilled water and then air-dried in a clean environment or wiped dry with a clean alcohol-wetted tissue. In order to remove a thin contaminated layer from a glass surface, sometimes it is necessary to use a 5 – 10% hydrofluoric (HF) solution prior to washing [61].

2.5.3 Surface deformations induced by laser melting

A material surface which is affected by laser beam irradiation usually undergoes permanent deformations in the form of ripples, corrugations, bumps or craters. The shaping effects are almost always related to surface melting, evaporation or ablation, and they may appear even if the intensity distribution of the incident laser beam is uniform [60].

The basic sequence for deformation by laser melting is that a material melts, allowing the molten layer to flow, and finally resolidifies following irradiation, making the deformation permanent. The deformation mechanism depends on the absorbed fluence as well as on the material composition [62]. For instance, deformations on an Al substrate coated with amorphous Ni-P results from the gradient of capillary forces which act on the surface of the molten pool. Since the surface tension of the melt decreases with temperature, the liquid tends to be pulled away from hotter towards cooler sites. This results in meniscus-shaped deformations in the case of stationary

beams and in ripple formation in the case of scanned beams. This phenomenon is called the Marangoni effect.

In glasses, the surface deformations caused by laser melting usually have the form of either dome-shaped or W-shaped bumps. This specific shape of the bumps may result from the Marangoni effect [10, 63] and a local increase of fictive temperature due to a fast cooling rate of the material following laser treatment [58, 64]. In the case of chemically strengthened glass substrates, the mechanism of bump formation may be additionally amplified by release of the glass surface from embedded stresses during laser treatment [65, 66].

The bump formation mechanism due to the local fictive temperature change in a glass substrate has been explained by Bennett *et al* [64]. In order to identify the thermal physical nature of bump formation, they did several experiments using three types of glasses: aluminosilicate glass, zinc silicate glass, and partially re-crystallized lithium disilicate glass ceramic. The glasses were irradiated by single CO_2 laser pulses of specific energy and duration, and by multiple laser pulses with 20 ms pulse repetition. In both cases a spiral pattern of bumps was generated on the surface. The samples of glass were also annealed at different temperatures both prior to and after laser irradiation. From the results of these experiments, they concluded that a local increase in glass volume, and consequently the generation of bumps, resulted from the density reduction due to an increased fictive temperature. The development of bump geometry depended on basic laser processing parameters, such as a total treatment time of the substrate and the pulse energy used. They also found that all glasses used in their experiments had a distinct energy threshold at which there was a rapid growth of the bump. This implies that there was an activation temperature for the process, below which the glass did not undergo any surface changes. Above the energy threshold, they specified two processing regimes. The first regime was called the “principle regime” in which a gradual growth in bump height with respect to pulse energy was observed. The second regime, named the “terminal regime”, defined an energy range in which a dimple occurred in the centre of the bump and grew more pronounced as the pulse energy or the number of laser pulses was increased further. In this regime, a large vapour recoil pressure in combination with thermocapillary flow inhibited the vertical growth of bumps.

The study of annealing effects by Bennett *et al* [64] showed that the height of bumps written in glass depended on the thermal history of the samples before laser processing. In the case when bumps were written in annealed glass, the height of these deformations was smaller than the height of the bumps generated in an unannealed glass substrate for the same values of energy and pulse duration. Built-in stresses in unannealed glass had influence on bump formation, increasing the height of bumps by approximately a factor of 2. However, the diameter of bumps was unaffected. Similar results have been obtained by other researches, e.g., Kuo *et al.* [65] who studied the behaviour of chemically strengthened and non-strengthened soda-lime glasses on CO_2 laser irradiation.

When the glass with laser-written bumps is heated and held at an elevated temperature, the whole substrate relaxes and the bump height is reduced significantly, more than in the case when bumps are created in annealed glass. The reduction in the bump height is most likely caused by the expansion of the surrounding glass, resulting in stress relief driven by annealing and by the densification of the bump material volume as the microstructure approaches an equilibrium corresponding to the annealing temperature [64].

Several numerical models of dome-shaped bumps formation by CO_2 laser pulse irradiation of silicate glasses have been developed [58, 66-68]. These models predict both a maximum height and diameter of bumps, showing good agreement with experimental results. Depending on the established mechanism of bumps growth, models include different input parameters which are related to both glass properties and laser processing conditions.

Tam *et al* assumed that bumps are generated by both localized thermal expansion of the glass within the heated zone and the relaxation of the embedded stresses [66]. The height of bumps, *H*, can be determined by the equation:

$$H = 4\sqrt{2\,\kappa\,\tau}\cdot\left(CTE\cdot T_p + \frac{\varepsilon}{K}\right) \tag{2.17}$$

where *CTE*, κ, and *K* are the thermal expansion coefficient, thermal diffusivity, and bulk modulus of the glass, respectively. T_p is the maximum temperature rise caused by the laser pulse heating averaged over the spot area, τ is the laser pulse duration, and ε is the compressive stress of the chemically strengthened glass.

Another model used to predict the dome-shaped surface topography of bumps was proposed by Shui *et al* [58]. The model is based on the concept that permanent structural changes in glass are induced by a higher glass transition temperature due to a faster cooling rate. The final topography of a bump is determined by the temperature history resulting from the absorbed laser energy. Using this model, the maximum height of bumps, H_{max}, is given by:

$$H_{max} = C \ \ln\left(\frac{F}{F_{th}}\right) \tag{2.18}$$

where F is the laser energy used per unit area (fluence), F_{th} represents the threshold laser fluence for bump formation, and C is the growth rate of the bump height with respect to the logarithm of laser fluence [58]. The C and F_{th} values were evaluated from the experimental results for a given laser fluence. The model also provides information on the diameter of generated bumps, d_B, and the new transition temperature of the glass, T_G. The equations are given as follows [58]:

$$d_B = w\sqrt{2 \ \ln\left(\frac{F}{F_{th}}\right)} \tag{2.19}$$

$$T_G = \left(\frac{CTE \cdot (1-R)}{\rho \cdot C_p}\right) \cdot F_0 \ exp\left(-\frac{{d_B}^2}{2 \cdot w^2}\right) \tag{2.20}$$

where R, ρ, and C_p are the reflectivity, density, and specific heat of glass, respectively, and w is the radius of laser beam used measured at $1/e^2$ of its maximum intensity.

The most sophisticated model of bump formation on a silicate glass surface, which employs a dynamic calculation of the glass transition temperature as a function of time and viscosity, was provided by Bennett *et al* [67, 68]. The model is based on a finite element solution to the heat diffusion equation:

$$\rho \cdot C_p \cdot \left(\frac{\partial T}{\partial t}\right) - \nabla(k \cdot \nabla T) - g = 0 \tag{2.21}$$

where g is the laser energy introduced as a volumetric heating source [67]. Bennett's calculations showed that the fictive temperature in silicate glass is increased by more than 300°C in relation to the conventional value during laser treatment. This fictive temperature increase causes the reduction in the glass density by about 1.3% for

unstrengthened glasses and 2 – 3% for chemically strengthened glasses. The model also provides information on the maximum thermal penetration depth of the glass transition temperature and surface stresses induced by laser pulse irradiation.

The same numerical model has been also used to study the thermophysical nature of silica glass as a result of rapid CO_2 laser heating by Zhao *et al* [69]. The numerical simulations showed that the fictive temperature of the heat affected zone is elevated by about 1000°C as the glass is heated to the boiling point of about 2900°C, in comparison to the initial value (T_F = 1090°C) at room temperature. Considering the fact that an increase in fictive temperature of silica causes an increase in its density (see Section 2.4.5), the deformation that results from CO_2 laser treatment should have a form of a depression on the surface rather than a dome-shaped bump. However, this shape of deformation has not been found in any publication.

The investigation of surface deformations in fused silica induced by a moving CO_2 laser beam was carried out by my colleague Dr E. Mendez [10]. He showed that the deformity in fused silica has the form of a W-shaped feature which contains a central bump surrounded by two prominent lateral lobes. According to his theory, the W-shape on the glass surface results from a non-uniform distribution of surface tension during laser irradiation due to varied oxygen concentration of the glass surface (the chemicapillary effect), impurities, and the temperature gradient generated by the incident Gaussian beam.

2.5.4 Thermal generation of stress

Glasses have low values of thermal conductivity in comparison to metals. Consequently, internal temperature gradients induced across some thickness of glass by a localized heat source are usually large. This means that stresses are generated either at the glass surface or inside this brittle material, causing a reduction in strength or even fractures.

In the case of CO_2 laser processing of glasses, inhomogeneous surface stresses are built-up because a thin layer at the glass surface is heated up above the annealing point and cooled down repeatedly. During laser heating, the laser energy is absorbed by glass and the temperature of the heat affected zone rises rapidly, reaching the maximum temperature within ~ 0.1 s of laser exposure [70]. Due to the low thermal diffusivity of glass, the heat from the affected zone slowly spreads radially towards the bottom

surface, generating a steep thermal gradient across the glass thickness. This means that the upper layer of glass expands more than the bottom layer, so that the glass temporarily bends towards the colder side (negative bending). The bending angle, in this case, is very small because only the laser irradiated area is expanded. When the upper surface of glass starts melting locally, the yield stress in the heat affected zone is reduced. This results in an appearance of compressive plastic strains. As the laser beam passes away, the temperature of the heat affected zone decreases quickly, trying to reach a thermal equilibrium state. The rapid cooling shrinks the upper layer of glass and consequently causes bending of the material towards the laser irradiated site (positive bending). The bending angle of glass is significantly larger than that observed for negative bending because the shrinkage of the upper layer is amplified by the expansion of the glass along the bottom surface. The expansion of the bottom surface is induced by the residual heat transfer from the upper surface.

Laser bending of mono-crystalline silicon, borosilicate glass sheets and Al_2O_3 ceramics have been recently studied by Wu *et al* [70, 71]. They showed that the bending angle of 150 µm thick glass sheets can be either negative or positive of up to 25 degrees, depending on the laser beam diameter and the scanning speed used. In the case when the laser beam diameter used is significantly larger than the glass thickness and the processing time is relatively slow, resulting in a small temperature gradient across the glass thickness, the glass sheet is bent away from the incident laser beam. A negative bending of the glass results from the mechanism called in the literature the "buckling mechanism" [72]. This mechanism (and others) is described in detail in Section 7.2. The positive bending of glass is observed when the laser beam diameter has the same order of magnitude as the glass thickness or less, whilst the scanning speed is large enough to generate a steep temperature gradient in the material. The bending of glass towards the incident laser beam has been also observed during CO_2 laser polishing of fused silica plates (see Chapter 7).

Generally, the magnitude of the internal stresses, σ, generated in bulk glass due to the temperature difference, ΔT, can be estimated using a simple formula [61, 73]:

$$\sigma = \frac{E \cdot CTE \cdot \Delta T}{1 - \nu} \tag{2.22}$$

From equation (2.22), it is clear that the internal stresses in glass are weaker for smaller thermal expansion coefficient and the Young's modulus. Thus, optical glasses with

large *CTE* and Young's modulus values are very sensitive to thermal shock and they crack easily during laser treatment. To reduce internal stresses in glass during laser processing, a common technique is to preheat glass to the temperature just below the transformation point in order to reduce the rapid temperature changes. Successful CO_2 laser polishing of initially preheated conventional glasses, such as Pyrex, BK-7, or B-270, has been already demonstrated by a few research groups [23, 74].

In addition, a preliminary study of stresses induced by CO_2 laser polishing of silica has been carried out in the Laser and Photonic Application group at Heriot-Watt University [10, 61]. The research work has indicated that the laser polishing process introduces an approximately 60 MPa residual stress at the glass surface. Although the stress has the same order of magnitude as the tensile strength of mechanically polished fused silica [30], the glass does not break during laser polishing because the laser-irradiated surface is healed from pre-existing micro-cracks which are the main reason of glass cracking. This mechanism explains why CO_2 laser polished fused silica optical surfaces reveal a higher laser-damage resistance at 355 nm and 1064 nm wavelengths, in comparison to mechanically polished fused silica optics [11, 12].

2.5.5 Annealing

The development of internal stresses in glass due to thermal treatment may result in either instantaneous or delayed cracking along a boundary of the heat affected zone, depending on the magnitude of the generated tensions. The delay time can be in a range from a few milliseconds to many days, so it is important to make sure that glass after processing is relieved from stresses before final use. The process in which frozen internal stresses in glass are substantially removed is called annealing.

The principle of the annealing process is shown in Figure 2.6. In the first stage of annealing, the glass is heated up to some point between the strain point and the annealing point (for information on these characteristic points see Section 2.4.4) and then is kept at this temperature until the entire glass reaches thermal equilibrium. The heating rate and the holding temperature depend on the type of glass. For glasses with a high coefficient of thermal expansion, the heating rate must be significantly lower than for low expansion glasses, such as fused silica or quartz. In general, the heating rate has to be low enough to prevent thermal fracture of glass due to its thermal expansion.

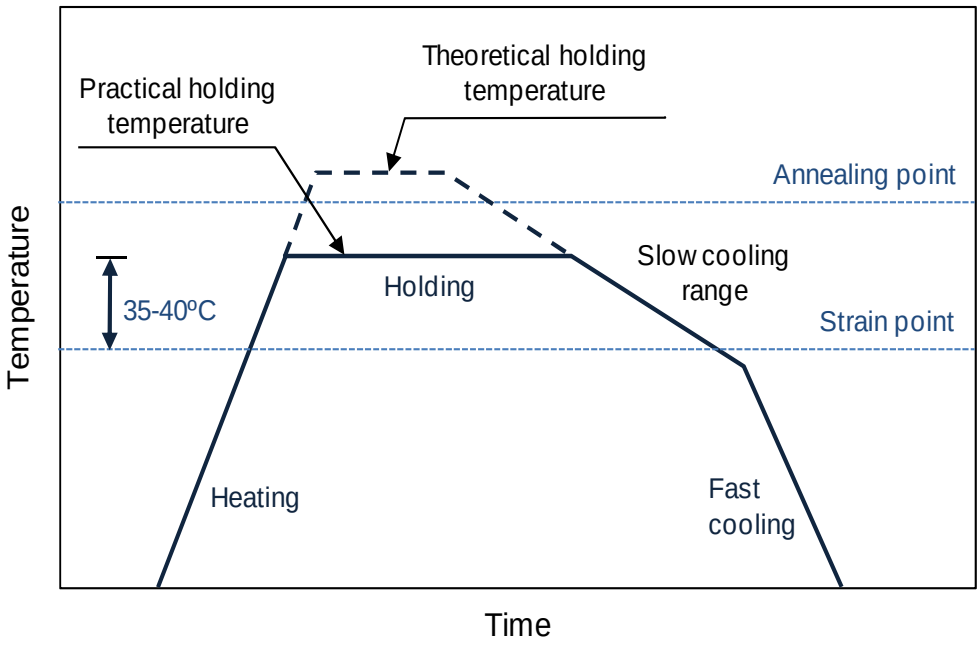

Figure 2.6: Typical schedule of glass annealing, according to [75].

The holding temperature is a temperature at which the glass relaxes without deforming. The theoretical holding temperature is approximately 10°C above the annealing point, but in practice the holding temperature can be slightly below this point to prevent deformation of glasses, especially for thin and delicate samples. The time required at the holding temperature depends on the size and the shape of the glass sample. A thin walled tube, for example, requires significantly shorter holding time than a large and thick block of glass. A holding temperature of approximately 30 minutes is generally adequate for most glasses.

The most critical stage of annealing is the cooling process from the holding temperature to 10 – 20°C below the strain point, because in this range significant permanent stresses can be developed if the cooling rate is too fast. Using the engineering formula from [75], the maximum rate of cooling, $R_{C/sec}$, for a glass plate with thickness, d, is given as follows:

$$R_{C/sec} = \frac{24\,\kappa\,\sigma_{ac}\cdot(1-\nu)}{E\cdot CTE\cdot d^2} \tag{2.23}$$

where σ_{ac} is the acceptable stress at the mid-plane of glass. To obtain the residual stress of less than 1 kPa in a 1 mm thick fused silica plate, the cooling rate has to be less than 20°C per minute.

As the temperature of the glass decreases below the strain point, the cooling rate can be significantly increased. Thermal stresses which result from this rapid cooling are present temporarily in glass, but they disappear when the glass reaches room temperature.

2.6 Laser micro-machining of glasses

This section includes a brief survey of three laser machining techniques used for the fabrication of microstructures in optical glass materials. Processing of glass using ultrafast lasers, lasers operating in deep ultraviolet, and CO_2 lasers are described here. The mechanism of interaction between laser beam and glass is explained for each technique. Their applicability, advantages and disadvantages are also presented. Key features of each process are highlighted in Section 2.6.4.

2.6.1 Micro-machining using ultrafast lasers

Ultra-short laser pulses in the femtosecond range are an attractive solution for high quality micro-machining of glass materials. Such short laser pulses combined with high peak intensity results in laser-induced optical breakdown, a process in which a normally transparent material is transformed into absorbing plasma. As a result of the laser-induced absorption, the material undergoes locally either phase or structural modifications. These modifications cause a permanent change in the refractive index or even material removal through direct vaporization [76].

There are two nonlinear processes that cause laser-induced breakdown in a material: multi-photon absorption and avalanche ionization [77]. Multi-photon absorption is dominant when the laser beam intensity is very high ($> 10^{12}$ W/cm^2). For laser pulses greater than 100 fs, when the laser field strength is significantly lower, multi-photon absorption is negligible and laser-induced breakdown is dominated by avalanche ionization. Since both nonlinear processes last less than picoseconds, there is the absence of thermal diffusion in a material which leads to a very thin heat-affected zone in the machined area.

The first demonstration of the use of femtosecond laser pulses to ablate micrometer sized features on fused silica was reported in 1994 [78]. It was shown that the laser-induced optical breakdown threshold for femtosecond pulses is much smaller

than for pico- or nano-second laser pulses. The benefit of the use of femtosecond laser pulses also includes the fact that both the optical breakdown threshold and the ablation rate are more deterministic. Additionally, laser pulses with duration longer than 1 ps introduce defects during the first laser pulse, which leads to a disruptive effect in subsequent processing. The well-defined breakdown threshold combined with the marginal heat-affected zone in the machined area offers the possibility of ablating the material with a diameter smaller than the size of the laser spot [77]. This means that the dimension of machined features can be smaller than the laser wavelength used. Since femtosecond laser pulses have negligible thermal diffusion, they are ideally suited to precise deep micro-cutting and micro-drilling of glass materials, such as fused silica, quartz, or borosilicate glass [79-83].

A very interesting application of ultrafast lasers is the generation of microstructures within bulk glasses by the modification of refractive index ($\Delta n \sim 10^{-5}$ to 10^{-2}). In this process, the focused laser beam with average laser power below the ablation threshold is injected into a glass substrate in order to induce a local change in its refractive index. When the substrate is moved along the optical axis of the focusing beam with a constant speed, a waveguide can be written inside the glass.

The fabrication of waveguides using femtosecond laser pulses has been already successfully applied for various types of glasses, such as fused silica, Ge-doped silica, borosilicate glass, fluoride glass, phosphate glass, and chalcogenide glass [84-87]. Since so many glasses can be used in this process, this allows the possibility to fabricate both passive and active micro-optical devices. To date, ultrafast laser sources have been used to fabricate Bragg grating waveguides [88], directional couplers [89], three dimensional fan-out devices [90], and rare-earth-doped waveguide lasers [91].

The disadvantages of using ultrafast lasers in glass processing are the low processing speed, the high cost of femtosecond laser sources, the appearance of micro-cracks, and relatively high surface roughness of machined surfaces which are still well below optical quality.

2.6.2 Laser processing of glass in deep-ultraviolet

Glass micromachining by ablation in the pico- or nano-second laser pulse regime requires the use of laser sources operating at wavelengths at which glass has relatively strong absorption. In the case of fused silica, for example, the bandgap energy is

~ 9.3 eV which is equivalent to 133 nm wavelength (deep-ultraviolet light). The lack of a laser source at this wavelength means that glass is difficult to machine using conventional UV lasers. However, the use of a 157 nm F_2 laser, which operates close to the energy bandgap of silica, provides the capability to machine this glass effectively.

Machining with the F_2 laser, in comparison with other excimer lasers (e.g. 193 nm ArF lasers) or ultrafast lasers (e.g. 1.054 µm Nd:glass lasers), gives an remarkable improvement in both the process control and the surface quality of the machined structures [92]. However, the coherence of this laser source is much higher than other excimers due to its narrow linewidth. This can give rise to coherent effects in the beam (a form of speckle) which results in increased surface roughness of the etched material [93]. The minimum etch depth of only 20 nm enables precise shaping of glass with a 120 nm resolution, giving a surface roughness of less than 15nm rms amplitude for an about 3600 μm^2 inspection area. Excellent surface morphology of the machined area without surface swelling, shock-induced micro-cracks and incubation effect enables F_2 lasers to be applied to the fabrication of micro-optical elements. Submicron surface-relief gratings [94], 16-level DOE devices [95], single-mode rib waveguides on silicate-based slabs [96], and microlenses [97] have been already manufactured with nanometre precision and high surface quality. The state-of-the-art of this machining technique is laser fabrication of microlenses directly at the end of a single-mode optical fibre [98]. Parabolic microlenses with a radius of curvature of approximately 10 µm have been generated by a uniform ablation laser spot which was initially projected onto the midpoint of a rotated fibre end and then was moved towards the fibre edge with varied speed, forming overlapping concentric circles. The surface roughness of the machined fibre-lenses was about 100 nm rms which is satisfactory for most optical applications. An analysis of the beam profile created by these microlenses showed that a clean Gaussian beam in the focal plane with the spot diameter of up to one fifth of the fibre core size can be obtained. Since the trajectory and the scanning speed are well-controlled during the fabrication process, this technique can be extended to fabricate spherical or concave microlenses on fibre tips.

The drawback of the use of F_2 lasers for micromachining of glass is the long processing time, low stability of the laser beam, and high cost and complexity of the machining system. Since the 157 nm laser beam is absorbed by the atmosphere,

the laser systems require specialised optical materials (e.g. CaF or MgF), and nitrogen- or argon- or vacuum-filled tubes to transport laser energy to the target.

2.6.3 CO_2 laser micro-machining

A competitive approach for the fabrication of refractive micro-optical components in fused silica is the CO_2 laser direct-write micro-machining process. In this process, the glass is efficiently machined without micro-cracks and splashes due to its strong absorption at the 10.6 µm wavelength, a well-controlled laser power source, and the flexibility of a high pulse repetition frequency.

CO_2 laser micro-machining is a purely thermal process in which melting, vaporization, thermal diffusion, and re-solidification of glass take place. Since all these processes generate residual stresses in the material, only glasses with a low coefficient of thermal expansion, such as fused silica or Pyrex, can be successfully machined without cracking [23]. Depending on the CO_2 laser processing parameters, notably the pulse duration, pulse repetition frequency, peak power, and spot diameter, one can distinguish two kinds of processes: laser polishing and laser cutting.

In the laser polishing process, high repetition rate laser pulses with relatively low axial irradiance generate a raised temperature on a glass surface, sufficient to melt a thin surface layer that flows under surface tension. For fused silica, the generation of a highly mobile glass layer is obtained without significant mass loss when the glass viscosity is in the range between 10^2 and 10^5 Pa·s. This range corresponds to surface temperatures from 2000 to 2700ºC. At temperatures above 2700ºC, melt displacement or melt ejection takes place [9]. In this case, the irradiated glass area evaporates rapidly, leaving a crater surrounded by a molten rim. This evaporation (ablation) effect is used in the CO_2 laser cutting process. To minimize thermal diffusion in the glass, short laser pulses (~ tens of microseconds) with a low repetition rate are used [99]. Significant mass loss by ablation is obtained by the production of large peak irradiance, normally focusing the laser beam to a spot of < 50 µm diameter. Since CO_2 lasers operate in the infrared spectrum, the minimum feature sizes that can be generated in the cutting process are greater than 10 µm.

Fine control over the glass viscosity below the ablation threshold using a CO_2 laser beam has been found to provide an enhancement of the surface damage resistance in fused silica optics [11, 12], laser polishing of conventional glasses [74] and optical

fibre end surfaces [15, 16], localized repairing of damages in fused silica optics [1], and also in the manufacturing of micro-optical components.

The first fabrication of a micro-optical element using a CO_2 laser was demonstrated by U. Paek and A. Weaver [100] who produced a hemispherical lens at the end of an optical fibre. They used a 0.5 cm diameter laser beam that was focused on a fibre end in order to generate heat in the material. By precise control of the laser power and exposure time, the flat fibre end was transformed into a spherical shape due to the effect of surface tension. The microlenses formed in fibres by localized CO_2 laser heating usually have short focal length and extremely low surface roughness. Using this CO_2 laser melting method one can also fabricate rod microlenses, as reported by Calixto *et al* [101].

A more sophisticated, two-step approach for the fabrication of microlenses in tapered fibre ends was reported by Malki *et al* [102]. In the first step, the fibre was melted using a CO_2 laser beam and stretched to the point of separation, creating two symmetrical tapers. In the second step, the fibre tip was simultaneously rotated and laser melted, which resulted in the formation of microlens. Depending on the size of the fibre tip, microlenses with a different focal length were obtained. It has also been shown that microlenses or microlens arrays can be fabricated directly on a glass plate surface [103]. Parabolic-shaped microlenses with a diameter in the range from 100 to 200 µm are formed due to surface tension generated by localized CO_2 laser irradiation of glass. The size and focal length of the microlens depend on the laser beam size, irradiation time and laser power used.

Utilizing a focused CO_2 laser beam as a heat source, one can also manufacture high-performance optical fibre couplers [104, 105]. In this approach, two stripped fibres are aligned parallel and placed in an elongation setup. During the laser irradiation at well-defined laser power, the fibres are fused and stretched by the tension provided by weights, creating a taper shape. The coupling ratio of fused-fibre couplers is monitored by the measurement of fibre outputs during the process. When the desired ratio is obtained, the fibre tension is released. Such method allows fabricating fibre couplers with any coupling ratio and low losses.

Recently, it has also been reported that a scanning CO_2 laser beam focused on a photonic crystal fibre (PCF) may periodically collapse micro-holes in the fibre,

generating a long-period grating [106]. To enhance the contrast of the fibre grating, weights can be attached to the fibre ends to introduce frozen-in strains across the PCF which tend to decrease strongly the refractive index of the fibre [107]. Gratings written in the tensioned PCF with a contrast of about 16 dB and insertion losses of < 0.5 dB have been achieved.

A very interesting approach for the fabrication of micro-optical elements is the use of very short CO_2 laser pulses with high intensities to ablate locally small amounts of glass from a bulky material. The first demonstration of the CO_2 laser cutting process was presented by Presby *et al* [99] who used 10 µs laser pulses with 7.1 MW/cm^2 peak power intensity for the fabrication of efficient microlenses on single-mode optical fibres. In this process, a spinning fibre end placed in a precise XY translation stage was irradiated from the side by the focused laser beam in order to ablate redundant material and generate a tapered shape of the fibre end. Due to strong absorption of glass at 10.6 µm, the cut region of the fibre was melted during the radiation, leaving a nicely-smoothed area with a rounded tip (microlens). The advantage of this technique is the one-step generation of any shape on a fibre end by programmable movement of the translation stage.

A more sophisticated approach for the direct fabrication of refractive micro-optics in fused silica plates was demonstrated by Baker *et al* [108], at Heriot-Watt University. They constructed a CO_2 laser machining workstation which ensures delivery of the laser beam to the target with micrometre precision. An important component of the system is an acousto-optic modulator which enables an online-control over the energy, shape, and duration of the laser pulses. The advantage of this machine is the capability of accurate material processing in both the thermal and ablative regimes. This means that the fabrication of micro-optical components, laser cutting with a depth accuracy better than ± 50 nm and then laser polishing that reduces surface roughness to < 1 nm, is performed using a single machining station. Such an approach significantly reduces the production cost of micro-optics and makes the laser setup more flexible. However, the key advantage of this machine is the capability to generate an arbitrary shape on the glass surface in one processing step. A good example of the uniqueness is the fabrication of corrective phase plates for high power laser diode (HPLD) bars and stacks [5, 6].

To summarize, the CO_2 laser machining process is well-suited for the generation of free shapes in fused silica. The minimum size of machined features is approximately 10 µm. Both strong absorption of the glass at a 10.6 µm wavelength and an approximately 50 µm diameter laser beam used in processing mean that the machining rate for a CO_2 laser is an order of magnitude greater than for the F_2 laser with similar energy fluence [9]. This means that the use of CO_2 lasers for the fabrication of micro-optical components speeds up the process significantly. Moreover, CO_2 lasers are generally cheaper than the ultrafast or excimer laser systems therefore the overall production cost of micro-optics is reduced. The capability of the CO_2 laser machining system to generate freeform optics with an optical grade of surface quality makes this process competitive with the ultrafast and deep-ultraviolet laser machining techniques.

2.6.4 Comparison of laser-based techniques for micro-optics fabrication

This section provides a brief summary of laser-based machining techniques for the fabrication of micro-structures and micro-optical components in glasses. Table 2.7 presents a comparison of different techniques, in which ultrafast lasers, excimer lasers, and CO_2 laser slabs are used as machining tools.

Table 2.7: Advantages and disadvantages of ultrafast, deep-UV, and CO_2 laser micro-machining. Examples of products performed by means of these techniques are also given.

Technique	Advantages	Disadvantages	Products
Ultrafast laser micro-machining	Suitable for many glasses Fabrication of optical devices by refractive index modification High resolution (~ 0.1 µm)	Expensive laser machining systems Long processing time High surface roughness	Simple micro-structures Active and passive micro-optical devices
Deep-UV laser micro-machining	Excellent surface morphology High resolution (< 1 µm)	Slow machining process High cost and complexity of laser systems	DOEs Microlenses Waveguides
CO_2 laser micro-machining	Low fabrication cost Low surface roughness Short processing time Generation of free-form micro-optics	Suitable only for fused silica Low resolution (~ 10 µm)	Microlenses Beam shapers Passive devices Corrective phase-plates for HPLDs

The fabrication of micro-structures using femtosecond lasers offers the capability to machine many types of glasses with high resolution if the laser pulse energy is above the ablation threshold. Ultrafast laser pulses with lower energy can be also used to change locally the refractive index of glass. This approach is utilized for direct writing of waveguides and Bragg gratings into glass substrates. Since the surface quality of optical components machined by ultrafast lasers is quite poor, more often the F_2 excimer lasers are used, giving a roughness of machined surfaces in the optical grade regime. However, the drawback of both the ultrafast and deep ultraviolet laser systems is their high cost. For instance, the UV-laser systems require the use of special optics and gases to minimize absorption of the beam.

The most cost-effective solution for the fabrication of refractive optical components in fused silica is the use of a CO_2 laser source. Strong absorption of fused silica at 10.6 µm wavelength and the larger diameter of the incident beam used makes the CO_2 laser a very efficient and quick micromachining tool in comparison to others lasers. Many processing parameters like the laser power, beam size, or the irradiation time can be controlled online with high accuracy. Thus, the fabrication of 3D micro-optics with an arbitrary shape is now possible. The use of CO_2 laser polishing in the fabrication process enables one to reach an extremely low surface roughness of the machined glass. This makes the CO_2 laser-based technique preferable to both the ultrafast and F_2 laser fabrication techniques.

Chapter 3
Hardware used in the thesis experiments

3.1 CO_2 laser setup operating in CW-mode

The CO_2 laser processing workstation described in this section has been used to perform all the experiments which are described in Chapters 4 - 7. This system is similar in overall design to the workstation used by Dr Enrique Mendez, a former member of the Lasers and Photonics Applications (LPA) group, to study laser polishing of silica micro-optics and to investigate a laser-based technique for surface damage repair of silica optical components. Originally, the intention had been to use this laser system to conduct the research described in this thesis. Unfortunately, this was not possible since the main laser unit suffered a terminal failure and it was necessary to replace it. Since the replacement laser was a different model, it became necessary to completely re-design and re-build the overall laser workstation system. In comparison to the original laser setup, the new workstation was equipped with a wavelength monitoring system, and in addition (as an option) the laser was configured to be driven at a very high pulse repetition frequency (50 kHz), resulting in a quasi-CW (continuous-wave) output beam – referred to as CW operation in this thesis.

3.1.1 Optical arrangement of the laser setup

A schematic diagram and photograph of the rebuilt CO_2 laser processing workstation are shown in Figure 3.1 and Figure 3.2, respectively.

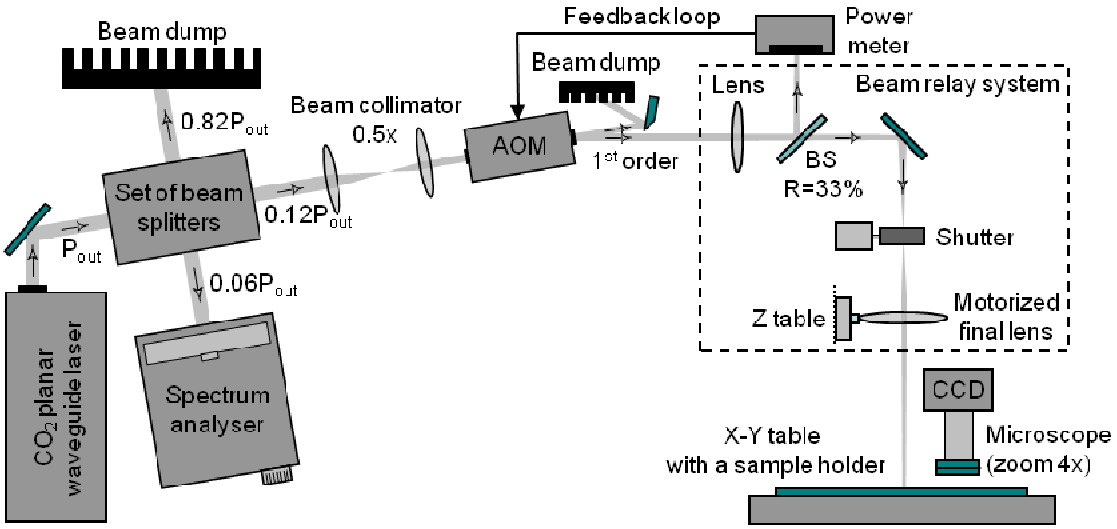

Figure 3.1: Schematic block diagram of CO_2 laser-based system operating in a CW-mode.

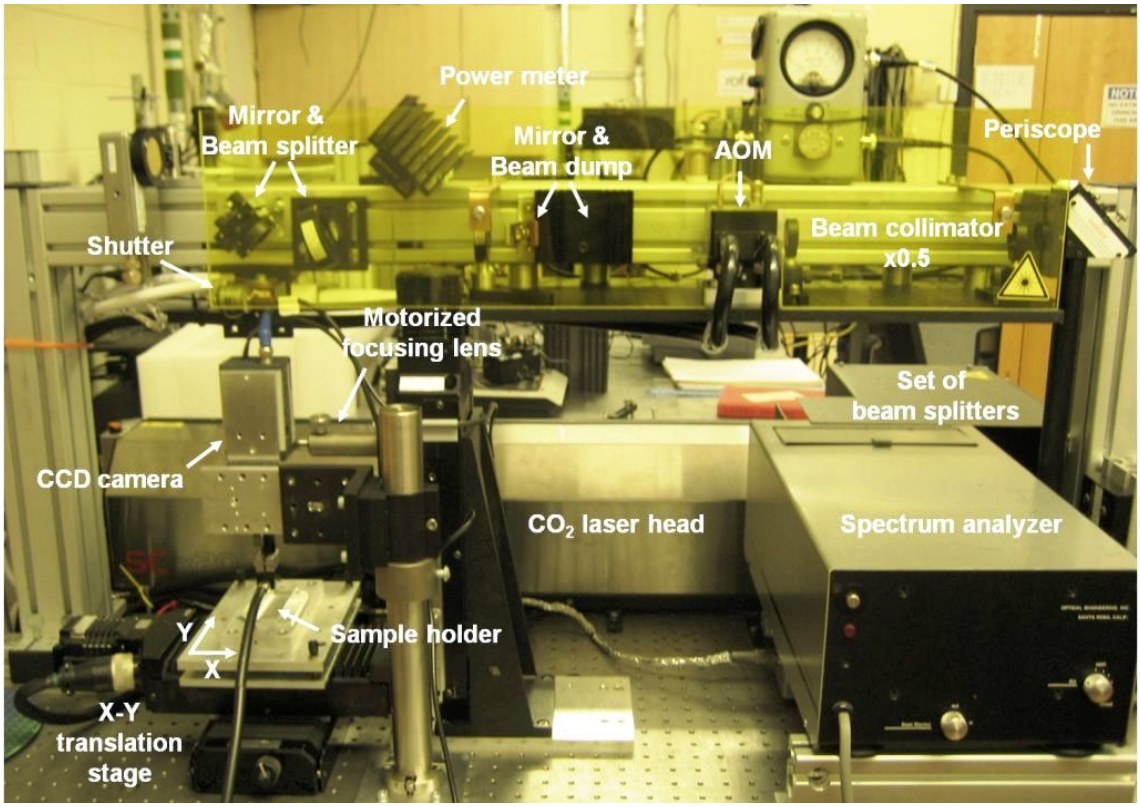

Figure 3.2: Photograph of CO_2 laser-based system operating in a CW-mode.

The key elements of this setup are: a CO_2 planar waveguide laser, a spectrum analyser, an acousto-optic modulator (AOM), a beam relay system, laser power meter, beam shutter, high precision positioning tables, and a CCD camera equipped with

a microscope objective. Some parts of the system, such as the AOM, power meter, shutter, and motorized tables, have been interfaced to a PC and controlled by using custom-written software based on LabVIEW™, written by Dr Francisco Villarreal, a former member of the LPA group.

The core of the laser setup is a commercial RF-discharge excited, diffusion-cooled CO_2 slab laser (Rofin SC x20, UK) operating from 10.4 µm to 11.2 µm. The laser was set to generate 7 µs wide pulses with a repetition of 50 kHz, thereby giving a modulation factor of the RF laser signal as low as 20% (a quasi-CW mode of operation). The output laser power (P_{out}) at the 35% duty cycle was measured to be approximately 240 W. The output laser beam was slightly elliptical with an M^2 value of about 1.2. Based on the laser specification, the beam leaving the laser head was 7.5 mm high and 9 mm wide (measured at the $1/e^2$ intensity).

The AOM (NEOS Technologies, USA) had a restriction on the incident optical average power of 35 W due to the risk of thermal lensing in the germanium crystal and even the possibility of optical damage to the modulator. Therefore, the high-power output beam from the laser had to be distributed into several lower power beams by the use of a set of beam splitters. A small ratio of the total output power (about 0.06 P_{out}) was directed to the spectrum analyzer providing real-time information on the laser wavelength used, 0.82 P_{out} was dumped, and only 0.12 P_{out} was transmitted to the AOM. Fortunately, this restriction matched well to the requirements for laser machining of glasses since the average laser power necessary for vaporization of fused silica is approximately 8.5W (see results in Chapter 5), whilst the maximum laser power on the target available by this system was 10.5 W. In the case of silicon-oxide based glasses (e.g. Borofloat®33), the laser power required for machining was determined to be lower than that for machining of fused silica.

Since the AOM aperture was only 5 mm, the laser spot was reduced by a factor of 2 using the beam telescope which contained two ZnSe meniscus lenses with focal lengths (FLs) of 152.4 and 76.2 mm. The input laser beam was partially deflected into the first diffraction order by the AOM and then was directed towards the target, whilst the non-deflected laser beam was dumped safely. To achieve an approximately 1 mm diameter laser spot on the target, the deflected (first-order) beam was transmitted through the beam relay system containing two additional ZnSe lenses with 340 mm and 95 mm focal lengths. The laser spot with accurate size on the target was achieved by

adjusting only the 95 mm FL lens. This lens was mounted to the translation stage (Z table) which allowed the optics to be moved along the optical axis with a 5 µm resolution.

The laser power delivered to the target was controlled via a PC card interface which provided a modulation signal to the AOM driver. Since the laser had a long-term instability of ± 7% (as will be shown later), the laser setup was equipped with a LABVIEW-based proportional-integral-derivative (PID) feedback loop. The feedback loop allowed the laser power fluctuations on the target to be reduced below 1% (peak-to-valley). The PID loop was applied between the thermopile power meter (Gentec, Canada) and the AOM, as can be seen in Figure 3.1. The response time of the power meter was about 0.6 s and the laser power was sampled with a rate of 5 Hz.

The precise X-Y movement of the glass target during laser operation was provided by two stepper motor tables (Ealing Electro-Optics, UK). The step resolution of the tables was 1 µm in the X axis and 5µm in the Y axis (see Figure 3.2), while the travel range was 49 mm and 99 mm, respectively. The X-Y translation stage ensured both linear and raster scan movement of the workpiece during laser treatment with a maximum speed of 12.5 mm/s.

The laser system was also equipped with a 4× magnification online video microscope which was mounted alongside the motorized final focusing lens. The microscope allowed the determination of the point on the target for laser machining with the 5 µm accuracy. Additionally, it permitted an observer to see machined features larger than 2.5 µm on the glass workpiece with sufficient contrast [1].

Finally, the laser system was connected to a chiller which was placed outside the laboratory building. This means that the temperature of the laser coolant was fixed in principle. Although the chiller allowed the temperature to be set with a 0.1°C accuracy, temperature fluctuations of the coolant coming in and going out from the laser head were measured to be 0.6°C peak-to-valley within an about 4 minute cycle.

3.1.2 Experimental protocol

As mentioned in the previous section, the CO_2 laser setup operating in a quasi-CW mode was not sufficiently stable over a long time period, since the laser had a tendency to change spectral lines frequently and even operate simultaneously on multiple wavelengths. Therefore, it was decided to develop a suitable experimental protocol to

enable the experiments performed using this laser system to be repeatable. Thus, for the experiments in which the continuous laser treatment time of the workpiece was shorter than a few minutes, such as those covered in Chapters 5 and 6, the experimental results could be achieved with the laser operating at only a single wavelength of 10.59 µm. In other experiments which were required to be conducted over longer time periods, the results were achieved under conditions which were selected to enable the laser output to be relatively stable despite operating in a multi-wavelength modes, including the wavelengths from the R-branch ($\lambda < 10.4$ µm).

Typical laser power fluctuations produced by the CO_2 laser are shown in Figure 3.3. The fluctuations were measured with the aid of the power meter placed behind the AOM, as shown in Figure 3.1. For this particular measurement, the AOM voltage was set to be 4.5 V and the PID feedback loop was switched off.

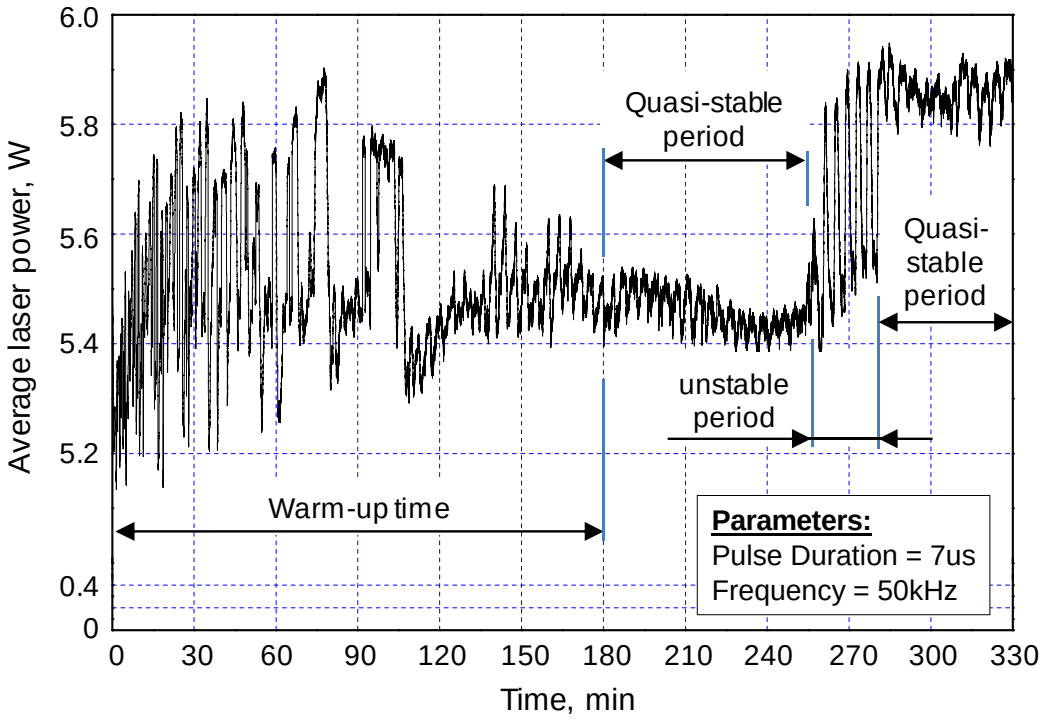

Figure 3.3: Laser power fluctuations measured by power meter. The AOM voltage was set to 4.5 V. The PID feedback loop was inactive.

The laser power fluctuations shown in Figure 3.3 may derive from a number of different possible causes. Among the most likely sources of the observed fluctuations are: density changes of the laser gases as the RF power to the discharge changes [109] and thermal fluctuations of the laser cavity physical length [110]. Other potential

sources include: acoustic vibrations of the resonator mirrors, noise from electrical devices, instabilities of the RF power supply, and variations of the laser modulation signal.

Based on results presented in Figure 3.3, it is possible to distinguish three characteristic regions in the CO_2 laser operation: a warm-up time, quasi-stable periods, and unstable periods. The warm-up time of this laser was observed to be about three hours. Within this period, the laser power fluctuations were observed to vary significantly ($\Delta P = \pm 7\%$), while following the warm-up time, the laser power was relatively stable over a time period of up to two hours with fluctuations of less than $\pm 1\%$, despite the fact that the laser operated at a few wavelengths simultaneously. The most common wavelengths registered by the spectrum analyzer were as follows: 10P14-10P24 (10.53-10.63 µm) and occasionally 10R16 (10.27 µm) and 10R20 (10.25 µm). Generally, this quasi-stable period of the laser operation was used for smoothing multi-level etched structures (see Chapter 4) and for producing the surface stress in fused silica plates (see Chapter 7).

On some occasions, the CO_2 laser was unstable following the warm-up time, possibly due to thermal changes in the laser cavity length. Within this period, the laser power fluctuations increased to about $\pm 5\%$. Such large fluctuations were found to result from the transient appearance of a wavelength in the R-branch, with the laser operating predominantly at 10.59 µm (10P20). Since the R-branch wavelengths occurred periodically, the laser power fluctuations were observed to be in the form of a comb, as shown in Figure 3.4. Generally, the experiments were not carried out when the laser was in this unstable state because the PID feedback loop applied in the system could not handle effectively such large and rapid laser power variations. More details will be given later.

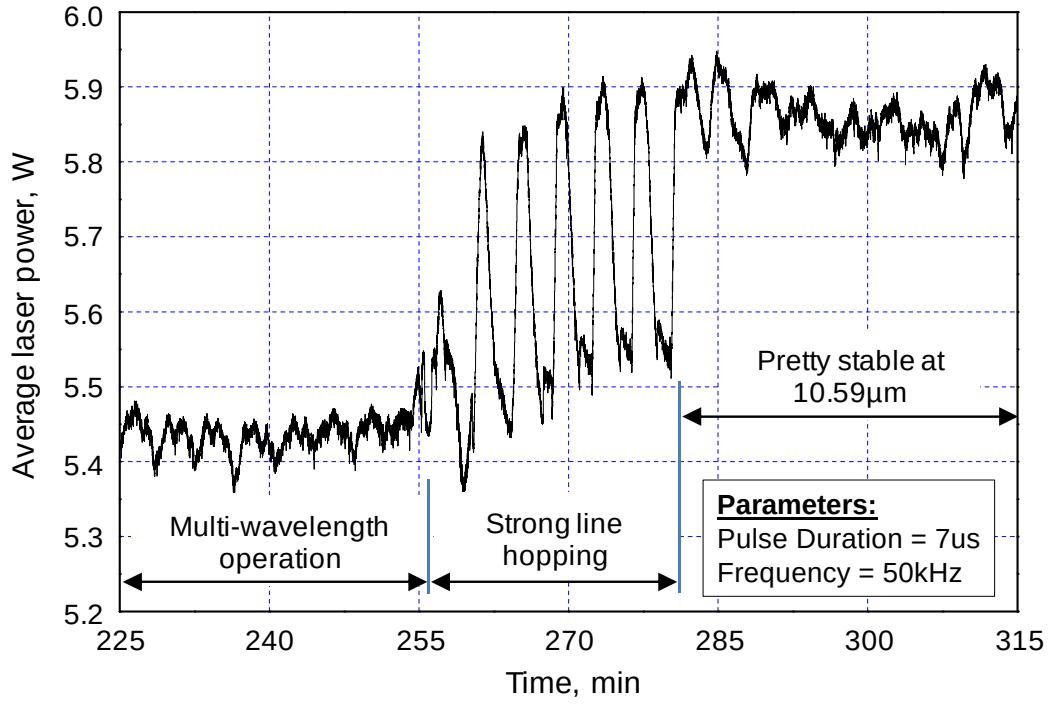

Figure 3.4: Zoom-in of selected region of Figure 3.3.

As can be seen in Figure 3.4, the laser was also able to work only at the 10.59 µm wavelength over a time period longer than 30 minutes. Within this period, the laser power fluctuations were as low as ± 1%. As mentioned at the beginning of this section, this stable period of the laser operation was used for studying laser-induced surface deformations in fused silica and Borofloat®33 glass (see Chapter 5) and for fabricating toroidal mirrors in fused silica substrates (see Chapter 6).

There are at least three reasons why experiments were not carried out while the laser was operating in the R-branch. The first one is related to an inaccurate response of the PID feedback loop to the rapid changes in the output laser power when the R-branch spectral lines occur. Then, the PID loop has a tendency to produce a few percent spikes with reference to the nominal optical power delivered to the target, thereby generating non-uniform heating at the glass surface. The second reason is associated with the fact that the optical properties of glasses are wavelength-dependent. For instance, the reflectivity of fused quartz (Vitreosil®) at 10.23 µm is approximately 60% greater than that at 10.59 µm, as shown in Figure 2.3. This simply means that the laser energy coupled into the glass varies for different wavelengths. Actually, it was found experimentally that fused silica machined with the assistance of a 10.23 µm wavelength evaporates slower than the glass machined only at 10.59 µm. Finally, it was

found that the appearance of the R-branch wavelengths during laser treatment may introduce a significant beam positioning error along the laser scan direction. Since the laser beam passing through the AOM is deflected differently at different wavelengths, the line hopping during laser treatment may result in non-uniform heating of the glass along the laser scan direction. The Bragg angle (θ_B) calculated for the 10.25 and 10.59 µm wavelengths (λ) by using the following formula [111]:

$$\Theta_B = \frac{f_A \lambda}{2 V} \tag{3.1}$$

showed that the Bragg angle difference between these two wavelengths is about 0.85 mrad. This means that the laser beam delivered to the target (see Figure 3.1) can be shifted by approximately 0.2 mm regarding the nominal position (at 10.59 µm), thereby causing a serious beam positioning error at the target. The error was calculated by using the ABCD matrix method, while the Bragg angle difference was achieved for an acoustic drive frequency (f_A) of 27.12 MHz and an acoustic velocity of the germanium crystal (V) of 5500 m/s [111].

In conclusion, stable and single-wavelength operation of the laser was particularly required in the experiments covered in Chapter 6, in which the laser system was used for fabricating toroidal mirrors for planar waveguide laser applications. In these experiments, however, it was found that current performance of the laser setup needs to be improved in the future because laser power fluctuations as low as 1% (peak-to-valley) are still too high to achieve high surface quality of the machined mirrors. Discussion on the potential improvement of the laser setup performance will be given in Section 6.6.4.

3.1.3 Customized sample holder for glass preheating

In Chapter 5, laser-induced deformations in Borofloat®33 glass samples preheated to 350°C are described. In order to allow the glass samples to be preheated to this temperature level, it was necessary to design and construct a special sample holder with an embedded heat source. A photograph of this sample holder is shown in Figure 3.5.

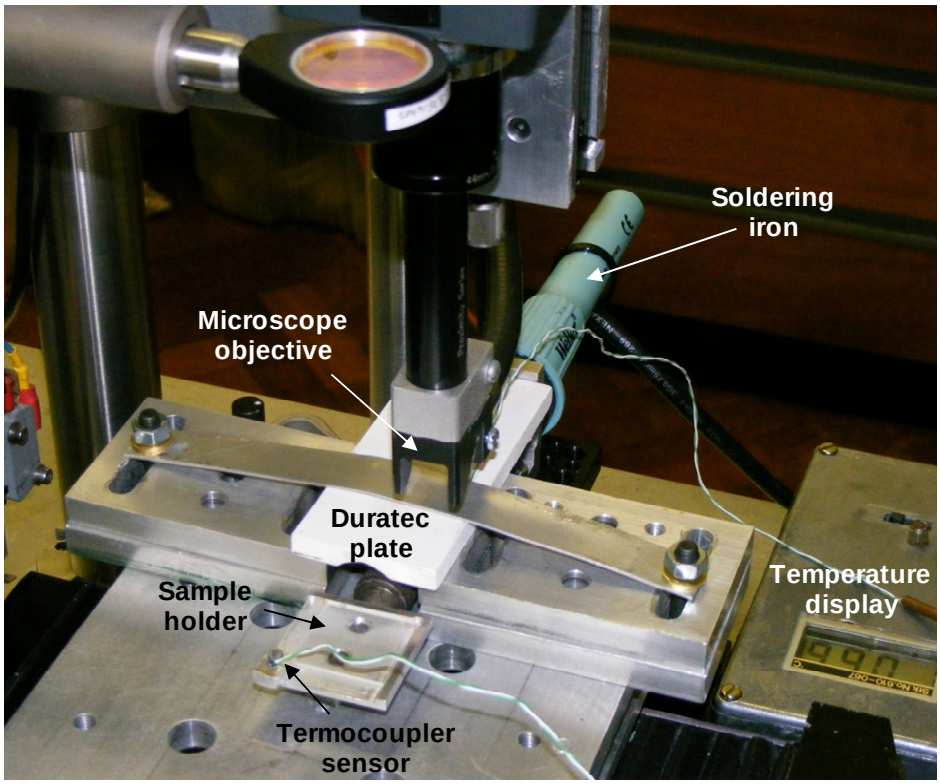

Figure 3.5: Soldering iron-based hot plate for glass preheating.

The heat source for this holder was a soldering iron (Weller, USA) with an exchangeable "temperature sensing" soldering tip. Depending on the type of soldering tip, the maximum temperature of the hot plate could be varied in the range of 315°C to 430ºC. In this simple heating system, the soldering tip was attached on to an aluminium plate. The size of the plate was 35 × 35 × 2 mm, which was sufficiently large to support a 25.4 mm square glass sample. In order to achieve good thermal contact between the plate and the heat source, the soldering tip was flattened before being attached to the aluminium plate.

In the experiment described in Chapter 5, the soldering iron with the attached sample holder was clamped to the X-Y translation stage, as can be seen in Figure 3.5. The microscope objective, which was just above the soldering iron, was protected against heat damage by the use of an intervening 5 mm thick block of Duratec® material. Duratec® is an asbestos-free calcium silicate ceramic which is commonly used in electrical insulation applications requiring durability in high temperature environments of up to 1000ºC.

The system used for glass preheating was also equipped with a thermo-couple sensor attached to the sample holder (see Figure 3.5), thereby providing real-time temperature monitoring of the heated sample with a 1°C resolution. Generally, the temperature oscillations produced by the soldering iron at a nominal value of 350°C were found to be ± 5°C, whilst the heating and cooling rates in the temperature range from 250°C to 350°C were approximately 40°C per minute.

3.2 Pulse-mode CO_2 laser system

To investigate CO_2 laser machinability of Borofloat®33 glass and lead silicate glasses (see Chapter 8 for more details), it was necessary to use a different CO_2 laser setup from that described in Section 3.1. For convenience, the experiments covered in Chapter 8 were carried out using facilities located at the company PowerPhotonic Ltd., a high-tech spin-out from Heriot Watt University.

Chapter 4

Laser smoothing of etched structures in fused silica

4.1 Introduction

The work covered in this chapter is focused on CO_2 laser smoothing of binary gratings and multi-level etched optics fabricated in fused silica. By utilizing a CO_2 laser beam as a heat source, it is possible to generate a melt pool on the glass surface that flows under the action of surface tension, thereby causing relaxation of sharp step corners of the etched structures in a controllable manner [10].

There are two main objectives of the work carried out in this chapter. The first is to develop a method to characterize fully the laser smoothing effect of binary gratings. As shown by E. Mendez in [10], the surface relaxation of the binary steps cannot be measured accurately by the stylus-based surface-profile-measurement devices, such as AFM and DEKTAK, since neither of these instruments is able to respond correctly to the near-vertical sidewalls of the etched steps. The second objective of the work carried in this chapter is to investigate CO_2 laser smoothing of multi-level etched optics. In this part of the study, there is an interest in checking whether it is possible to fabricate a continuous surface by combining a CO_2 laser smoothing process with the well-established technique for silica etching. In the event of success, this new approach may be used in the future for the fabrication of customized micro-optical components in fused silica with superior properties to those with sharp edges.

As mentioned in the previous paragraph, some preliminary work on CO_2 laser smoothing of etched structures was already carried out by Dr Enrique Mendez, a former member of the Laser and Photonics Applications (LPA) group at Heriot-Watt University. He performed some simple experiments using a binary grating as a workpiece, providing basic information on laser smoothing conditions for the rounding of sharp step corners presented in etched structures. His studies showed that the magnitude of the surface relaxation of etched steps depends on the laser power and the number of laser scans used. He also showed that it is possible to transform a binary grating into an "analogue" periodic structure by applying sufficiently high laser power. Although some results of his research were covered in his thesis [10], they are also presented here in Section 4.4 since they are strongly linked to the rest of the results presented within this chapter.

The structure of this chapter is as follows. Some background information on CO_2 laser polishing of fused silica is provided in Section 4.2, whilst the laser smoothing mechanism of etched steps is explained in Section 4.3. Information embedded within these two sections is necessary to understand the results presented in the remaining sections of this chapter. As mentioned already, Section 4.4 contains the experimental studies of CO_2 laser smoothing of binary gratings. The initial experiment designed to calibrate the smoothing process using single line laser scans is described in Section 4.4.1, whilst the smoothing effect of the binary structures using laser beam raster scanning is shown in Section 4.4.2. The results presented within these two sections provide information on the extent of the relaxation of the binary steps smoothed by using 1 mm and 550 µm diameter laser beams at different laser power levels. Section 4.5 shows that the laser smoothing effect on binary gratings may be represented by the diffraction pattern which results from He-Ne laser illumination of the periodic structure. The diffraction spectra measured for the laser-smoothed gratings with initial step heights of 0.8 and 3 µm are presented and discussed within this section. In order to gain better understanding of the spectra measured with the aid of the optical method, a mathematical procedure for simulating He-Ne laser illumination of laser-smoothed gratings is developed in Section 4.6. As will be shown there, the simulations allows us to characterize fully the laser smoothing effect on binary gratings. The work presented in this section arose with the help of Prof. Howard Baker. Finally, CO_2 laser smoothing of multi-level etched structures is presented in Section 4.7. The possibility of fabricating

micro-optics by using the multi-level etched component and CO_2 laser beam smoothing is studied within this section.

In conclusion, it should be noted that the work presented within this chapter is the basis of a publication in Applied Optics [112].

4.2 CO_2 laser polishing of fused silica

An excellent match between CO_2 laser beam characteristics and some key thermo-optical properties of glass materials (discussed in Section 2.4) has led to the development of an advanced technique for glass processing, called CO_2 laser polishing. This thermal process relies on the generation of a thin layer of melt pool on a glass surface that flows under surface tension forces, thereby removing small surface defects or reducing the degree of roughness on the glass surface [1, 10].

Due to the high mechanical strength and low thermal expansion coefficient (*CTE*) of fused silica, which is at least 5 times smaller than the *CTE* of other glasses, this material was found to be the most suitable for CO_2 laser polishing. As reported by Xiao and Bass in [23], glasses with low *CTE* (< 3.3 ppm) are able to be laser polished from room temperature without material cracking during and after the process.

In order to achieve the smoothing effect in fused silica, it is necessary to generate a mobile melt pool on the glass surface. According to G. Markillie *et al.* [9], this melt pool is produced at temperatures above 1950°C, where the viscosity of the glass is below the softening point ($\eta = 10^{6.6}$ Pa·s) and its vapour pressure is below atmospheric pressure (1 bar), as can be seen in Figure 4.1. As the temperature is increased, the viscosity of the glass decreases and therefore the laser-generated melt pool becomes more mobile. This results in a stronger smoothing effect so that larger defects on the glass surface can be reduced or even removed. Based on K. Nowak's work [3, 61], the most efficient laser polishing effect in fused silica is achieved for temperatures below 2700°C. Above this temperature, the vapour pressure exceeds 1 bar and the glass begins loosing mass by evaporation [113].

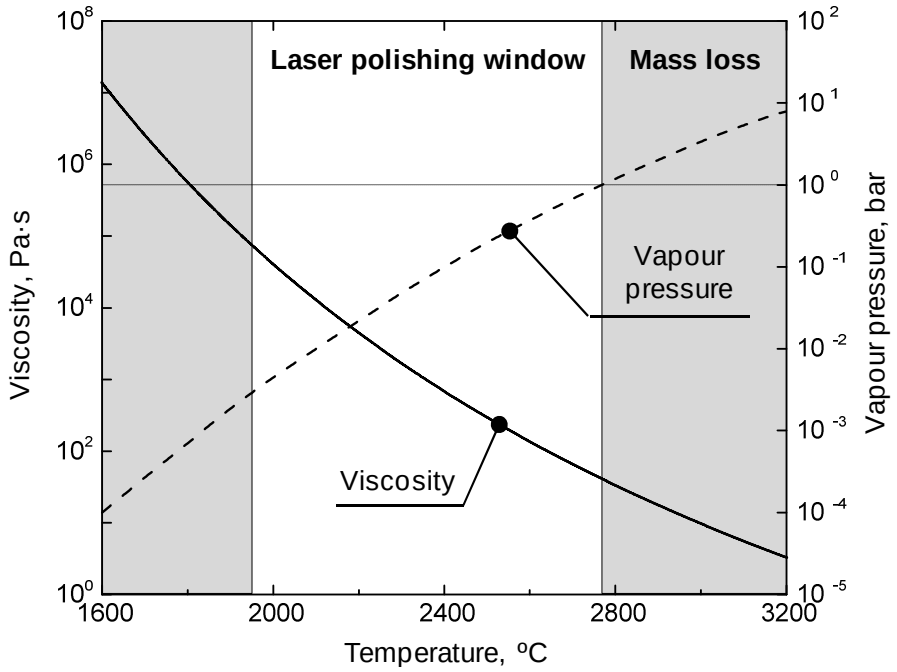

Figure 4.1: The change of viscosity and vapour pressure of fused silica in the range of temperatures from 1600ºC to 3200ºC, based on [9].

The pioneering work on CO_2 laser polishing of fused silica was carried out by Peak and Weaver in the mid of 1970s [100]. They investigated the use of a CO_2 laser beam to produce a hemispherical lens at the end of an optical fibre. The experimental technique was based on the use of a 5 mm diameter stationary laser beam with a 1.8 W laser power, focusing on a fibre end. The results showed that the fibre end when heated to the softening point of the material tends to become spherical in shape, as a result of the action of surface tension. Similar work to that reported by Peak and Weaver was carried out also by Calixto *et al* in 2005 [101]. They applied CO_2 laser melting of silica fibres for the fabrication of rod and spherical micro-lenses.

The use of a CO_2 laser beam for smoothing of larger surfaces of fused silica, in the dimension range of a few of centimetres, was for the first time presented by Temple *et al* in 1982 [12]. The aim of their research was to increase the surface-damage resistance of silica optics by CO_2 laser irradiation of mechanically pre-polished surfaces. For this purpose, they used a CW moving laser beam with a diameter of ~ 10 mm (measured at $1/e^2$ intensity). The laser power used in this process was changed in the range from 75 to 250 W, depending on surface treatment schemes. As an outcome of their experiments, they showed that CO_2 laser heating of optical components reduces efficiently defects and micro-cracks present on the surface, thereby

increasing the surface damage threshold in comparison to the optics polished only mechanically. A similar result for CO_2 laser polishing of optical components was also observed by Brusasco *et al* [11].

Within the LPA group at Heriot-Watt University, CO_2 laser polishing processes have been exploited in the fabrication of free-form micro-optical components, such as phase corrective plates for high power diode lasers [5, 6, 61] or flat-top beam shapers for laser beam transformation in fibre laser applications [7]. In comparison to the works presented in the previous two paragraphs, CO_2 laser polishing of the micro-optics is carried out with a moving laser beam as small as 1 mm. There are several advantages of the use of such a small laser spot in the laser polishing process:

a) the accurate control of laser power delivered to the polishing glass,
b) avoiding the need for expensive laser-beam shaping optics, e.g. a multifaceted integrating mirror [114], which is essential in a laser polishing system to achieve a uniform temperature distribution over a large area of glass surface,
c) the ability to localize polishing without heating a large area of the glass.

High-accuracy power control is achieved by using a closed-loop beam power controller based on a reference power meter and an acousto-optic modulator (see a CO_2 laser system described in Section 3.1). The conversion of a Gaussian beam to the flat-top intensity profile beam using expensive optics is unnecessary because a small laser beam traversed across the glass surface following a raster scan pattern, as will be shown later in Figure 4.6, produces excellent treatment uniformity [3]. Finally, the localized laser treatment enables defects and roughness to be reduced from the glass surface without affecting the surrounding areas. This property of polishing has been used for the localized damage repair of fused silica optics [1].

CO_2 laser polishing of fused silica with a small diameter laser beam has been characterized as a fourth order low-pass filter in the Fourier domain by Nowak *et al* [3]. The mathematical formula describing the filter, which was originally proposed by White *et al* [115] to describe the viscous flow properties of fusible borophosphosilicate glasses deposited on planar silicon substrates, is given by:

$$A_f = A_i exp\left(-4\pi^2 \frac{\gamma\, h^3\, t}{\eta\, \lambda^4}\right) \tag{4.1}$$

where A_f and A_i are respectively the final and initial amplitude of the undulation (surface roughness), λ is the spatial period of undulation, γ is the surface tension, whilst η, h and t are the viscosity, depth, and flow time of the glass molten layer, respectively. To clarify, equation (4.1) was derived with the simplifying assumptions of $\lambda > h > A_i$, constant value of the surface tension, constant viscosity throughout the depth of molten layer, and ignoring any gravitational effects [3].

The concept of the use of the low-pass filter to represent the CO_2 laser polishing effect allows us to determine the laser smoothing conditions at which the surface roughness represented by high spatial frequencies is significantly reduced, whilst the overall shape of the polished structure represented by low spatial frequencies is minimally disturbed. This approach is especially convenient from the point of view of laser polishing of micro-optical components.

Based on equation (4.1), the spatial frequency cut-off of the filter is determined by four parameters: γ, η, h, and t. In general, the values of these parameters can be varied, depending on the material properties and the laser machining conditions, such as laser power (axial peak irradiance), heating dwell time or laser pulse duration, and laser spot size.

In the case of CO_2 laser polishing of fused silica, the glass viscosity (η) is varied in the range from 10^5 to 10^2 Pa·s, depending on the temperature generated at the glass surface (see Figure 4.1). The temperature is controlled by the laser power and the laser pulse duration. According to the results published in [1], the depth of molten glass layer (h) can range from 4 - 30 µm, depending on the laser spot size and heating dwell time (t). The melt depth is defined here as a depth at which the viscosity increases by a factor of 10 with reference to the viscosity value at the glass surface. The increase of viscosity by an order of magnitude corresponds to temperature drop of 230°C. The lower limit of the melt depth, h = 4 µm, is determined by the absorption depth of high-temperature fused silica at 10.59 µm wavelength, as shown in Figure 2.4 (see Section 2.4.2). Finally, the surface tension of fused silica (γ) has not been found in the literature, however, the assumption of γ = 0.3 N/m is a good approximation to use in equation (4.1), as shown by Nowak *et al.* in [3].

In conclusion, the smoothing experiments carried out with a laser beam in the diameter range from 400 µm to 1 mm showed that a spatial period cut-off

between 50 - 200 µm can be achieved [3, 61]. This fact has been used to achieve efficient smoothing of CO_2 laser-cut micro-optics fabricated in fused silica. The CO_2 laser cutting process was described in Section 2.6.3.

4.3 Surface relaxation of etched structures by CO_2 laser smoothing

To gain a better understanding of the dynamics of laser melting for sharp steps in etched structures, it is useful to consider the Young-Laplace equation. This equation describes the capillary pressure sustained across the interface between two fluids, such as air and liquid, due to the phenomenon of surface tension. For any point at the interface surface, the Young-Laplace equation is expressed as follows:

$$\Delta P = \gamma \left(\frac{1}{R_1} + \frac{1}{R_2} \right) \tag{4.2}$$

where ΔP is the pressure difference across the fluid interface, γ is the surface tension, and R_1, R_2 are the principal radii of curvature at that point. Based on this simple formula, it can be seen that the highest pressure difference occurs in areas with the smallest curvature radius, whilst the pressure difference decreases to zero when the curvature radius goes to the infinity.

The Young-Laplace equation can be used to represent the laser smoothing mechanism of etched structures in fused silica because the melt depth produced by a 1 mm diameter laser beam is typically 20 - 25 µm [1], which is considerably larger than the size of the etched features studied within this chapter. In the case of the etched steps of the binary gratings studied in Section 4.4, one principle radius of curvature is infinite, thus equation (4.2) is modified to be:

$$\Delta P = -\gamma \frac{1}{R} \tag{4.3}$$

The negative sign in equation (4.3) denotes the direction of the driving force relative to the radius of curvature [115].

As the etched structure is exposed to CO_2 laser irradiation, the highest pressure is produced in the sharp edges of the L-shaped steps, as shown in Figure 4.2 (a), because these areas have the smallest curvature radius. This means that the viscous

molten layers immediately adjacent to sharp corners of the steps are moved from this location towards sites of lower pressure, thereby causing a reduction in the curvature of the edges, as illustrated in Figure 4.2 (b) and (c). The rate of the melt flow occurring on the glass surface increases with increasing temperature, thus it depends on the viscosity of the material (see Figure 2.5), while the total movement of the melt is controlled by the time for which the surface is maintained above the softening point. Thus, in a qualitative sense, one can distinguish stages in the surface relaxation of stepped structures, as shown in Figure 4.2.

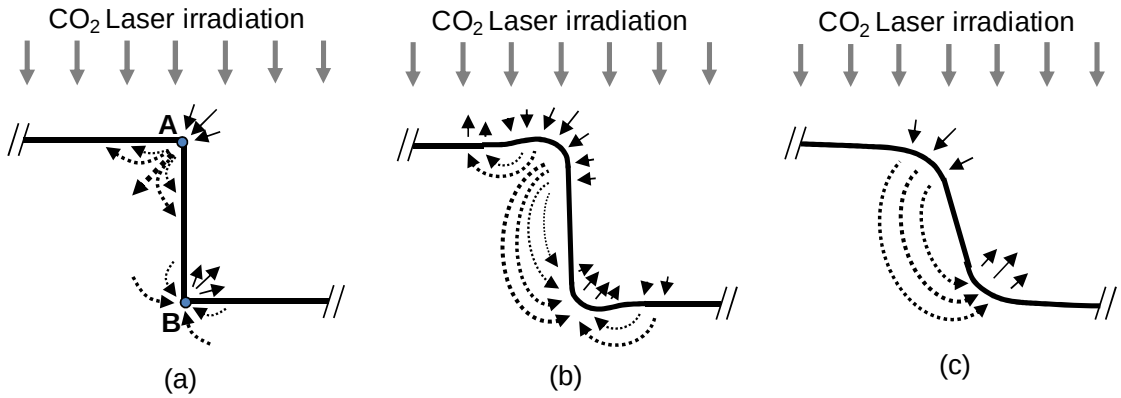

Figure 4.2: Surface relaxation of etched structure by CO_2 laser irradiation. Solid arrowed curves indicate the significant pressure acting on the molten edges, whilst dotted arrowed curves indicate the direction of the liquid flow. Published in [112].

As the temperature of the glass surface is relatively low, the viscous molten layer is pushed from the top corner (Point A) towards lower pressure sites creating a small bulge, whilst the bottom corner (Point B) is subjected to negative pressure that draws glass towards the sharp tip creating a small hollow. At this stage, sharp edges are gently rounded without mass transfer down the step, as shown in Figure 4.2 (b). As more intense or subsequent laser irradiation is applied to the now-rounded steps, the viscous forces are acting on a larger area of glass. This reduces bulges and hollows, forming a slope between the top and bottom corners, as shown in Figure 4.2 (c). At this stage, the molten viscous layer is efficiently transferred from the top corner directly to the bottom corner, thereby reducing significantly the slope of the previously near-vertical step. Such strong relaxation leads eventually to complete removal of sharp steps, making the structure smooth as occurs in the thermal reflow process [116].

4.4 Laser smoothing of binary gratings

This section contains the experimental study of CO_2 laser smoothing of binary gratings with step heights of 0.8 µm, 1 µm, and 3 µm. Here, it should be noted that the experiments described within this section were carried out by E. Mendez, who initiated the work on CO_2 laser smoothing of binary structures [10]. This section, however, includes additionally the description and outcome of his studies because they are strongly related to the rest of the results presented in the remaining sections of this Chapter. For instance, the results presented within this section provide a verification of the theory shown in Section 4.3.

4.4.1 Relaxation of etched steps using single linear laser scans

In an initial set of experiments designed to calibrate the CO_2 laser smoothing process, a single linear scan laser treatment was performed on a simple binary grating fabricated in fused silica. The height of the binary steps was 1 µm and their spatial period was 22.6 µm, as illustrated in Figure 4.3. This binary structure was fabricated by reactive ion etching (RIE), performed within the Diffractive Optics group at Heriot-Watt University.

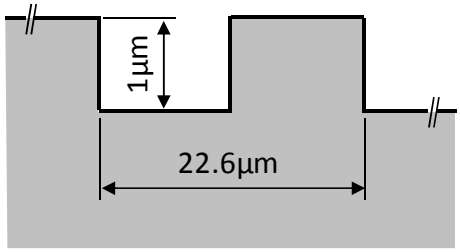

Figure 4.3: Illustration of binary grating with a 22.6 µm spatial period and a 1 µm step height. Published in [112].

In the experiment presented in this section, a fundamental mode Gaussian beam with a diameter of approximately 1 mm was moved perpendicular to the edges of the etched structure with a speed of 5 mm/s. From previous work reported in [3], it was known that a 1 mm diameter laser spot produces up to a 200 µm wide melt pool, which is significantly larger than features of the machined object. Based on the laser polishing protocol "D" [3], the effective smoothing effect of etched steps was expected to be achieved at laser power values not exceeding 10 W. For these laser irradiation

conditions, the relaxation of the sharp edges presented in the structure was investigated for an increasing number of overlapped laser scans (*N*) and different laser power levels. The upper limit of the laser power corresponded to the point above which mass loss started appearing due to evaporation of fused silica.

Figure 4.4 shows an initial view of the smoothing effect, which was achieved by using 10 overlapped linear laser scans at fixed laser powers. The visible smoothing effect was first observed at a laser power of 7.35 W, as shown in Figure 4.4 (a). In this case, the melting of the edges is seen as an approximately 120 µm wide modification of the steps' appearance. As the laser power was increased to 7.85 W, the visible modification of the etched steps was observed to be stronger. This can be seen in Figure 4.4 (b) as an approximately 200 µm wide blurred vertical line with the horizontal lines being more difficult to distinguish. This smoothing effect corresponds probably to the situation in which the molten viscous layer is being transferred efficiently from the top to the bottom corners of the etched steps, as shown schematically in Figure 4.2 (c). Finally, a noticeable mass loss of the glass was observed at a laser power of 9.0 W. At this laser power, the steps of the etched structure were completely removed from a 300 µm wide area by the moving laser beam. The characteristic feature of this removal is an approximately 100 µm wide trench which is visible in the smoothed region, as shown in Figure 4.4 (c). Further information on the trenches produced by a moving laser beam will be given in Chapter 5.

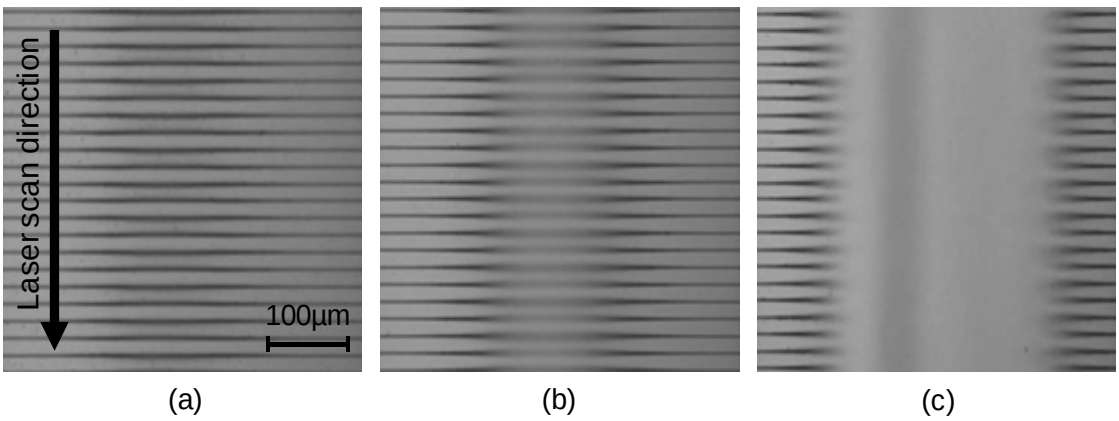

Figure 4.4: Micrographs of the binary structure after laser treatment with N = 10 unidirectional laser scans in the direction perpendicular to step edges for laser powers of (a) 7.35 W, (b) 7.85 W, and (c) 9.00 W. The horizontal lines represent the edges of etched steps in the grating. Micrographs copied from [10] and also published in [112].

Based on the results presented in Figure 4.4, it can be concluded that the CO_2 laser smoothing process is characterized by a limited range of laser powers between conditions for the onset of the smoothing effect and the removal of glass by evaporation. Therefore to exploit fully the process, it is necessary to have a power-controlled laser source with a stable beam shape and diameter at the machined target, e.g., as that described in Section 3.1.

Since the optical micrographs presented in Figure 4.4 do not show directly the extent of the relaxation of etched edges, it was necessary to perform a scan of laser-irradiates surfaces. For this purpose, a DEKTAK surface profilometer (Veeco Instruments, USA) was involved. The set of edge profiles obtained at a constant laser power of 7.35 W but for different numbers of laser scans (*N*) is shown in Figure 4.5.

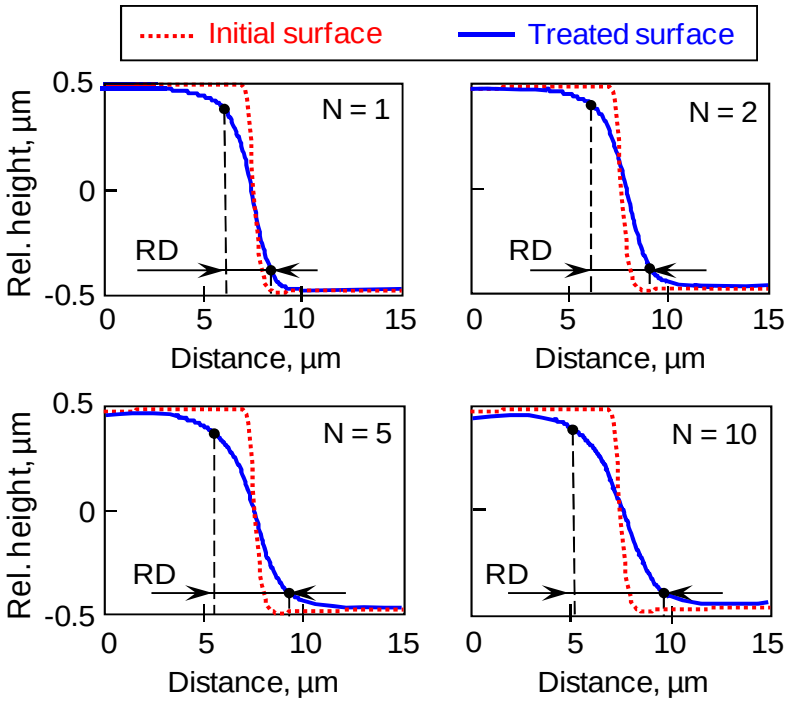

Figure 4.5: Evolution of the step profile of a 1 µm step height binary grating as a function of the number of laser line scans (*N*) at constant laser power of 7.35 W. The relaxation distance (*RD*) is marked for each case. The diameter of laser beam used was an approximately 1 mm. Published in [112].

To quantify the relaxation of etched steps, a parameter called the relaxation distance (*RD*) is introduced here. This parameter is defined as the distance between two points at which the profile of a step edge reaches 10 and 90% of the original step height.

Based on the surface profiles shown in Figure 4.5, the steps are relaxed over a 2 µm distance with no mass loss for a single laser scan (N = 1). Increasing the number of laser scans builds up the smoothing effect, thus the relaxation distance is increased up to about 4.5 µm (for N = 10) with a slight decrease in the step height. The stronger smoothing effect at larger numbers of laser scans is caused by the longer total time at which the glass surface is above the temperature for viscous melt flow. In this case, the maximum measurable value of *RD* is limited by the width of a single step of the binary grating. In conclusion, the smoothing effect of a binary grating with a 1 µm step height seems to be symmetric in all cases shown in Figure 4.5. This symmetry is consistent with linear viscous flow and uniform temperature across the laser-irradiated surface.

4.4.2 Laser beam raster scanning of binary structures

From a practical point of view, a raster scan area treatment of etched structures is more desirable because a moving laser beam covers a larger area of binary grating, producing a uniform smoothing effect [1]. In this experiment, the raster scan pitch (Δx) was chosen to be much smaller than the diameter of the melt pool (d_m) so that successive laser scans partially overlap each other, re-melting many times a certain area of the glass. As a result of this, the smoothing effect was expected to be stronger than in the case of a single line laser scanning (see Section 4.4.1) due to the accumulated dwell time. This dwell time can be comparable to the treatment time in single line laser scanning for some number of overlapping laser scans (N). The estimated value of N is given by:

$$N \approx \frac{\pi}{4} \cdot \frac{d_m}{\Delta x} \tag{4.4}$$

on conditions that $d_m \geq 10 \cdot \Delta x$ and the laser beam diameter and laser power used in both laser treatment schemes (in the single line laser scanning and the raster scan area treatment) are equal.

Laser beam raster scanning was performed on binary grating samples with step heights of 0.8 and 3 µm. The spatial period of both gratings was 22.6 µm. Raster scan area treatment of samples was carried out using a Gaussian laser beam with a diameter of approximately 550 µm. According to laser polishing protocols reported in [61], such a large laser spot produces an approximately 100 µm diameter melt pool. In this experiment, the beam was moved normal to the etched edges, as shown in Figure 4.6,

with a speed of 5 mm/s. The raster scan pitch was chosen to be 10 µm. The laser power used for polishing of both gratings was in the range from 4.7 - 8.95 W. Such a wide range of laser powers used in the experiment allowed us to observe a gradual transformation of the sharp step edges into rounded corners, including the possibility in the determination of the onset of the smoothing effect.

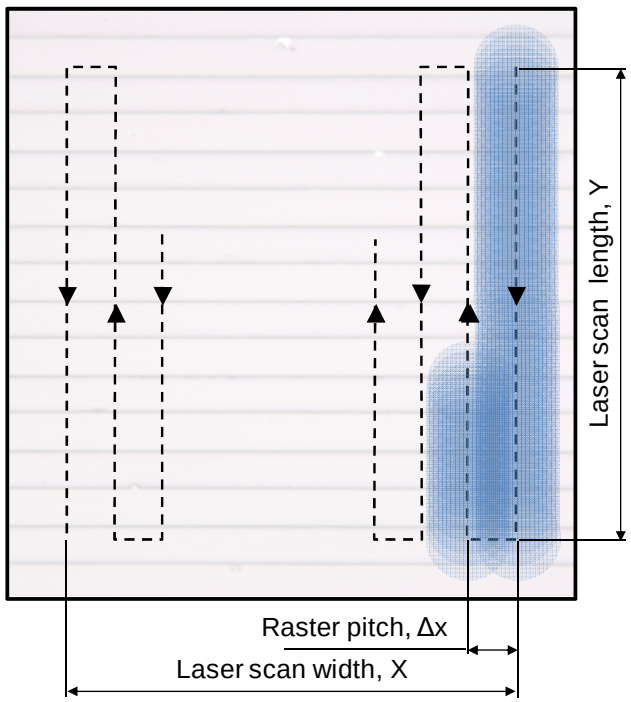

Figure 4.6: The movement of laser beam in the raster scan area treatment of materials.

Figure 4.7 shows a surface profile of laser-irradiated binary gratings with an initial step height of 0.8 and 3 µm. These profiles were taken with the aid of an atomic force microscope (AFM).

For the 0.8 µm step height binary grating treated with laser powers of 5.7 and 6.7 W (see Figure 4.7 (a)), some bulges and hollows near the step corners were observed. These features are consistent with the situation illustrated in Figure 4.2 (b). For laser power of 6.7 W, the bulges and hollows disappeared and the height of the etched steps began to be reduced. In this case, the temperature produced at the glass surface is sufficiently high to transfer the molten viscous layer from the top corners towards the bottom ones. This situation corresponds to the smoothing conditions shown in Figure 4.2 (c). Almost complete relaxation of the etched steps in the binary structure

was observed at laser powers of 7.7 W and above. The height of steps was reduced significantly and the binary grating was converted into the sinusoidal-shaped one with the same initial spatial period.

Surface profiles of the binary grating with a 0.8 µm step height showed good symmetry of the smoothing effect for both top and bottom half periods (see Figure 4.7 (a)). In the case of the binary grating with a 3 µm step height, however, the smoothing effect was observed to be asymmetric. This asymmetry was especially noticeable for samples treated with laser powers from 5.7 - 6.7 W. There was a tendency for the lower corners to be less smoothed in comparison to upper corners, as shown in Figure 4.7 (b). This imperfection of smoothing was accentuated to some extent by the inability of the AFM profilometer stylus to follow the actual shape of the bottom corners, as shown in the surface profile of the grating smoothed at 5.7 W. However, the asymmetry in the smoothing effect remained clearly defined at laser powers of 6.2 W and above, where the grating was relaxed towards the weak sinusoidal shape.

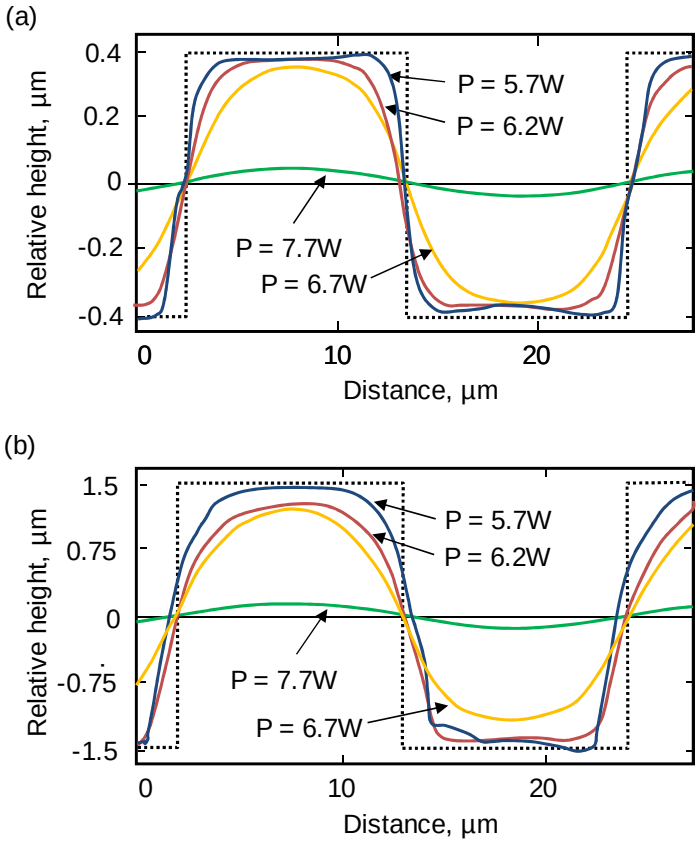

Figure 4.7: AFM surface profile of laser-irradiated binary gratings with an initial step height of (a) 0.8 µm and (b) 3 µm. Dotted lines indicate an ideal shape of a binary grating before laser smoothing. The diameter of laser beam used was about 550 µm. Published in [112].

The asymmetry in the relaxation of 3 µm high steps was probably associated with the absorption depth of high-temperature fused silica, *1/α*, which is comparable with the height of steps in the grating. As shown in Figure 2.4, the absorption depth of fused silica is approximately 4 µm at a temperature of 1800°C and wavelength of 10.59 µm. The extrapolation of the absorption depth for 2500°C, where strong relaxation of etched steps is obtained, gives us $1/\alpha \approx 3$ µm. This number corresponds to the height of the etched steps. Such a small absorption depth could cause a non-uniform heating effect on the etched surface, so that the upper part of the steps would be better smoothed than the bottom section. The asymmetry in the relaxation of the steps could also be amplified by the fact that the extent of features in the structure, i.e., the step height and the spatial period of grating, was comparable with the laser wavelength. In this situation, the gaps between positive steps of the grating could diffract the incident beam, producing a non-uniform heat distribution along the glass surface. The interaction of light with subwavelength features has been described, e.g., by Kapany *et al* [117] or Mansuripur *et al* [118], but these publications do not provide a simple answer to this particular problem.

4.5 Study of the smoothing effect of gratings using optical method

Surface profiles of the laser-smoothed gratings were measured using a DEKTAK surface profilometer and an AFM (see Figure 4.7). However, neither measurement technique was able to respond accurately to the near-vertical sidewalls of the etched steps. This means that the weak smoothing effect, as illustrated in Figure 4.2 (a), cannot be measured by the stylus-based instruments. Since the objective of the study was to fully characterize the small-scale relaxation of the etched steps and determine the smoothing threshold for the process, a simple optical method was developed. With the aid of this method, it was possible to observe the smoothing effect by monitoring changes in the diffraction spectrum which resulted from the illumination of a laser-smoothed binary structure using a He-Ne laser ($\lambda = 632.8$ nm). The optical setup illustrating this method is shown in Figure 4.8.

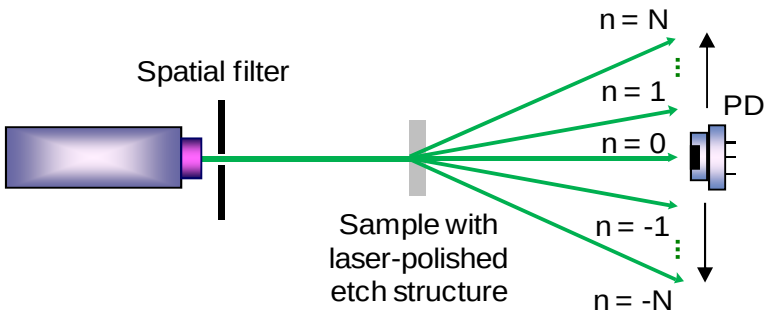

Figure 4.8: Optical setup used for the measurement of light scatter produced by laser-smoothed binary gratings.

In this simple optical arrangement, the He-Ne laser beam transmitted normal to the surface of a binary grating is split into a large number of diffraction orders. In this case, the periodic structure acts on He-Ne laser illumination as a grating with a phase shift determined by the height of the etched steps. The intensity of each diffraction order is measured by a moveable photo-detector (PD). In order to "clean up" the He-Ne laser beam from aberrations, a spatial filter is placed in front of the He-Ne laser output.

Diffraction spectra produced by CO_2 laser-smoothed gratings were measured first by E. Mendez, and the outcome of his measurement was published in Applied Optics [112]. Unfortunately, the results of these measurements were found to be inconsistent with the simulation results of the optical method, presented later in Section 4.6. The magnitude of the intensity changes in the diffraction orders as measured in these earlier experiments (by E. Mendez) were observed to be much smaller (by two orders) than predicted by the simulation. A possible reason for this is the overloading of the photo-detector by allowing too much light to strike the sensor. Due to this discrepancy between this first set of experimental results and the theoretical prediction, it was decided to repeat the diffraction spectrum measurement for both gratings (with step heights of 0.8 and 3 μm).

The diffraction spectra produced by the gratings with initial step heights of 0.8 and 3 µm are shown in Figure 4.9 and Figure 4.10, respectively. These spectra are presented only for the positive diffraction orders because they were found to be symmetric in regard to the zero diffraction order.

0.8 µm step height grating

The diffraction spectrum produced by the non-smoothed grating with a step height of 0.8 µm is shown in Figure 4.9 (a). In this case, upon He-Ne laser illumination the sample acted as a square-wave grating with an approximately 1.2π phase-shift (see equation (4.6) in Section 4.6.2). The characteristic feature of the spectrum produced by this sample is that the intensity in the even diffraction orders is significantly lower (up to three orders) than that observed in the odd diffraction orders. As will be seen later in Section 4.6.3, this spectrum is consistent with the simulation results obtained for the 0.8 µm step height grating with a relaxation distance of 0.25 µm.

The onset of the smoothing effect for the 0.8 µm step height grating was determined at a laser power of 4.7 W, as shown in Figure 4.9 (b). At this laser power, the intensities in the even diffraction orders are observed to be slightly higher in comparison with the spectrum shown in Figure 4.9 (a). This indicates that the initial shape of the grating was modified by CO_2 laser smoothing. Based on the theory provided in Section 4.3, it is very likely that the glass started to flow by the sharp corners of the periodic structure creating bulges and hollows as shown in Figure 4.2 (b).

For the 0.8 µm step height grating smoothed with a laser power of 5.7 W, it can be seen that the intensities in the odd diffraction orders and their neighbouring even orders become equalized, forming a characteristic slope as shown in Figure 4.9 (c). This slope is observed to be steeper for the grating smoothed at higher laser powers ($P > 5.7$ W). An increase of the slope angle is associated with the fact that the binary steps are more relaxed, as can be seen from the AFM surface profiles in Figure 4.7 (a).

The strongest relaxation of the etched steps is observed at laser powers as high as 7.7 W, where the intensities in the zero and first diffraction orders are only measurable (see Figure 4.9 (e)). The appearance of the two diffraction orders means that the rectangular-shaped structure is converted into a sinusoidal phase grating, as can be observed in Figure 4.7 (a). This conversion, however, is achieved at the cost of the significant reduction of peak-to-valley height from 0.8 µm to approximately 100 nm.

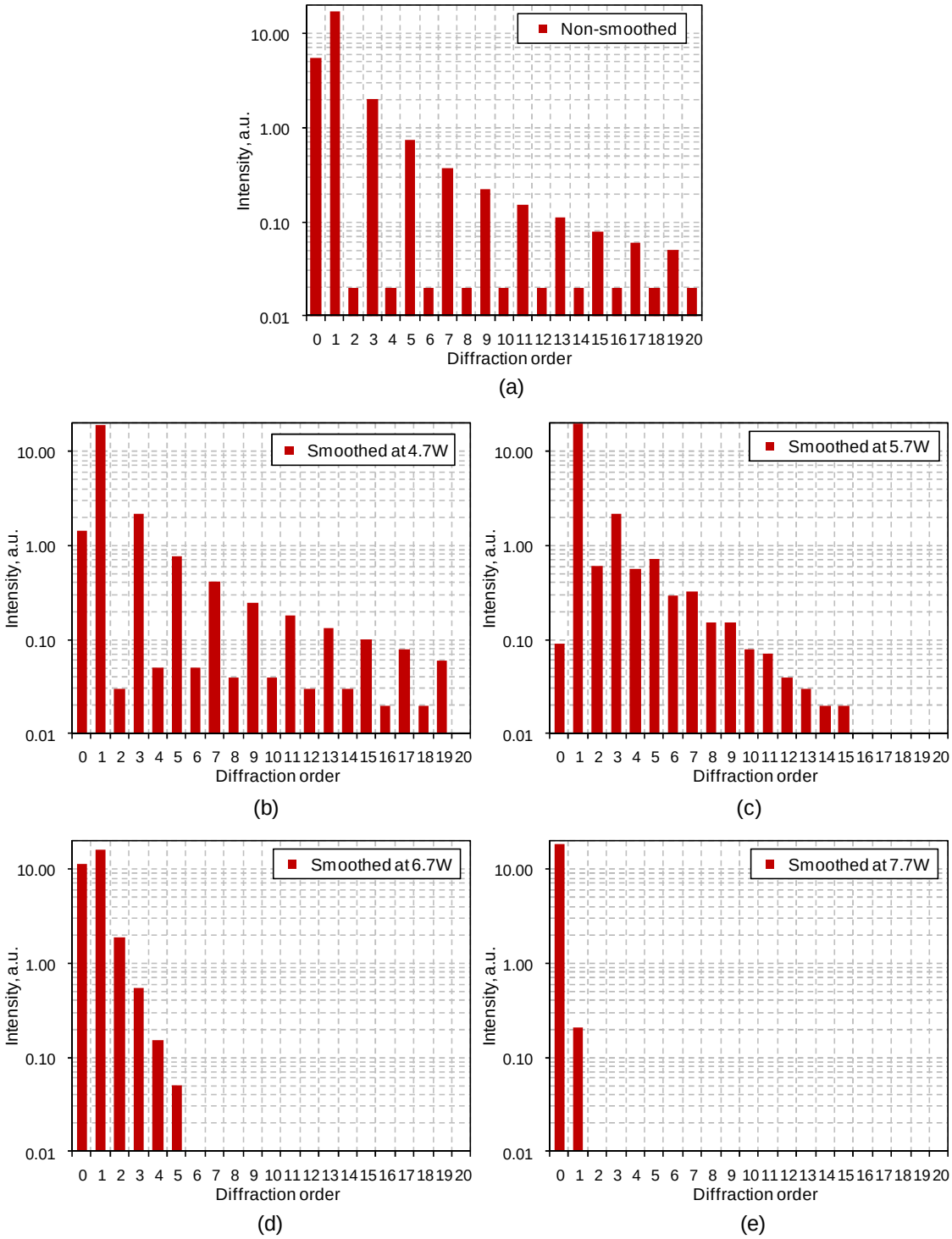

Figure 4.9: Diffraction spectra measured for the 0.8 µm step height grating: (a) non-smoothed and (b) – (e) smoothed at a laser power of 4.7, 5.7, 6.7, and 7.7 W, respectively.

3 µm step height grating

Upon He-Ne laser illumination, this sample acted as a square-wave grating with an approximately 4.4π phase shift, thus the spectra produced by this grating are very difficult to interpret in some cases, as can be seen in Figure 4.10. Nevertheless, the optical method still allows us to observe the smoothing effect in this structure.

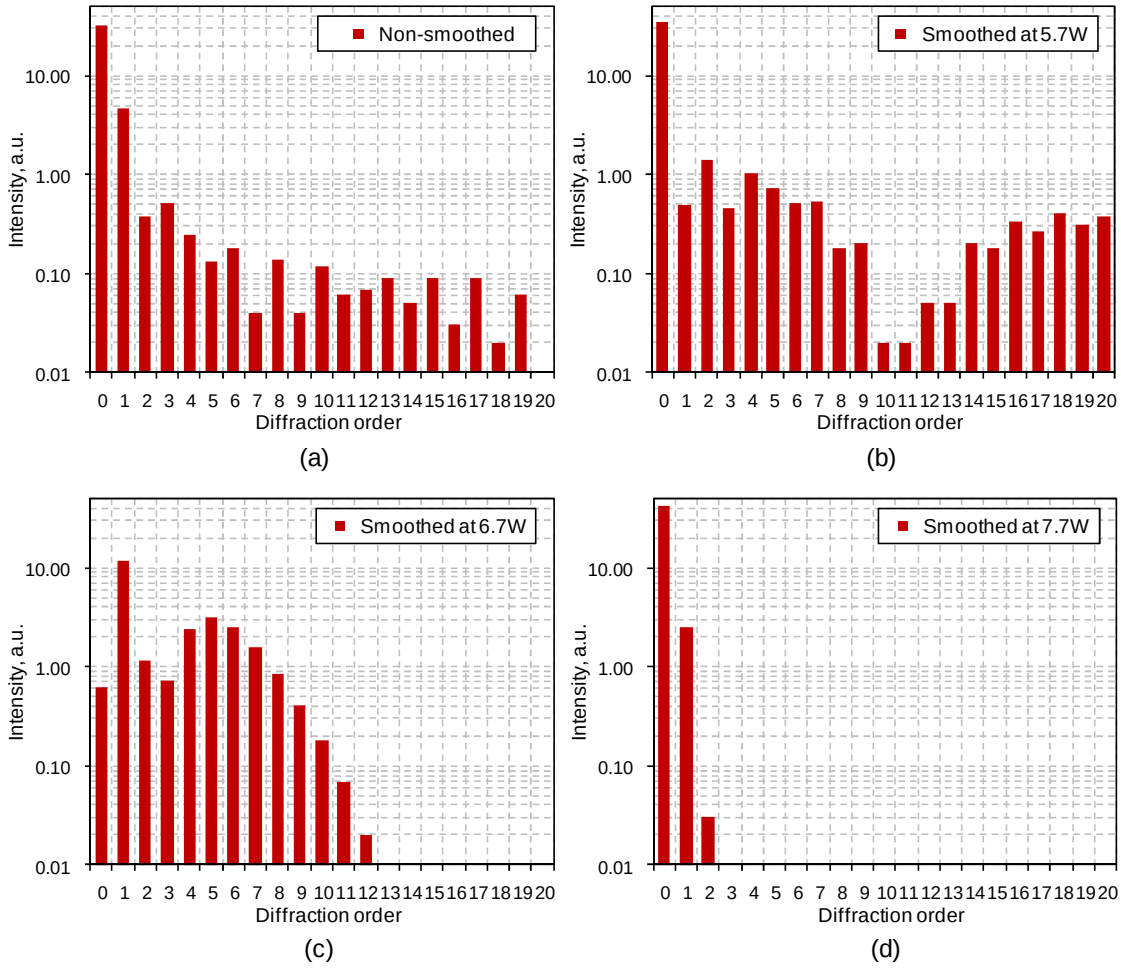

Figure 4.10: Diffraction spectra measured for the 3 µm step height grating: (a) non-smoothed and (b) – (d) smoothed at a laser power of 5.7, 6.7, and 7.7 W, respectively.

In comparison to Figure 4.9 (a), the 3 µm step height non-smoothed grating generates a spectrum with significant intensities in the even diffraction orders, as shown in Figure 4.10 (a). This may mean that this structure contains undercut steps which could not be detected by the AFM.

The diffraction spectrum produced by the 3 µm step height grating smoothed at a laser power of 5.7 W is shown in Figure 4.10 (b). This spectrum is also difficult to interpret because the intensity is redistributed into the diffraction orders without forming the characteristic slope, as observed previously in Figure 4.9 (b). This may mean that the taller steps are more difficult to relax. This hypothesis will be verified in Section 4.6.4.

Finally, the spectra with a characteristic cut-off slope are shown in Figure 4.10 (c) and (d). These spectra were obtained for the 3 µm step height grating smoothed at laser powers of 6.7 and 7.7 W, respectively. At these laser powers, the binary structure is converted into a near-sinusoidal shape, as can be seen from the AFM surface profiles presented in Figure 4.7 (b).

Conclusions

The optical method presented in this Section was found to be very sensitive to the surface profile changes in the binary structures. In comparison to the conventional stylus-based surface-profile-measurement devices, e.g. AFM and DEKTAK, the optical method allows us to detect the onset of the relaxation of very steep sidewalls. As shown in Figure 4.9 and Figure 4.10, the diffraction patterns carry information on the relaxation distance of the binary steps. Considering this fact, the optical method seems to be an attractive approach for the characterization of the CO_2 laser polishing process, completely different from that proposed by K. Nowak in [3, 61].

4.6 Simulation of He-Ne laser illumination of laser-smoothed gratings

This section is focused on the development of a simple mathematical model for simulating He-Ne laser illumination of CO_2 laser-smoothed binary gratings. The aim of this model is to provide a better understanding of diffraction patterns obtained by using the optical method (see the previous section). As will be shown below, it is possible to quantify the laser smoothing effect of binary structures by the use of only a single parameter, called a relaxation distance (*RD*). This parameter has been already introduced in Section 4.4.1.

4.6.1 Mathematical description of the laser-smoothed binary surfaces

Generally, the relaxed steps of a binary grating may be represented by the sum of two Gaussian error functions:

$$f(x) = \frac{1}{2}A \sum_{i=-\infty}^{\infty} \left[erf\left(\frac{x + i\Lambda + a\frac{\Lambda}{4}}{\frac{RD}{1.81}} \right) + erf\left(\frac{-x + i\Lambda + a\frac{\Lambda}{4}}{\frac{RD}{1.81}} \right) \right] - \frac{A}{2} \qquad (4.5)$$

where:

A defines the initial step height of the grating,

Λ defines the spatial period of the grating,

a defines the mark-to-space ratio of the grating (when *a* = 1, the fill factor is 50%),

RD defines the relaxation distance of the etched steps.

Figure 4.11 shows the surface profiles which simulate a 0.8 µm step height grating with different values of *RD*. Based on the simulation results that were performed using Mathcad®, it can be concluded that equation (4.5) describes successfully an ideal surface relaxation of the etched steps. Therefore, it may be applied in a procedure for simulating He-Ne laser illumination of laser-smoothed binary structures (see the next section).

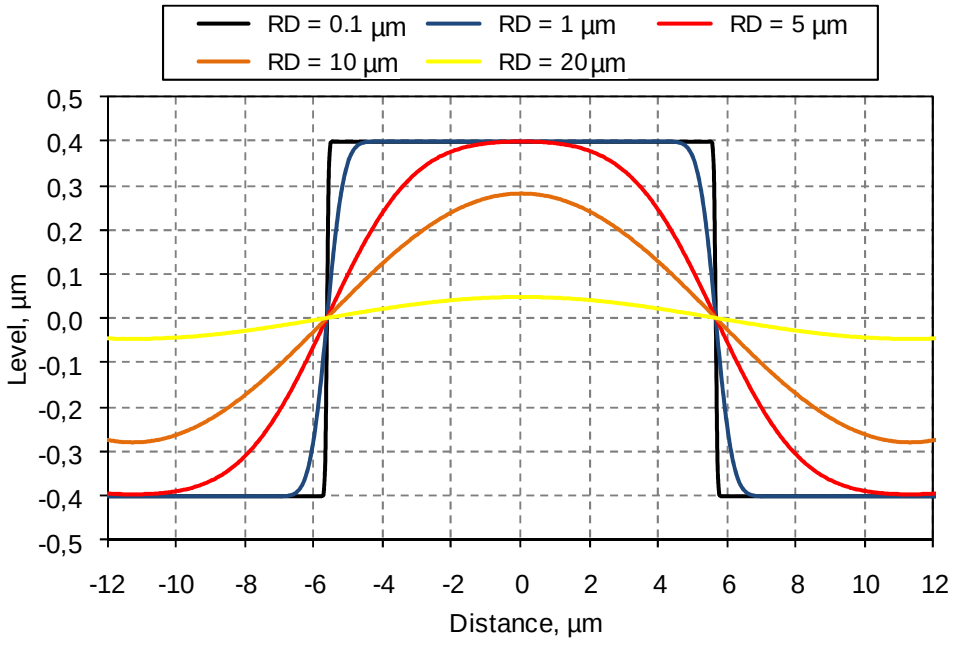

Figure 4.11: Surface profiles which simulate a binary grating with different *RDs*. An initial step height of the grating is 0.8 µm and the spatial period is 22.6 µm. Profiles plotted using equation (4.5).

4.6.2 Procedure to calculate light scatter distribution produced by gratings

In order to calculate the spectrum produced by a He-Ne laser beam passing through a binary structure, one has to execute the following procedures. At first, it is necessary to determine a phase change distribution along the surface profile of the grating. The phase change distribution as a function of distance (x) is given by:

$$\phi(x) = \frac{2\pi}{\lambda} \cdot (n-1) \cdot f(x) \tag{4.6}$$

where n is refractive index of fused silica at the He-Ne wavelength (λ), whilst $f(x)$ is a function described by equation (4.5). Since the incident light is modulated by the periodic structure, the resultant diffraction pattern may be evaluated by using the following formula:

$$\mathbb{F}_m = \int_{-\frac{\Lambda}{2}}^{\frac{\Lambda}{2}} exp\big(-i\phi(x)\big) \cdot exp\left(i\frac{2\pi x}{\lambda}\,\varphi_m\right) dx \tag{4.7}$$

where φ_m defines an angle of the m harmonic in the following way:

$$\varphi_m = \frac{m\,\lambda}{\Lambda} \tag{4.8}$$

Finally, the intensity in the diffraction orders (m) is calculated as:

$$I_m = C \cdot |\mathbb{F}_m|^2 \tag{4.9}$$

where C is the scale factor.

The procedure presented in this section is general. Therefore, it may be applied to the calculation of the diffraction spectrum produced by any surface profile which represents the periodic structure.

4.6.3 Light scatter distribution calculated for non-smoothed binary gratings

In this section, the mathematical formulae derived in Sections 4.6.1 and 4.6.2 are used to evaluate the light scatter distribution for two non-smoothed (ideal) binary gratings with a step height of 0.8 and 3 µm; the spatial period of both gratings is 22.6 µm. Based on these calculations, it will be possible to assess the degree of imperfection in the surface profile of the samples used in Section 4.4.2 (laser beam raster scanning of binary gratings).

The diffraction spectra calculated for the "ideal" binary gratings are shown in Figure 4.12. These spectra were found to be symmetrical in regard of the zero diffraction order, thus only the positive parts of the spectra are plotted.

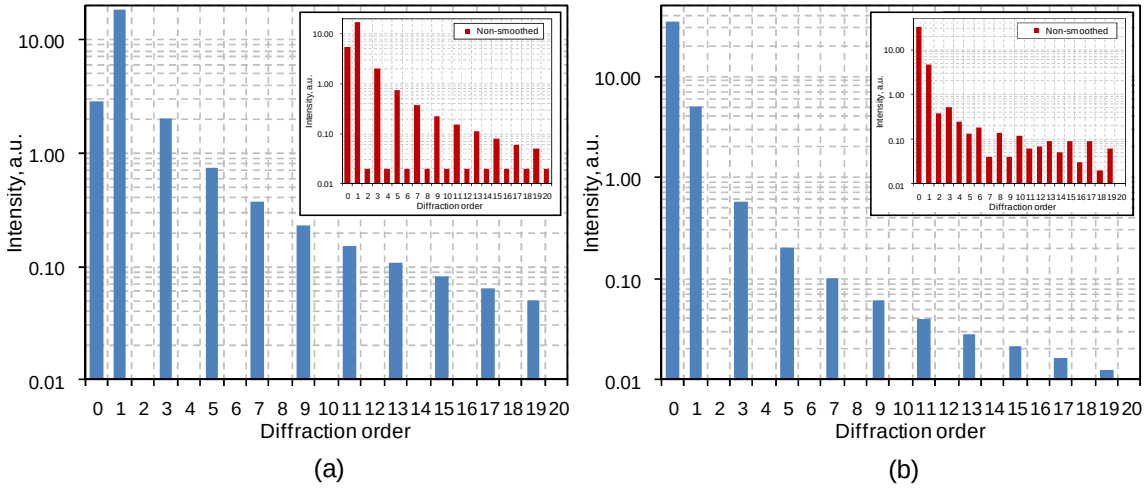

Figure 4.12: Diffraction spectra calculated for the "ideal" binary gratings with a step height of: (a) 0.8 µm and (b) 3 µm. The spatial period of both gratings is 22.6 µm. The spectra measured for the "real" non-smoothed gratings are presented in the insets.

To achieve a rectangular shape of the gratings, it was necessary to use very small *RD* values in equation (4.5). The *RD* values are listed in Table 4.1.

Table 4.1: Constants used in equations (4.5) to generate a surface profile of an "ideal" binary grating.

Gratings	A, µm	Λ, µm	RD, µm	a
0.8 µm step height	0.8	22.6	0.02	1
3 µm step height	3.0	22.6	0.06	1

Both spectra presented in Figure 4.12 are characterized by reduced intensity in the even diffraction orders. Since such spectra were not observed experimentally in Section 4.5, as shown in the insets of Figure 4.12, it seems to be obvious that the samples used in the experiment must have profiles which were distorted initially by etching.

By increasing the *RD* value in equation (4.5), there was an attempt to find the best match between the theoretical spectra and the experimental results achieved for the non-smoothed gratings. The best matching results, as judged by my subjective inspection, are presented in Figure 4.13. Here, it must be noted that an *RD* increment of 0.05 µm was sufficient to account for the observed difference in the shape of the spectra. The 0.05 µm increment was added to the *RD* value starting from 0.05 µm in the case of the grating with a step height of 0.8 µm and to the *RD* value of 0.1 µm in the case of the 3 µm step height grating.

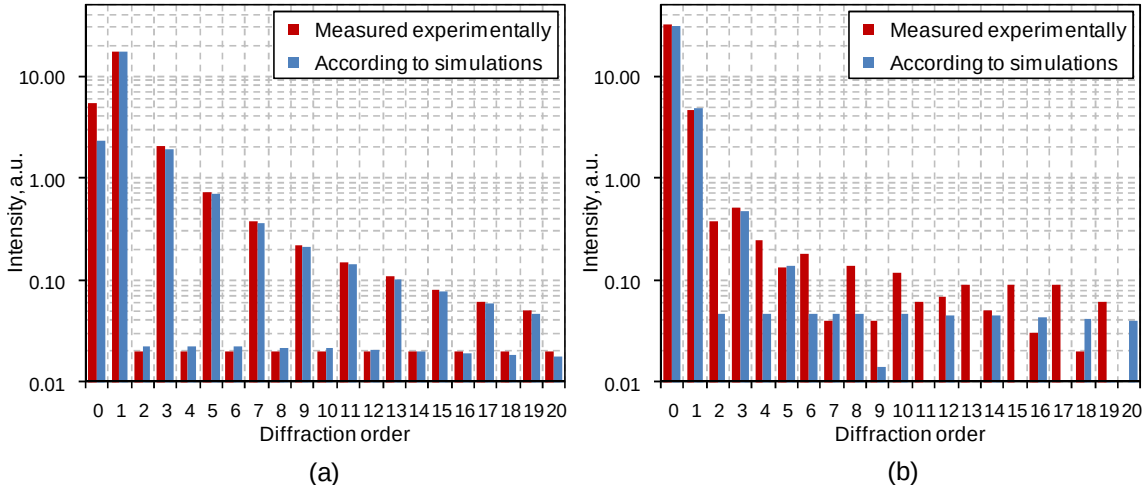

Figure 4.13: Diffraction spectra produced by: (a) 0.8 µm step height grating with *RD* = 0.25 µm and (b) 3 µm step height grating with RD = 0.4 µm.

For the grating with an initial step height of 0.8 µm, the best match was found at *RD* = 0.25 µm. As shown in Figure 4.13 (a), the calculated spectrum is consistent with the spectrum measured by using the optical method. A small discrepancy in the intensity of the zero diffraction order results from the mismatch between the real and simulated height of the etch steps. For the grating with an initial step height of 3 µm, the matching unfortunately failed. As can be seen in Figure 4.13 (b), good matching was achieved only for a few odd diffraction orders when *RD* = 0.4 µm. Due to this discrepancy between the theoretical and experimental results, it may be surmised that the 3 µm step height grating is more complex in shape than the grating with the lower steps. It is quite likely that the 3 µm step height grating contains an unequal mark-to-space ratio and undercut steps, resulting perhaps from deep etching.

In conclusion, it was shown in this section that the mathematical formulae derived from Sections 4.6.1 and 4.6.2 can simulate the He-Ne laser illumination of periodic grating structures. By choosing an appropriate value of the relaxation distance (*RD*) in equation (4.5), it was possible to achieve good mapping of the spectrum measured experimentally for the 0.8 µm step height grating. Based on this result, it may be concluded that equation (4.5) represents more faithfully the profile of the grating with the lower magnitude steps because this structure apparently does not contain undercut steps.

4.6.4 Quantification of the laser-smoothing effect in the binary structures

In this section, there is an attempt to achieve good matching between the experimental and theoretical spectra for the laser-smoothed gratings with an initial step height of 0.8 and 3 µm, using equation (4.5) with an appropriate value of the *RD* parameter. Based on these results, it will be possible to affirm that laser smoothing of the binary steps can be quantified by the relaxation distance, the parameter introduced earlier in Section 4.4.1.

The best mapping of the diffraction spectra measured with the aid of the optical method was achieved for the *RD* values listed in Table 4.2. The simulation results compared with the experimental spectra are shown in Figure 4.14 and Figure 4.15, respectively, for a 0.8 and 3 µm step height gratings. As can be seen there, the simulations are quite consistent with the experimental results for both structures. Some insignificant discrepancy in the intensities results from the fact that equation (4.5) represents the simplest case of laser smoothing of the binary steps, i.e., the structures are relaxed symmetrically without the appearance of any bulges and hollows by the step corners, as shown schematically in Figure 4.2 (see Section 4.3).

Table 4.2: Results of the spectra mapping.

Spectrum measured for gratings smoothed at:	RD values to achieved the best match	
	0.8 µm step height grating	3 µm step height grating
4.7 W	0.35	-
5.7 W	1.5	2.0
6.7 W	6.2	6.8
7.7 W	20.5	22.2

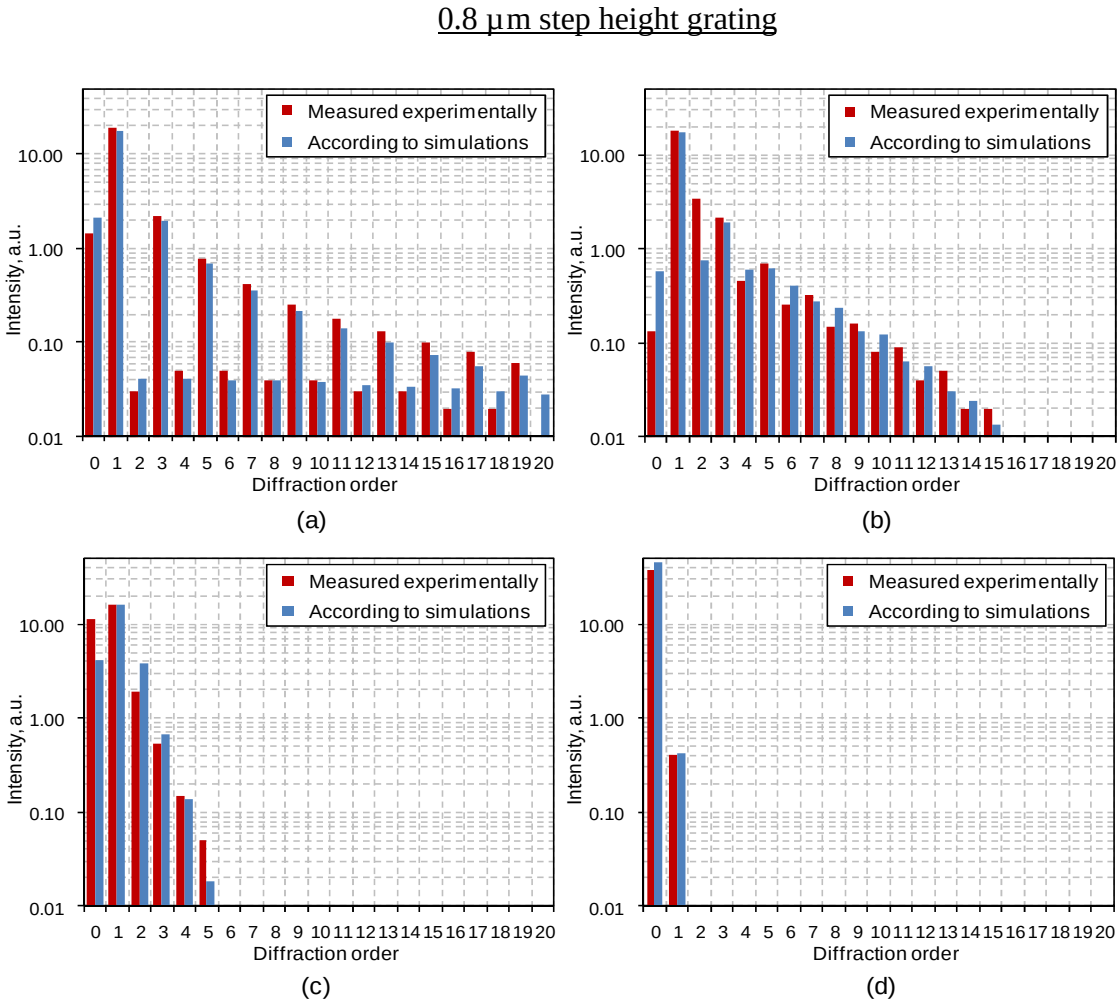

Figure 4.14: Experimental and theoretical diffraction spectra for a 0.8 µm step height grating. Results presented for the gratings: (a) smoothed at P = 4.7 W and calculated at *RD* = 0.35 µm, (b) smoothed at P = 5.7 W and calculated at *RD* = 1.5 µm, (c) smoothed at P = 6.7 W and calculated at *RD* = 6.2 µm, and (d) smoothed at P = 7.7 W and calculated at *RD* = 20.5 µm.

3 µm step height grating

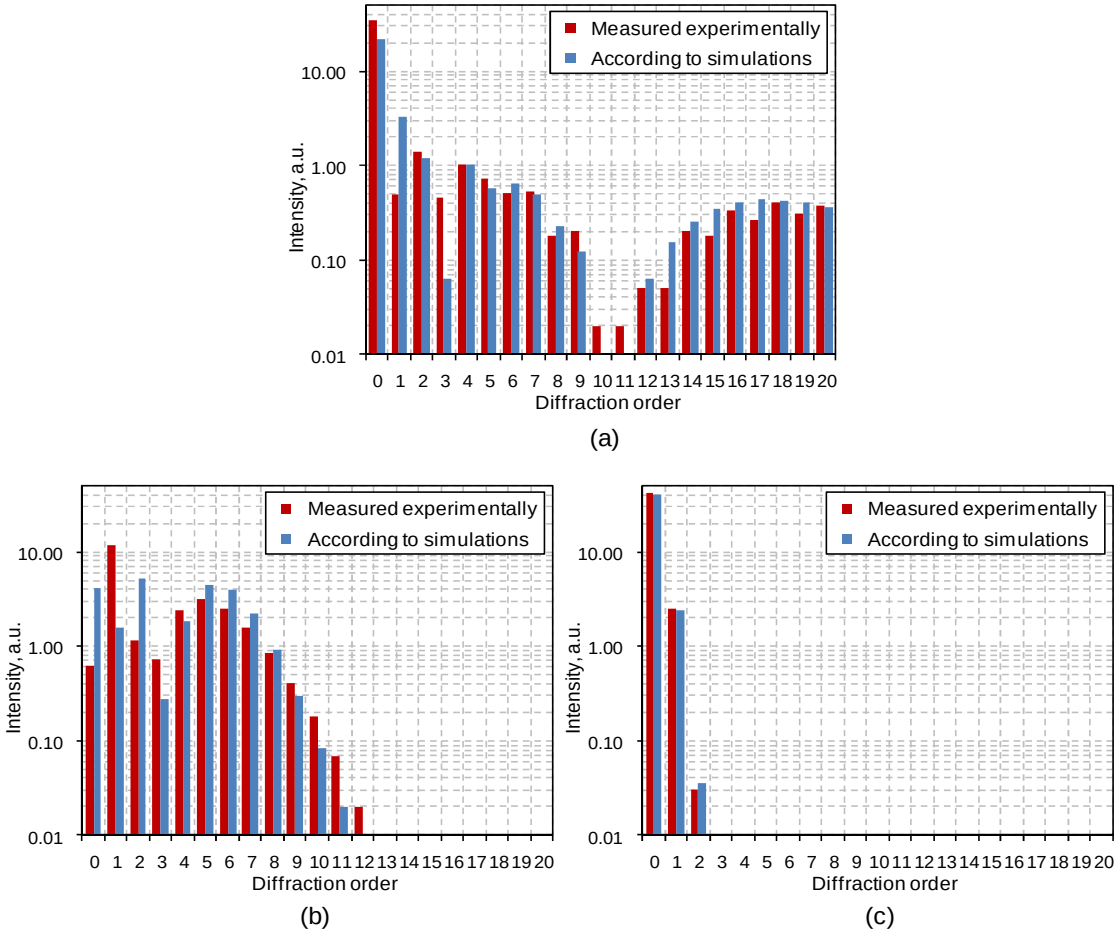

Figure 4.15: Experimental and theoretical diffraction spectra for a 3 µm step height grating. Results presented for the gratings: (a) smoothed at P = 5.7 W and calculated at *RD* = 2.0 µm, (b) smoothed at P = 6.7 W and calculated at *RD* = 6.8 µm, (c) smoothed at P = 7.7 W and calculated at *RD* = 22.2 µm

In general, the matching procedure was similar to that carried out in Section 4.6.3. To find the best match between the theoretical and experimental spectra, a great number of spectra were generated for different values of *RD*, and then by using careful inspection and judgment those which showed the best agreement with the overall shape of the experimental spectra were selected. An *RD* increment used for generating spectra was varied, depending on the *RD* value. For the relaxation distances up to 1 µm, the *RD* increment was chosen to be 0.05 µm. When the relaxation distance was above 1 µm, the *RD* increment was changed to 0.1 µm due to a lack of sufficient difference in the overall shape between two spectra. Since the best matching of the spectra was achieved by the use of my personal judgement, it is quite difficult to determine a quantitative

matching error. However, the assumption that the matching error is twice as large as the *RD* increment used for generating spectra seems to be reliable.

In conclusion, the results presented in Table 4.2 show firm evidence that the laser smoothing effect of binary structures can be quantified by using the relaxation distance parameter (*RD*). As can be seen in Figure 4.16, the relaxation distance is strongly dependent on the laser power used for smoothing (quasi-linear dependency in the semi-log scale). Horizontal error bars correspond to laser power fluctuations of 50 mW (typical for the laser polishing system covered in Section 3.1); whilst the vertical ones correspond to the *RD* increment multiplied by 2.

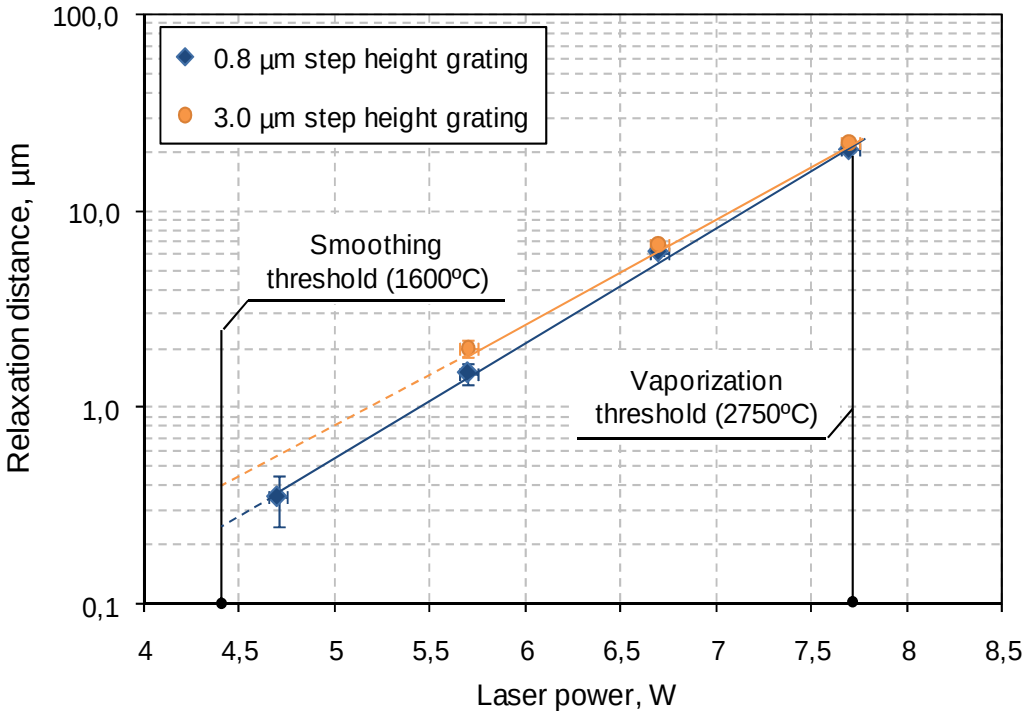

Figure 4.16: Relaxation distance of the 0.8 and 3 µm binary steps vs. laser power used (plotted in semi-log scale). Graph plotted based on the simulation results listed in Table 4.2.

Based on the simulation results presented in Figure 4.16, one may define a smoothing threshold for fused silica. This can be done by extrapolating the trends (see solid lines) to the *RD* values which correspond to the relaxation distance of the unsmoothed gratings, i.e., *RD* = 0.25 and 0.4 µm, respectively, for 0.8 and 3 µm high steps. Following these extrapolations, the smoothing threshold is determined to be at 4.45 W. This laser power level probably corresponds to the softening point of fused silica (T_S = 1600°C). At this temperature, the glass has a viscosity ($\eta = 10^{6.6}$ Pa·s)

which is low enough to move the material near the sharp corners, where the pressure difference is the highest (see Section 4.3).

The maximum scale length of the surface features (λ), which are able to be relaxed within a time of τ at the viscosity of $\eta = 10^{6.6}$ Pa·s, can be estimated by using the following formula [10, 119]:

$$\lambda = \frac{\tau \gamma}{\eta} \tag{4.10}$$

where γ is the surface tension of a fluid (γ = 0.3 N/m for fused silica, as given in Section 4.2). As already indicated in Section 4.4.2, a 550 µm diameter laser beam produces a melt spot with a diameter of 100 µm. This means that a single line laser scan with a speed of 5 mm/s causes the glass to melt within a 20 ms time period. Since the binary samples were treated by laser beam raster scanning with a raster pitch of 10 µm, the accumulated dwell time (τ) was approximately 8 times longer than that for a single line laser scan, based on equation (4.4) given in Section 4.4.2. Thus, by substituting the dwell time of 160 ms for the τ constant of equation (4.10), the λ value is estimated to be 12 nm. This value means that the features which are smaller than 12 nm are relaxed at the temperature of 1600°C. Since the sharp corners of the unsmoothed gratings have probably a curvature radius below 10 nm, it is reasonable to say that the softening point corresponds to the smoothing threshold (see Figure 4.16), thereby confirming the assumption given in the previous paragraph.

Finally, by assuming that the thermal properties of fused silica do not change with temperature, it is possible to estimate roughly the laser power level at which the glass begins to evaporate. Since the surface temperature produced in a solid by a moving laser beam is proportional to the laser power used (see equation (7.10) in Section 7.4.3), the vaporization point of fused silica (T = 2750°C based on Figure 4.1) is calculated to be at a laser power of approximately 7.7 W. This means that a 550 µm diameter laser beam is able to smooth the binary steps (both 0.8 and 3 µm high) up to a 22 µm relaxation distance. Above 7.7 W, the glass begins to lose its mass, thereby removing completely the etch steps, as shown in Figure 4.4 (c). In order to relax the etch step over a distance longer than 22 µm, it is necessary to increase the depth or dwell time of the molten glass layer. This can be achieved by using a larger laser spot or by applying more laser scans, based on equation (4.1) given in Section 4.2.

4.6.5 Summary

It was shown in this section that the mathematical formulae derived in Sections 4.6.1 and 4.6.2 allow us to simulate the optical method developed in Section 4.5, thereby providing a better understanding of the diffraction spectra and quantifying the surface relaxation of the etched steps. Based on the simulation results presented in Sections 4.6.3 and 4.6.4, it can be concluded that the surface relaxation of binary steps is controlled by the laser power. As shown in Figure 4.16, the relaxation distance up to 20 µm may be easily achieved by using a 550 µm diameter laser spot. Such a large relaxation of the etched steps seems to be appropriate for the fabrication of micro-optical components by combining a CO_2 laser smoothing process with a well-established technique for etching. Some simple demonstrations of this approach are presented in the next section.

4.7 Laser smoothing of multi-level etch structures

The experiments described in Section 4.4 showed that CO_2 laser smoothing provides an efficient and controllable relaxation of single-level steps in binary gratings. The aim of this Section is to extend the smoothing process to multi-level etched elements. Such an approach may be a useful alternative to the glass reflow process in which fused silica is used to fabricate refractive micro-optical components, such as single microlenses or microlens arrays [116].

To demonstrate the usefulness of laser relaxation of multi-level etched structures, the CO_2 laser smoothing process was applied to two identical samples with 64 etched steps, as shown in Figure 4.17. The samples were produced by a multi-mask RIE process. The fabrication of multi-level etch structures was performed within the Diffractive Optics group at Heriot-Watt University.

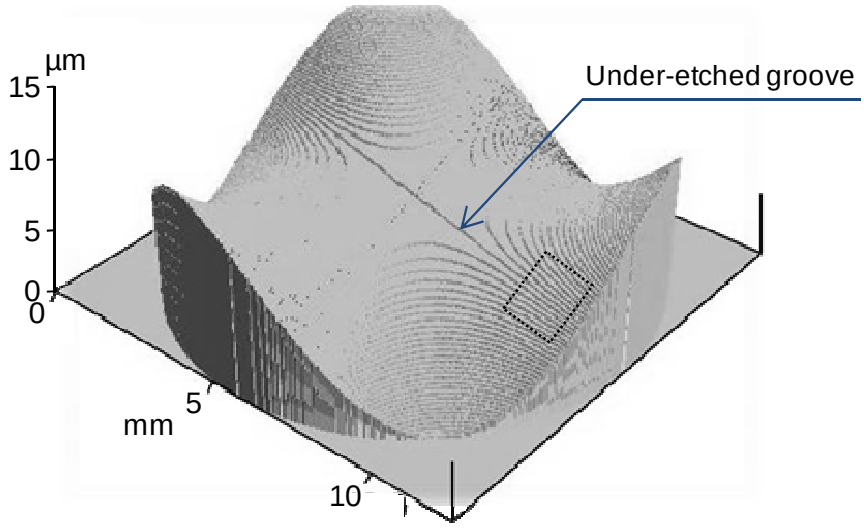

Figure 4.17: A 64-level etched structure used for demonstration of the surface relaxation by CO_2 laser smoothing, by courtesy of G. Muyo from the Imaging Concepts group at Heriot-Watt University. The area inside the dotted box is shown in details in Figure 4.18 (a).

The height of each step was 200 nm, giving a total structure height of 12.8 µm. The horizontal distance between steps ranged from 50 to 1500 µm at various positions across the sample. Such a large variety in the horizontal distance between steps provided an opportunity to study long-range relaxation of steps using only one sample. A microscope analysis of the samples showed that some of the transitions in etched structures had undercut steps or deep grooves. These surface imperfections were created presumably by mask misalignment during the photolithographic process, combined with a large overall etch depth. Such a diversity of features on etched surfaces, however, made these samples very valuable from the research point of view because they included all extreme etching cases on one piece.

Since laser beam raster scanning of the binary grating with a 0.8 µm step height produced a uniform smoothing effect of the etched steps (see Section 4.4.2), this mode of laser treatment was also used for multi-level etched samples. The laser smoothing conditions were similar to those used for the raster scan area treatment of binary structures, with the exception of the laser beam diameter which was increased back to approximately 1 mm, thereby providing the ability to achieve relaxation distances larger than 20 µm. Since the number of samples used in this experiment was limited to only two pieces, the laser power used for smoothing was chosen to be 7.6 and 7.9 W.

From the previous experiment, it was known that such values of laser power should provide efficient relaxation of etched steps in the range between 20 and 30 µm (see Figure 4.16). The profile of surfaces with relaxed features was measured by a DEKTAK surface profilometer and then compared with the initial surface shape (before laser smoothing). In addition, an optical microscope was used to examine the overall structure of samples.

The microscope image of the localized area marked in Figure 4.17 is shown in Figure 4.18 (a). There are visible, sharp zigzag steps which fall from top to bottom, crossing an approximately 8 µm wide groove which is represented by a horizontal zigzag line in the middle of the micrograph. According to Figure 4.17, this wide groove is located between the 31st and 32nd levels and was produced presumably by a mask registration error in the second photolithographic step. This means that the groove could be as deep as 6.4 µm. After laser smoothing with a laser power of 7.6 W, the zigzag steps seemed to be softened, as expected, whilst the groove appeared to be wider, as can be seen in Figure 4.18 (b).

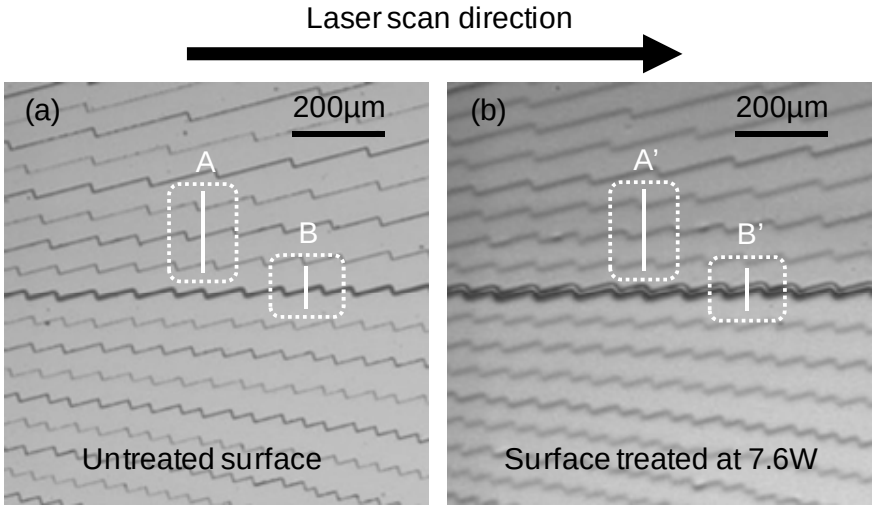

Figure 4.18: Optical microscope image of: (a) a fragment of multi-level etched structure before laser polishing and (b) the same sample after laser smoothing with laser power of 7.6 W. The sample contained an under-etched groove (see a horizontal zigzag line in the middle). Published in [112].

To investigate the surface relaxation of etched steps in the staircase structure, the selected regions in Figure 4.18 (see dotted boxes) were scanned using the DEKTAK

surface profilometer. Since the radius of the profilometer stylus used for the measurement was 12.5 µm, the width of 200 nm height steps was measured to be approximately 2.2 µm greater in comparison to the actual width. Figure 4.19 shows the surface profile of steps taken along the solid lines within areas of A and A' (see Figure 4.18). Additionally, the surface profile of steps relaxed at laser power of 7.9 W is also presented.

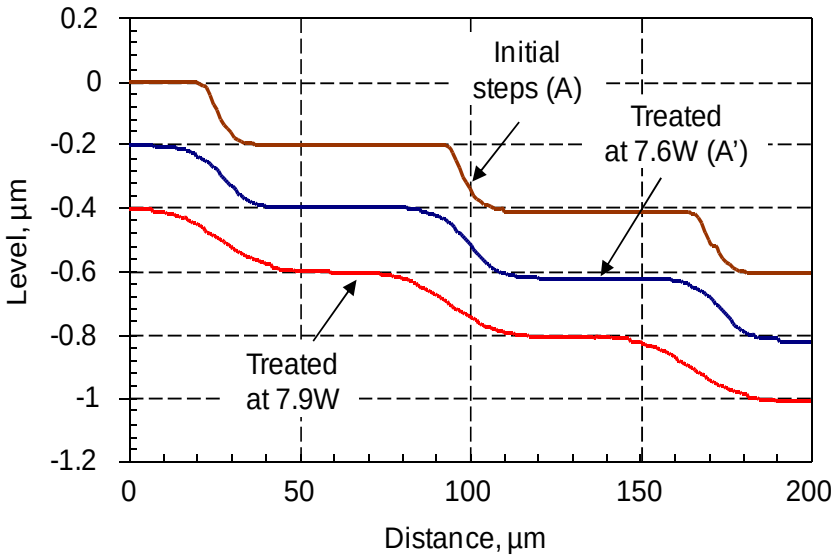

Figure 4.19: Laser smoothing effect of "normal etched" steps, from an area "A" in Figure 4.18 (a), at laser powers of 7.6 and 7.9 W. Each profile is offset by 0.2 µm to provide a better view on the surface changes. Published in [112].

Based on the surface profiles, the width of step transition in the initial surface was found to be approximately 9 µm. This value was significantly larger than the broadening caused by the profilometer stylus, thus the slope was probably associated with the etching process. Laser smoothing of the structure with laser powers of 7.6 and 7.9 W showed a symmetrical relaxation of steps. The relaxation distances of about 20 and 30 µm were determined from Figure 4.19 for laser powers of 7.6 and 7.9 W, respectively. Such a large relaxation of the etched steps was found to be consistent with the previous results presented in Figure 4.16 (see Section 4.6.4).

The microscope examination of the laser-smoothed structures showed that the areas with non-undercut step edges are smoothed uniformly (see the area A' in Figure 4.18). The laser smoothing effect was observed to be the same for step edges

oriented at all directions relative to the scan direction. This means that the polarization direction of the incident laser beam does not have an effect on the smoothing quality.

Laser smoothing of deep grooves and undercut steps existing in the structure was investigated separately because these features behaved differently with laser beam irradiation in comparison to "well etched" steps. The under-cut grooves shown in areas B and B' of Figure 4.18 were scanned using the DEKTAK surface profilometer. The surface profiles of these grooves are shown in Figure 4.20.

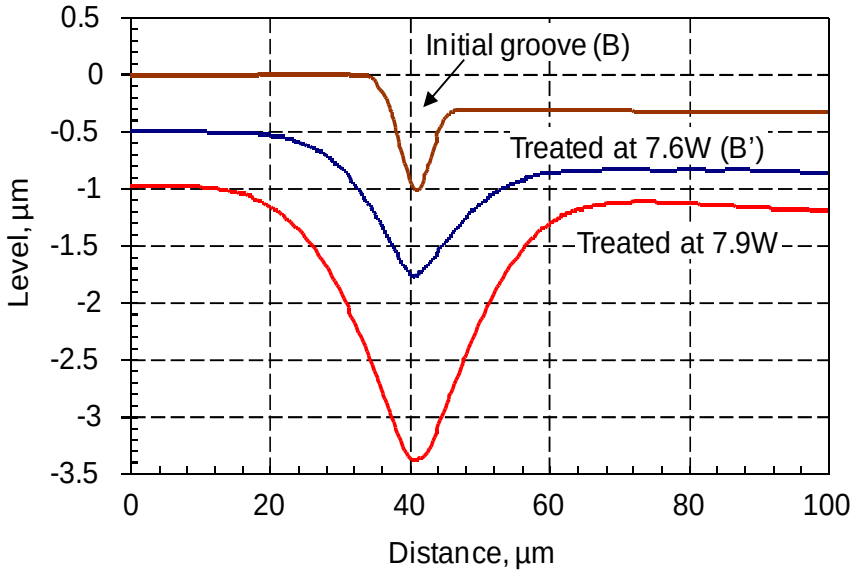

Figure 4.20: Laser smoothing effect of under-etched groove, from an area "B" in Figure 4.18 (a), at laser powers of 7.6 and 7.9 W. Each profile is offset by 0.2 µm to provide a better view on the surface changes. Published in [112].

The initial groove was found to be 8 µm wide and ~ 700 nm deep. This trace, however, was purely limited by the profilometer stylus response because the size of the tip used for the measurement was significantly larger than the width of the initial undercut feature. After laser treatment, the groove trace was observed to be wider and deeper, especially at a laser power of 7.9 W where the groove was found to be about 40 µm wide and 2.2 µm deep. Although the increase in the groove width at its surface was indicated correctly, the profilometer stylus probably did not reach the bottom of the groove, so its depth may be underestimated. If we include this assumption into the calculation of the groove areas before and after laser treatment, we find that the groove area after laser smoothing with a 7.9 W laser power is larger than the area of the initial

groove. This means that some amount of glass may have been removed by evaporation, although this was unexpected at this laser power value. The generation of localized hot spots inside the groove may be explained by the interaction of CO_2 laser light with subwavelength features of the initial groove [118, 120].

For deep grooves and undercut features, it was observed that the laser scan direction matters now. As shown in Figure 4.21, the misregistered features orientated normal to the laser scan direction became longitudinal pits after laser smoothing, whilst the grooves oriented parallel to the direction of the moving laser beam were filled in by a molten glass layer.

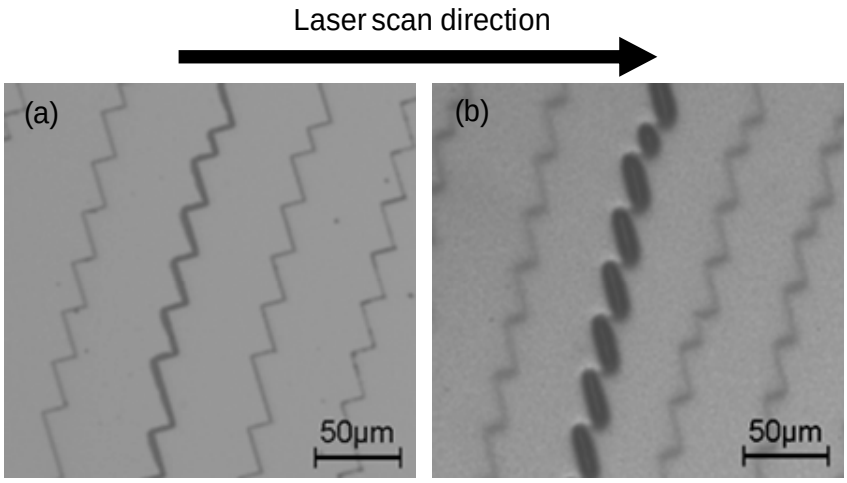

Figure 4.21: Misregistered etch steps oriented perpendicular to the scan direction: (a) before and (b) after laser smoothing with laser power of 7.6 W. Published in [112].

The appearance of longitudinal pits may be associated with the capillary effect occurring during the laser smoothing process when glass becomes a liquid flowing under the action of surface tension. The capillarity of the molten glass was previously observed by E. Mendez who studied laser smoothing of diamond scribed lines in fused silica [1]. Another explanation of the pattern of longitudinal pits may be the polarization dependency between the submicrometer features and the laser beam used. However, this assumption is difficult to be proved, based on the publications studied so far [117, 118, 120, 121].

Summary

The results of laser smoothing of multi-level etched structures revealed that CO_2 laser irradiation provides well-controlled relaxation of 200 nm high steps. The steps are able to be relaxed symmetrically over a distance of up to 30 µm by using a 1 mm diameter laser beam at a laser power of 7.9 W. Such a large relaxation of etched steps seems to be a viable alternative to the glass reflow process, in which a "digital" structure manufactured in fused silica is used for the fabrication of micro-optical components [116]. The concept of the use of CO_2 laser smoothing of multi-level etched structures for making micro-optics is shown in Figure 4.22 (a). As presented in Figure 4.22 (b), the 30 µm relaxation distance of etched steps is a promising proof of the concept.

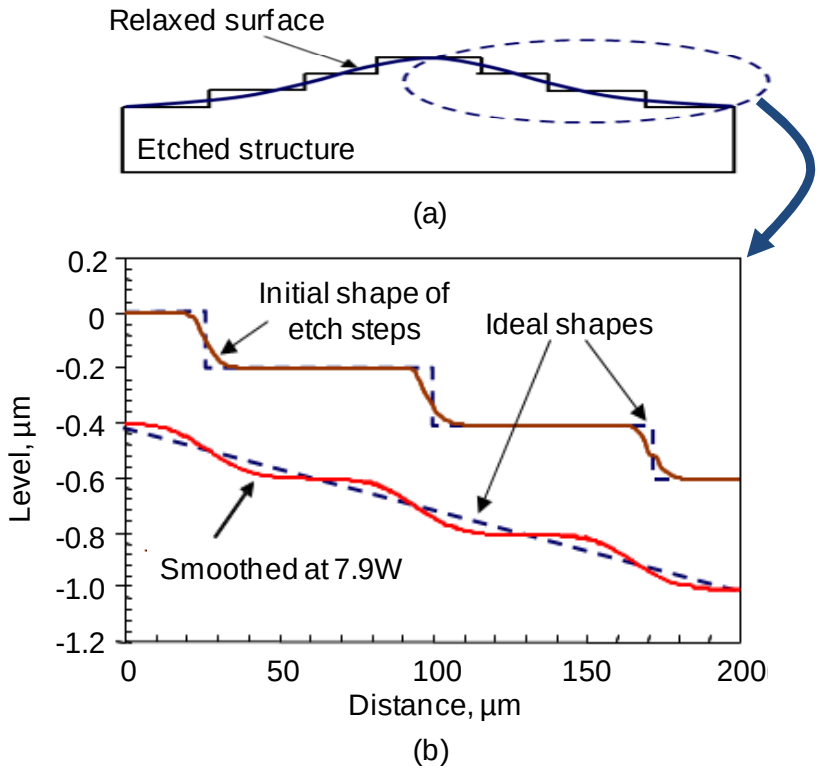

Figure 4.22: (a) The concept of the fabrication of micro-optics by laser smoothing of multi-level etched structures. (b) Relaxation of 200 nm high steps obtained by using a 1 mm diameter laser beam at 7.9 W laser power and comparison of the result with the desired shape of surface.

Also, it has been shown in this section that undercut steps are a serious limitation in the fabrication of micro-optical components by laser smoothing. Laser treatment of the undercut steps revealed that a CO_2 laser beam cannot smooth them

out, producing polarization-dependent distortions in the structure, and consequently enhancing the appearance of the defects. This means that etching of the multi-level structures used for laser smoothing must be carried out with high precision, perhaps using more advanced techniques than multi-mask reactive ion etching.

4.8 Summary and conclusions

The aim of the work covered in this chapter was to fully characterize the laser smoothing effect of binary gratings (i.e. building on the work of E. Mendez) and to study CO_2 laser smoothing of multi-level etched structures.

As shown in Section 4.4, the steps of binary gratings with a spatial period of 22.6 µm are able to be relaxed over a distance from submicron to approximately 22 µm, depending on the laser power used. The submicron resolution means that laser smoothing may be applied for fine relaxing of the etch steps of the diffractive optics in order to increase the diffraction efficiency of these optical components. Also, it was shown in this section that the binary steps as low as 1 µm (and most likely lower) are relaxed equally from the top and bottom corners, whilst the asymmetry in the relaxation occurs in the higher gratings.

The experiments with CO_2 laser smoothing of multi-level etched structures revealed that a 1 mm diameter laser beam at a 7.9 W laser power is able to relax symmetrically the 200 nm high steps over a distance of 30 µm. As shown in Figure 4.22, such a large surface relaxation of the steps seems to be a promising result that may be used for the fabrication of micro-optics in fused silica, as a viable alternative to the glass reflow process.

In the same experiment, it was also shown that CO_2 laser irradiation of undercut steps and deep grooves cannot smooth them out. Moreover, the appearance of these surface defects was found to be enhanced after laser treatment. This means that multi-level structures prepared for subsequent laser smoothing must be fabricated with a high precision of mask alignment in the etching process.

Finally, the optical method developed in Section 4.5 was found to carry information on the relaxation distance of binary steps. As shown there, this method is very sensitive to the laser-induced surface changes in the structure. In comparison to

the conventional stylus-based surface-profile-measurement devices (e.g. AFM and DEKTAK), the optical method allows us to measure the relaxation of very steep sidewalls, thereby detecting the onset of the smoothing effect. In combination with the mathematical formulae presented in Section 4.6, the optical method seems to be a complete tool for measuring the smoothing effect of the periodic structures. Therefore, this measuring technique is proposed as a novel approach for characterizing the CO_2 laser polishing process. By utilizing the optical method and a simple binary grating as a test piece for smoothing, it is possible to achieve an efficient tool for calibrating CO_2 laser polishing systems, which are used for the fabrication of micro-optical components. There are four advantages of the proposed calibration method. The first one is quick measurement of the diffraction patterns generated by the laser-smoothed gratings. Currently, measurement of the intensity in the diffraction orders takes approximately a couple of minutes because it is carried out manually. In the future, however, the measurement may be easily automated and carried out via a computer. Also, the best matching of the spectra may be automated by using a mathematical algorithm. The second advantage is a low fabrication cost of the test samples, because the binary structures may be manufactured in large quantities using only a one-step etching process. The simplicity of the test structure used in the proposed calibration method is another advantage. In comparison to the previous technique used for characterizing a CO_2 laser polishing process, which was proposed by Nowak *et al.* [3], the binary structures are manufactured with high precision, thus the proposed calibration technique allows us to achieve very repeatable results. Finally, the optical method allows us to detect surface changes as low as 10 nm. This means that CO_2 laser smoothing may be applied for a controllable relaxation of nano-scale surface features, thereby opening the possibility of using the smoothing process for nano-structures fabricated in fused silica.

Chapter 5
Study of CW CO_2 laser-induced surface deformations in fused silica and Borofloat®33

5.1 Introduction

This chapter is focused on quantitative and qualitative analysis of surface deformations generated by single linear laser scans in fused silica (HPFS®7980 Corning, USA) and Borofloat®33 glass (Schott AG, Germany). The deformations produced by a 1.1 × 0.9 mm elliptical Gaussian laser beam moved along a line track with a speed of 5 mm/s are studied here for a wide range of laser power levels (from 0.5 to 10 W). In addition, this chapter contains preliminary results related to CO_2 laser smoothing of Borofloat optical windows supplied by Edmund Optics (UK).

Surface deformations produced by a moving laser beam in fused silica (probably manufactured by Heraeus) were initially studied by E. Mendez [10]. His research has shown that single linear laser scans modulate the glass surface, generating micro-deformations in the form of W-shaped bumps transverse to the scanning direction. The peak-to-valley height of these deformations was measured to be in the range from 5 to 15 nm per laser scan, depending on the laser power used. These W-shaped bumps were explained in terms of the thermocapillary and chemicapillary effects which occur during CO_2 laser irradiation of the glass. These surface tension effects were covered briefly in an earlier section (Section 2.5.3).

The characterization of surface deformations generated by single linear laser scans has particular importance in CO_2 laser polishing of micro-optical components. Although laser polishing typically employs laser beam raster scanning to achieve a smoothing effect over a large area of the glass surface, the investigation of surface deformations generated by an elementary laser scan at different laser power levels seems to be the best method to determine a potential mechanism which is responsible for the formation of these distortions.

As already mentioned at the beginning, laser-induced surface deformations have been investigated in two optical glasses: high purity fused silica (HPFS®7980 Corning) and Borofloat®33 (manufactured by Schott AG). The HPFS®7980 glass was chosen for study here because this material is typically used as a substrate for the fabrication of micro-optical components, using CO_2 laser cutting and polishing processes. Therefore, knowledge of the extent of surface deformations produced by a moving laser beam and understanding of the relevant mechanism are highly desirable for this material. The second glass which is studied in this chapter is Borofloat®33. This glass belongs to the borosilicate family. It contains approximately 81% SiO_2, 13% B_2O_3, 4% Na_2O/K_2O and 2% Al_2O_3 [26]. As shown in Table 5.1, Borofloat®33 has similar optical and thermal properties to fused silica, apart from the coefficient of thermal expansion which is approximately 5 times larger than the *CTE* of HPFS®7980 Corning. Due to presence of various oxides in Borofloat®33 (in particular Na_2O/K_2O), the critical parameters for this material (e.g. the softening point) occur at significantly lower temperatures than those of fused silica.

Table 5.1: Physical properties of HPFS 7980 Corning and Borofloat®33 at room temperatures.

Properties	HPFS 7980 Corning [30]	Borofloat®33 [26]
Refractive index, n	1.46 @ λ = 632.8 nm	1.47 @ λ = 632.8 nm
Density, ρ	2.2 g/cm^3	2.2 g/cm^3
CTE	0.6	3.2
Thermal conductivity, k	1.31 W/m·K	1.20 W/m·K
Specific heat, C_p	770 J/kg·K	830 J/kg·K
Annealing point, T_A	1042°C	560°C
Softening point, T_S	1580°C	820°C

There are two main reasons why there is an interest to study the interaction between Borofloat®33 and a moving CO_2 laser beam. Firstly, Borofloat®33 is relatively inexpensive and has similar optical properties to fused silica (e.g. refractive index). Secondly, Borofloat®33 has the lowest *CTE* of all commercial non-silica optical glasses. These two reasons mean that this glass seems to be an attractive candidate for non-cracking CO_2 laser processing at room temperatures, thereby being a lower-cost alternative to fused silica – currently the ideal material for CO_2 laser micro-machining.

5.2 Study of laser-induced surface deformations in fused silica

The experiments described within this section were performed on two 25.4 mm square high purity fused silica samples (HPFS®7980 Corning). The first one was 1 mm thick while the other was 1.5 mm. Based on Table 2.1 (see Section 2.3.1), the samples were free of metallic impurities and contained a high quantity of OH ions (about 900 ppm).

5.2.1 Description of the experiment

Prior to laser treatment, the glass samples were cleaned using isopropanol in order to remove residual contamination and dust from the surfaces. This procedure avoided the glass being laser-overheated in places where dust and contamination occur.

The set of single line laser scans was performed for each sample equally, as shown in Figure 5.1. The scans were 20 mm long and the separation distance between them (Δx) was 2 mm. Each laser scan was carried out with a 5 mm/s speed, using a 1.1 × 0.9 mm laser spot (the larger radius was in the X-axis) and average laser power levels in the range of 4.5 to 10.5 W. The laser was operating at 10.59 µm wavelength.

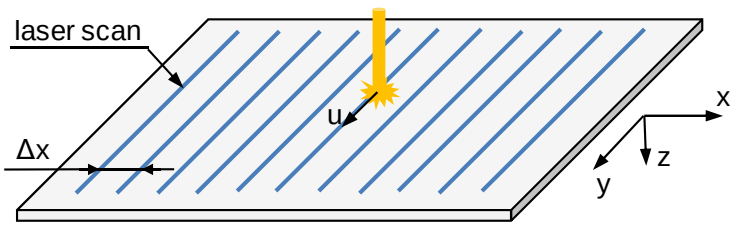

Figure 5.1: Illustration of the experiment. Blue stripes indicate single linear laser scans.

To determine shape and extent of the laser-induced deformations, the glass surface was scanned using a non-contact surface measurement instrument Proscan 1000 (Scantron

Industrial Products Ltd, UK). The profilometer enabled the laser-irradiated area to be scanned with a 10 µm spatial resolution, giving a resolution in the height measurement of approximately 10 nm. Since the measurement device generated a random noise of up to 60 nm peak-to-valley, the surface scans were further processed in Matlab® (Mathworks, US). By averaging the measured points with their neighbouring cells, it was possible to reduce the Proscan noise by a factor of 3, thereby detecting laser-induced surface deformations which were smaller than 25 nm in height.

5.2.2 Experimental results

The Proscan examination of the laser-irradiated areas revealed that a 1.1 × 0.9 mm Gaussian laser beam moved along a line track with a 5 mm/s speed distorts the glass surface when the laser power used exceeds 6 W. The surface deformations were found to be in the form of longitudinal trenches, which are thus different in shape to the W-shaped bumps observed by E. Mendez in [10]. The average depth of the trenches (D_{av}) measured as a function of the laser power is shown in Figure 5.2. The results are presented for 1 and 1.5 mm thick samples. The average depth was calculated based on measurement of the depth in at least 48 points along a trench over a 16 mm distance.

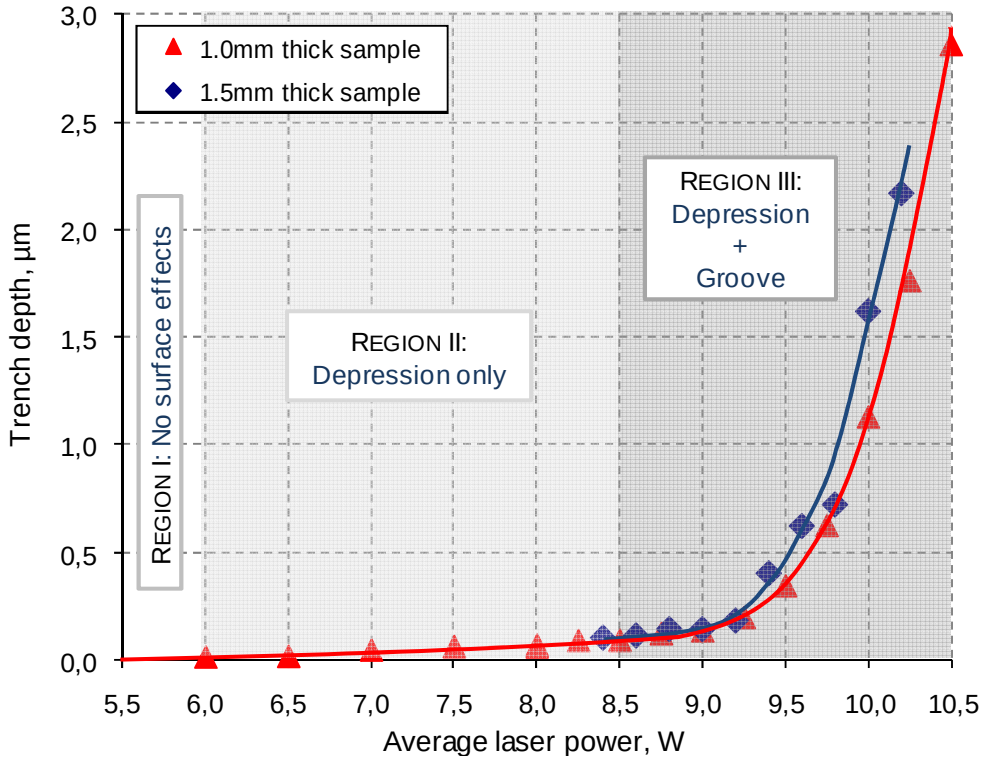

Figure 5.2: Average depth of trenches measured at different laser power. Results obtained for 1 and 1.5 mm thick fused silica samples.

Following the curves indicated in Figure 5.2, one may distinguish three characteristics regions in the laser power domain:

REGION I (below a 6 W laser power)

In this region, no surface modifications have been discerned in the glass.

REGION II (between 6 and 8.5W laser powers)

In this region, the depth of the trenches increases linearly with increasing laser power. Detailed Proscan examination of these surface distortions showed that they are in the form of shallow depressions, as shown in Figure 5.3. The maximum depth (D) of these depressions was measured to be an approximately 150 nm, whilst the width (W) was observed to be as large as 600 µm at laser powers slightly below 8.5 W.

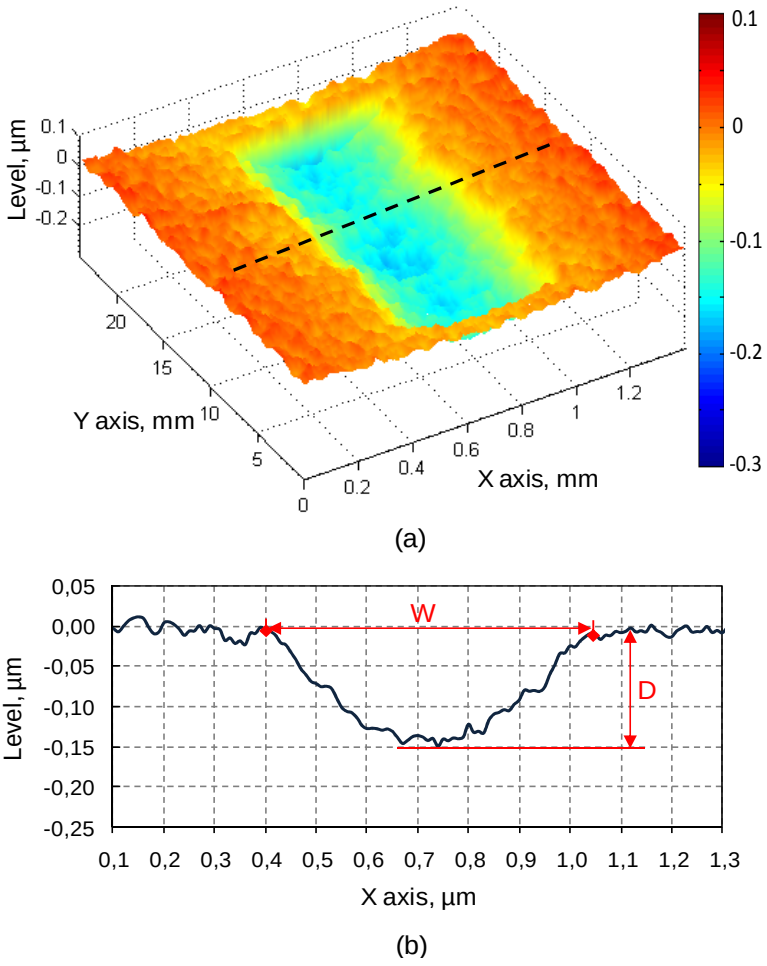

Figure 5.3: Surface deformation generated by a single linear laser scan at P = 8.4 W: (a) its 3D surface scan (140 ×96 pts) and (b) its cross-section taken along the dashed line indicated in (a). The depression was generated in a 1.5 mm thick fused silica substrate.

Based on the laser polishing protocol "D" published by K. Nowak *et al.* [3], it should be noted that the depressions are wider (up to three times) than the effective melt pool in which fused silica may undergo evaporation. This means that the shallow trenches are surely not produced by laser-induced vaporization, and thus they must be generated while the glass is only melted. Based on information covered in Section 2.5.3, there are three potential mechanisms which may be responsible for the appearance of the shallow depressions at the glass surface. They are as follows: the thermocapillary effect, the chemicapillary effect, and laser-induced densification of the glass.

The laser-induced densification was found to be the most likely mechanism which is responsible for the formation of the depressions in fused silica. As discussed in Section 2.5.3, the densification results from a local increase of fictive temperature of the material. The value of the fictive temperature depends on how fast the molten glass is cooled through the transformation range (see Figure 2.1 of Section 2.2). Generally, commercial optical glasses have a low fictive temperature (plausibly near the strain point) because they are cooled slowly in the manufacturing process, typically a few °C per hour [46]. In our case, however, the molten area was cooled rapidly through the transformation range after the laser beam had passed by, with the cooling rate estimated to be about 10^4°C/s [60]. Thus, it can be concluded that the laser-irradiated region of the glass reached a high fictive temperature. Since fused silica is categorized as an 'anomalous' glass (see Section 2.4.5), an increase of fictive temperature resulted in a local densification of the material, thereby forming shallow depressions in the laser-irradiated areas (see Figure 5.3). Based on work reported by Matthews *et al.* [122], the HPFS®7980 Corning sample cooled at a rate of 68°C/s reaches a fictive temperature of about 1550°C. Since the samples used in the experiment reported here were cooled down from high temperatures (T > 1600°C, as will be shown later) with the rate much higher than that used by Matthews *et al.*, we may assume that the fictive temperature was increased to approximately 2000°C. This value of fictive temperature was found to be consistent with the experimental results achieved for similar laser processing conditions by Zhao *et al.* [69].

The Marangoni effect, which includes both the thermocapillary and chemi-capillary effect, has been also considered as a potential source of the depressions. Since the depressions were produced above the softening point (as will be shown later), the surface tension forces were able to displace the glass. However, a lack of visible

bulges alongside the depressions means that the Marangoni effect played a minor role in forming these surface features. As reported in [10], the surface deformations generated in fused silica by the Marangoni effect are possibly 5 - 15 nm high and thus are significantly smaller than the depressions shown in Figure 5.3.

REGION III (above an 8.5 W laser power)

In this region, the average depth of the trenches increases in a non-linear manner with increasing laser power. Detailed Proscan examination of these surface deformations revealed that they are more complex in shape than those observed in REGION II. Trenches produced in REGION III contain typically a 200 µm wide (ΔW) ditch surrounded by shallow depressions, as shown in Figure 5.4.

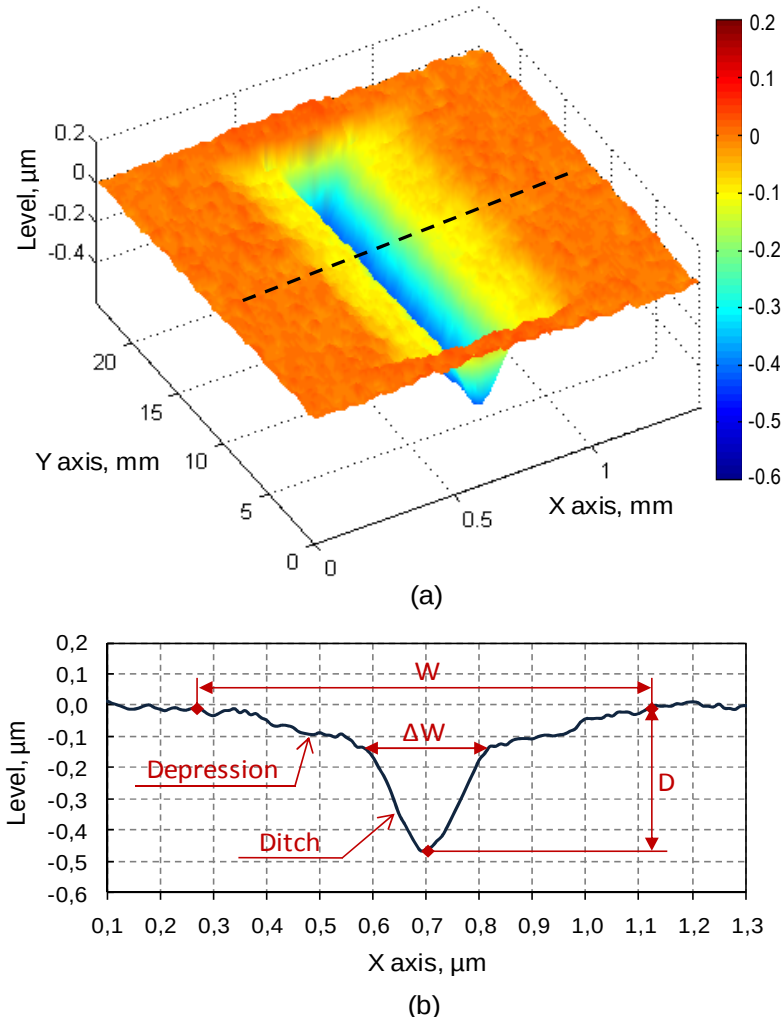

Figure 5.4: Surface deformation produced by a single linear laser scan at a laser power of 9.4 W: (a) 3D surface scan (140 × 96 pts) and (b) its cross-section taken along the dashed line indicated in (a). The trench was generated in a 1.5 mm thick fused silica substrate.

Since the width of the central ditches matches the size of the melt pool generated by a 1 mm diameter laser beam [3], it can be concluded that these surface features are almost certainly produced by vaporization of fused silica. This means that the laser power value of 8.5 W may be considered as a vaporization threshold for this material (at these particular laser processing conditions). Based on Figure 4.1 (see Section 4.2), the vaporization point corresponds to temperature of about 2800°C. Assuming that the thermal properties of fused silica are constant above the softening point (T_S > 1600°C) and the surface temperature is proportional to the laser power (see equation (7.10) given in Section 7.4.2), it is possible to estimate the temperature at which the depressions begin to occur at the glass surface. This temperature was determined to be about 1950°C, thereby confirming the initial assumption that the depressions are produced when the glass is melted. Here, it has to be noted that this estimation is consistent with the recent results reported by Yang *et al.* in [123].

Generally, the depressions shown in Figure 5.4 are similar in shape to those observed in REGION II. In comparison to the depressions from REGION II, however, they expand over a wider distance (W) and are slightly shallower. The reduction in depth of these surface features seems to be related to redeposition of the glass vapour coming from the central ditches, but may also be associated with the Marangoni effect which pulls the molten glass towards the colder sites.

Finally, it can be concluded that the central ditches are similar in shape to a parabola, as can be seen in Figure 5.4. This fact opens the possibility for fabricating highly-curved longitudinal grooves which may be used as mirrors for some selected applications including as resonator mirrors for planar waveguide laser. Fabrication of the grooves on both flat and curved substrates will be presented in detail in Chapter 6.

5.2.3 Annealing of the laser-induced surface deformations in fused silica

As already discussed in Section 2.5.5, the annealing process relieves the glass of the laser-induced surface stress. Since annealing enables the material to be cooled through the transformation range with a slow cooling rate, this process also allows an elevated fictive temperature to be reduced within the laser-irradiated area. This means that it is possible to demonstrate experimentally that the depressions observed in fused silica result from the laser-induced densification of the material.

Annealing of the glass plates (both 1 and 1.5 mm thick) was performed in a laboratory furnace (Cole-Parmer, USA). This furnace enabled the temperature to be controlled accurately in the range of 20 to 1100°C. A detailed temperature schedule used for annealing of the samples is shown in Figure 5.5.

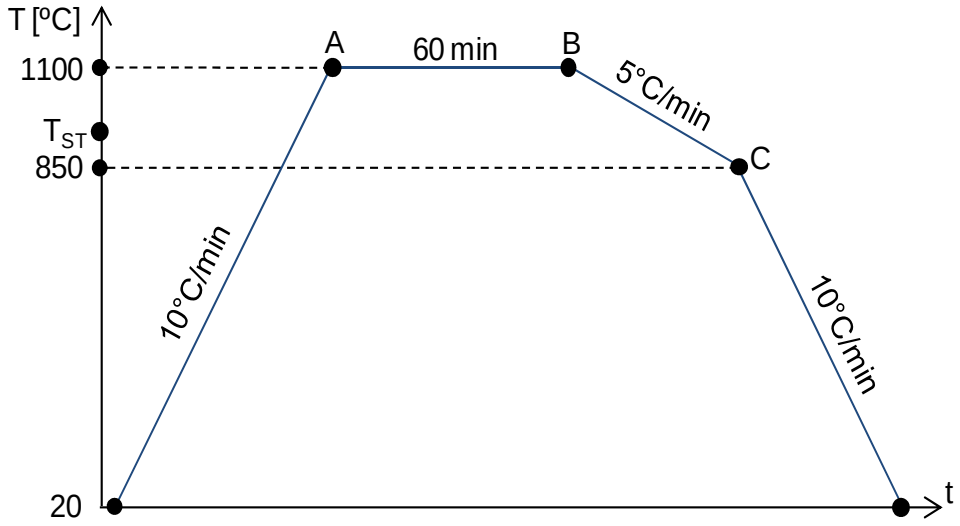

Figure 5.5: Temperature schedule used for annealing of fused silica samples containing trenches. T_{ST} indicates the strain point of HPFS®7980 Corning glass (T_{ST} = 893ºC).

In the first stage of annealing, the samples were heated to a temperature of 1100°C (see Point A) with a rate of 10°C per minute. Afterwards, they were held at this temperature for an hour (see Point B) in order to achieve a uniform temperature distribution in the bulk. Following the "soaking" period, the plates were cooled slowly to a temperature of 850°C (see Point C) with a rate of 5°C per minute. Such a low cooling rate was assumed to be low enough to achieve significant reduction of fictive temperature within the laser-irradiated areas. When the temperature in the furnace crossed over Point C (the conventional transformation range), the cooling rate was increased to 10°C per minute and held at this rate up to the point where the samples reached room temperature.

Figure 5.6 shows the effect of annealing of the laser-irradiated areas which were presented in Figure 5.3 and Figure 5.4, respectively. The 3D surface scans show clearly that the shallow depressions are completely removed from the glass surface by annealing. This most likely means that the fictive temperature in the laser-irradiated

areas was restored, confirming the assumption that the shallow depressions in fused silica result from the local densification of the material and are removable by annealing.

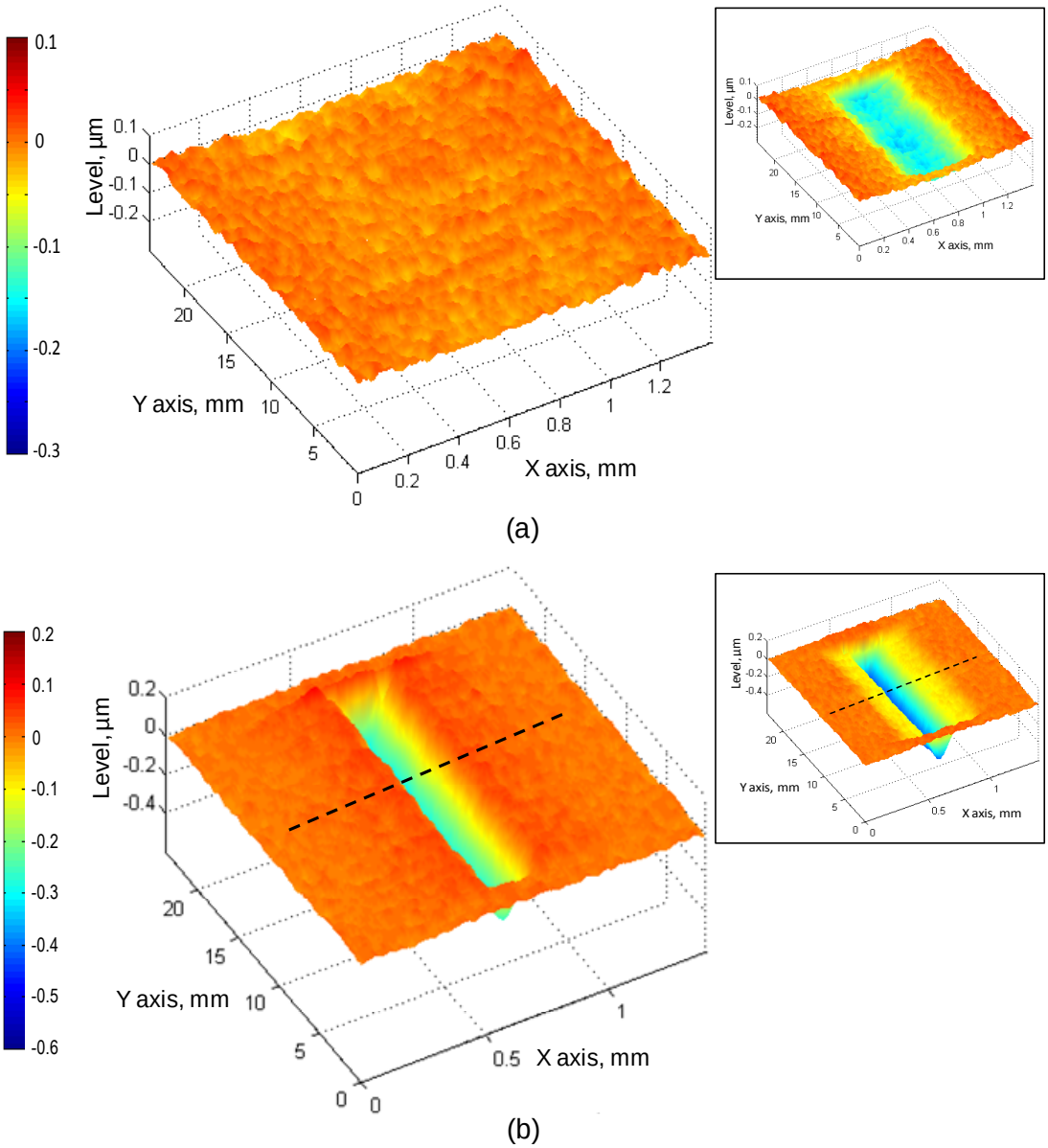

Figure 5.6: Effect of annealing of the laser-irradiated area produced by a single line laser scan at laser powers of: (a) 8.4 W and (b) 9.4 W. The areas before annealing are presented in the insets.

In the case of the trenches generated in REGION III, the annealing process removes the shallow depressions and retains only the central ditch, as can be seen in Figure 5.6 (b). Cross-sections of the laser-irradiated area, which were taken along the dashed lines indicated in Figure 5.6 (b), show than the whole laser-irradiated region is raised up by annealing, as can be seen in Figure 5.7.

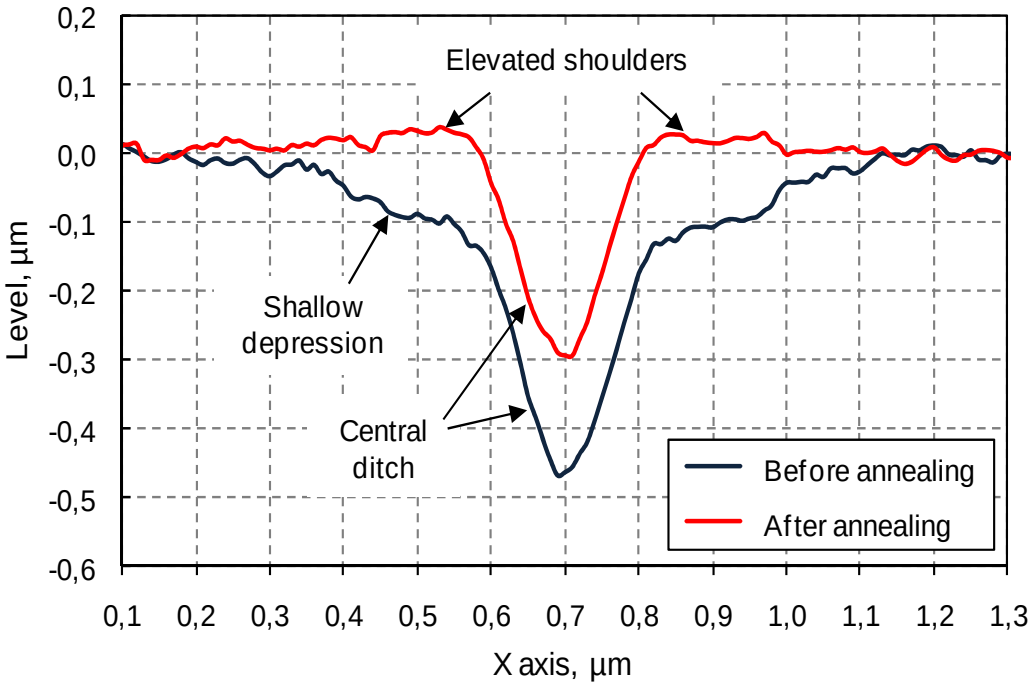

Figure 5.7: Cross-sections of the surface deformation produced by a single line laser scan at P = 9.4 W. The cross-sections were taken along the dashed lines indicated in Figure 5.6 (b).

Moreover, the cross-section taken after annealing shows that the central ditch is surrounded by two elevated shoulders. These two shoulders result from either redeposition of the glass vapour or the Marangoni effect, as already mentioned in Section 5.2.2. The raised shoulders were measured to be an approximately 250 µm wide and maximum 150 nm high at a laser power of 10.2 W.

5.2.4 Summary

Section 5.2 has shown that the deformations in the form of shallow depressions are produced at the surface of fused silica due to local densification of the material while the glass is rapidly cooled down following laser treatment. Since the densification is strongly related to the fictive temperature, it can be concluded that this parameter plays a major role in CO_2 laser processing of fused silica (HPFS®7980 Corning). Therefore, it should be considered seriously as a potential source of surface deformations induced by the laser radiation. This issue is especially addressed to CO_2 laser polishing in which the submicron surface finishing is highly desirable.

Based on the results from Section 5.2.3, it can be concluded that the shallow depressions can be removed from the glass surface by annealing, following the

temperature schedule presented in Figure 5.5. This means that annealing is an essential procedure which must to be performed in the fabrication process of micro-optical components by using CO_2 laser cutting and laser polishing of fused silica.

5.3 Study of laser-induced surface deformations in Borofloat®33

Until the present time, knowledge concerning CO_2 laser treatment of Borofloat®33 glass has been very limited within the LPA group since this glass had not been considered until recently as a candidate material for CO_2 laser-processed optical components. Also, the literature (e.g. scientific journals) does not provide much information concerning CO_2 laser treatment of this glass. As a consequence of there being an absence of literature on this topic, the work covered in this section is ground-breaking and provides valuable information to the science community working on laser processing of optical glasses.

In this section, there is an interest in investigating deformations which occur on the surface of Borofloat®33, when the material is treated by a moving CO_2 laser beam. To determine the character and formation mechanism of the deformations, the glass surface will be affected by a set of single linear laser scans. Since each laser scan will be carried out at a different value of laser power (from 0.5 to 10 W), it will be possible to observe the development of the surface deformations. These results will be used to provide an estimate of the damage threshold and the vaporization threshold for this material. Also, the substrate cracking problem will be investigated within this section. For this purpose, single linear laser scans were carried out on the surface of the glass preheated to a temperature of 350ºC. The aim of these experiments was to determine whether the surface deformations, and thus the laser-induced surface stress (the likelihood of cracking), can be reduced if the material is preheated prior to the laser treatment. Finally, laser beam raster scanning will be investigated for a 3.3 mm thick Borofloat optical window. The aim of this experiment was to provide information as to whether it is possible to polish a large area of the glass without causing cracking of the material. Based on the results of these experiments, an ‘operating window’ for successful CO_2 laser polishing of Borofloat®33 glass has been finally established.

5.3.1 Potential laser polishing window for Borofloat®33

In this section, the main interest is to estimate the value of laser power which is required to achieve melting and vaporization effects on the surface of Borofloat®33. Using the approach and procedure introduced by G. Markillie *et al.* in [9], it is possible to develop a model from which a predicted estimate of a potential laser polishing window for this material may be determined. The window can be established based on a combination of the curve displaying the temperature dependence of viscosity for Borofloat®33 with the vapour pressure curves of SiO_2 and B_2O_3, as shown in Figure 5.8. The viscosity curve is reproduced from the glass specification sheet [26], whilst the vapour pressure curves are derived from [113] and [124]. Since the actual data points (solid lines) do not cover the full required range of relevant temperatures, it was necessary to extrapolate the curves over the full temperature range of interest (see dashed lines).

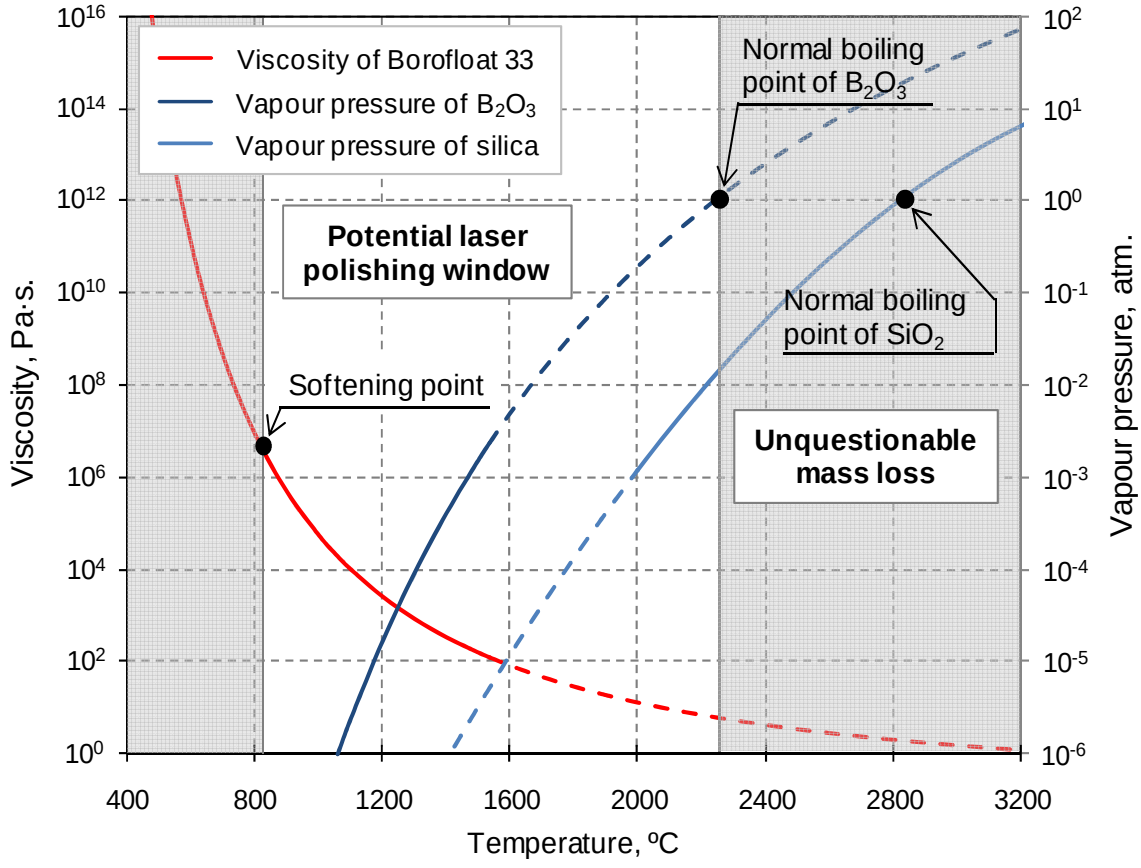

Figure 5.8: Potential laser polishing window for Borofloat®33 determined using the viscosity and vapour pressure curves.

The onset of the laser smoothing effect in Borofloat®33 is assumed to begin at the temperature corresponding to the softening point of the glass (T_S = 820°C). If it is assumed that the surface tension of Borofloat®33 is the same as that of fused silica (γ = 0.3 N/m), then it can be concluded that at this temperature surface features with a scale length of about 10 nm are already relaxed. This calculated estimate is produced using equation (4.10) of Section 4.6.4.

Since Borofloat®33 glass is a mixture of different oxides (mainly SiO_2 and B_2O_3), it is difficult to predict exactly the vaporization threshold of this glass. Based on Figure 5.8, however, we may assume that Borofloat®33 begins to evaporate surely at a temperature of about 2250°C because beyond this point the vapour pressure of B_2O_3 exceeds the ambient atmospheric pressure (known as the normal boiling point in the literature).

The estimated window for laser polishing shown in Figure 5.8 is a valuable guide for the experiments which are covered in the subsequent sections of this chapter. Since it is planned for Borofloat®33 to be treated using the same laser processing conditions as those used for fused silica (see Section 5.2.1), it is possible to represent the temperature axis in Figure 5.8 directly in terms of the laser power. This can be done because the thermal properties of both glasses are very similar (see Table 5.1 in Section 5.1). Based on the results presented in Section 5.2.2, a temperature of about 2800°C corresponds to a laser power of 8.5 W. By assuming that the thermal and optical properties of Borofloat®33 are constant with temperature and the laser power is proportional to the temperature generated at the glass surface (see equation (7.10) of Section 7.4.2), the ratio between the temperature at the glass surface and the laser power used is determined to be about 330°C/W. With these assumptions, it is estimated that Borofloat®33 begins to melt at a laser power of 2.5 W. Thus, beyond this value of laser power, laser-induced deformations are expected to be observed at the glass surface. Using a similar approach, it is estimated that vaporization effects in Borofloat®33 may be expected to be observed at a laser power of about 7 W.

5.3.2 Single line laser scanning of Borofloat®33 at room temperature

The experimental procedure used for characterizing laser-induced surface deformations in Borofloat®33 was similar to that described in Section 5.2.1 (for fused silica). Prior to laser irradiation, the Borofloat samples (25×25×1.1 mm plates) were cleaned using isopropanol, and then dried using lens tissues. This procedure allowed the glass surface to be free of dust, debris, and stains. Following the cleaning process, single line laser scanning was performed at the glass surface. The scans were 10 mm long and each scan was carried out at a different value of laser power in the range 0.5 - 10 W. During the scanning, the laser was operating at a 10.59 µm (10P20) wavelength with a beam which was elliptical (1.1 × 0.9 mm). Following the laser treatment, the laser-irradiated areas were measured using the Proscan 1000 profilometer. The areas were scanned with a spatial step of 10 × 200 µm, respectively, across and along the laser scan direction. In order to reduce noise generated by the profilometer, the surface scans were processed in Matlab, as mentioned previously in Section 5.2.1.

Selected laser-induced deformations observed on the surface of Borofloat®33 are shown in Figure 5.9. Based on the profiles, it is easily seen that these deformations are completely different in shape from those observed in fused silica (see Figure 5.3 and Figure 5.4). Generally, the laser-irradiated areas are in the form of longitudinal bumps.

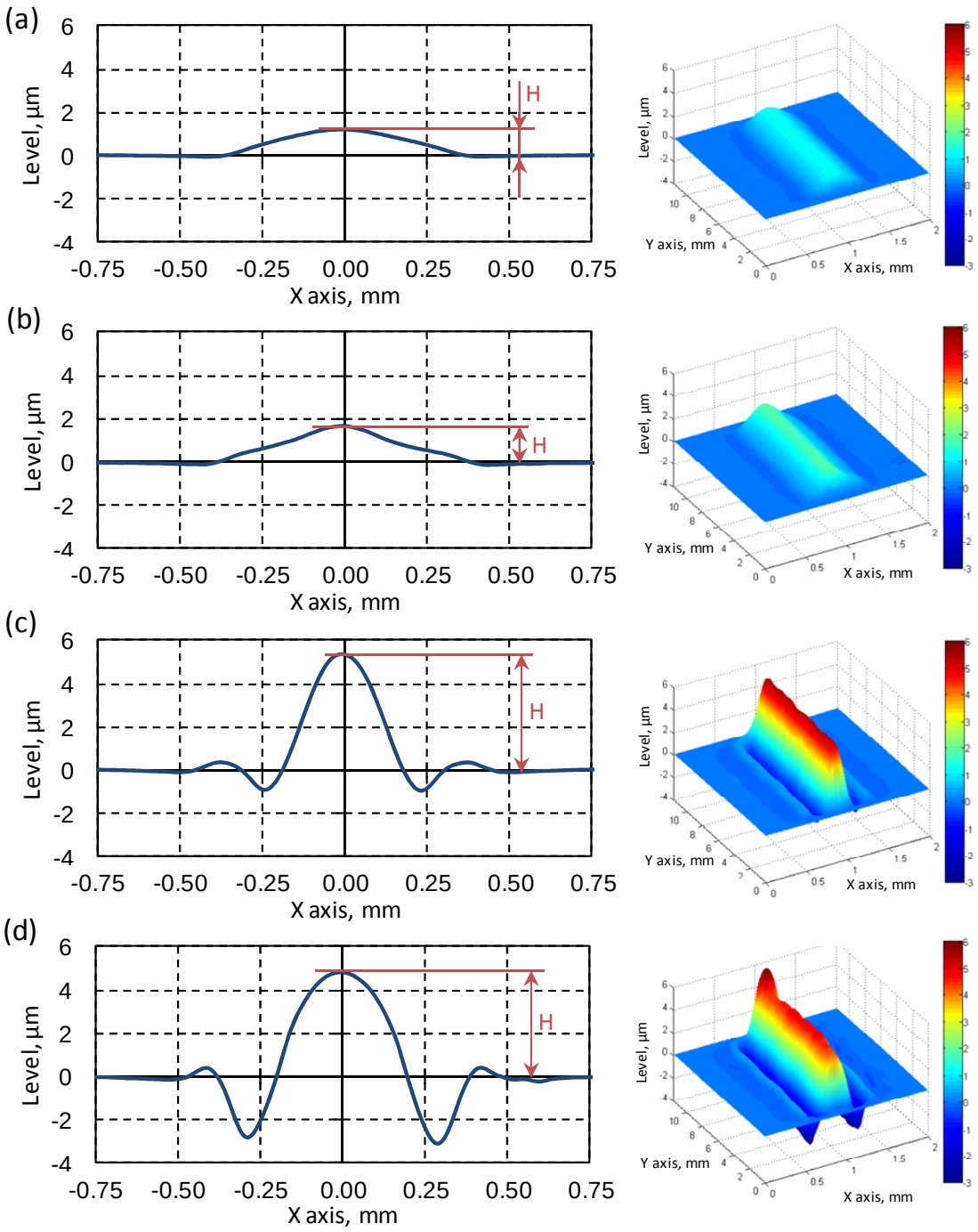

Figure 5.9: Cross-section (left side) and 3D scan (right side) of the areas affected by a moving CO_2 laser beam at different laser powers: (a) P = 5 W, (b) P = 6 W, (c) P = 8 W and (d) P = 9.5 W. Cross-sections were taken at Y axis = 6 mm. Parameter H indicates the maximum height of bumps.

Figure 5.10 shows the height of the bumps as a function of both the laser power used and the surface temperature. The height of the deformations (H) was measured as indicated in Figure 5.9. The surface temperature was estimated following the method given in Section 5.3.1.

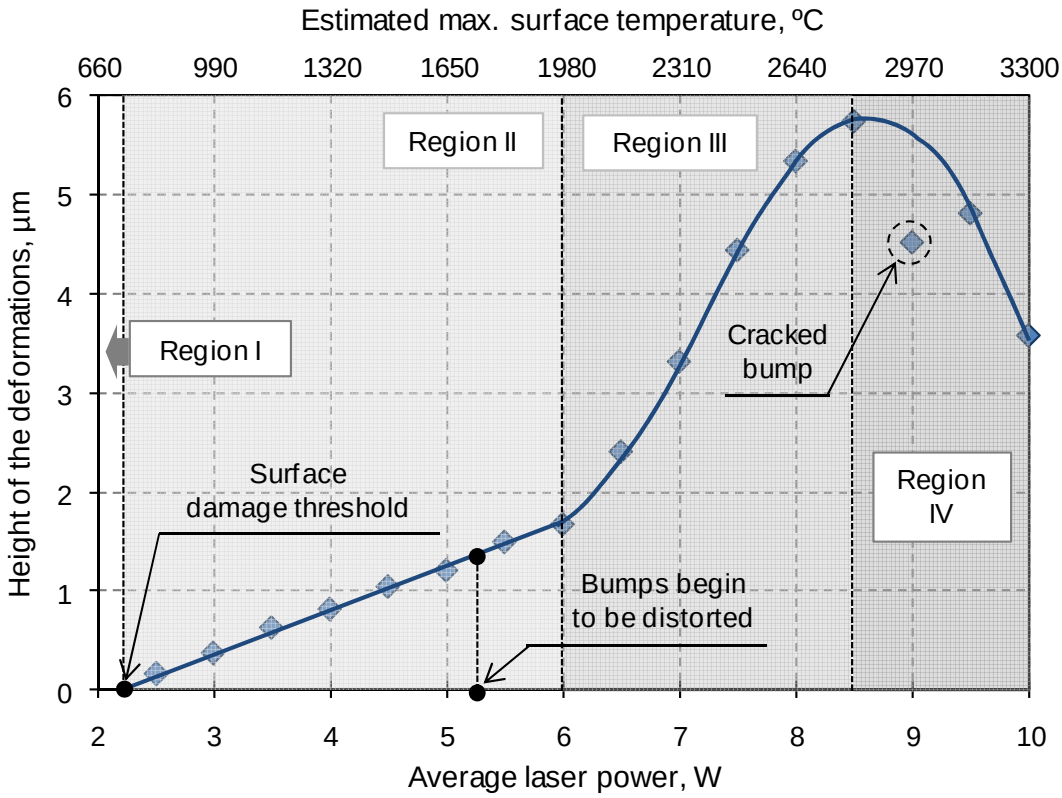

Figure 5.10: Height of the bumps (H) as a function of the average laser power and temperature estimated in Section 5.3.1. The height was determined as shown in Figure 5.9.

Based on the results shown in Figure 5.10, one may distinguish four characteristic regions in the laser power (temperature) domain. These regions are as follows:

REGION I (below a 2.2 W laser power)

In this region, the glass surface is apparently unaltered by a single linear laser scan. Based on the temperature scale shown in Figure 5.10, this region is below the softening point of Borofloat®33 (T_S = 820°C).

REGION II (between 2.2 and 6 W laser powers)

In this region, there is a linear dependency between the height of the deformations and the laser power used. The growth rate of these deformations has been measured to be about 0.45 µm/W. As can be seen in Figure 5.10, the onset of REGION II is determined by the surface damage threshold, which occurs at a laser power of 2.2 W. This value of the laser power corresponds to a surface temperature of 730°C. Here, it should be noted that this temperature is similar in value to that predicted in Section 5.3.1.

As shown in Figure 5.9 (a) and (b), the surface deformations from REGION II are in the form of either non-distorted or slightly distorted cylindrical-shaped bumps. Distortions in the bump area are observed when the laser power used is higher than 5 W. This laser power value possibly corresponds to a temperature of about 1650°C.

Based on the literature reviewed in Section 2.5.3, it can be concluded that the cylindrical-shaped bumps which are produced in REGION II result from the impact of the Marangoni effect and also an increase of the fictive temperate within the laser-irradiated area. A broader discussion related to this subject is given below in Section 5.3.3.

REGION III (between 6 and 8.5 W laser powers)

In this region, the height of the bumps increases in a non-linear manner with increasing laser power used (see Figure 5.10). This is related to the fact that the surface changes within the laser-irradiated area are more pronounced. As can be seen in Figure 5.9 (c), the longitudinal bumps simply become bigger. The appearance of two visible trenches within the bumpy region possibly means that the Marangoni effect starts to play a major role in the formation of the bumps, masking sufficiently the vaporization threshold which almost certainly occurs within this range of laser powers. The strong Marangoni effect is related to the fact that the viscous material produced at this temperature ($T > 1650$ºC) is able to flow over a long-scale distance under the action of surface tension.

REGION IV (above an 8.5 W laser power)

In this region, central bulges are observed to be wide and short, as can be seen in Figure 5.9 (d) and Figure 5.10, respectively. Such shape development of the bumps is most likely associated with three effects of fictive temperature gradient, the Marangoni effect, and the glass vaporization.

Based only on an examination of the results shown in Figure 5.10, it is difficult to determine the vaporization threshold of Borofloat®33. To overcome this problem, the cross-sectional area of each of the deformations shown in Figure 5.9 was calculated using the following expression:

$$V = \sum_{n=-75}^{75} f(n \cdot \Delta x) \cdot \Delta x \tag{5.1}$$

where Δx is the scan resolution along the X axis and $f(n \cdot \Delta x)$ is the height of the deformation measured at the point of $(n \cdot \Delta x)$. Generally, the V value given by equation (5.1) represents a change in the glass volume.

The curve presented in Figure 5.11 shows the relative change in the glass volume (V) as a function of the laser power used. Based on these results, it can be concluded that Borofloat®33 begins to evaporate when the laser power used is as high as 8 W (T = 2650ºC). This value, however, seems to be an overestimate since the volume change shown in Figure 5.11 is a consequence of the competition that exists between two mechanisms: the fictive temperature (which causes a positive volume change) and the vaporization pressure (which causes a negative volume change).

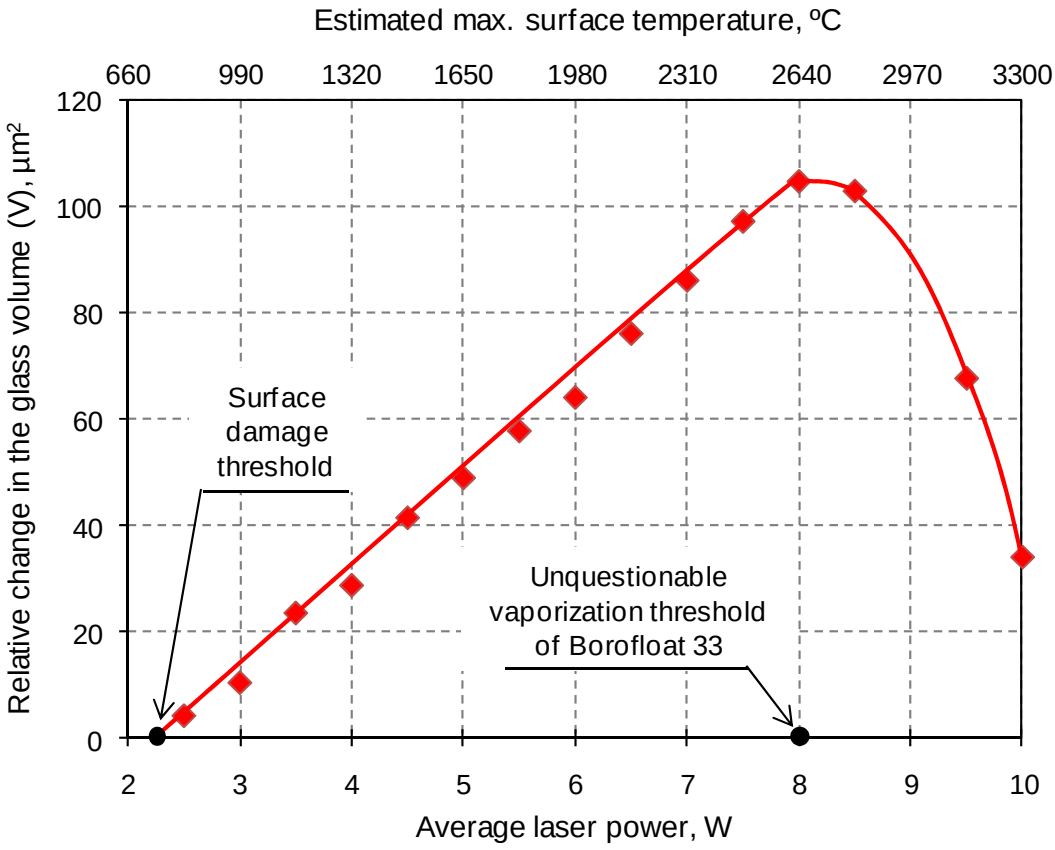

Figure 5.11: Relative change in the glass volume (Borofloat®33) vs. laser power used. The volume (V) was calculated using equation (5.1). The glass volume was changed by a 1 mm diameter laser beam that was moved along a line track with a speed of 5 mm/s.

Finally, it must be noted that a single linear laser scan is able to generate fractures within the laser-irradiated area, either during or subsequent to laser treatment; in some cases they first became apparent even the following day. Generally, the fractures have been observed at the glass surface when the laser power used was higher than 6 W. Based on the results shown in Figure 5.10, this value of the laser power corresponds to the bumps which are higher than 1.6 µm. Thus, it can be concluded that the bumps as high as 1.6 µm can lead to the appearance of fractures within the laser-irradiated area, and consequently to material damage.

5.3.3 Mechanisms responsible for the creation of deformations on the surface of Borofloat®33

As can be seen in Figure 5.9, the laser-induced deformations that have occurred on the surface of the Borofloat®33 substrate are different in shape, depending on the laser power used. Thus, it is highly likely that such dissimilar deformations are produced by different mechanisms. The possible mechanisms which should be taken into account in seeking to explain the various laser-generated shapes are as follows: laser-induced fictive temperature gradient, the Marangoni effect, glass vaporization, and finally redeposition of the glass vapour.

As discussed in Section 5.2, the fictive temperature plays an important role in the creation of surface deformations in fused silica (HPFS®7980 Corning). Due to a local increase of fictive temperature, the glass density is increased within the laser-irradiated area. This, in turn, leads to the appearance of a shallow depression at the glass surface. In the case of borosilicate glasses, however, an elevated fictive temperature causes the opposite effect to that observed in fused silica. As indicated in Section 2.5.3, a fictive temperature increased within the laser-irradiated area causes the glass density to be locally reduced, with the result that a positive bump is formed. Since Borofloat®33 belongs to the borosilicate glass family, it seems very likely that the raised fictive temperature is responsible for the appearance of the longitudinal bumps shown in Figure 5.9. Some strong evidence for this can be seen in Figure 5.11 which indicates that Borofloat®33 glass increases in volume only if the glass surface is heated up to a temperature greater than 730ºC, and then later on is rapidly cooled down through the transformation range. Since the transformation range of Borofloat®33 is somewhere between 518 - 560ºC [26], it is very likely that the fictive temperature

is increased within the laser-irradiated area if the glass is treated using a laser power greater than 2.2 W.

Laser-induced deformations observed on the surface of Borofloat®33 are also produced by the Marangoni effect because a CO_2 laser beam generates a surface tension gradient which may dislocate a melt within the laser-irradiated area. Normally, the surface tension of a liquid decreases with an increasing temperature [125], which means that the liquid flows from hotter towards colder sites, producing a dimple inside the hottest area. However, in the case of Borofloat®33 the surface tension gradient is positive, which means that the melt produced at the glass surface is pulled towards the (hotter) centre of the laser-irradiated area. This surface effect can be seen in Figure 5.9. Evidence that Borofloat®33 has a positive surface tension gradient has been found in the literature related to the surface tension of glass melts [113, 126, 127]. These papers report that the surface tension gradient of SiO_2 and B_2O_3 melts (main components of Borofloat®33) is positive because the oxides dissociate with temperature. For instance, SiO_2 undergoes decomposition into SiO and O_2 when the temperature exceeds 2000°C [113].

As shown in Figure 5.8, Borofloat®33 may begin to evaporate at a temperature of about 2250°C. This means that the deformations shown in Figure 5.9 (c) and (d) are possibly affected by the laser-induced mass loss. Once the glass begins to evaporate, the glass surface may also be affected by the redeposition of the glass vapour.

To summarize this section, the bump-shaped deformations observed on the surface of Borofloat®33 mainly result from a local increase of fictive temperature and the Marangoni effect. An elevated fictive temperature results in the appearance of bumps within the laser-irradiated areas, whereas the Marangoni effect causes distortion in the shape of these bumps. The laser-irradiated surface may also be distorted by the vaporization effect which is expected to occur at laser powers greater than 7 W.

5.3.4 Laser scanning of Borofloat®33 preheated to a temperature of 350°C

As already mentioned in Section 5.3.1, the laser-irradiated areas sometimes undergo cracking when treated at high value of laser power (P > 6 W). The appearance of fractures was found to be related to the surface stress induced by a moving laser beam. In order to reduce this stress, in this section the idea is to perform CO_2 laser scanning of Borofloat®33 with the glass substrate preheated to a high initial temperature (T = 350ºC). As reported by other researchers, e.g., Laguarta *et al.* [74], glass preheating is an effective solution to avoid the appearance of fractures in the laser-irradiated areas. Since specialized commercial systems for glass preheating are quite bulky and expensive, it was necessary to construct a simple hot plate for the purpose of this particular experiment. This hot plate is described in detail in Section 3.1.3.

In this experiment, a 1.1 mm thick plate of Borofloat®33 has been subjected to two sets of single linear laser scans. The first set was carried out when the glass had an initial temperature of 20°C, whilst the second set was executed when the same sample had an initial temperature of 350°C. In both cases, laser scans were carried out at laser powers in the range from 0.5 to 5.5 W. Following laser treatment, the sample was cooled down to room temperature with a rate of approximately 40°C per minute. Later on, the laser-irradiated areas were investigated using the Proscan 1000 profilometer. The scan resolution was chosen to be 10 µm in both directions, to give sufficient resolution of the surface features.

Cross-sections of the surface deformation produced at a laser power of 3.5 W, when the initial temperature of the glass substrate was 20°C and 350°C, are shown in Figure 5.12 (a) and (b), respectively. Based on these profiles, it is easily seen that the deformations in the "hot" glass are significantly larger than those generated in the "cold" sample (when treated at room temperature). This means that glass preheating does not solve the problem with cracking since the bumps generated after preheating are even larger in size. As already mentioned in Section 5.3.2, fracture may occur at the surface of Borofloat®33 when the bumps are higher than 1.6 µm.

Figure 5.13 shows the height of surface deformations measured as a function of the laser power used. The results are presented for both "cold" and "hot" glass. The height (H) was measured as indicated in Figure 5.12.

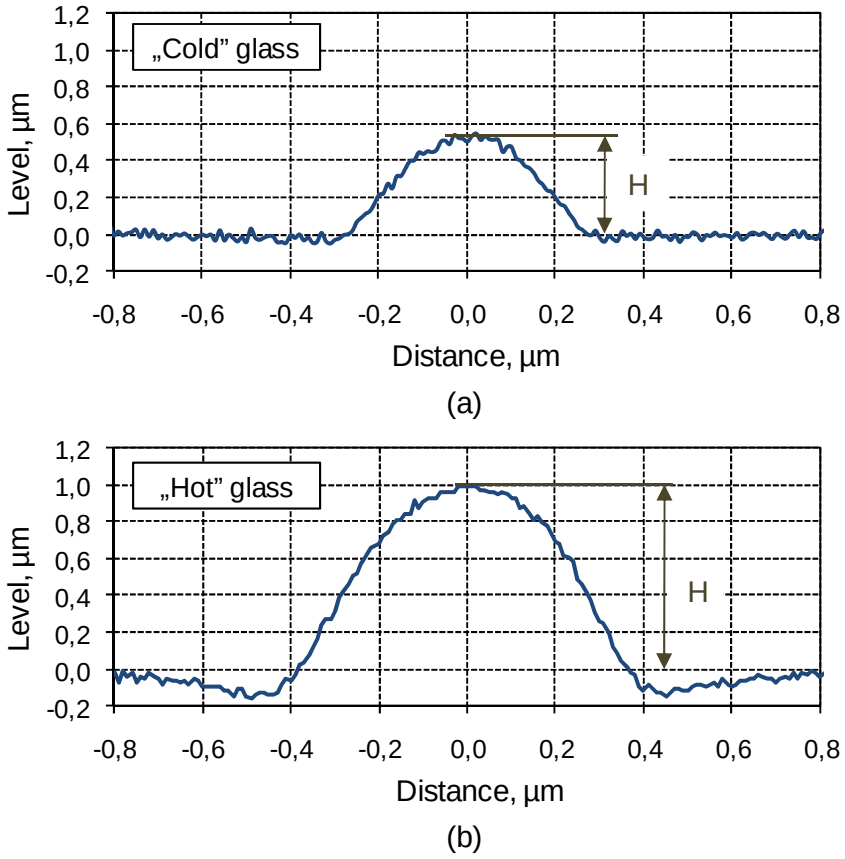

Figure 5.12: Cross-section of surface deformations produced by a single linear laser scan at a 3.5 W laser power when: (a) the initial temperature of the glass was 20°C and (b) the glass was preheated to 350°C.

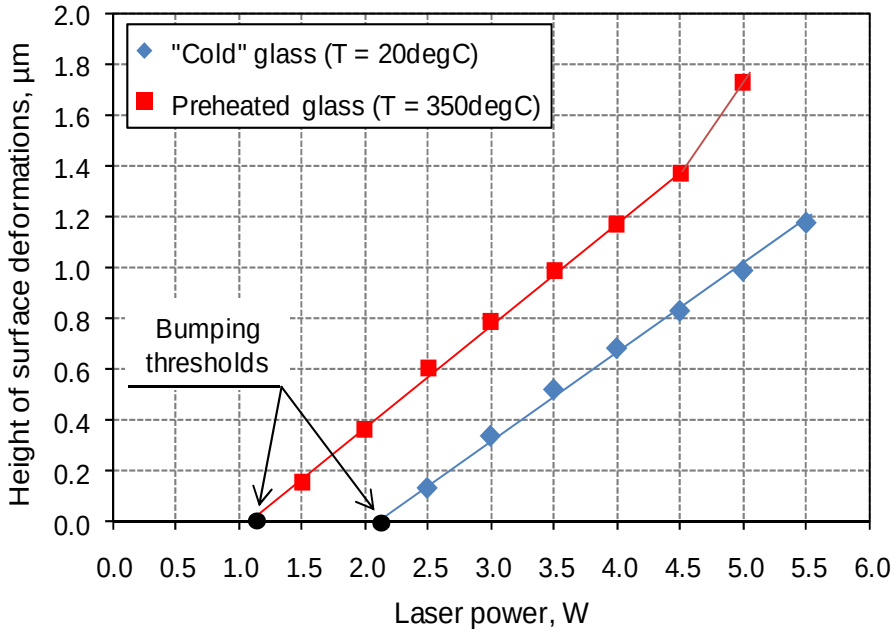

Figure 5.13: Height of surface deformations produced by single linear laser scans at different laser powers. The results presented for the "cold" and "hot" glass.

As shown in Figure 5.13, the height of the deformations presented in Figure 5.12 increases in a linear manner with an increasing laser power (up to 4.5 W for the "hot" glass and up to 5.5 W for the glass treated at room temperature). A slightly higher growth rate of the bumps is achieved for the glass when preheated to 350°C. This probably indicates that Borofloat®33 is a better absorber of CO_2 laser radiation when is hot.

The bumping threshold of the "hot" glass was determined to be about 1.2 W. This value, therefore, is approximately 1 W lower than that determined for the glass treated at room temperature. This means that the 1 W increase in the laser power causes an increase on about 330°C in the glass temperature ($\Delta T = 350 - 20$°C). This value has been found to be consistent with the calculations carried out in Section 5.3.1.

In conclusion, this section showed that preheating does not reduce the size of bumps produced on the surface of Borofloat®33, and thus there is still a high risk of the appearance of fractures within the laser-irradiated area.

5.3.5 Annealing of the laser-induced surface deformations in Borofloat®33

As concluded in Section 5.3.3, the cylindrical-shaped bumps generated at the surface of Borofloat®33 result from the Marangoni effect and the local increase of fictive temperature. The aim of this section is to determine the size of the deformations produced by these two mechanisms, and in order to investigate this, the bumpy surface from Figure 5.12 was subjected to annealing. As already shown in Section 5.2.3, annealing is an effective method which allows a high fictive temperature to be reduced within the laser-irradiated area. This means that the post-annealed surface would contain only deformations resulting from the appearance of the Marangoni effect (and the vaporization of Borofloat®33 if they were produced at high temperatures).

The annealing schedule used in these experiments is shown in Figure 5.14. Since the specific annealing schedule appropriate for Borofloat®33 was unknown, it was decided to adopt the annealing schedule which had been developed for Borosilicate Glass 3.3 (ROBU® Glasfilter-Geraete GmbH, Germany). Since the chemistry of Borosilicate Glass 3.3 is very similar to that of Borofloat®33 [128], it was assumed that the annealing schedules are also very similar.

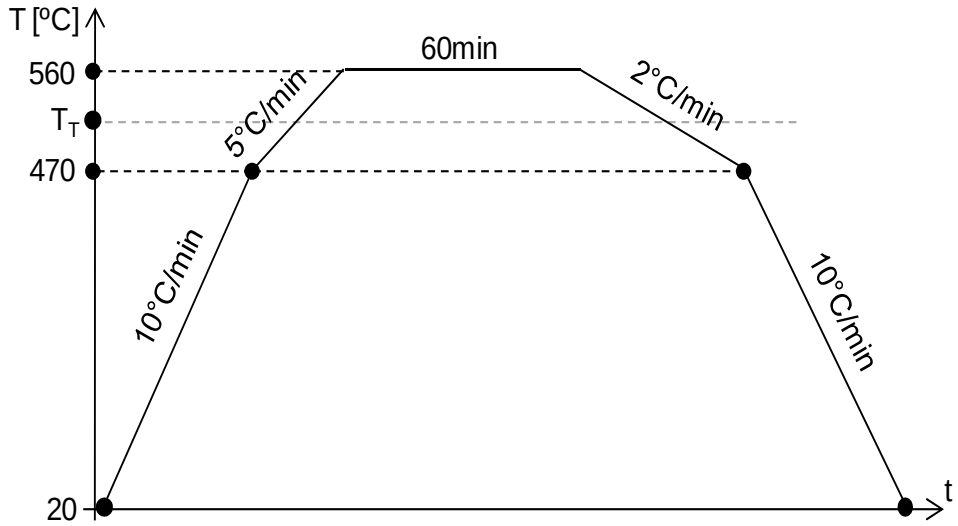

Figure 5.14: Temperature schedule used for annealing of Borofloat®33. T_T indicates the transformation point of Borofloat®33 (T_T = 525°C).

The post-annealed surface deformations shown previously in Figure 5.12 are now visible in Figure 5.15. From the examination of these surface profiles, it is apparent that the cylinder-shaped bumps are significantly reduced in size following annealing. In comparison to fused silica, however, annealing does not completely remove the deformations from the surface of Borofloat®33. Measuring the *V* area of the deformations after annealing (following the procedure given in Section 5.3.2), it was found that the W-shaped bumps are not swollen, i.e., the volume change is zero within the limits of the Proscan measurement accuracy (± 30 nm). This means that annealing efficiently reduces the high fictive temperature induced by laser treatment, leaving only deformations which were produced by the Marangoni effect.

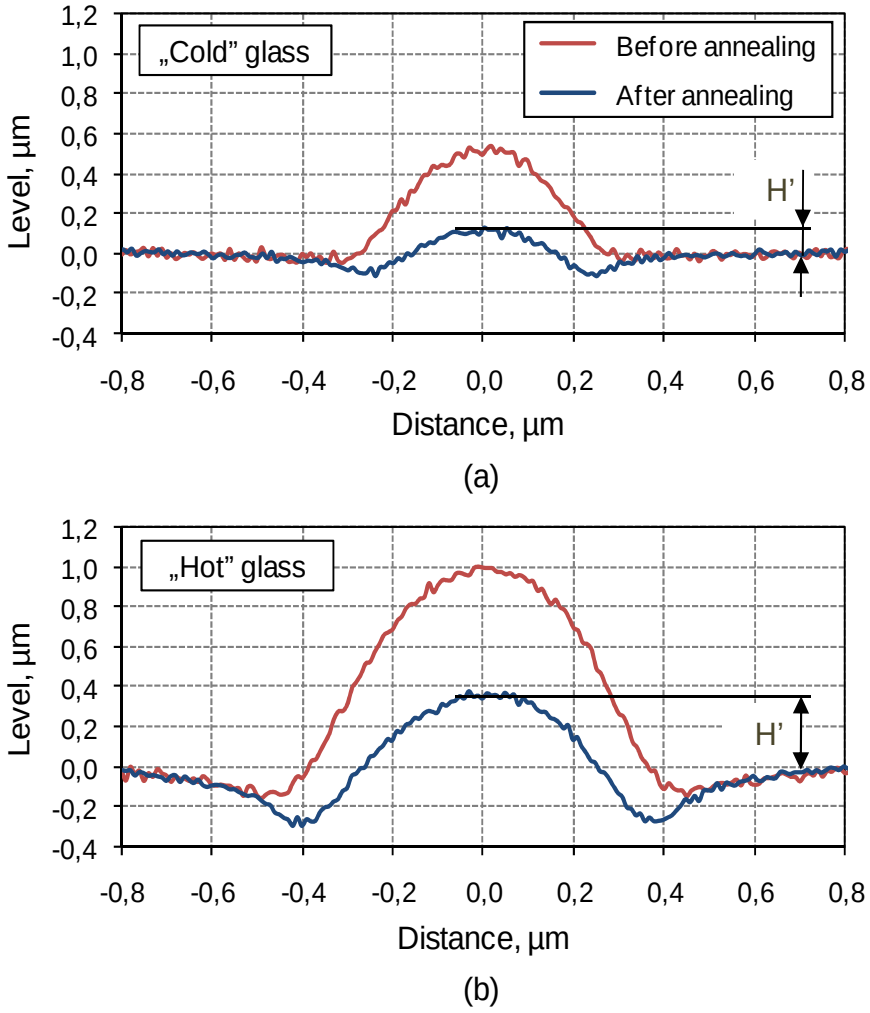

Figure 5.15: Cross-section of the laser-induced deformations observed on the surface of (a) the "cold" and (b) the "hot" (preheated) glass before and after annealing. The bumps were produced at a laser power of 3.5 W.

The height of post-annealed surface deformations (H') measured as a function of the laser power used is shown in Figure 5.16. The graph also contains results achieved for the glass prior to annealing (see the dashed lines).

Based on the results presented in Figure 5.16, the bumping (surface damage) thresholds have not been changed significantly after annealing. Thus, it can be concluded that the surface deformations in Borofloat®33 are produced almost simultaneously by two mechanisms: the Marangoni effect and the fictive temperature rise. This means that the deformations are driven effectively by the surface tension forces when the glass is heated above 800°C. Beyond this temperature, the glass viscosity decreases below $10^{6.6}$ Pa·s and the softened glass layer is apparently then able

to move along the surface. This leads to the formation of W-shaped bumps, as can be seen in Figure 5.9. Since the glass viscosity decreases rapidly with increasing temperature, as shown in Figure 5.8, the bumps produced by the Marangoni effect become larger with increasing laser power.

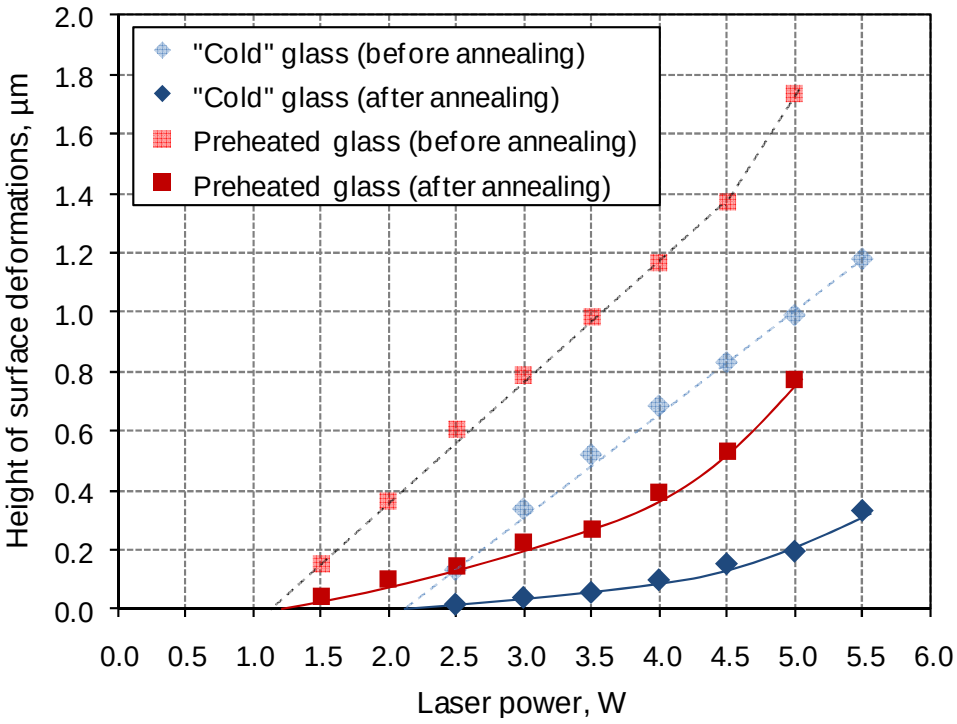

Figure 5.16: Height of surface deformations produced in the "cold" and preheated glass vs. laser power used. Measurements were taken before (see dashed lines) and after annealing (see solid lines).

An elevated fictive temperature has a significant effect on the shape of the bumps that result from laser treatment. As can be seen in Figure 5.16, the laser-induced deformations are about 4 times higher than the post-annealed bumps. This means that annealing is an essential procedure for removing deformations produced by the fictive temperature phenomenon in Borofloat®33. Since bumping also causes stress at the glass surface, it is reasonable to assume that the elevated fictive temperature contributes to the appearance of fractures within the laser-irradiated areas. This means that in the future it is necessary to develop a technique for controlling the fictive temperature of the glass during its processing. It is suggested that this approach may reduce the risk of the generation of fractures and also may decrease the extent of surface deformations produced by the moving laser beam.

5.3.6 Preliminary results of laser beam raster scanning of Borofloat®33

This section contains preliminary results related to CO_2 laser polishing of a Borofloat window which was supplied by Edmund Optics (UK). In this experiment, a 3.3 mm thick uncoated plate was raster scanned at room temperature, using varied values of laser power as shown in Figure 5.17.

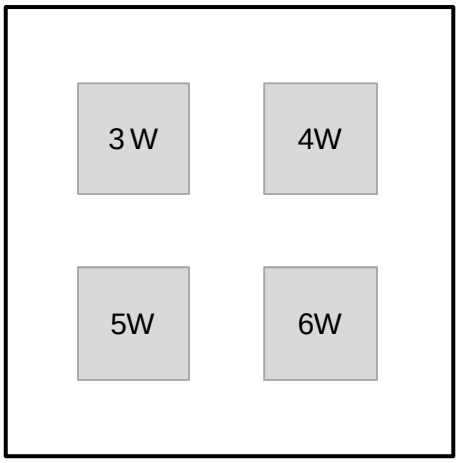

Figure 5.17: Location of the laser beam raster scanned areas at the surface of Borofloat window.

The laser beam raster scanned areas were as large as 5×5 mm^2. A raster pitch was chosen to be 10 µm. This raster pitch value is typically used for smoothing fused silica optics. The remaining laser processing parameters, e.g. the laser beam size and scan speed, were the same as those in the previous experiments described in this chapter.

Figure 5.18 shows the cross-sections of the areas treated at 3, 4, and 5 W. This figure does not contain a surface profile of the area treated at 6 W since for this case material cracking was observed. The cross-sections shown in Figure 5.18 were measured with 5 µm resolution using the Proscan 1000 profilometer. Measurements were obtained for the sample before and after annealing. Here, it should be noted that the raster scan progression was from left to right.

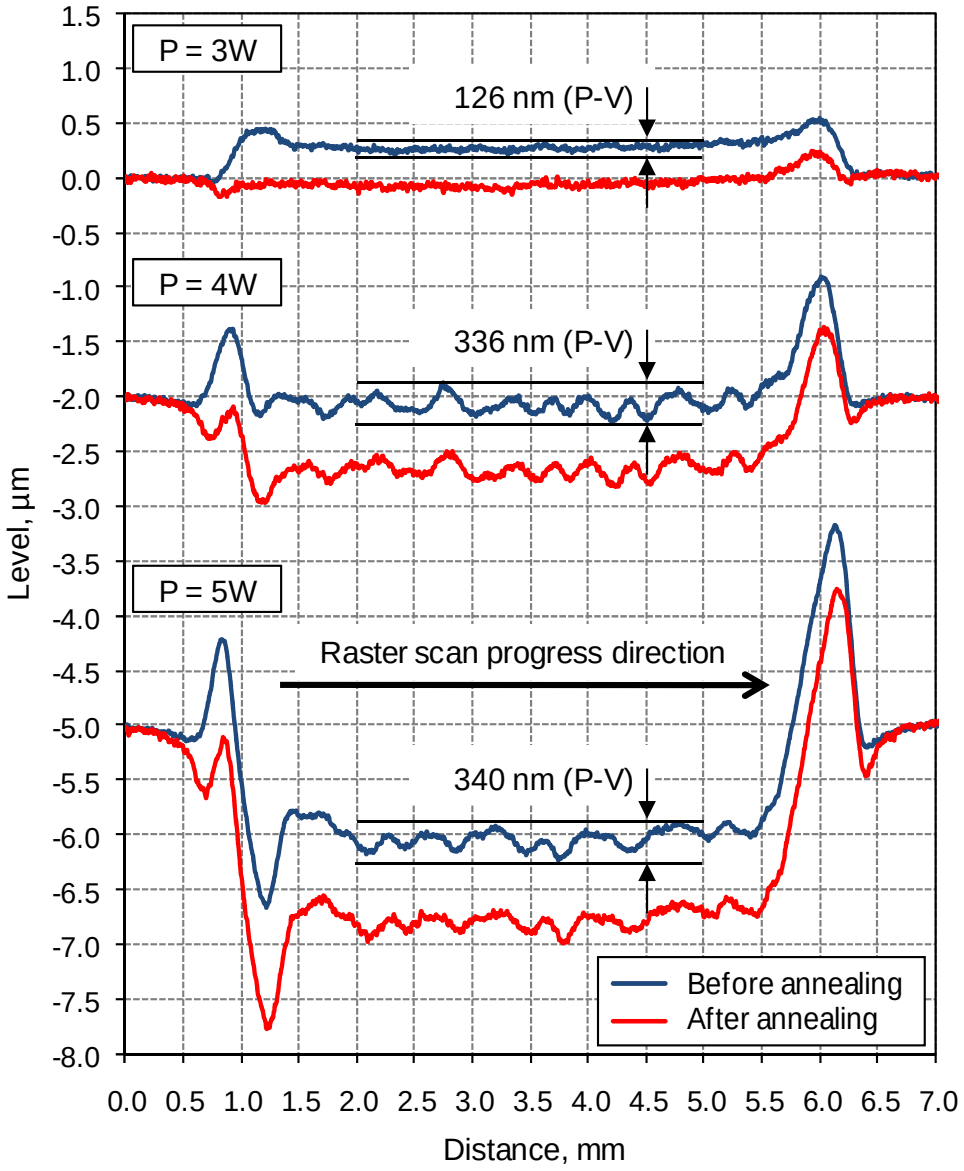

Figure 5.18: Cross-sections of the areas treated at different laser powers, using laser beam raster scanning. Surface profiles were taken before and after annealing. Laser scan progression was from left to right.

As can be seen in Figure 5.18, Borofloat®33 begins to evaporate when is treated at 3 W. Since this value of the laser power corresponds to temperature of about 1000°C (3 W × 330°C/W), it can be concluded that the vaporization threshold of Borofloat®33 is significantly lower than that established in Section 5.3.1.

As will be shown in Section 6.3, the depth of the glass layer being removed by laser evaporation is proportional to the number of laser scans (*N*). This indicates that the glass removal rate is proportional to the laser dwell time. Although this

proportionality has been found to be valid for fused silica, this dependency may also be relevant for Borofloat®33. With this assumption it is possible to calculate a vaporization rate for Borofloat®33 for an individual laser scan at a fixed laser power, based on the results presented in Figure 5.18. Since laser beam raster scanning is a process in which individual laser scans partially overlap each other, the dwell time in this machining mode is sufficiently longer. Taking into account that a 1 mm laser beam produces a 200 µm melt spot [3] and a raster pitch is 10 µm, it can be calculated that the dwell time in the laser beam raster scanning mode is approximately n = 16 times longer in comparison to the dwell time caused by a single laser pass (see equation (4.4) for more details). This means that the removal rate of Borofloat®33 is as follows: about 40 nm per scan when treated at 4 W and 112.5 nm per scan when treated at 5 W. These removal rates were calculated by dividing a depth of the removed glass layer (see Figure 5.18) by the n number defined above in the text.

Laser beam raster scanning with a raster pitch of 10 µm generates some waviness at the glass surface, as can be seen in Figure 5.18, and the waviness is observed to be unchanged after annealing. Generally, an increasing laser power generates more pronounced waviness. For a 3 W laser-irradiated area, the peak-to-valley was measured to be approximately 126 nm over a 3 mm distance (see the top profiles in Figure 5.18). Based on the knowledge gained so far, it is most likely that this waviness is produced by the Marangoni effect. In the case of the areas treated at 4 and 5 W, the surface waviness was measured to be about 340 nm peak-to-valley over a 3 mm distance. There are two reasons of such a large waviness. The first is related to the fact that the Marangoni effect is more pronounced at high values of laser power because a molten layer of the glass flows more easily when is hotter. The second reason, in turn, is related to imperfect operation of the laser used in this experiment. As mentioned in Section 3.1, the laser used in these experiments has a tendency to operate at different wavelengths, and thus it is not perfectly stable during laser treatment. Since each square area shown in Figure 5.17 was machined over a time period of approximately 10 minutes, it is likely that the laser was unstable for this time. Based on information given in Section 3.1.2, the laser power fluctuations were about 1%, whilst the wavelength ranged from 10.3 - 10.7µm. Assuming that the reflectivity of Borofloat®33 varies with wavelength, as observed in the case of fused quartz (see Figure 2.3), it is reasonable to suggest that the line hopping could modify

the fraction of laser energy coupled into the glass, producing significant waviness as shown in Figure 5.18.

Finally, the areas shown in Figure 5.18 are surrounded by two ridges. These ridges are different in size, i.e., the right one is significantly larger than the left one. Based on the knowledge gained so far, it can be concluded that the ridges are most likely produced by the Marangoni effect. This can be explained as follows. Since the laser beam was moved progressively from left to right, as shown in Figure 5.18, the melt was dragged towards hotter sites by the subsequent laser scans, forming a large ridge at the end of this process.

5.3.7 Verification of CO_2 laser polishing window for Borofloat®33

Taking into account the fact that Borofloat®33 begins to evaporate when treated at 3 W (see Figure 5.18), the laser polishing window, which was established initially in Section 5.3.1, must be verified. Since the laser power of 3 W corresponds to the temperature of about 1000°C, the "new" polishing window defined for Borofloat®33 is now embedded between 820 and 1000°C. In this temperature range, the glass does not evaporate significantly, and thus it can be polished with a nearly zero mass loss. Since the viscosity of Borofloat®33 is relatively high within this temperature range ($\eta = 10^{6.6}$ - $10^{4.7}$ Pa·s, as shown in Figure 5.8), it can be concluded that this material cannot be smoothed as effectively as fused silica since it does not 'flow' as well. In order to characterize the extent to which surface features may be smoothed, it would be necessary to perform future experiments using a 'special' glass plate with either a highly-scattering texture or an etched binary structure. Similar experiments with a highly-scattering texture have been described by Nowak *et al.* [3], whilst the method using a binary etched structure as a test piece is detailed in Chapter 4.

5.4 Summary and conclusions

Within this chapter, a detailed examination of deformations produced on the surface of fused silica (HPFS®7980 Corning) and Borofloat®33 (Schott AG) has been carried out. The results covered here provide detailed information of considerable value to the scientific and technical community working on laser processing of glasses. The key results of the experiments carried out in this part of the thesis are listed in Table 5.2.

Table 5.2: Key results of the experiments performed in this Chapter.

	Laser-induced deformations produced on the surface of:	
	HPFS®7980 Corning	**Borofloat®33**
Shape	Depressions	Cylindrical and W-shaped bumps
Maximum size	200 nm deep and 850 µm wide	6 µm high and 1 mm wide
Thresholds	Approx. 6 W	1.2 W – glass preheated to 350ºC 2.2 W – glass at room temperature
Effect of annealing	Complete removal	Partial removal
Major formation mechanisms	Fictive temperature increase	Fictive temperature increase Surface tension gradient
Laser polishing window	Between 1600°C and 2750°C (see Chapter 4 for details)	Between 820°C and 1000°C (without significant mass loss)

Based on work covered in Section 5.2, laser-induced deformations measured on the surface of fused silica (HPFS®7980 Corning) are in the form of shallow depressions. These depressions are produced even if vaporization does not occur at the glass surface. As proven experimentally in Section 5.2.3, depressions result from fictive temperature which is increased within the laser-irradiated area due to rapid cooling of the glass when the laser irradiation is terminated. Here, it must be noted that the same surface effect in fused silica has been recently reported by Feit *et al.* [129].

As found in Section 5.2.3, an effective removal of the depression can be achieved by annealing because this process allows the elevated fictive temperature to be reduced. This means that annealing is an essential procedure for fabricating micro-optical components in fused silica. Apart from releasing the laser-induced stress from the glass surface, as will be shown in Chapter 7, this process also allows us to remove deformations which are produced by an elevated fictive temperature. Finally, the deformations produced by the Marangoni effect have not been observed at the surface of fused silica because it is possible that they were masked by the relatively noise output of the Proscan profilometer. Based on work reported by

Mendez [10] or Feit *et al.* [129], however, it is already known that the deformations produced by surface tension forces vary from 5 - 15 nm in peak-to-valley height.

As found in Section 5.3, laser-induced deformations measured on the surface of Borofloat®33 are significantly larger and different in shape to those observed on fused silica (HPFS®7980 Corning). Rather than shallow depressions, a moving CO_2 laser beam produces either cylindrical or W-shaped bumps which grow in height up to 6 µm with increasing laser power. Such a large change in the glass structure causes the generation of stresses, which can lead to the appearance of fractures at the glass surface. Although CO_2 laser treatment of glasses preheated to high temperature may reduce the risk of the fracture, as shown by Laguarta *et.al* [74], in the case of Borofloat®33 this approach is not effective, most likely because the deformations still remain as large as those which occur when the glass was treated at room temperature. Finally, it was shown that annealing of Borofloat®33 allows the deformations to be reduced in size. In comparison to fused silica, however, these deformations cannot be smoothed out completely. As shown in Figure 5.15, an annealed area contains a W-shaped bump which is significantly larger (up to 100 times) than that observed in fused silica. This means that Borofloat®33 is a more demanding material in terms of its capacity to be polished by a CO_2 laser beam.

In conclusion, the experimental results shown in Section 5.3 confirm the prediction of an operational CO_2 laser polishing window for Borofloat®33. Based on the results shown in Section 5.3.6, it is already known that CO_2 laser polishing of Borofloat®33 should be carried out at laser-induced temperatures between 820 and 1000°C. In this temperature range, the glass does not lose significant mass by evaporation and a moving laser beam does not produce fractures inside laser-irradiated areas. However, the results obtained so far suggest that to take this subject forward, the future work on CO_2 laser polishing of Borofloat®33 should be focused on raster scan area laser treatment of highly-scattered surfaces or binary etched structures in order to determine the extent to which surface features can be smoothed without material cracking.

Chapter 6
Rapid prototyping of toroidal mirrors with a high ratio of two principle curvature radii

6.1 Introduction

The aim of work covered in this chapter is to develop a CO_2 laser-based technique for rapid prototyping (fabrication) of toroidal mirrors with a high ratio of the principal radii of curvatures ($RoC_1/RoC_2 > 10$). Optics of this type have a number of uses, including as mirrors for hybrid resonators in the planar waveguide lasers. The approach here is for toroidal mirrors to be fabricated on a cylindrical lens substrate made of fused silica, using a set of partially overlapped laser scans at laser power levels at which the glass evaporates into the air. Based on the results presented in Section 5.2, it is already known that a single linear laser scan can produce an approximately 200 µm wide parabolic-shaped ditch in silica (HPFS®7980 Corning), when the laser power used exceeds 8.5 W. Here, it must be noted that this value of the laser power is valid for a 1.1 × 0.9 mm laser beam moved along a line track with a speed of 5 mm/s.

The toroidal mirrors, the fabrication of which is presented within this chapter, are designed to be used in a mode-selective resonator configuration for a 150 µm core Yb:YAG planar waveguide laser (see Section 6.5 for more details). In order to fulfil the resonator mode-selective requirements, one of the mirrors must be at least 220 µm high (transverse direction) and 16 mm wide (lateral direction), and must have the curvature

radii of 16 and 230 mm in the transverse and lateral directions, respectively. Since this component must be capable of operating at high values of laser power (about 400 W), the surface quality of the mirror is required to be very high.

An idea to fabricate slit-shaped toroidal mirrors using a moving CO_2 laser beam arose with the help of Prof. Howard J. Baker and Dr Ian J. Thomson, who are members of the LPA group at Heriot-Watt University. There are four main reasons why we decided to employ the laser-induced vaporization process to fabricate such optics in fused silica. The first is associated with a high cost of this commercially available optic. Since toroidal mirrors with a high ratio of two principle radii of curvature are not "off-the-shelf" products, they are very expensive to procure as individual components. The second reason results from the promising results presented in the previous chapter. As shown in Figure 5.7, a single linear laser scan can produce a parabolic-shaped ditch which almost fulfils the requirements listed in the previous paragraph. The third reason is related to the fact that an approximately 1 mm diameter laser beam, which is planned to be used for fabricating mirrors, is characterized by a small value of beam divergence ($\theta < 10$ mrad, as calculated for the laser processing workstation covered in Section 3.1). This means that the laser system used for fabricating mirrors does not require any precise laser-beam-focus tracking control, even if the substrate is significantly curved, thereby making this process original. Here, it must be mentioned that a lens used as a workpiece to fabricate the mirror with a 230 mm RoC in the lateral direction had sag of about 0.3 mm. Finally, CO_2 laser evaporation of fused silica enables the glass to achieve a smooth surface (roughness < 10 nm peak-to-valley), as reported in [1, 3]. This means that the glass surface is simultaneously shaped and polished using a single processing step, which takes about 30 seconds, and thus the laser machining process of this "off-the-shelf" optic is relatively rapid.

6.2 Detailed analysis of ditches produced by single line laser scans

Based on work shown in Section 5.2, a laser beam with a diameter of about 1 mm can produce longitudinal ditches of width approximately 200 µm on the surface of fused silica. In this section, the aim is to characterize these ditches (as for example shown in Figure 5.6 (b)), to assess whether these surface features are appropriate for use as

mirrors suitable for the mode-selective resonator configuration mentioned above. To fulfil the mode-selective criteria, firstly, a ditch must be represented by a quadratic function because this function tells us that a ditch can be characterized by a radius of curvature whose value is well determined. Secondly, a ditch must have a low degree of the surface roughness so that it can be used as a low-loss optical component.

The second order polynomial fit to the surface profile of ditches produced in the range of laser powers from 8.5 - 10.2 W was achieved using the facilities of MS Excel®. The quadratic fitting was applied for ditch cross-sections measured following sample annealing, as can be seen in Figure 6.1. Using this simple approach, it was found that only ditches produced in the range of laser powers between 9.2 - 9.8 W can be represented credibly by a quadratic function, *f(x)*. For these ditches, the residual value, *f(x) - g(x)*, was determined to be lower than 50 nm over a width (ΔW) of 160 µm.

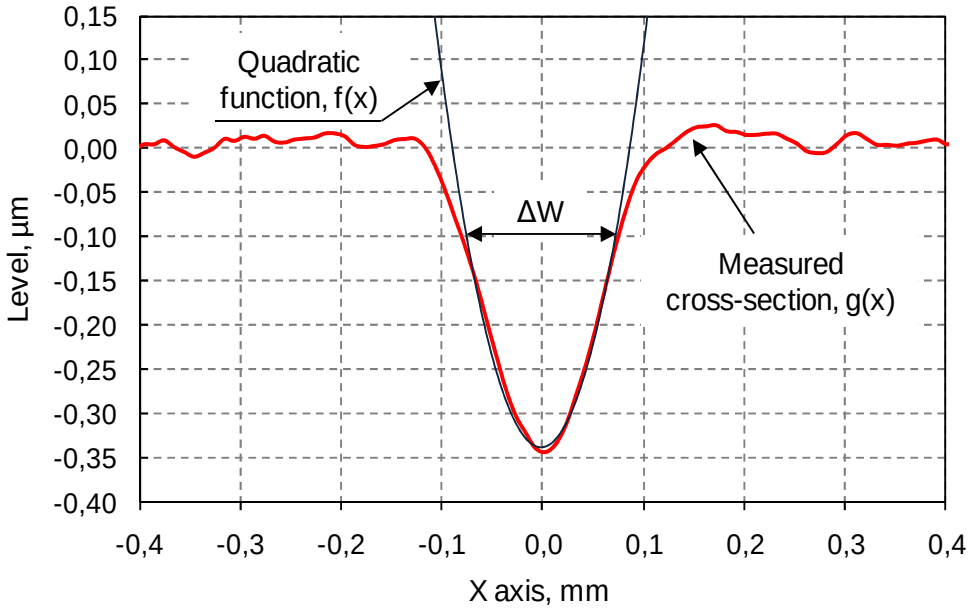

Figure 6.1: Cross-section of a ditch produced at P = 9.5 W, using a 1.1 × 0.9 mm laser beam moved along a line track with a 5 mm/s speed. The profile was taken after annealing.

In the case of the ditches produced near the vaporization threshold (P = 8.5 - 9.2 W), the second order polynomial fit was achieved with great uncertainty due to low signal-to-noise ratio of the measured surface profiles. On the other hand, for laser powers above 9.8 W, the residuals over the 160 µm width were measured to be greater than 50 nm. This means that a ditch, which is deeper than 750 nm (see Figure 5.2),

begins to lose its parabolic shape which results from the intensity distribution of the Gaussian laser beam.

Since a quadratic function, *f(x)*, can be used to represent reliably a shape of the ditches produced in the range of laser powers from 9.2 - 9.8 W, the radius of curvature (*RoC*) of these surface features can also be determined. Including the fact that these ditches are very shallow (< 1 µm deep) and relatively wide (about 160 µm), the *RoC* can be calculated using the following formula:

$$RoC = \left(\frac{\partial^2 f}{\partial x^2}\right)^{-1} \tag{6.1}$$

As shown in Figure 6.2, the curvature radius of the ditches decreases in a nonlinear manner with an increasing laser power. This nonlinear dependency between the *RoC* and the laser power used results from the fact that the depth of the ditches increases also in a nonlinear manner with increasing laser power, as already shown in Figure 5.2, while the width (ΔW, as indicated in Figure 6.1) remains to be almost constant.

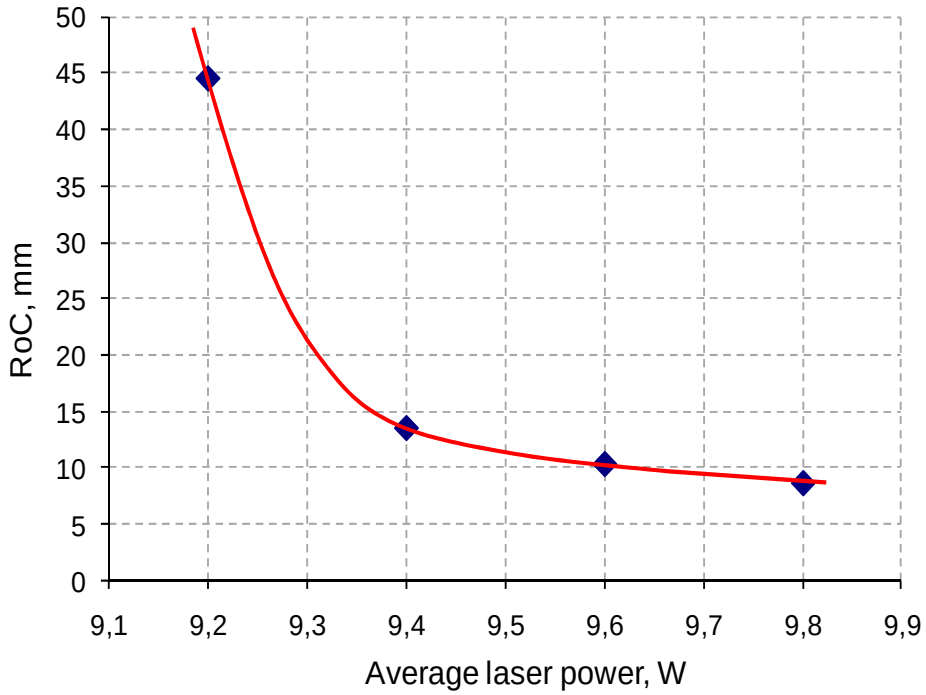

Figure 6.2: Radius of curvature calculated for the ditches produced in the range of laser powers from 9.2 to 9.8 W. Results presented for a 1.5 mm thick sample.

Generally, the ditches suffer from surface irregularities (referred to as "surface waviness"). As can be seen in Figure 6.3, the waviness is more pronounced when the laser power used is increased. Based on information given in Section 3.1 and work covered in Section 5.2, it can be concluded that this waviness results from the laser power fluctuations occurred during laser treatment of the glass ($\Delta P < 40$ mW), and the fact that an evaporation rate of fused silica increases rapidly with an increasing laser power, as shown in Figure 5.2.

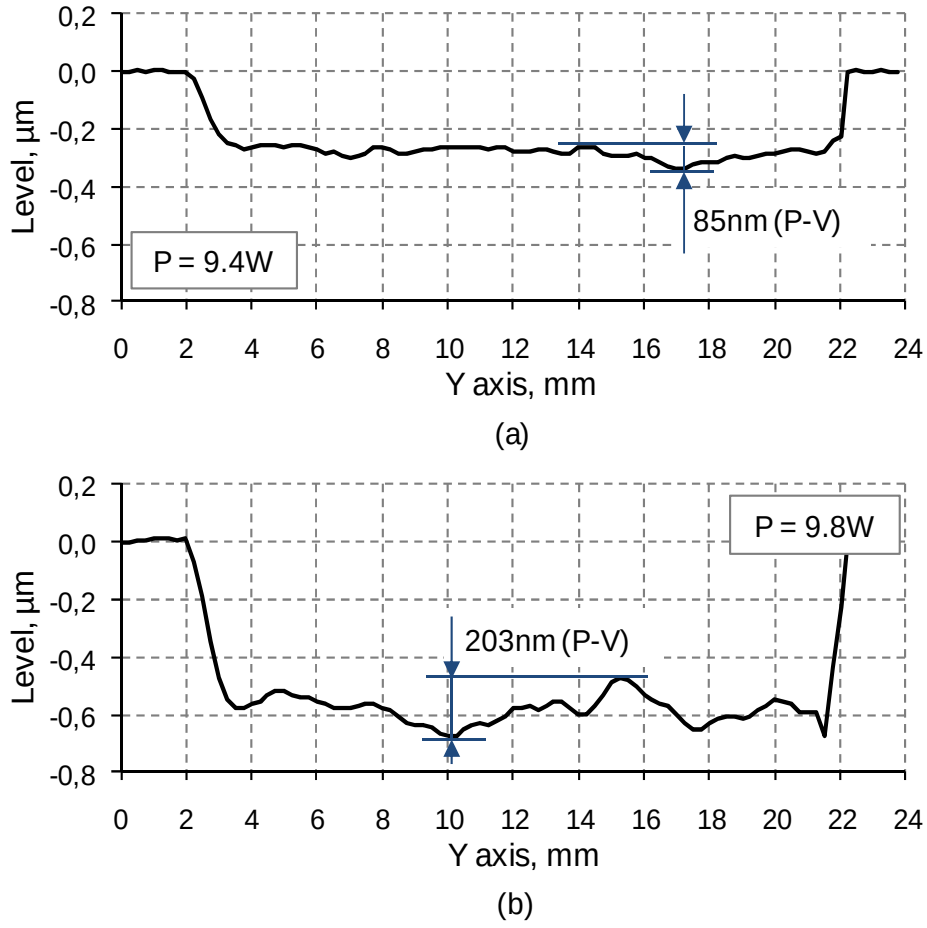

Figure 6.3: Depth of the ditches measured along their bottoms. Results presented for the ditches produced at (a) 9.4 W and (b) 9.8 W. The P-V stands for the peak-to-valley depth.

Based on the results presented in Figure 6.4, the peak-to-valley (P-V) of the bottom of ditches produced in the range of laser powers from 9.2 - 10.2 W varies from 60 to 300 µm. The low surface quality of the ditches, especially those produced at high laser power values ($P > 9.6$ W), seems to be a serious limitation in the fabrication of slit-shaped mirrors with a RoC less than 10 mm. Since the objective is to use the

ditches as the basis for reflective optics, surface waviness as high as 125 nm (P-V) would cause wavefront changes in the Yb:YAG laser beam of about λ/4 (where λ = 1.03 μm).

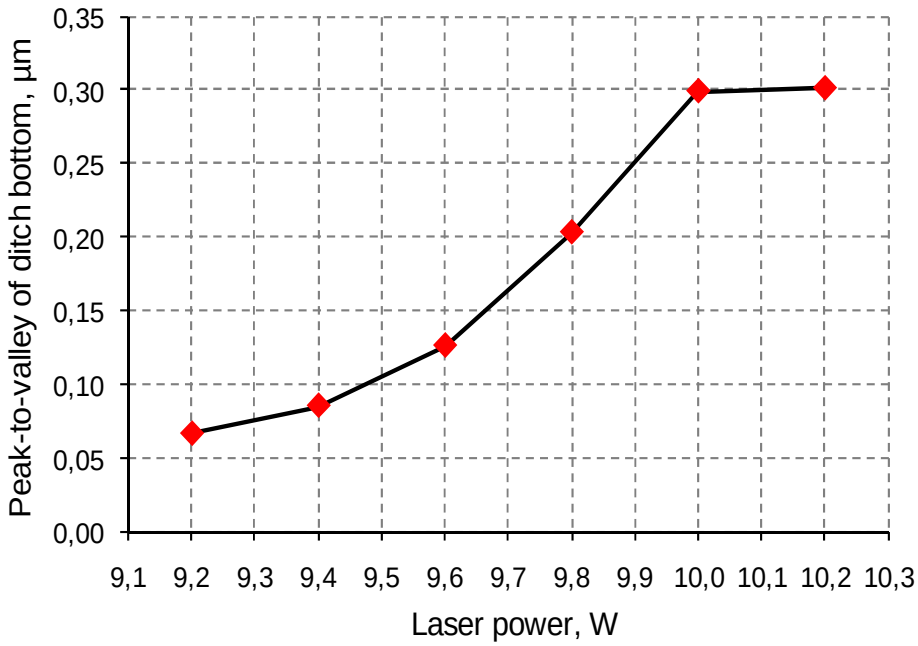

Figure 6.4: Surface waviness of the ditch bottom vs. laser power used.

6.3 Generation of grooves by laser scan overlapping

In this section, results are presented related to the special case of laser beam raster scanning in which the laser scans overlap each other, thereby increasing a local depth of the laser-evaporated area. The aim of this study was to determine the shape of the ditches produced by the use of different numbers of laser scans (*N*), since this knowledge is essential for the development of a procedure for fabricating parabolic-shaped mirrors with an aperture wider than that generated by single line laser scans for the case when a laser spot of approximately 1 mm in diameter is applied.

The cross-sections of the ditches produced by 1, 2, and 5 overlapped laser scans are shown in Figure 6.5. These narrow grooves were generated at a fixed laser power of 9.5 W, using a 1.1 × 0.9 mm elliptical Gaussian laser spot which was moved along a line track with a speed of 5 mm/s. The surface profiles presented in Figure 6.5 were measured: (a) before and (b) after annealing. The sample was 1.5 mm thick.

Based on Figure 6.5 (a), it can be concluded that subsequent laser scans develop deformations on the glass surface. Generally, a central ditch is observed to be deeper with an increasing number of laser scans due to an accumulative vaporization effect, while depressions become slightly shallower due to the appearance of bulges alongside these grooves. As noted in Section 5.2.3, these bulges result from the redeposition of the glass vapour and partially from the appearance of the Marangoni effect. As can be seen in Figure 6.5 (a), the depressions are constant in depth when $N = 1$ and 2. This means that the subsequent laser scans do not increase the value of fictive temperature within the laser-irradiated area. This effect is explained by the fact that the glass sample was always cooled down with an equal cooling rate when the subsequent laser scans passed.

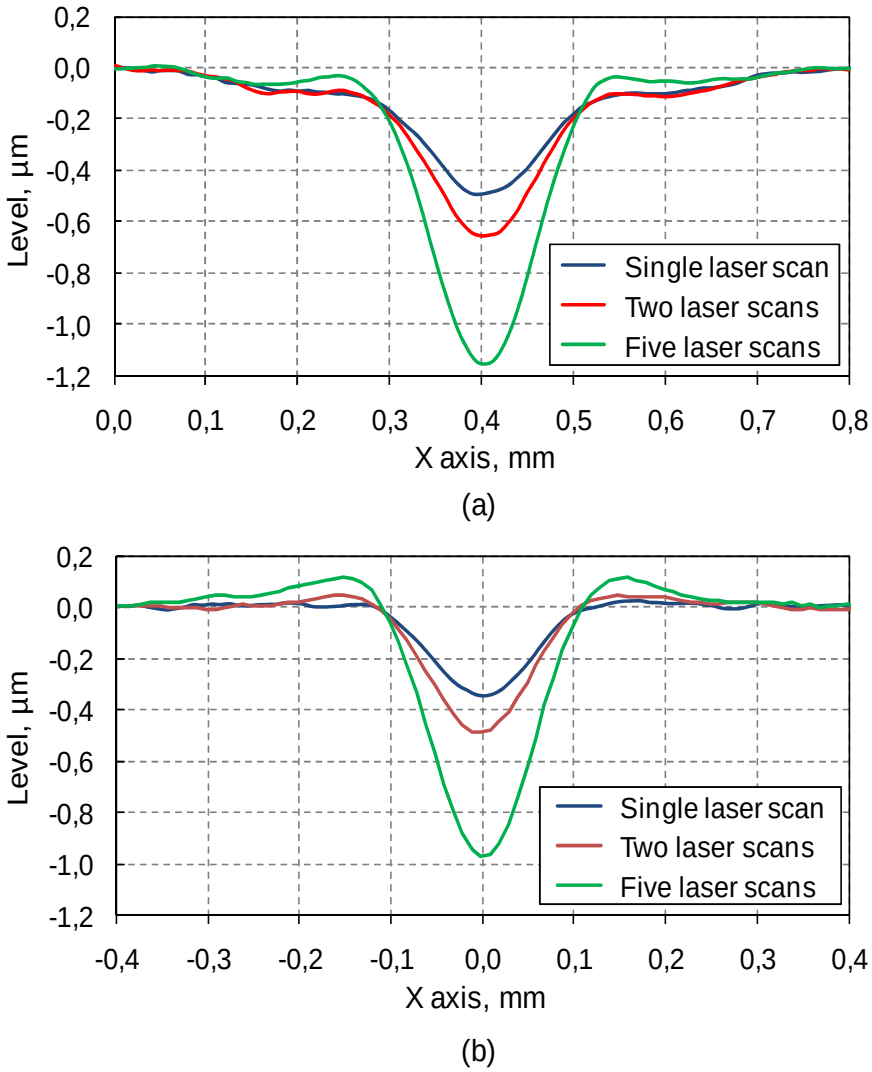

Figure 6.5: Cross-section of the grooves produced by laser scan overlapping at P = 9.5 W. Surface profiles were measured: (a) before and (b) after annealing of the glass.

As can be seen in Figure 6.5 (b), the laser-irradiated areas from Figure 6.5 (a) are uplifted. This means that an elevated fictive temperature in this region has been effectively reduced by annealing. More details regarding to this phenomenon may be found in Section 5.2.3.

Based on the results shown in Figure 6.6, the average depth of the ditches (D) is increased in a linear manner by the subsequent laser scans ($N > 1$). Here, it must be noted that the D value was calculated based on measurement of a depth in at least 48 different points along the Y axis, see Figure 5.6 (b) of Section 5.2.3, over a 16 mm distance. As can be seen in Figure 6.6, the straight red line is offset by $D_0 \approx 0.15$ µm. Though this offset is difficult to explain, it nevertheless provides strong evidence that fused silica evaporates faster from the blank surface. One explanation could be that untreated glass absorbs more CO_2 laser power, and thus a higher temperature is produced at the glass surface.

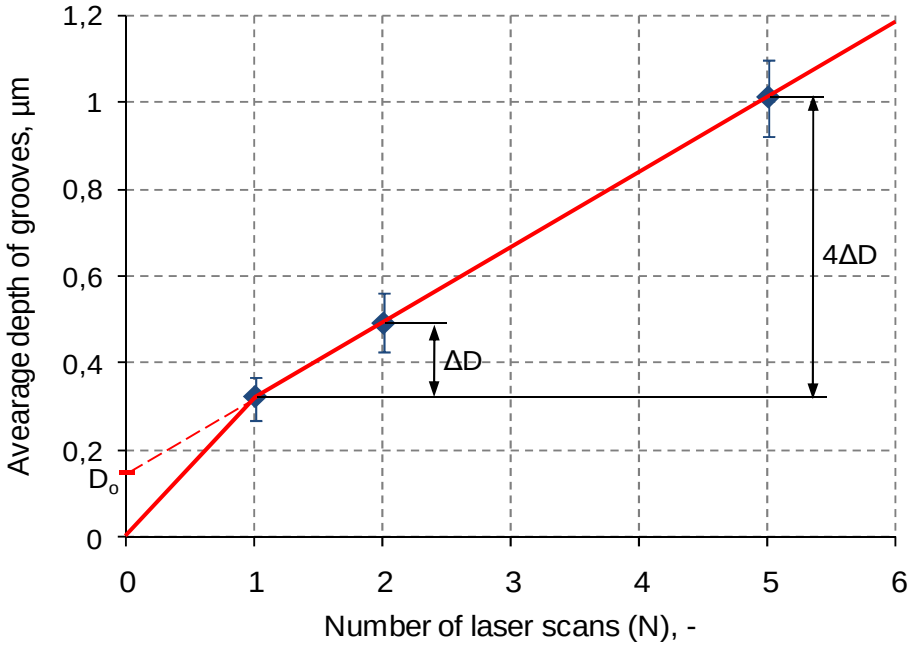

Figure 6.6: An average depth of the grooves presented in Figure 6.5 (b) as a function of N. The error bars indicate a peak-to-valley depth of the grooves.

There are two potential reasons why the glass surface absorbs less laser power for the subsequent laser scans. The first may be related to the fact that the glass surface becomes smoother after the first laser scan, thus more laser power is reflected. The second reason may be associated with the increase of fictive temperature within the

laser-irradiated area. Since the glass reaches high fictive temperature following the first laser scan, as can be seen in Figure 5.6 (a), it is quite likely that this increase modifies the properties of the glass, such as reflectivity and thermal conductivity, which values have significant influence on a laser-induced temperature distribution on the glass surface (see equation (7.10) of Section 7.4.2). This assumption, however, cannot be easily validated since a literature search has failed to unearth any information with regard to this issue. Finally, it must be noted that the normal laser irradiation of the glass plate was preserved for subsequent laser scans since the machined grooves are very shallow. This means that the laser beam was coupled into the material without polarization losses.

6.4 Fabrication of grooves using partially-overlapping laser scans

In this section, results are presented on the use of partially-overlapping laser scans to fabricate grooves with an aperture larger than 220 μm, since then these structures can be used as mirrors for planar waveguide laser applications, as will be described in Section 6.5.

Based on the results presented in the previous section, it is already known that the depth of the laser-produced ditches increases in a linear manner with an increasing number of laser scans (N). Therefore, it can be assumed that the resultant shape of the grooves produced by partial-overlapped laser scans may be estimated by using a simple subtractive model. In general, the subtractive model is based on the assumption that the resultant surface profile, $G(x)$, is the sum of N constituent surface profiles, $g(x)$, as illustrated in Figure 6.7.

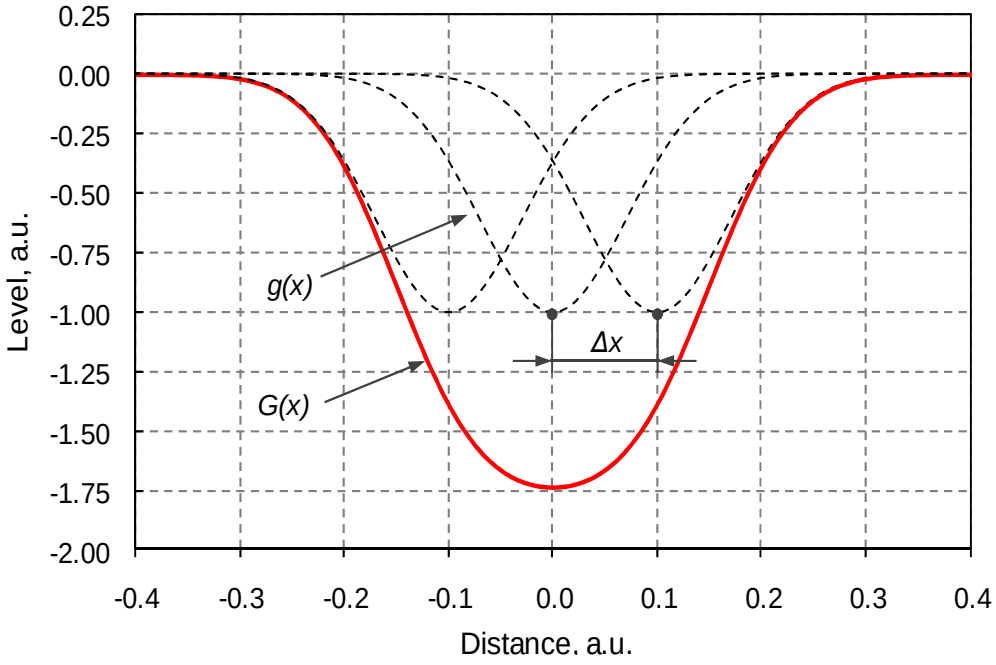

Figure 6.7: Concept of the subtracting model for estimating the shape of the groove produced by laser beam raster scanning.

In the present case, the function *g(x)* represents the profile which is generated by a single linear laser scan performed at a certain value of laser power, whereas *G(x)* represents the profile which is produced by partial-overlapped laser scans. Following the principle of the subtractive model, the function *G(x)* can be calculated as follows:

$$G(x) = \sum_{i=1}^{N} g\left(x + \left(i - \frac{N+1}{2}\right) \cdot \Delta x\right) \tag{6.2}$$

where *N* is the total number of laser scans and *Δx* defines the pitch between individual laser scans (see Figure 6.7).

As shown in Section 6.2, the central ditch which is produced by a single line laser scan can be described by a quadratic function; so that the radius of this surface feature may be determined. In the subtractive model, however, it is better to use a Gaussian function to represent the ditch shape (see equation (6.3)), since this function decreases naturally to zero as it approaches the origin. This means that it can be simply subtracted in the model.

$$g(x) = A \cdot exp(-Bx^2) \tag{6.3}$$

The *A* constant in equation (6.3) defines the average depth of a ditch, whilst it is necessary to determine the *B* parameter experimentally in order to obtain the best match between the Gaussian profile and the ditch shape.

Figure 6.8 shows the Gaussian representation of the groove which was produced by a single line laser scan at P = 9.5 W. The *A* and *B* constants used in equation (6.3) were $-0.345 \cdot 10^{-6}$ and $2 \cdot 10^{8}$, respectively.

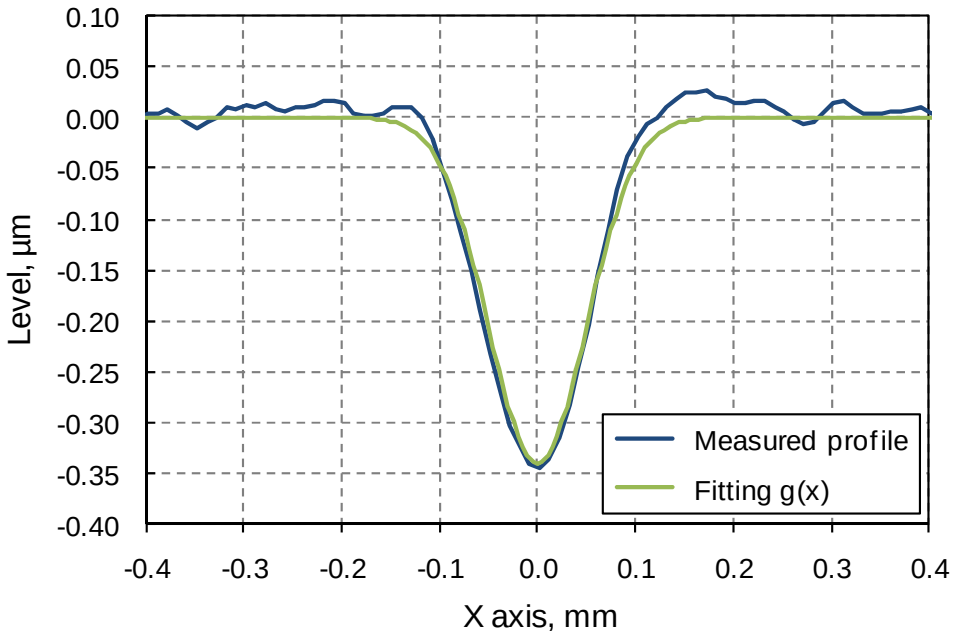

Figure 6.8: Gaussian fitting of the ditch produced by a single line laser scan at P = 9.5 W.

To demonstrate usefulness of the subtractive model, a simple experiment was performed. In this experiment, a 1 mm thick fused silica sample was treated by a set of single linear laser scans (N = 5) shifted with respect to each other by Δx = 50 µm. The laser scans were carried out at a constant laser power of 9.5 W and using a 1.1 × 0.9 mm elliptical Gaussian laser spot. The individual laser scan generated a ditch with a profile as shown in Figure 6.8 when the scan speed was 5 mm/s. Following the laser treatment, the sample was annealed according to the schedule shown in Figure 5.5. Then, the glass surface was scanned using the Proscan 1000 in order to provide information about the cross-section of the ditch produced by multiple-line laser scanning. Finally, the ditch profile was compared with the theoretical profile obtained with the aid of the subtractive model. The comparison of both profiles is shown in Figure 6.9.

As can be seen is Figure 6.9, the profile described by equation (6.2) is similar in shape to the cross-section of the laser-evaporated area generated by 5 partially overlapped laser scans. The difference between the experimental result and theoretical prediction was found to be as small as 0.1 µm. Thus, it can be concluded that the subtractive model developed in this section is an appropriate tool for predicting the surface profile of the grooves produced by partially-overlapped laser scans.

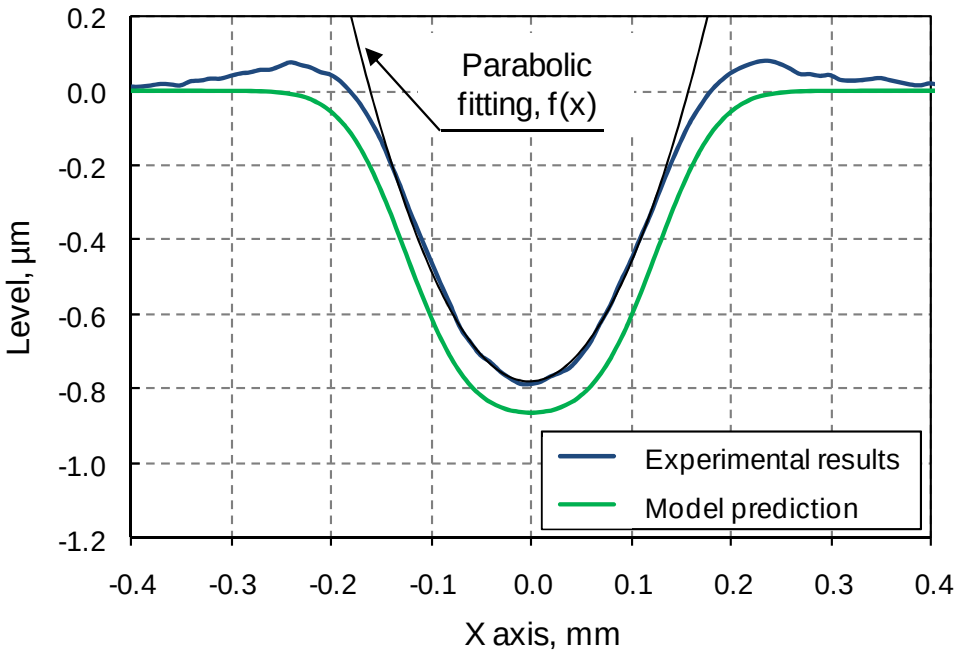

Figure 6.9: Cross-section of the groove produced by 5 laser scans overlapped each other with a 50 µm raster pitch, using P = 9.5 W and a 1.1 × 0.9 mm elliptical laser spot (see the experimental results). The surface profile calculated by using the subtractive model is also shown.

In order to determine the surface quality of the groove shown in Figure 6.9, surface irregularities were measured along the bottom of the groove, following the dashed line shown in Figure 6.10 (a). As can be seen in Figure 6.10 (b), surface waviness of the ditch bottom is about 225 nm peak-to-valley. Thus, it is approximately twice the peak-to-valley of the ditch bottom produced by a single line laser scan at equal laser power (see Figure 6.4). Since surface waviness along the ditch bottoms is characterized by a random distribution (no correction between Figure 6.10 (b) and Figure 6.3), it is most likely that the P-V value increases as the square root of N, where N is referred to as the number of laser scans.

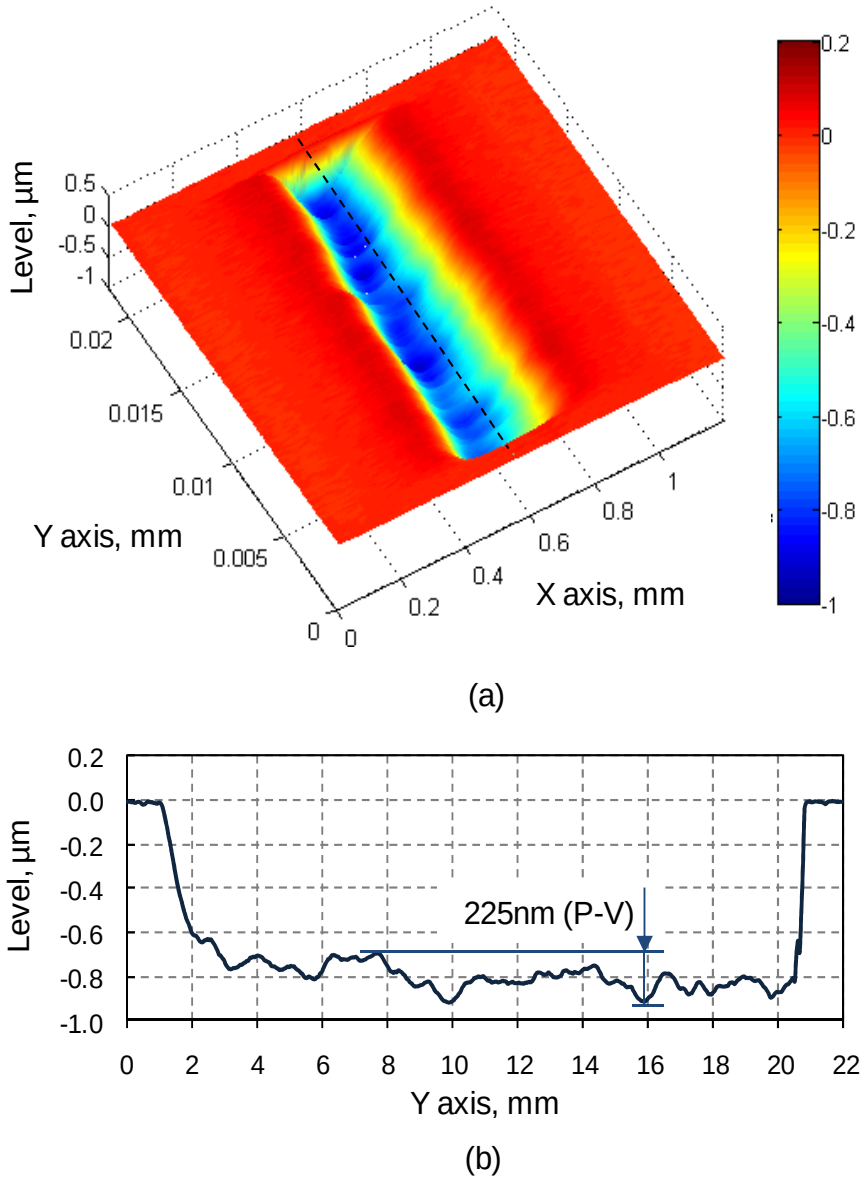

Figure 6.10: (a) 3D surface scan (120×440 pts) of the groove produced by 5 scans with Δx = 50 µm and at P = 9.5 W. Surface profile shown in (b) was taken along the dashed line shown in (a).

Finally, a quadratic function was applied for the ditch shown in Figure 6.10 in order to determine its radius of curvature. Based on fitting shown in Figure 6.9, the *RoC* was measured to be about 16 mm over a 260 µm distance. This means that this ditch may be used as a mirror in the mode-selective resonator configuration for a 150 µm core Yb:YAG planar waveguide laser. Test results of this highly-curved structure are presented briefly in the next section, and further laser-related details have been reported at an international conference and published in the corresponding SPIE Conference Proceedings [130].

6.5 Test of laser-machined cylindrical ditches

A planar waveguide used for testing of the laser-machined grooves consisted of a 150 µm thick 2% doped Yb:YAG core surrounded by two 1 mm thick sapphire claddings. The waveguide was 12 mm wide and 13 mm long. Maximum average power produced by this laser was approximately 400 W (at 75% slope efficiency). Such a large laser power was achieved in the plano-concave resonator setup, as reported in [130]. However with this resonator configuration, in the lateral direction the laser operated in a highly multi-mode fashion and in two-mode operation in the transverse direction. The overall beam quality of this laser system was therefore inadequate for many applications and is uncompetitive, for instance, with high power fibre lasers in which the beam quality (M^2) factor is typically close to the Gaussian diffraction limit.

One of the solutions to improve the transverse beam quality of a planar waveguide laser is to use a mode-selective resonator configuration, which was called Case III by Degnan and Hall [131]. In this configuration, a mirror with a curvature radius two times greater than the free-space Rayleigh range ($RoC = 2 \cdot z_R$) is placed at the Rayleigh distance from the waveguide end-facet ($z = z_R$). The Rayleigh range (z_R) for the waveguide core thickness (a) is given by:

$$z_R = \frac{\pi a^2}{8 \lambda} \tag{6.4}$$

where λ is the laser wavelength. In the case of the 150 µm core Yb:YAG planar waveguide laser, the z_R value is about 8.6 mm, whereas the *RoC* of the mirror required for Case III is approximately 17.2 mm.

Testing of the 16 mm *RoC* ditch in the Case III resonator configuration for the Yb:YAG planar waveguide laser was carried out with the assistance of Dr Ian J. Thomson within the LPA group. Prior to use the ditch as an optical component, the sample was HR coated for 1030 nm.

The optical setup used for testing the laser-machined mirror in the Case III resonator configuration is shown in Figure 6.11. In this configuration, the test mirror was aligned 8 mm from the rear waveguide facet, while the second mirror (an 80% reflectivity plane mirror) was aligned 0.5 mm from the opposite waveguide facet. The output laser beam achieved in this optical setup was directed on a diffusive screen

placed at a 250 mm distance from the plane mirror. The beam profile was recorded using a CCD camera operating with Spiricon beam profiling software.

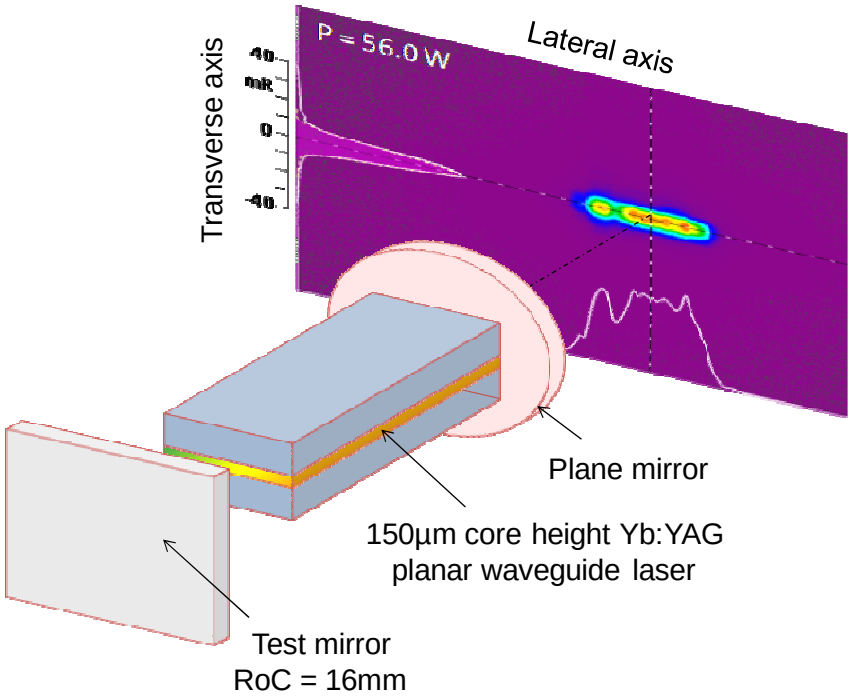

Figure 6.11: Mode-selective resonator configuration (Case III) applied in the Yb:YAG planar waveguide laser setup and the output beam profile observed by a CCD camera operating with Spiricon beam profiling software.

As can be seen in Figure 6.11, the output laser beam in the transverse direction matches closely the theoretical TE_1 waveguide mode propagated in the air, thereby showing successful operation of the laser-fabricated mirror in Case III. Some extra power in the wings was found to be caused by either weak higher order modes or diffraction from the edges of the ditch structure [132].

The output laser power was measured to be 56 W at the pumping power of 250 W. This value of the output power was found to be comparable with the power value produced by a commercial cylindrical HR coated lens. The output power for this lens placed at an 8 mm distance from the waveguide facet was measured to be 58 W [132]. During measurement of the laser power, it was found that HR coating applied to the ditch resulted in 10% leakage of the multi-mode laser power through the substrate. Since the damage threshold of the HR coating was not known, as a conservative

measure to prevent possible catastrophic damage, measurement of the output power was carried out only at the pumping power of 250 W. This operation allowed us to reduce the risk of the mirror damage.

6.6 Fabrication of toroidal mirrors

The aim of the work covered in this section is to fabricate a toroidal mirror which is 220 µm high and 16 mm wide with radii of curvature of 17.2 and 230 mm in the transverse and lateral directions, respectively (see Figure 6.11). It is planned that this mirror would be one element in the resonator configuration used to provide improved mode-selectivity and power efficiency for the 150 µm core high-power Yb:YAG planar waveguide laser, as described in Section 6.5. The aim is to achieve excellent laser beam quality improvement in both lateral and transverse directions. The optical setup and properties of this type of resonator configuration have been recently detailed in [132].

6.6.1 Efforts made to improve fabrication process of toroidal mirrors

Although the 16 mm *RoC* cylindrical ditch from Section 6.4 has not been tested for the maximum pumping power of 800 W, the test results presented in Section 6.5 provide valuable information with regard to the surface quality of the laser-machined grooves. As can be seen in Figure 6.11, the output laser power is non-uniformly distributed in the lateral direction since the test ditch contained quite significant irregularities along its bottom.

As mentioned in Section 6.2, the surface irregularities which occur within the laser-evaporated area result from the fluctuations of CO_2 laser power when the glass surface is treated by a moving laser beam. Although the laser system described in Section 3.1 limits the fluctuations to less than 80 mW (peak-to-valley), they are still sufficient in magnitude to produce significant surface waviness along the bottom of the laser-generated ditch.

A detailed analysis of the laser power fluctuations revealed that they are correlated with the temperature oscillations of the CO_2 laser coolant. Generally, it was found that the temperature and laser power fluctuations have the same cycle period. Since the temperature of the laser coolant was varied typically in the range of 19.8 – 20.4°C, it seemed to be obvious that such a high variation must have a negative influence on the stability of the laser power delivered to the target (glass). Therefore,

prior to fabricating the mirrors on a curved substrate, the laser was connected to a new precise refrigerated chiller which allowed the temperature oscillations to be reduced by a factor of 3. Since the new chiller was placed adjacent to the laser system (in contrast to the previous arrangement which uses chilled water supplied to the whole lab and generated external to the building), it was now easy and convenient to make changes to the temperature of the laser coolant, thereby ensuring constant operation of the laser at the 10.59 µm wavelength.

6.6.2 Fabrication procedure

Regarding to a curvature in the lateral direction

To achieve fabrication of a toroidal mirror with an approximate 230 mm curvature radius in the lateral direction, an uncoated cylindrical lens supplied by Thorlabs Ltd. was chosen for use as a substrate [133]. This plano-concave lens was 30 mm long, 45 mm wide, and 3-3.5 mm deep (sag = 0.5 mm). Based on the quadratic fitting approach shown in Figure 6.12 (a), the radius of curvature of the lens was verified to be 226 mm. As can be seen in Figure 6.12 (b), surface irregularities along the lens curvature were determined to be as large as 320 nm (peak-to-valley). These irregularities correspond to a residue between the quadratic fitting curve and the measured surface profile of the uncoated and untreated lens.

Although the low-frequency surface roughness of the lens was found to be consistent with the optical specification given by Thorlabs [133], it is most likely that in reality this waviness was smaller than 320 nm (P-V). This conclusion was reached because recently it has been found when calibrating the Proscan 1000 profilometer, using a *tilted* optically flat mirror as a test piece (see the inset of Figure 6.13), that this instrument does not cope well with surfaces as curved as the 230 mm *RoC* lens, because the Proscan interface has a tendency to introduce both systematic error and sufficient noise into the actual profile of the measured surface, as can be seen in Figure 6.13.

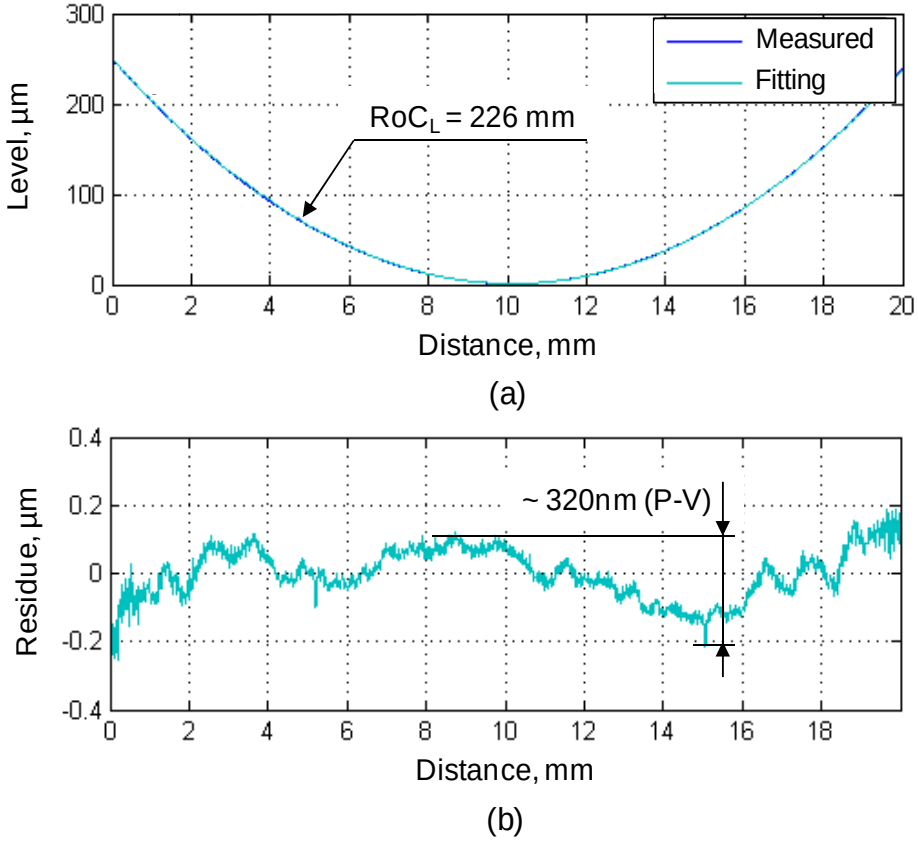

Figure 6.12: Uncoated plano-concave cylindrical lens used for fabricating toroidal mirrors: (a) cross-section and (b) surface irregularities measured along the lens curvature. Profiles measured by using the Proscan 1000 profilometer.

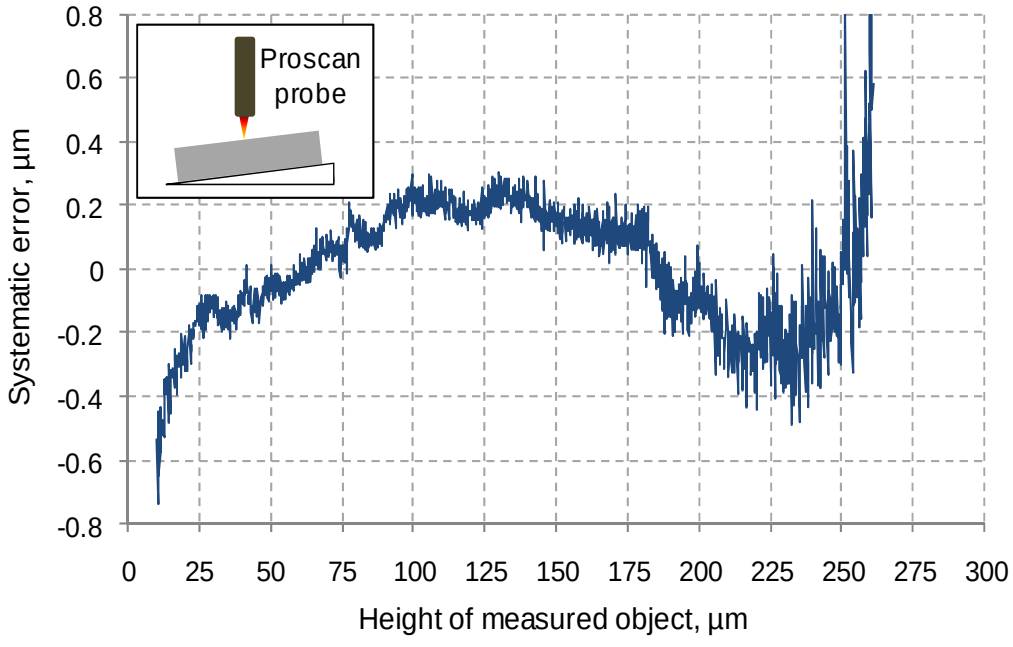

Figure 6.13: Calibration curve of the Proscan 1000 profilometer.

Regarding to a curvature in the transverse direction

To generate the required curvature in the transverse direction, partially-overlapped laser scans were carried out along the lens curvature, thereby producing a toroidal shape. Generally, laser processing conditions were chosen to be the same as those used for producing the 16 mm *RoC* cylindrical ditch described in Section 6.4, apart from the value of the laser power used. Due to a lack of the calibration curve for a 3 mm thick sample (the calibration curves for 1 and 1.5 mm thick samples are shown in Figure 5.2), it was decided to fabricate four mirrors at different values of laser power each. The laser power values were as follows: 9.3, 9.35, 9.4 and 9.45 W.

Surface cleaning of the laser-fabricated grooves

An optical microscope examination of the laser-machined grooves revealed that the groove surroundings are affected by redeposition of the glass vapour, as shown in Figure 6.14 (a). In order to remove the deposit, it was decided to apply CO_2 laser polishing. This process was carried out by laser beam raster scanning, using a raster pitch of 10 µm and a laser power of 7 W. As can be seen in Figure 6.14 (b), the CO_2 laser beam enabled the deposit to be removed effectively from the glass surface, as shown in Figure 6.14 (b).

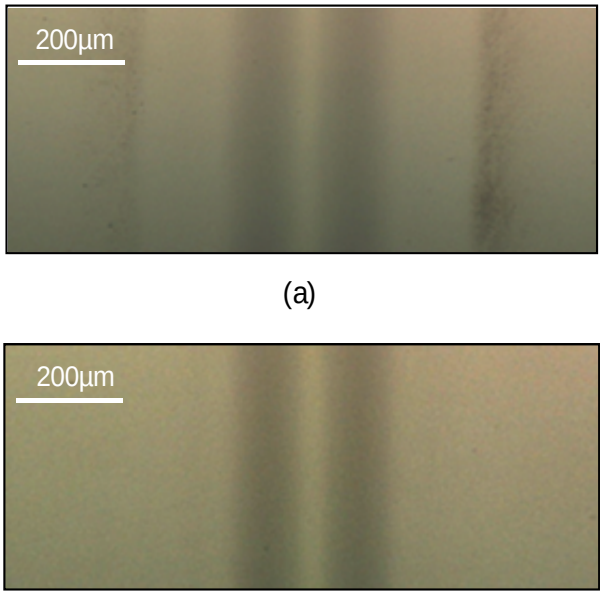

Figure 6.14: Optical micrograph of the groove produced at a 9.45 W laser power: (a) as machined and (b) after laser polishing at a 7 W laser power.

Annealing

In the final stage of the fabrication process, the glass plate with four ditches was annealed using the temperature schedule presented in Section 5.2.3. Following the annealing, the ditches (now called mirrors) were measured using the Proscan 1000 profilometer (see results in Section 6.6.3), and then the glass plate was carefully cleaned, packed, and sent for HR coating.

6.6.3 Characterisation of toroidal mirrors

Measurement results of the lateral (RoC_L) and transverse (RoC_T) curvature radii of the four mirrors produced at different values of laser power are listed in Table 6.1. This table also contains the laser power fluctuations (ΔP), which were recorded during laser scanning, and the peak-to-valley (P-V) of surface irregularities measured along the bottom of the mirrors over a 16 mm distance. Here, it must be noted that the irregularities were measured relative to the untreated surface level, so that any surface irregularities that were initially in the substrate (see Figure 6.12 (b)) were normalized out.

Table 6.1:.Laser power and laser power fluctuations (ΔP) during laser scanning, curvature radii of the mirrors in the lateral (RoC_L) and transverse (RoC_T) directions, and peak-to-valley surface waviness measured along the mirror bottoms.

Mirror	Power, W	ΔP, mW	RoC_L, mm	RoC_T, mm	Waviness (P-V), µm
1	9.30	-30 / +20	225.9	21.3	0.17
2	9.35	-22 / +29	226.6	20.1	0.23
3	9.40	-36 / +25	225.8	12.9	0.38
4	9.45	-27 / +24	225.8	12.3	0.25

Based on results listed in Table 6.1, the geometrical properties of Mirror 2 was a good match to the requirements of the mode-selective, high-efficient resonator configuration detailed at the beginning of Section 6.6. Surface irregularities (waviness) measured along the bottom of Mirror 2 are shown in Figure 6.15.

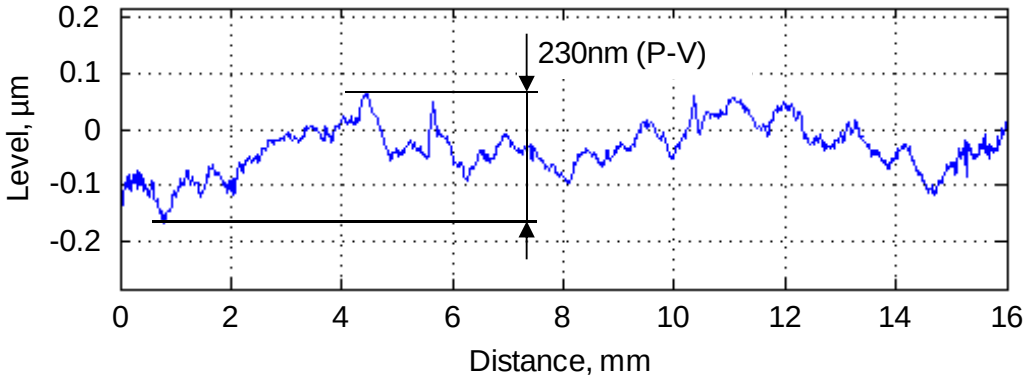

Figure 6.15: Surface irregularities measured along the bottom of Mirror 2 (using Proscan).

Finally, the width of the laser-machined mirrors was found to have negligible variation along the lateral curvature. As already mentioned in Section 6.1, this is related to the fact that an approximately 1 mm diameter laser beam had a small divergence (θ < 10 mrad), thereby varying insignificantly in size over an approximately 0.5 mm depth.

6.6.4 Discussion on further improvement of CW-mode laser system

Based on results presented in Table 6.1, it can be concluded that better temperature stability of the laser coolant did not result in any significant reduction in the degree of surface waviness along the bottoms of the machined mirrors. This means that more work towards an improvement of the laser system used for fabricating mirrors needs to be done in the future. There are two solutions which should be applied in the current CO_2 laser setup:

a) eliminate an influence of the ambient temperature by insulating thermally the laser housing,
b) replace a slow power meter, which currently co-operates with the PID feedback loop (see Section 3.1), by a fast-response detector which will be able to capture the laser power data with a high sampling rate (f > 10Hz).

Although some work towards an improvement of thermal stability of the laser has been already done (see Section 6.6.1), the thermal insulation of the laser housing may help to hold a 10P20 wavelength over a long time period.

Currently, the CO_2 laser system used for fabricating mirrors is equipped with a slow laser power meter which has a response time of about 0.6 s. This power meter is connected in-line with an acousto-optic modulator (AOM) via a PID feedback loop, as shown in Section 3.1, to control the value of the laser power delivered to the glass workpiece during its processing. Since the laser power is sampled with a 10 Hz rate by the power meter, laser power fluctuations with a period lower than 200 ms cannot be cancelled out. To overcome this problem, a clear solution would be to replace the current power meter by a fast-response detector (e.g. an infrared pyroelectric sensor) which would allow the laser power to be read with a sampling rate much faster than 10 Hz. This solution should accelerate the response time of the PID loop in the system, thereby reducing laser power fluctuations at the glass target, and consequently the surface waviness along the bottom of laser-generated mirrors should be eliminated.

6.7 Summary and conclusions

This chapter has reported on a novel approach for the rapid prototyping (fabrication) of fused silica toroidal mirrors with a high ratio of the two principle radii of curvature ($RoC_1/RoC_2 > 10$). In this fabrication technique, one radius of curvature (RoC_1) is determined by the shape of the substrate used for machining, whilst the other curvature radius (RoC_2) is achieved by CO_2 laser-induced vaporization of the glass. Generally, the curvature produced by vaporization is controlled by the laser spot size, laser power, number of laser scans, and raster pitch between them.

The notable feature of the mirrors fabricated by the laser irradiation technique and presented in this chapter is their dimension. Since the mirrors are generated by using a low number of partially-overlapped linear laser scans ($N = 5$), they can be infinitely long but nevertheless relatively narrow, since the width of the mirrors is limited to a few hundred microns due to the fact that they are produced using an approximately 1 mm diameter laser spot.

Since the laser-machined mirrors are characterized by a peculiar shape of the aperture and a high ratio of the principle curvature radii, they are very suitable for use for some selected planar waveguide laser applications. As shown in Section 6.5, these mirrors may be successfully applied in the mode-selective resonator configuration (called Case III by Degnan and Hall [131]) to improve the laser beam quality of a planar

waveguide laser in the transverse direction. To the author's knowledge, this is first time that this kind of mirror has been fabricated and demonstrated in use for a high power planar waveguide laser. In the near future, this non-standard optic will be tested in a novel resonator configuration for the Yb:YAG planar waveguide laser, to achieve an output laser beam profile with the value of M^2 equal to about the Gaussian diffraction limit in both directions.

Finally, the low surface quality of the laser-machined mirrors may be significantly improved by introducing a more effective power control system for the current CO_2 laser system, as described in Section 6.6.4. These improvements should reduce laser power fluctuations, thus surface waviness along the bottom of the mirrors should be also reduced. Since the evaporating rate of fused silica increases in a non-linear manner with increasing laser power, as shown in Figure 5.2, reduction of the laser power fluctuations by (say) a factor of 2 would be expected to decrease sufficiently the degree of surface irregularities of the mirrors. This means that the CO_2 laser-based technique covered in this chapter will be able to compete to some extent with diamond turning [134], which is currently used for fabricating toroidal mirrors.

Chapter 7

Investigation of stresses induced by CO_2 laser polishing

7.1 Introduction

The work covered in this chapter is focused on an investigation of CO_2 laser-induced distortions of fused silica plates. The distortions are produced by laser beam raster scanning, using a laser beam of diameter approximately 1 mm that is moved along a 10 µm-pitch raster track with a speed of 5 mm/s (see Figure 7.3 of Section 7.3.1 for more details). Here, it should be noted that these laser treatment conditions have not been chosen randomly since laser beam raster scanning with a 1 mm diameter laser beam is typically used for polishing surfaces of CO_2 laser-cut micro-optics, such as corrective phase plates [5, 6, 61] and beam shapers [7]. In addition, the same laser processing conditions can be successfully applied for relaxing sharp step edges of the binary and multi-level etched structures, as shown in Chapter 4.

The aim of the work carried out in this chapter is to determine the extent and character of the stress produced in fused silica plates, when treated by a moving CO_2 laser beam. Among the questions which are posed in this chapter are:

- Does laser beam raster scanning produce an anisotropic stress at the glass surface?
- What is the magnitude of the laser-induced stress in fused silica?
- Is a thin glass plate more prone to breakage due to the stress than a thick plate?
- Can the laser-induced stress be relieved by annealing?

To answer these questions, the laser-induced distortions of the plates are investigated with respect to different values of the laser power used, the geometry of the laser-irradiated area, and finally the glass thickness. In addition, the influence of annealing on the value of the laser-induced stress is also studied here.

Finally, I would like to acknowledge that work covered in this chapter arose with the help of Dr Roy McBride, Managing Director of PowerPhotonic Ltd, who explained to me how to estimate the value of the CO_2 laser-induced stress that occurs on the surface of a glass plate, based on the experimental results shown in Section 7.3.

7.2 Background information

A material when heated typically expands. The transient and non-uniform temperature distributions resulting from localized laser heating cause different zones of the material to expand by different amounts [60], which in turn results in the development of surface stresses. If the stresses are small, they are absorbed by the elasticity of the material. On the other hand, if stresses exceed the yield point, the material undergoes permanent deformations and may even fracture.

The earliest mention in the literature of CO_2 laser-induced distortions in fused silica plates appears to be following observations by Temple *et al.* in 1982 [12]. In their experiments, 38.6 mm diameter fused silica samples with a thickness of 6.35 mm were irradiated by a 5.2 mm diameter moving laser beam, using different values of laser power (up to 250 W). In order to cover a large area of the glass, the laser beam traversed the sample surface with a speed of 8 cm/s, following a raster scan pattern similar to that shown in Figure 7.3. During laser treatment, the samples were in air and were held in position by a three-point aluminium holder which was, in turn, mounted to a microscope slide manipulator. The examination of the laser-irradiated samples by the use of a polariscope and a wavefront interferometer revealed, respectively, residual stress and wavefront distortions in the glasses. The magnitude of the stress and distortions were observed to increase monotonically with increasing severity of the laser treatment. As explained indirectly by the authors, the observed distortions resulted from the temperature gradient mechanism (TGM).

The TGM is widely used to explain out-of-plane bending of metal sheets, towards an incident laser beam [135]. Generally, this mechanism requires high

temperature gradients to be established across the material thickness. Since glasses (e.g. fused silica) have a small absorption depth at a 10.6 µm wavelength (see Section 2.4.2) and low thermal conductivity (much smaller than in metals), a steep temperature gradient is easily produced across the glass thickness.

The laser-induced temperature gradient generated in a fused silica glass plate results in differential thermal expansion of its isothermal layers, thus the layers of the material close to the laser-irradiated surface expand more than those further away from the surface [136]. This differential thermal expansion generates thermoelastic stress in the material, leading to counter-bending of the plate in the direction away from the incident laser beam, as can be seen in Figure 7.1 (a). Since fused silica has a small thermal expansion coefficient (*CTE* = 0.6 ppm/K), the counter-bending is relatively small in comparison to other glasses and in particular metals [137]. With continued heating, the bending moment of the glass plate opposes the counter-bending and the mechanical properties of the material (e.g. viscosity) are reduced with increasing temperature. When the temperature exceeds the transformation point, the laser-irradiated area becomes viscoelastic [68]. Then, further thermal elastic expansion is converted into plastic deformations and the surface stress begins to be released [73, 137]. The stress relaxation is increased with increasing temperature. When the glass becomes very viscous (above the softening point), the stress in the molten zone is dissipated.

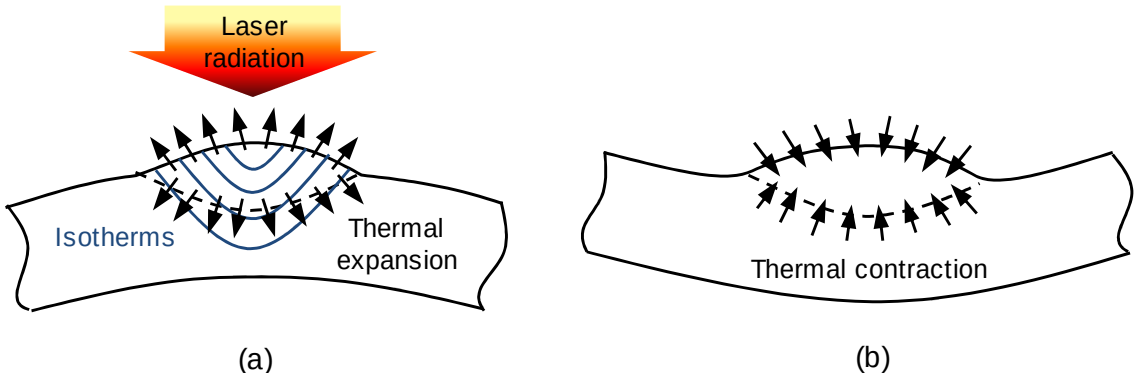

Figure 7.1: Laser bending by the temperature gradient mechanism (TGM): (a) heating stage (counter bending) and (b) cooling stage (positive bending), reproduced from [138].

During cooling the material contracts in the upper layers, as shown in Figure 7.1 (b). Due to the difference in lengths between the upper and bottom layers of the material,

the glass plate is bent towards the incident laser beam and the upper layer undergoes tensile strain as the body collectively cools [139]. In metals with a specific thickness, for instance, the final bending angle induced by the temperature gradient mechanism depends on the size of the laser spot, laser power, and the translation speed of the laser beam in relation to the workpiece [140].

Recently, Wu *et al.* [70, 71] reported that a continuous-wave CO_2 laser beam can be employed successfully for bending of borosilicate glasses. They showed that the rectangular glass plates with a thickness of 0.15 mm can be bent significantly either towards or away from the incident laser beam. Bending of the plates was achieved by using a laser beam moved perpendicularly to the longer glass edges. The laser scanning path was chosen to be 5 mm from one end of the glass plate, whilst the other end was clamped. To avoid laser-overheating of the samples, the starting and finishing points of the laser scanning path were located outside of the specimen.

Based on results provided by Wu *et al.* [70, 71], the bending angle and its direction were determined by the laser beam size, laser power, laser scan speed, laser scan number, and the width of the workpiece. The positive bending of the glass plates, which was caused by the TGM, was achieved for a 0.3 mm diameter laser beam, laser powers from 13 to 16.25 W, and scan speeds in the range between 50 and 200 mm/min. For scan speeds over 200 mm/min, the glass samples fractured. Bending angles up to 24 degrees were achieved by using multiple laser scans. Based on the results provided by the authors, the bending angle was proportional to some extent to the number of laser scans. Laser treatment of the glass plates with various widths showed that larger bending angles could be achieved for wider samples. As explained by the authors, stronger bending in wider specimens resulted from the fact that the thermal stresses induced by the laser beam were more difficult to release along the scanning path, and thus more forces were converted into the bending moments [70].

Counter-bending of 150 µm thick borosilicate plates was achieved by using a 0.8 mm diameter laser beam, laser powers from 11.75 to 15.5 W, and scan speeds in the range from 10 to 60 mm/min. For these laser processing conditions, the bending effect was dominated by the buckling mechanism. This mechanism has been explained in detail in many textbooks and journal publications, for instance in [70, 135, 136]. In comparison to the TGM, the buckling mechanism occurs when steep temperature

gradients are not generated in a material [135]. In such cases, the residual stress developed in the laser-irradiated region tend to buckle the material, thereby bending the workpiece away from the incident laser beam while the laser beam leaves the scanning path after traversing the whole width of the material. The bending angles achieved by Wu *et al.* were reported to be up to 13 degrees and were larger for wider specimens.

In comparison to the work reported by Wu *et al* [70, 71] and Temple *et al* [12], the experiments covered in this chapter are significantly different mainly because of the difference in the size of the laser-irradiated area. In the experiments described in the subsequent sections, a CO_2 laser beam traverses along the glass surface following a raster pattern (see Figure 7.3), and covering only the middle section of a glass plate. This means that the thermal stresses induced by the laser beam raster scanning are possibly trapped in the material, thereby preventing the glass from being bent in one direction only, as reported for the experimental conditions described by Wu *et al*.

7.3 Investigation of CO_2 laser-induced deformations of silica plates

The aim of the experiments covered in this section is to determine the extent of the surface distortions produced in fused silica plates when laser irradiated using typical CO_2 laser polishing conditions. The laser-induced distortions were investigated with respect to: different values of the laser power (see Section 7.3.2), geometry of the laser-irradiated area (see Section 7.3.3), and the glass thickness (see Section 7.3.4). Based on these experimental results, the value of the laser-induced surface stress has been estimated as described in Section 7.4.

7.3.1 General experimental procedure

The experiments covered in the following subsections were performed on 25.4 mm square fused silica plates (HPFS® Corning 7980) supplied by Valley Design Corp. (USA). The thickness of the samples was in the range from 0.254 to 1.5 mm, and the laser treatment of the plates was carried out using the CO_2 laser processing workstation described in Section 3.1.

The glass samples used in the experiments were optically flat. This was proven by a test for flatness in which the glass plate was placed on a reference flat surface (a fused silica mirror, P/N: PF30-02, Thorlabs) to observe an interference pattern in the

form of Newton's rings. It should be noted that this test was performed only for a few randomly-chosen glass plates.

Prior to CO_2 laser treatment, the samples were washed and dried using isopropanol and lens tissues, thereby removing residual surface contamination and dust. Afterwards, each sample was placed separately in a custom-made sample holder, as can be seen in Figure 7.2, in which the back side of the glass plates was in direct contact with an aluminium block. Since the sample holder was designed initially for 75 × 25 mm fused silica slides, it was necessary in addition to place two brass blocks, one at each side of the glass plate, to prevent any accidental movement of the workpiece during laser treatment.

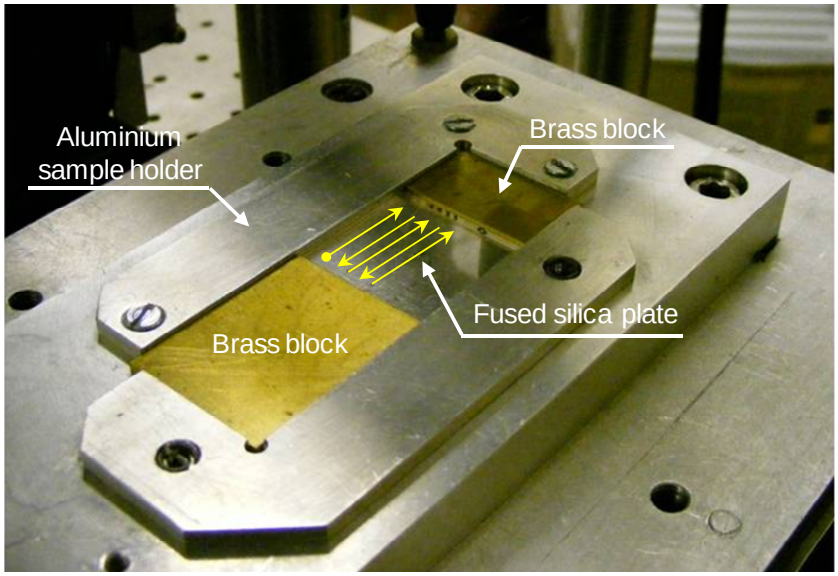

Figure 7.2: Mounting of samples in sample holder. Arrows illustrate the movement of the laser beam.

The area of the glass surface treated by a moving CO_2 laser beam, here referred to as the laser-irradiated area (LIA), is illustrated in Figure 7.3. As can be seen in this figure, only the central region of the glass plate was directly affected by CO_2 laser irradiation. The laser beam used in these experiments was elliptical, having a 1.1 mm diameter in the X-direction and a 0.9 mm diameter in the Y-direction. To cover the W × L area of the glass (see Figure 7.3), the laser beam was moved along the Y-axis with a constant speed of 5 mm/s, moving also progressively along the X-axis with a pitch (Δx) of 10 μm. The laser beam movement along the Y-axis was bidirectional.

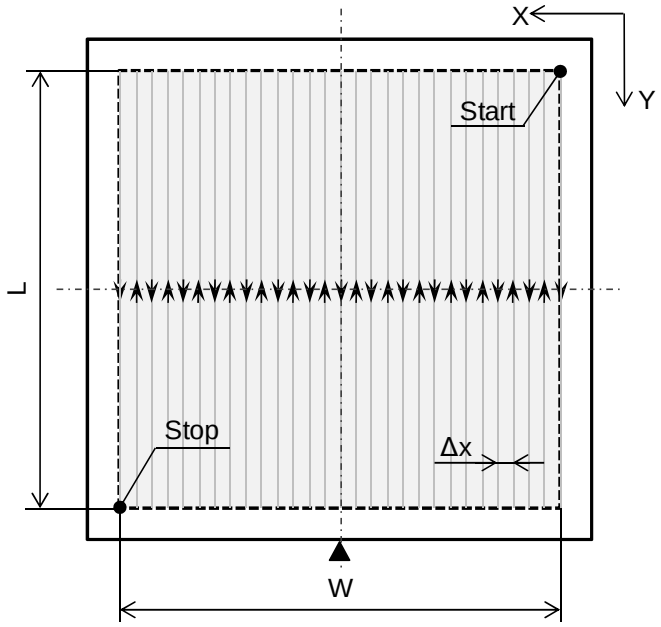

Figure 7.3: Illustration of laser beam raster scanning of fused silica plates. Shaded area surrounded by dashed square indicates the laser-irradiated area (LIA). The black triangle is a marker which indicates the laser beam movement.

Following laser treatment, the shape of the glass plates was measured using the Proscan 1000 profilometer. The samples were gripped in the Proscan sample holder as shown in Figure 7.4. The glass plates were measured with a 100 µm spatial resolution in both scanning directions. Data processing was carried out with the aid of Matlab (Mathworks, USA), in order to determine the extent of the laser-induced deformations of fused silica plates.

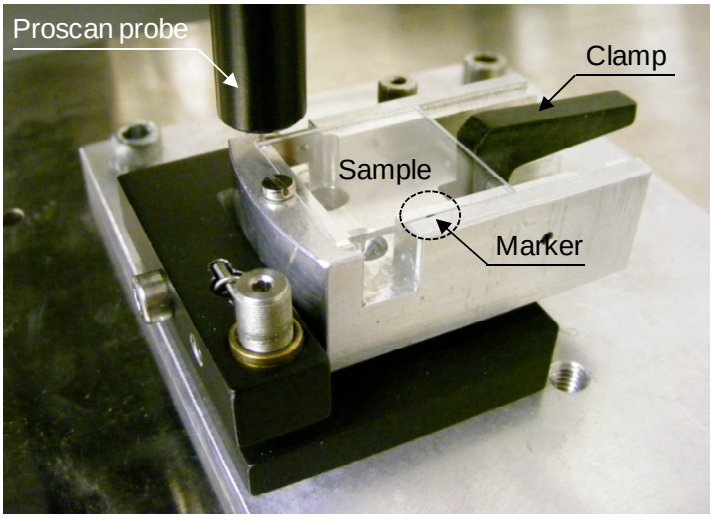

Figure 7.4: Sample holder used in Proscan 1000 profilometer.

Figure 7.5 shows a typical surface profile of the 25.4 mm square fused silica plate, measured before and after CO_2 laser treatment. Prior to laser treatment, the plates were nearly flat. The small surface distortions, which can be seen in Figure 7.5 (a), were possibly caused by the clamp which had been used in the Proscan sample holder (see Figure 7.4). Following laser treatment, the glass plates were always curved towards the laser-irradiated side, as can be seen in Figure 7.5 (b).

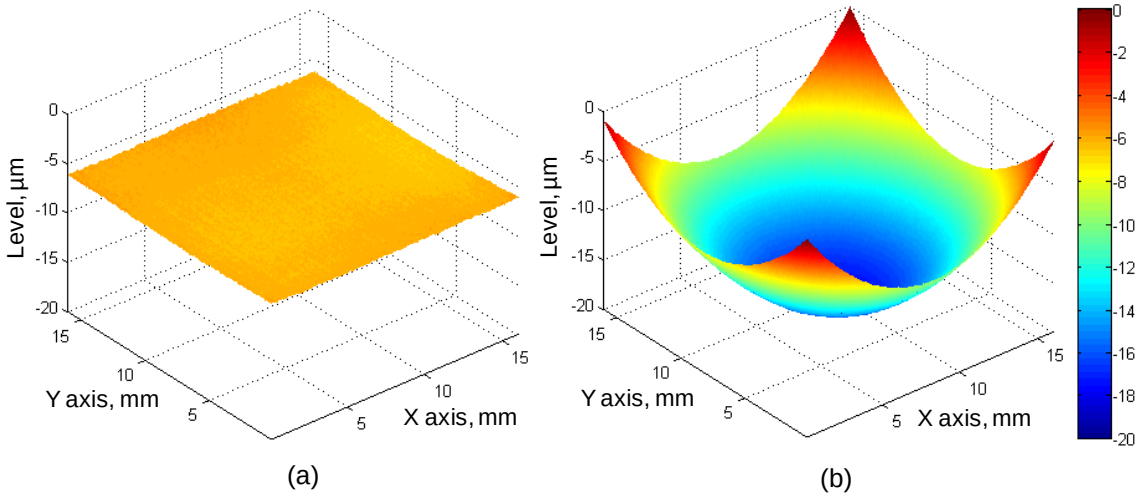

Figure 7.5: Surface profile of a 1 mm thick fused silica plate: (a) as-manufactured and (b) after laser polishing at a laser power of 8.46 W. Polishing was performed by using an approximately 1 mm diameter laser beam moved with a speed of 5 mm/s. Raster pitch (Δx) was 10 µm. Coordinates are consistent with Figure 7.3.

To evaluate the extent of the laser-induced distortions in the quantitative sense, the principle curvatures of the measured surface profiles were determined. This was achieved by calculating the coefficients of a second-order polynomial function that had been found to be a good representation of the surface profiles of the laser-curved plates. The second-order polynomial function, *f(x, y)*, was given by:

$$f(x,y) = b_0 + b_1 \cdot x + b_2 \cdot y + b_3 \cdot x^2 + b_4 \cdot x \cdot y + b_5 \cdot y^2 \tag{7.1}$$

where the b coefficients were computed using a nonlinear least-squares method, following the approach of Kumar and Shunmugam [141]. The principle curvatures, C_1 and C_2, for the point at which the function *f(x, y)* is minimal were calculated as follows:

$$C_1 = b_3 + b_5 + \sqrt{(b_5 - b_3)^2 + {b_4}^2} \tag{7.2}$$

$$C_2 = b_3 + b_5 - \sqrt{(b_5 - b_3)^2 + {b_4}^2} \tag{7.3}$$

The angles, θ_1 and θ_2, between the principle curvatures and the X axis were given by:

$$\theta_1 = atan\left(q + \sqrt{q^2 + 1}\right) \tag{7.4}$$

$$\theta_2 = atan\left(q - \sqrt{q^2 + 1}\right) \tag{7.5}$$

where the parameter q is equal to $(b_5 - b_3) / b_4$. The principles curvatures and angles are illustrated in Figure 7.6, whilst the derivation of equations from (7.2) to (7.5) is provided in the Appendix.

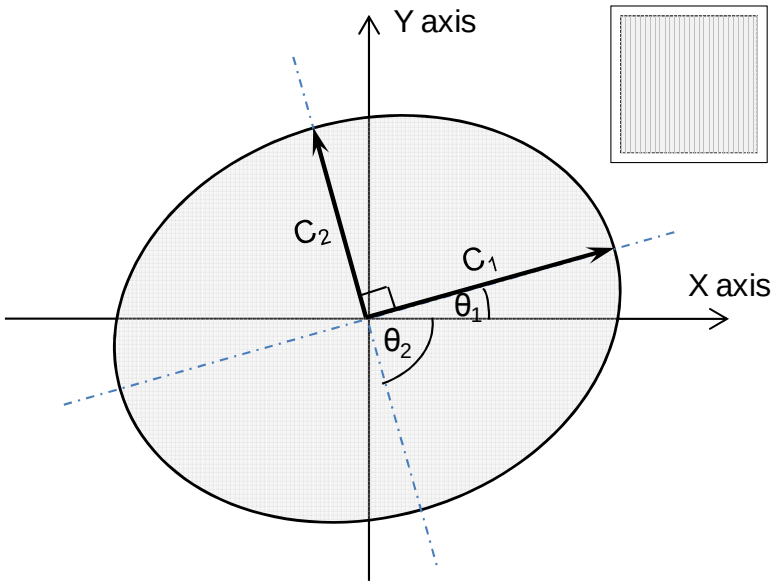

Figure 7.6: Illustration of the principal curvatures and the angle θ_1 and θ_2. The ellipse indicates a contour of deformation of the laser-irradiated plate.

As will be shown in the following subsections, the θ_1 and θ_2 angles of the laser-curved plates are small. This means that the curvatures along in the raster-progress direction (X-axis) and the laser-beam movement direction (Y axis) are represented directly by the values of the principle curvatures (C_1 and C_2).

7.3.2 Laser power dependence of the magnitude of silica sample distortions

In this section, the aim is to study the influence of the laser power on the magnitude of distortions of 1 mm thick fused silica plates. Since polishing of micro-optics may be carried out using different values of laser power, depending on the required degree of surface roughness (surface relaxation) of the component, it is highly desirable to know the relationship between the extent of sample distortions generated by CO_2 laser polishing and the laser power used.

In the experiment, CO_2 laser polishing was performed on three 1 mm thick samples. The laser-irradiated area (LIA) was 22 mm square (see Figure 7.3). Each sample was treated with a range of different laser power values, given as follows: 7.18, 7.94, and 8.46 W. The choice of these laser power values was not random since these values represent three different regimes of CO_2 laser polishing. At a laser power of 7.18 W, the glass surface is slightly melted. Although this value of laser power is too low to smooth effectively the rough surface of a CO_2 laser-cut micro-optical component, it is sufficient to provide a short-distance relaxation of the etched steps, as already shown in Section 4.4.1. The laser power of 7.94 W, in turn, produces an approximately 200 µm melt spot at the glass surface. As reported by Nowak *et al.* [3], this melt spot can reduce significantly the degree of the surface roughness characterized by a spatial period lower than 50 µm. A laser power of approximately 7.94 W is representative of polishing regimes for CO_2 laser-cut micro-optical components and it can be applied for relaxing the 200 nm height etched steps over an approximately 30 µm distance, as already shown in Section 4.7. Finally, the laser power of 8.46 W was chosen for these experiments because this value of laser power is closes to the upper limit of the CO_2 laser polishing window, as shown in Section 5.2. At this value of laser power, it is most likely that the distortions are the largest.

Table 7.1 shows the principle curvatures (C_1 and C_2) and the θ_1 angle calculated for the glass plates treated at different values of laser power. The principle curvatures and angle were achieved by averaging results of two measurements. The first measurement was performed for a sample gripped in the Proscan sample holder, as shown in Figure 7.4. The second measurement, in turn, was performed for a sample rotated 90 degrees with regard to the sample position of the first measurement. Such operation aimed to reduce an error in the evaluation of the principle curvatures, because the clamping system used in the sample holder introduced some additional

bending of the glass plates along the scanning direction. It was found experimentally that the clamp caused an approximately 5% increase of the principle curvatures. Finally, the θ_1 angle measured for samples treated at different laser power levels did not exceed 10 degrees. This means that the curvatures along the X and Y axes were comparable in value to the principle curvatures, C_1 and C_2, respectively.

Table 7.1: Calculated mean values of C_1, C_2, and θ_1 for 1 mm thick samples treated at different values of laser power.

Sample name	Laser power, W	Principle curvatures		Angle θ_1, deg
		C_1, 1/m	C_2, 1/m	
S1.0_22x22_8.46	8.46	0.30	0.25	- 6.4
S1.0_22x22_7.94	7.94	0.28	0.23	- 0.3
S1.0_22x22_7.18	7.18	0.20	0.18	- 8.7

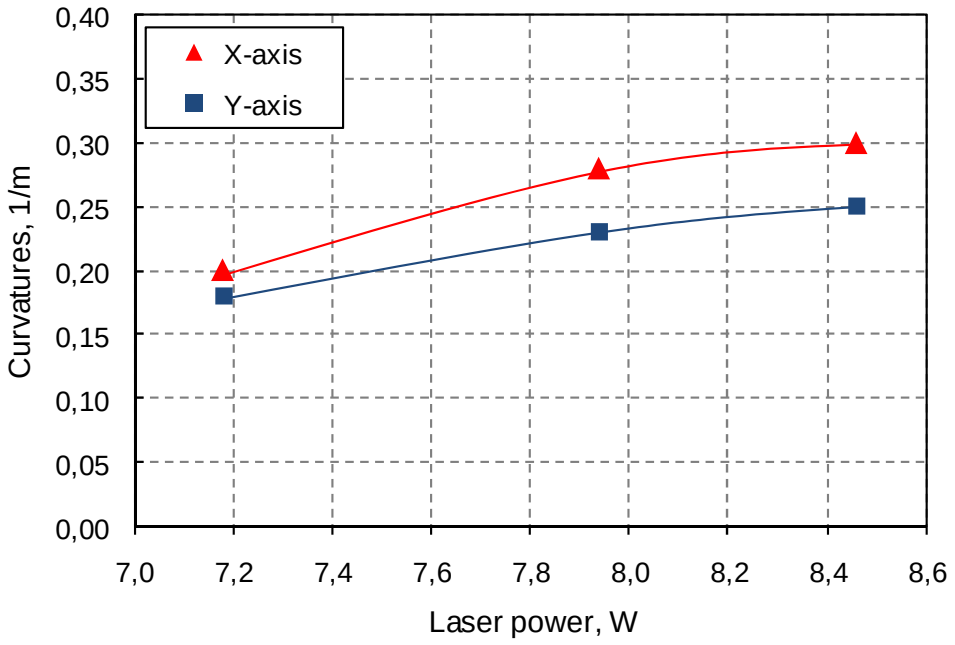

Figure 7.7: Curvatures along the raster-progress direction (X-axis) and the laser-beam movement direction (Y-axis) measured for the 1 mm thick samples treated at different laser powers. The laser-irradiated area was 22 mm long and 22 mm wide.

Based on the results shown in Figure 7.7, it can be concluded that an increase of laser power causes larger distortions of the glass plates. The larger curvatures are related to the fact that a higher laser power delivered to the glass surface produces more heat in the material. This heat, in turn, causes a larger temperature gradient along the glass thickness, increasing the effective depth of the stressed layer and consequently producing greater forces which are converted into a bending moment when the glass is rapidly cooled down. This explanation is consistent with the temperature gradient mechanism covered in Section 7.2.

As can be seen in Figure 7.7, curvatures along the raster-progress direction (X-axis) are more pronounced than those measured along the laser beam scanning direction (Y-axis). There are three potential reasons which may cause the asymmetry in bending of the glass plates. They are as follows:

a) the laser-induced stress anisotropy
b) the asymmetry of the (effective) laser-irradiated area
c) the influence of the geometry of the laser-untreated area

Since the fused silica plate was raster scanned using a relatively small laser beam (significantly smaller than the total laser-treated area), it is very likely that stress produced within the laser-irradiated area is anisotropic. This explanation, however, is difficult to prove because of the issues raised below.

As determined earlier by Mendez [10], the surface temperature produced by a moving laser beam does not immediately reach the steady state along the laser beam scanning direction. Based on the results of Mendez, it is known that a 1 mm diameter laser beam moved along a line track with a 5 mm/s speed generates a steady temperature at the surface of fused silica after a 1 mm distance from the laser scan origin. This means that in reality the laser-affected area used in the experiments was about 20 mm long rather than 22 mm, as stated at the beginning of this section. Since less glass was involved in the tension along the Y-axis, the bending was naturally less pronounced in this direction.

Finally, it must be noted that the laser-irradiated areas were surrounded by the laser-untreated frames of the glass (see Figure 7.3). As will be shown in the next section, the size and geometry of these frames have a significant influence on the final curvature of the laser-treated plates.

7.3.3 Influence of the geometry of laser-irradiated area on the magnitude of distortions of fused silica plates

When the surface of fused silica micro-optics is required to be polished using a CO_2 laser beam, usually the polishing process is carried out locally at the glass surface to save time. In this section, the interest is to determine the variation in the magnitude of distortions of fused silica plates, when the laser-treated area is varied in shape.

In this experiment, three 1 mm thick fused silica plates were treated at a fixed laser power of 8.46 W. The laser-irradiated area (LIA) of each sample was different, as can be seen in Figure 7.8. The LIAs were symmetric regarding to the centre of a plate.

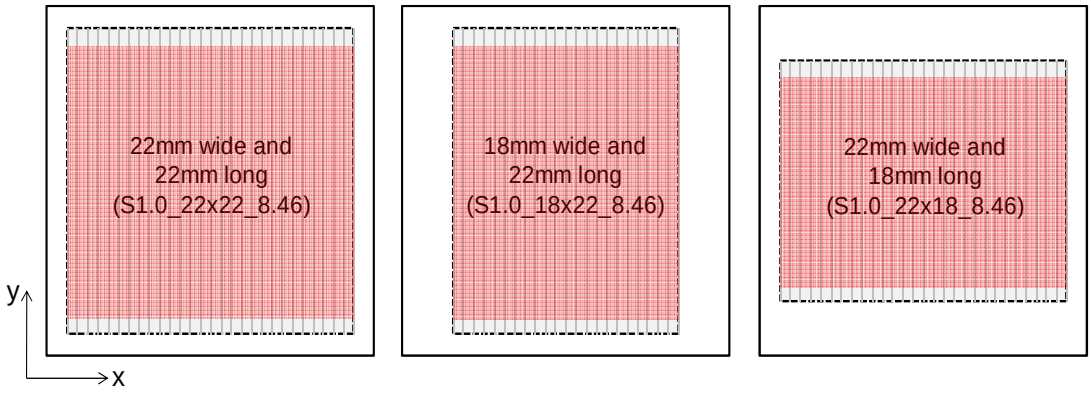

Figure 7.8: Geometry of the laser-irradiated area (LIA) of samples treated at a laser power of 8.46 W. The red areas indicate regions of the steady temperature reached on the glass surface.

The principle curvatures and the θ_1 angle determined for the samples with different geometry of the LIA are listed in Table 7.2. The procedure applied for calculating C_1, C_2, and θ_1 was the same as that described in the previous experiment.

Table 7.2: Calculated average values of C_1, C_2, and θ_1 for samples with different geometry of the laser-irradiated area (LIA).

Sample name	LIA		Principle curvatures		Angle θ_1, deg
	W, mm	L, mm	C_1, 1/m	C_2, 1/m	
S1.0_22x22_8.46	22	22	0.30	0.25	- 6.4
S1.0_18x22_8.46	18	22	0.33	0.24	- 1.1
S1.0_22x18_8.46	22	18	0.27	0.33	+ 3.3

The curvatures of the glass plates measured along the X and Y directions as a function of the geometry of the laser-irradiated area (LIA) are shown in Figure 7.9. Based on these results, it can be concluded that a 1 mm thick plate made of fused silica can be bent equally in both directions when the laser-irradiated area is approximately 19.6 mm long (L) and 22 mm wide (W) – see the intersection of two trend lines below.

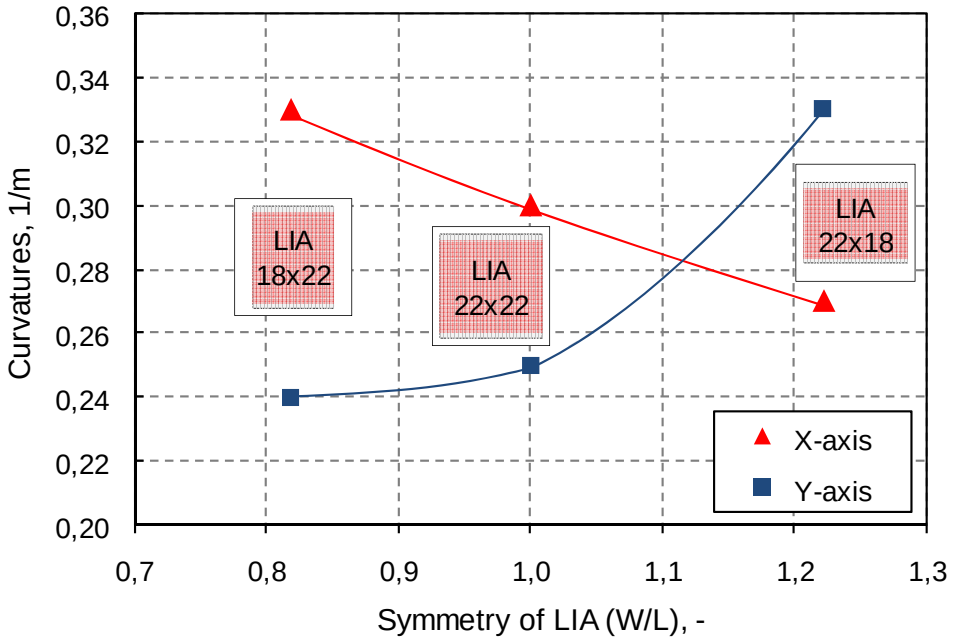

Figure 7.9: Influence of the geometry of the laser-irradiated area (LIA) on the curvatures of the 1 mm thick fused silica plates along the laser-scan direction (Y-axis) and the raster-progress direction (X-axis). Samples were treated at a laser power of 8.46 W.

Generally, the results presented in Figure 7.9 were found to be unusual due to the fact that the trend lines intersected when W/L ≈ 1.12. Based on the explanation given in Section 7.3.2 that a smaller curvature along the Y-axis results from the 2 mm shorter laser-treatment distance of the glass surface in this direction, there was an expectation that equal curvatures for the LIA symmetry of about 0.91 (W/L) would be achieved. Since this effect was not observed, it can be concluded that either laser-induced stress at the glass surface is anisotropic or the laser-untreated area (LUA) of the glass surface interacts with the laser-irradiated area (LIA) as shown in Figure 7.10, resulting in the appearance of the asymmetry in bending of the plates. Generally, the laser-untreated area acts on the middle section of the glass (LIA) like an elastic frame that resists the bending.

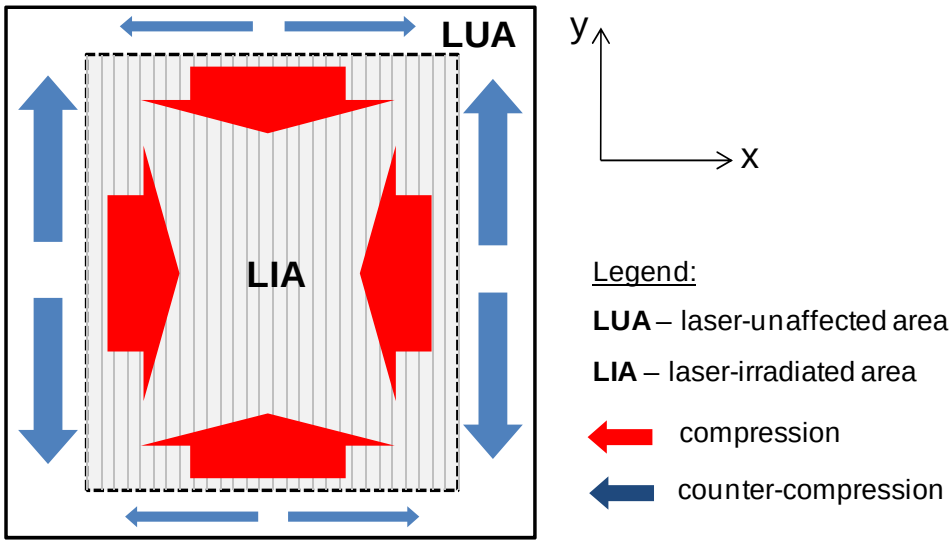

Figure 7.10: Illustration of laser-induced stresses in the curved-plates.

Although the illustration shown in Figure 7.10 seems to explain quite clearly the bending mechanism of glass plates with an unequal symmetry of the LIA, more study needs to be done in the future to confirm this theory. One of the options is to create a heat transfer model using, for instance, the COMSOL® Multiphysics package. In the future, it is also highly recommended that the experiment described in this section should be repeated, but with the difference that the laser-unaffected area is physically removed following laser treatment. It is believed that this experiment may provide an answer on the question whether the surface stress produced by a moving laser beam is anisotropic or isotropic.

7.3.4 Influence of the glass thickness on the magnitude of distortions of fused silica plates

The aim of the experiments described in this section is to determine the magnitude of laser-induced distortions of fused silica plates which are characterized by a different thickness. For this purpose, four 25.4 mm square samples with the thickness of 0.254, 0.5, 1.0, and 1.5 mm were used. The samples were treated at a fixed laser power of 7.94 W. The LIA was 22 mm wide and 22 mm long. The principle curvatures (C_1 and C_2) and the θ_1 angle measured for each sample are listed in Table 7.3.

Table 7.3: Calculated average values of C_1, C_2, and θ_1 for samples with different thickness.

Sample name	Thickness, mm	Principle curvatures		Angle θ_1, deg
		C_1, 1/m	C_2, 1/m	
S1.5_22x22_7.94	1.5	0.13	0.12	- 5.7
S1.0_22x22_7.94	1	0.28	0.23	- 0.3
S0.5_22x22_7.94	0.5	1.25	0.74	- 1.2
S0.25_22x22_7.94	0.254	-	-	-

The absence of results for the 0.254 mm thick sample is caused by the fact that this plate cracked during laser treatment. Material cracking appeared in the middle section of the laser-irradiated area, as can be seen in Figure 7.11. Broken pieces of the glass were found to be significantly curved near the cracked region.

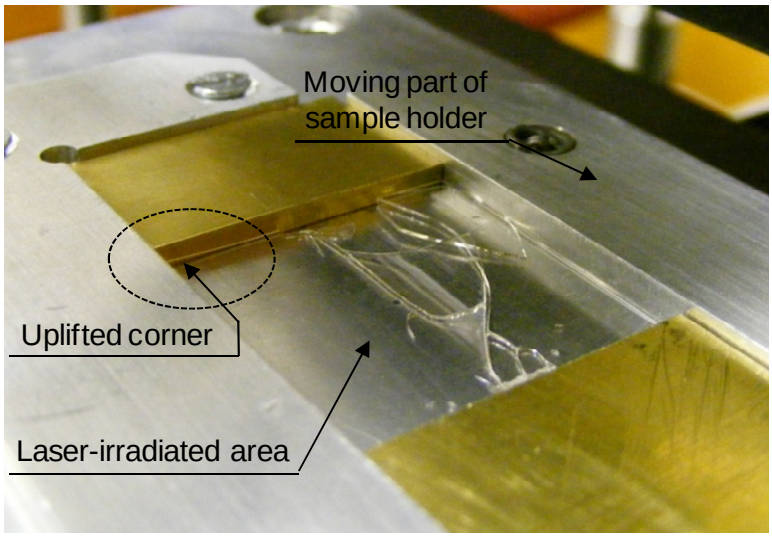

Figure 7.11: Fused silica plate with a thickness of 0.254 mm just after fracture.

The X and Y curvatures indicated for the glass plates with thicknesses of 0.5, 1.0, and 1.5 mm are presented in Figure 7.12. Based on these results, it can be concluded that bending is more pronounced in thinner fused silica plates. This is possibly related to the fact that thinner glass plates are less rigid, and thus they can be bent more easily.

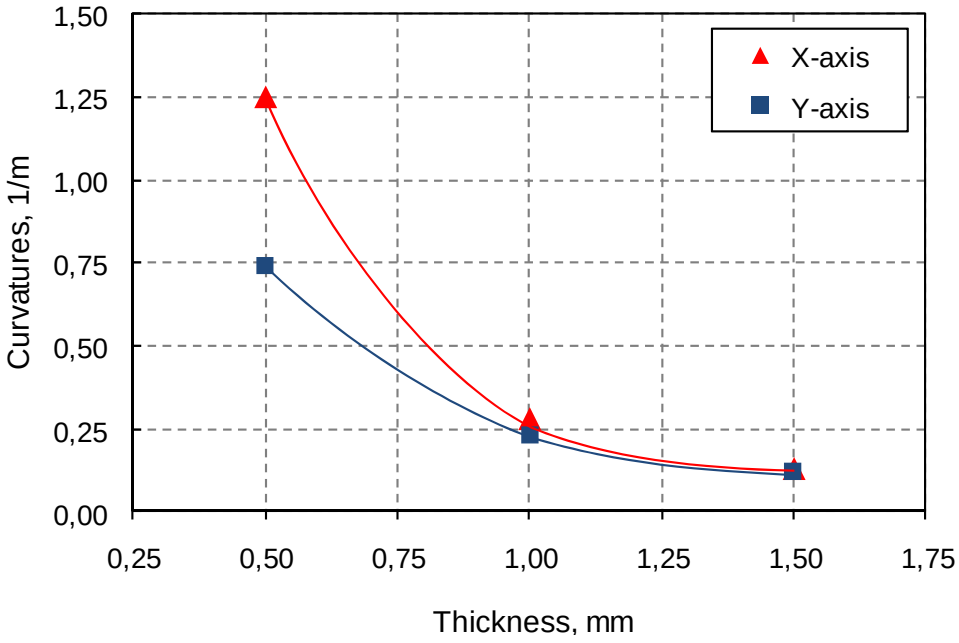

Figure 7.12: Influence of the glass thickness on the curvature of glass plates treated at a laser power of 7.94 W. The LIA of all samples was 22 mm long and 22 mm wide.

Finally, the results presented in Figure 7.12 show that thinner samples have a tendency for the curvature to be more pronounced in the raster-scan progress direction (X-axis). The curvature ratio (C_x/C_y) was measured to be about 1.7 for the 0.5 mm thick sample. Based on the results gained so far in this chapter, it can be concluded that this directional bending is caused by either the stress anisotropy or the mechanical forces coming from the moving part of the sample holder (see Figure 7.11). Since thinner plates are less rigid by nature, forces coming from the clamp are sufficient to squeeze a thin glass sample during laser treatment, thus the laser-induced bending becomes more pronounced in one direction.

7.4 Estimation of the magnitude of the laser-induced surface stress in fused silica plates based on the experimental results

The aim of this section is to estimate, based on the experimental results presented in Sections 7.3.2 - 7.3.4, the magnitude of the stress which is apparent in the laser-curved fused silica samples. Generally, the calculations carried out in this section provide an estimate of the stress induced by CO_2 laser polishing.

7.4.1 Stoney's equation

Based on background information given in Section 7.2, the CO_2 laser-curved fused silica plate can be considered as a two-layer plate with a total thickness of *d*. The top layer of the plate represents a layer that bends the whole plate towards the laser-irradiated region, as can be seen in Figure 7.13. The stress acting in this layer can be estimated by using Stoney's equation modified with Atkinson's correction factor, as found in [142].

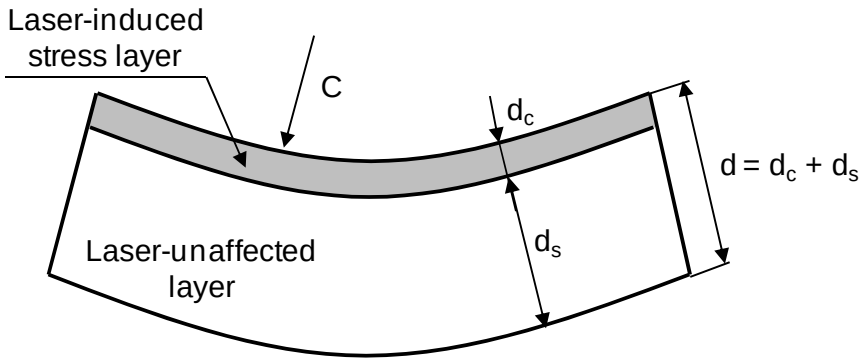

Figure 7.13: Illustration of the laser-curved glass plate.

Generally, Stoney's equation has been – and still is – extensively used to evaluate the biaxial macro-stress, σ, acting in a coating deposited on thick substrates [142-144]. The original form of Stoney's equation derived for a nickel-deposited steel beam (the one dimensional case) is given by [144]:

$$\sigma = \frac{E\, {d_s}^2\, C}{6\,(1-\upsilon)\, d_c} \tag{7.6}$$

where E is Young modulus, υ is Poisson's ratio, C is the curvature, whereas d_s and d_c are the thicknesses of a substrate and a coating, respectively. Since Stoney's equation is valid only when the thickness ratio (d_c / d_s) is smaller than 0.1 [142], equation (7.6) cannot be used directly to estimate the value of the laser-induced stress layer in fused silica unless a corrective factor in this formula is applied. As will be shown in Section 7.4.2, the thickness ratio (d_c / d_s) of the laser-curved glass plates possibly varies in the range of 0.1 to 0.35, and thus Stoney's equation must be multiplied by the correction factor (δ_{At}) introduced by Atkinson (equation (7.7)), as suggested by Klein [142].

$$\delta_{At} = \frac{d_s}{d_c \left(1 + \frac{d_s}{d_c}\right)} \tag{7.7}$$

The Atkinson's correction factor allows the surface stress to be estimated with an error smaller than 5% even if the d_c / d_s ratio is as high as 0.4. Including the fact that glass plates were bent differently in both directions following the laser treatment (see Sections 7.3.2 - 7.3.4), Stoney's equation must be transformed into the two dimensional case. As derived by Schwarzer and Richter in [145], Stoney's equation for a bi-directionally curved plate is given as follows:

$$\sigma_x = \frac{E\, {d_s}^3 \left(C_x + \upsilon\, C_y\right)}{6\,(1-\upsilon^2)\, {d_c}^2 \left(1 + \frac{d_s}{d_c}\right)} \tag{7.8}$$

$$\sigma_y = \frac{E\, {d_s}^3 \left(C_y + \upsilon\, C_x\right)}{6\,(1-\upsilon^2)\, {d_c}^2 \left(1 + \frac{d_s}{d_c}\right)} \tag{7.9}$$

where C_x and C_y are the curvatures indicated in the X and Y axes.

7.4.2 Depth of the laser-induced stress layer

To use equations (7.8) and (7.9) in order to estimate the magnitude of the laser-induced stress trapped in the fused silica samples (see the experiments described in Sections 7.3.2 - 7.3.4), it is necessary firstly to determine the depth of the laser-induced stress layer (see Figure 7.13). Since this depth (d_c) cannot be measured directly, its value has been estimated based on assumptions given below.

When fused silica is heated above the softening point (T_S = 1600°C), the highly-viscous zone persists in a zero stress state until the laser beam passes by and a rapid thermal quench ensues (see Section 7.2 for more details). Since the glass is quenched with a rate as high as 10^4°C/s (see Figure 7.14), the molten glass layer immediately contracts, producing visco-elasto-plastic deformations [137]. Therefore, it may be assumed that the tensile stress almost certainly occurs in the glass region which was laser-preheated to a temperature greater than 1600°C. To simplify calculations, it is assumed that the tensile stress is uniform in value across the d_c depth.

To estimate the depth of the layer under tensile strain (d_c), an equation describing the temperature distribution produced by a Gaussian laser source moving with a constant speed (u) along the Y axis is applied, as follows [60]:

$$T(x,y,z,t) = T_0 + \frac{2\,P_{av}}{\pi^{\frac{3}{2}}\,k}\int_0^d exp\left(-\frac{\left(y-ut+\frac{u\,\beta^2}{4\,\kappa}\right)^2+x^2}{\beta^2+w^2}-\frac{z^2}{\beta^2}\right)\frac{d\beta}{\beta^2+w^2} \qquad (7.10)$$

where T_0 is the initial temperature, P_{av} is average laser power, w is laser beam radius, k is thermal conductivity, and κ is thermal diffusivity of a solid. Although equation (7.10) is valid for the semi-infinite solid ($d = \infty$), it may also be used to evaluate a temperature distribution in fused silica because an absorption depth of this material at a 10.6 µm wavelength is sufficiently smaller than the thickness of the glass plates used in the experiments described in Section 7.3.2 - 7.3.4.

Figure 7.14 shows the transient temperature which occurs in a semi-infinite solid made of fused silica at the points of (0, 0, z), where z stands for the depth of the glass. The curves shown in Figure 7.14 were plotted based on equation (7.10), using material constants listed in Table 7.4. Calculations were carried out for the following laser powers (P_{av}): 7.18 W, 7.94 W, and 8.46 W. The negative value of time in Figure 7.14 indicates that a 1 mm diameter laser beam moved with a speed of 5 mm/s will reach the point (0, 0) in the time of t.

Table 7.4: List of material constants used to estimate a depth of the compressive stresses layer in fused silica samples, when treated at different values of laser power. These constants were used in equation (7.10).

Glass property	Value	Comments and references
Thermal conductivity, k	2.0 W/(m·K)	As suggested by [123].
Thermal diffusivity, κ	$7.27\cdot10^{-7}$ m^2/s	Based on equation (2.8).
Specific heat, C_p	1250 J/(kg·K)	Defined at T = 1630°C (suggested by [9])
Density, ρ	2.201 g/cm^3	Based on [30].

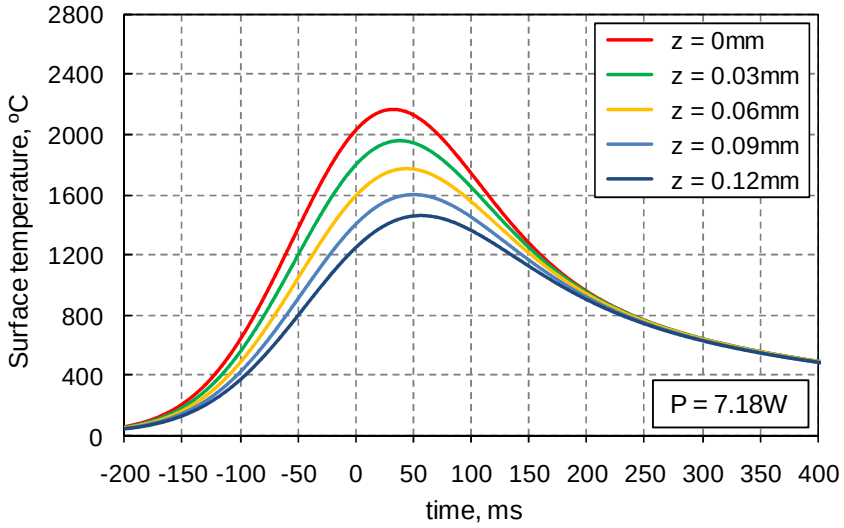

(a)

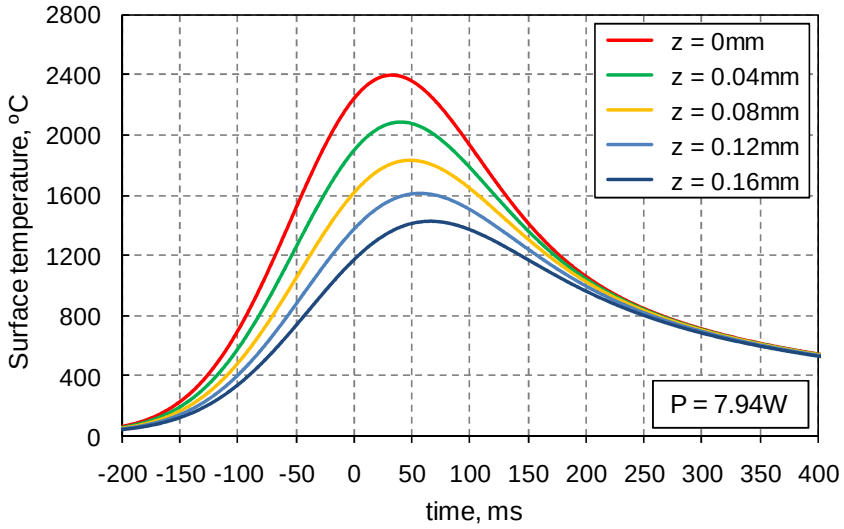

(b)

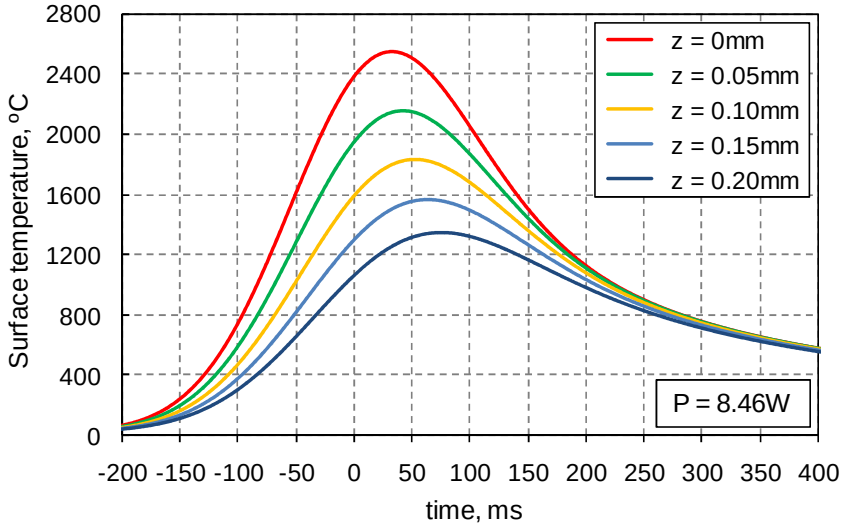

(c)

Figure 7.14: Transient temperature at the point of (0, 0, z), where z is a depth below the glass surface. Curves plotted at laser powers: (a) 7.18W, (b) 7.94 W and (c) 8.46 W, based on equation (7.10).

Based on the set of curves shown in Figure 7.14, it can be concluded that the depth of the laser-induced stress layer (d_c) is different for different values of laser power. The value of this depth was determined to be as follows: 90 µm at 7.18 W, 120 µm at 7.94 W, and finally 145 µm at 8.46 W.

7.4.3 Surface stress estimated for the laser-curved plates – final outcome

Based on the experimental results described in Sections 7.3.2 - 7.3.4 and using the estimates of the d_c value from Section 7.4.2, it is possible to evaluate the magnitude of the tensile surface stress occurring in the laser-curved fused silica samples using equations (7.8) and (7.9). As already mentioned in Section 7.4.2, the magnitude of the surface stress is calculated by assuming that this stress is produced above the isothermal layer established at the softening point of fused silica (T_S = 1600°C) and its value is constant over the d_c depth. In addition, it should be noted that Stoney's equation does not include the fact that the glass plates were only partially treated by a moving laser beam, and thus the stress value may be underestimated (more details later). Finally, it was assumed that the d_c value is associated with an absolute error of 20 µm.

Figure 7.15 shows the influence of laser power on the magnitude of stress produced at the surface of a 1 mm thick plate made of fused silica. Laser treatment conditions used for bending of these plates are detailed in Section 7.3.2.

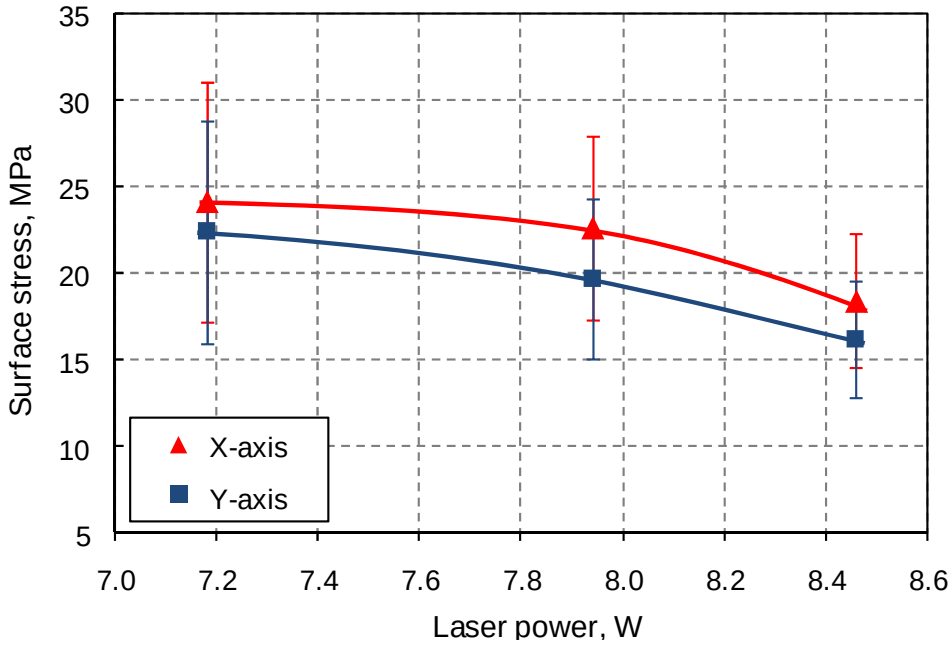

Figure 7.15: Influence of laser power on the magnitude of the apparent surface stress occurred in fused silica plates from Section 7.3.2. The LIA of each sample was 22×22 mm^2.

Based on the results shown in Figure 7.15, the magnitude of the surface stress produced in fused silica ranges from 16 to 24 MPa, depending on the value of laser power used. Generally, the surface stress decreases with increasing laser power, although the glass distortions are more pronounced (see Figure 7.7). This relationship between the stress and the laser power used links to the fact that a lower laser power produces a thinner tensile stress layer at the glass surface (d_c value decreases), as can be seen in Figure 7.14.

As shown in Figure 7.15, the surface stress is larger in value along the raster scan progress direction (Y-axis). As already mentioned in Section 7.3.2, this asymmetry in bending may result from the stress anisotropy, the asymmetry in the effective laser-irradiated area (LIA), and also the geometry of the laser-untreated area (LUA).

Figure 7.16 shows the influence of the laser-irradiated area (LIA) on the value of the stress generated at the surface of the 1 mm thick glass sample, when treated at a laser power of 8.46 W. Generally, the stress varies in the range of about 16 to 20.5 MPa. As can be seen in Figure 7.9, the stress value is consistent with the curvature of the laser-treated samples. This consistency results from the fact that the depth of the laser-induced stress layer (d_c) is fixed at constant laser power, thus the surface stress only depends on the magnitude of the distortions (see equations (7.8) and (7.9)).

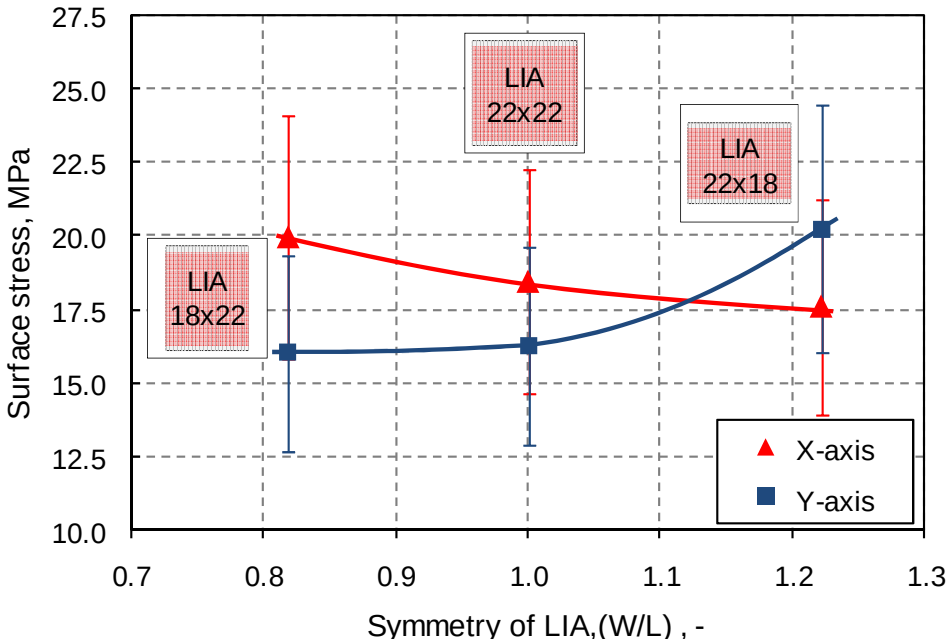

Figure 7.16: Influence of the laser-irradiated area (LIA) on the magnitude of the apparent surface stress. Result presented for a 1 mm thick fused silica plates, when treated at 8.46 W.

As already explained in Section 7.3.3, the laser-induced distortions of the glass plates result from the geometry of the laser-untreated area (LUA). Since the LUA is free of the laser-induced stress, it acts on the laser-irradiated area (LIA) like an elastic frame which partially resists bending of the glass. Generally, wider stripes of the laser-untreated area result in weaker bending of the whole plate towards the laser-treated site, as illustrated schematically in Figure 7.10.

Figure 7.17 shows the influence of the glass thickness on the extent of the laser-induced surface stress. Based on information provided in Section 7.3.4, the stress was produced at a fixed laser power of 7.94 W. The LIA was 22 × 22 mm^2.

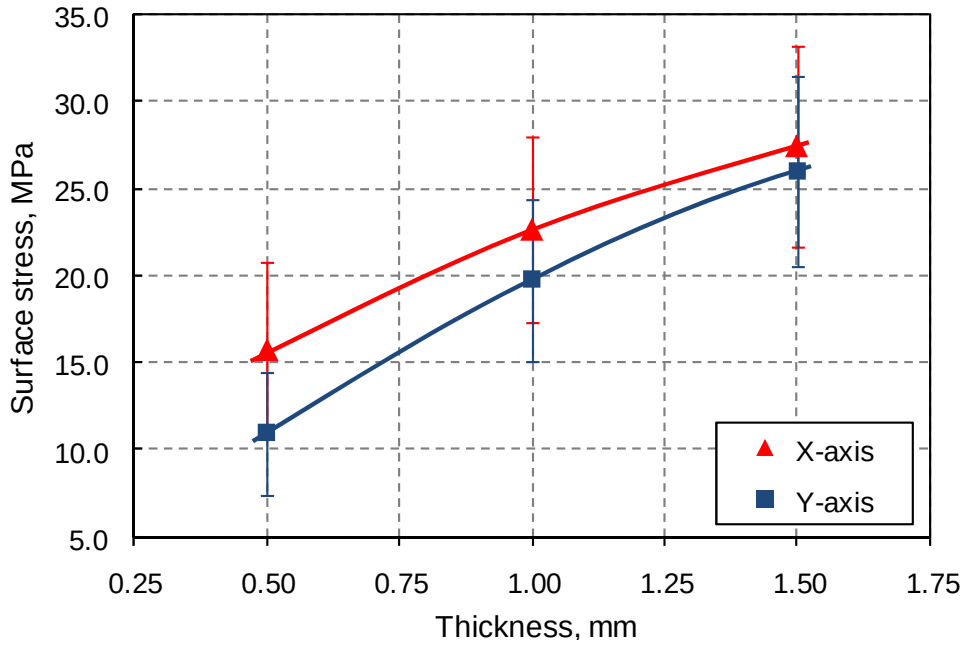

Figure 7.17: Influence of the glass thickness on the value of the laser-induced apparent surface stress. Results presented for the glass plates treated at P = 7.94 W. The laser-irradiated area was 22×22 mm^2.

Based on the results shown in Figure 7.17, it can be concluded that the magnitude of the laser-induced stress is smaller when the glass plate is thinner, although the thin plates have a tendency to bend more following laser treatment (see Figure 7.12). The lower value of the stress in thinner samples results from a higher ratio between the tensile and compressive stress layers (d_c and d_s, respectively). Here, however, it must be noted that the d_c depth estimated for a thin glass substrate was probably inaccurate since the d_c value was evaluated using formula (7.10) which is appropriate only for the

semi-infinite solid. Therefore, the results shown in Figure 7.17 for a 0.5 mm thick sample may not be valid.

7.4.4 Justification of the accuracy of use of Stoney's equation

The work covered in Section 7.4 allowed us to estimate the magnitude of the stress produced at the surface of fused silica, when treated using typical CO_2 laser polishing conditions (see Section 7.3). Based on the results presented in Section 7.4.3, the value of this stress ranges from 11 to 27.5 MPa, depending on the laser power used, the size and geometry of the laser-irradiated area, and also the glass thickness.

As already mentioned in Section 7.4.3, Stoney's equation assumes that the d_c layer is of infinite extent, and thus it does not take into account the laser-untreated area which most likely acts on the whole glass plate like an elastic frame that resists the bending. This means that the stress value determined using Stoney's equation was possibly slightly underestimated. This assumption, however, must be tested in the future using, for instance, the COMSOL® Multiphysics package. In the future, in addition it is necessary to perform an experiment which will tell us more about the influence of the laser-untreated area on the value of the laser-induced surface stress in fused silica plates.

Finally, it should be noted that the stress described by Stoney's equation is dependent on a depth of the tensile stress layer (d_c). Since this depth was not measured directly, there is a risk that its value may be different than the actual. This means that the laser-induced surface stress estimated in the previous section carries with it this possible error. By assuming that the d_c value was determined with 20µm accuracy, the stress described by Stoney's equation is associated with a relative error of about 20 - 30%. The error was calculated using a total differential equation.

7.5 Annealing of the laser-curved glass plates

The aim of this section is to determine whether the laser-induced surface stress in fused silica can be relieved by annealing. According to background information covered in Section 7.2, a CO_2 laser beam causes visco-elasto-plastic deformations of the glass plates, when the temperature at the surface exceeds the transformation point (approximately 1000°C for HPFS®7980 Corning). A likely consequence of this is that

the laser-curved fused silica plates achieved in Section 7.3 are permanently bent, and thus the laser-induced surface stress cannot be relieved by annealing.

Annealing was performed simultaneously for all laser-curved glass plates, using an annealing schedule shown in Section 5.2.3. The glass specimens were placed vertically between two ceramic combs, in the order as shown in Figure 7.18 (a). The notation of the glass plates shown in Figure 7.18 (a) is consistent with the sample name used in Tables 7.1 - 7.3. The first part of the notation (e.g. S1.0) stands for the glass thickness in millimetres, the second (e.g. 22×18) indicates the size of the LIA, and the last segment stands for the laser power used in Watts (e.g. 7.94). To achieve a more stable ceramic construction, the glass plates were covered from the top by a ceramic plate and several ceramic blocks. The final shape of the ceramic construction placed inside a furnace (Cole-Parmer, USA) is shown in Figure 7.18 (b). Here, it should to be noted that there was no contact between the glass specimens and the top ceramic plate.

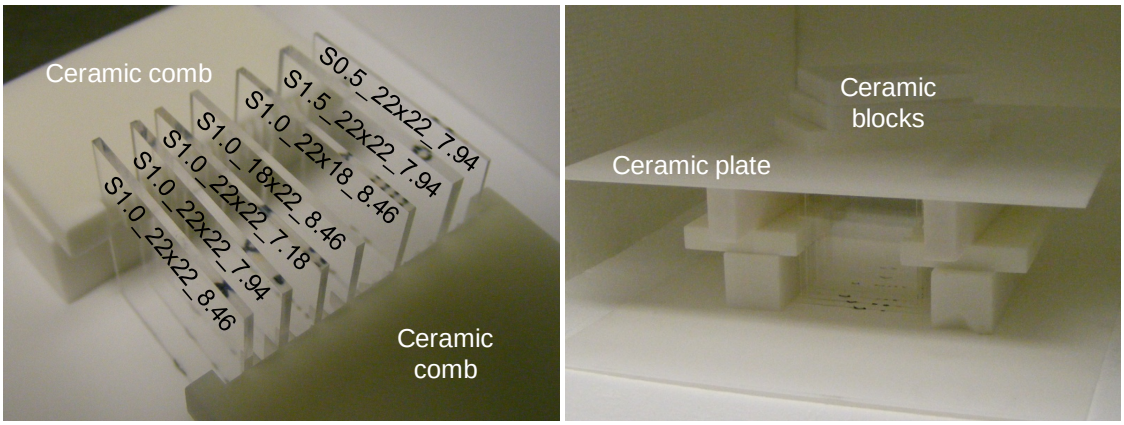

Figure 7.18: The way of placing the laser-curved samples in a furnace for annealing (reconstruction): (a) diagonal view of the samples placed between two ceramic combs and (b) ceramic construction.

3D surface profiles of the annealed laser-curved specimens are presented in Figure 7.19. Based on these results, it can be concluded that the fused silica plates are significantly less distorted following annealing. Three of seven glass plates became fairly flat (see Figure 7.19 (d) and (e)), one had a small saddle shape (see Figure 7.19 (f)), two were noticeable twisted (see Figure 7.19 (b) and (c)), and only one was curved, as shown in Figure 7.19 (a). The curvature in the last-mentioned sample, however, was oriented in the opposite direction to the initial state.

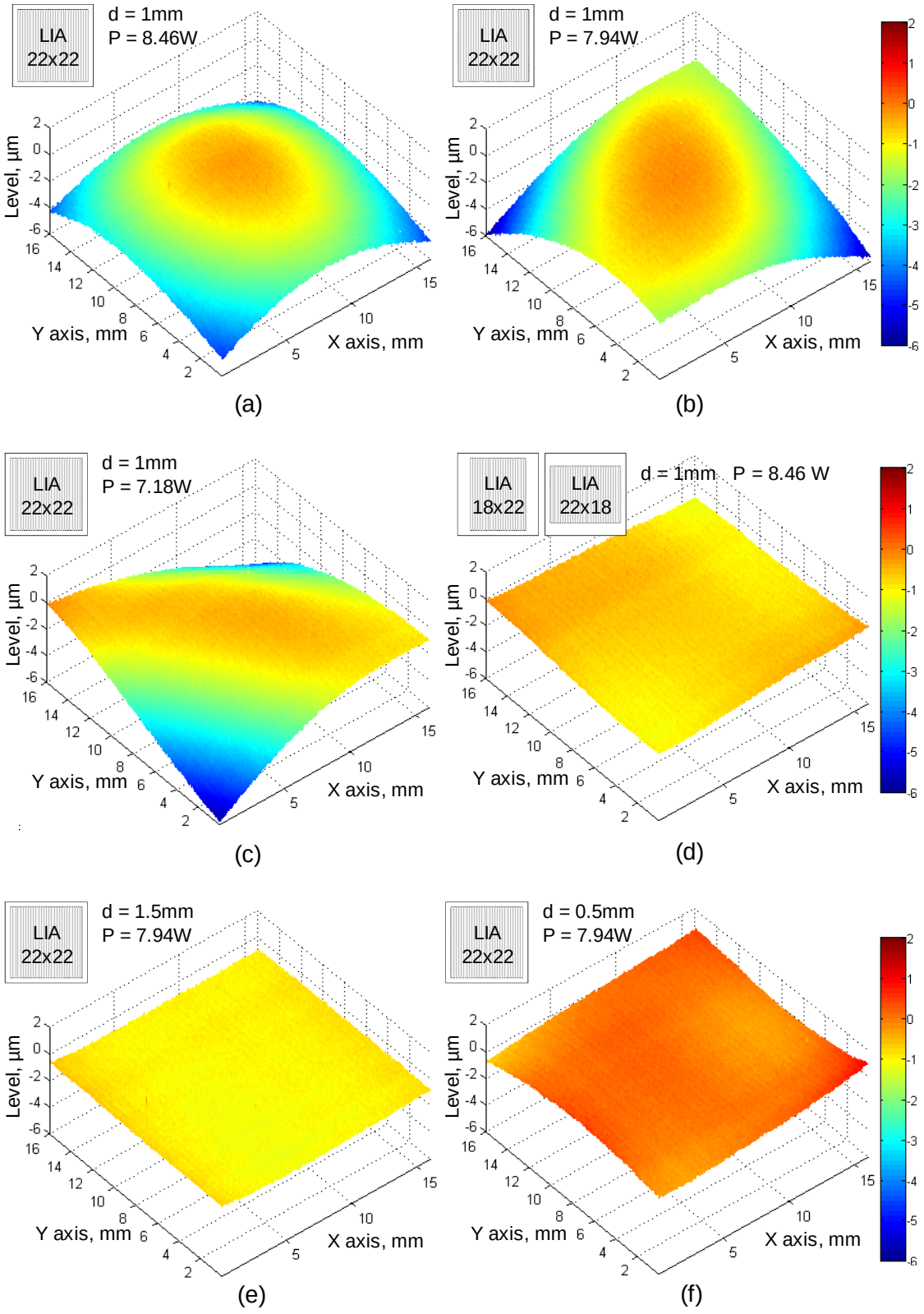

Figure 7.19: Shape of the laser-curved plates after annealing.

Following the localization of the specimens between two ceramic combs (see Figure 7.18 (a)), one may notice that only samples from the left edge were deflected whilst the rest were fairly flat after annealing. There a few potential hypotheses which could explain this effect. The first concerns a non-uniform temperature distribution in the furnace cell. This, however, seems to be unlikely because the furnace cell was tightly closed. The second assumption concerns the gravitational forces which could cause a distortion of the glass plates. This idea, however, generates another question: why deflections in a 1 mm thick plate are (not always) larger than those observed in a 0.5 mm thick sample although the thinner sample is less rigid? This question seems to eliminate the gravitational forces as a potential source of the distortions. The third conjecture, which is the most likely, concerns the case in which some samples were jammed between two ceramic combs during the building of the ceramic construction. This caused the laser-induced surface stress to be relieved by annealing; whilst the stress produced by jamming was trapped in samples when they were cooled to room temperature. Following this assumption, it can be concluded that annealing of laser-machined optics and micro-optics must be carried out very carefully since it is very easy to introduce accidently deformations when the glass is annealed in a furnace.

To summarize this section, the laser-curved plates became statistically flat following annealing. Based on the results shown in Figure 7.19, the surface distortions of four samples were smaller than 2 µm (peak-to-valley) over a 16 mm square area, whilst the others had deflections in the opposite direction to the initial state. As explained in the previous paragraph, the opposite deflections occurred due to careless annealing of the samples. Although some annealed samples were observed to be still deflected, nevertheless it can be concluded that the use of a suitable annealing regime can almost completely remove the laser-induced stress from the glass surface, making the plates flat again. Finally, flattening of the laser-curved samples by annealing seems to provide a positive outcome in terms of CO_2 laser polishing of fused silica micro-optical components. Based on the results shown in this section, it can be stated that micro-optics produced by CO_2 laser cutting and polishing are not affected by the laser-induced surface stress (distortions) if they are annealed.

7.6 Potential mechanism responsible for the creation of the surface stress in CO_2 laser-polished fused silica plates

As shown in Section 7.3, CO_2 laser beam raster scanning causes biaxial bending of 25.4 mm square plates made of fused silica. The plates are observed to be bent towards the incident laser beam. This bending indicates that the material is affected by surface stress. As explained by many researchers, e.g. [68, 137, 139], surface stress is produced by plastic and elastic deformations, which occur in the material when it is rapidly cooled down following the laser treatment. Since the plastic deformations are permanent by their very nature, it seems to suggest that laser-curved glass plates cannot be made flat again. However, the results shown in Section 7.5 reveal that this is actually not true since the glass plates become flat, when annealed using the temperature schedule shown in Figure 5.5. Therefore, there is a presumption that the biaxial bending is produced by a mechanism which is able to restore the initial (flat) shape of the glass plate, when the material is cooled down slowly from 1100°C to room temperature.

Based on the results presented in Chapter 5 and Section 7.5, it is reasonable to assume that laser-induced bending of the plates made of fused silica is strongly associated with the fictive temperature mechanism (detailed in Section 5.2). Since the laser-irradiated area (LIA) is characterized by an elevated fictive temperature, due to rapid cooling of the glass when the laser beam passes by, this laser-treated region undergoes densification. Since the densification causes a change in the glass volume (the localized material shrinkage), the LIA interacts with the surroundings (e.g. with the laser-untreated frame of the glass) and as a result, the whole glass plate is bent biaxially towards the laser-irradiated surface. On the other hand, when the glass is annealed using the temperature schedule shown in Figure 5.5, the high fictive temperature within the LIA is significantly reduced, and thus the whole sample becomes flat again due to lack of the density difference between the LIA and the surroundings.

Although the explanation above differs from that provided in Section 7.2, and thus some researchers may have doubts in terms of the truth of this concept, nevertheless this explanation seems to be fully consistent with the experimental results presented in this chapter.

7.7 Summary and conclusions

The aim of the work covered in this chapter was to determine the extent and character of surface stresses produced in fused silica plates, when treated by a moving laser beam using laser processing conditions which are typically used for CO_2 laser polishing of optics and micro-optics.

Based on the results shown in Section 7.3, it can be concluded that CO_2 laser beam raster scanning produces sufficient distortions of fused silica plates. Generally, the laser-irradiated samples were observed to be curved biaxially towards the incident laser beam. The largest curvature (up to 1.25 m^{-1}) was achieved for a 0.5 mm thick sample, whilst material cracking was observed for a 0.254 mm thick sample. From this fact it can inferred that it is more difficult to perform CO_2 laser polishing if the workpiece is very thin. It is most likely that thin fused silica plates should be smoothed using lower values of laser power than usual (P < 8 W).

As shown in Section 7.4, the laser-induced surface stress in fused silica samples was estimated to be in the range of 11 to 27.5 MPa, depending on the value of laser power used, the geometry of the LIA, and also the glass thickness. The value of the stress was estimated using Stoney's equation modified by the use of Atkinson's factor, assuming that the tensile stressed layer is uniform in value along the depth and is produced above the isothermal layer, which was established at the softening point of fused silica (T_S = 1600°C). As already mentioned in Section 7.4.4, it is most likely that the laser-induced surface stress was under-estimated in value since Stoney's equation does not take into account the fact that the laser-irradiated area was surrounded by the laser-untreated frame. As shown in Figure 7.13, this frame acts on the glass plate like an elastic solid which resists bending of the glass, and thus it is expected that the degree of curvature of the laser-treated plates would be larger if the laser-untreated frame had been removed following the laser treatment.

Based on the results presented in Section 7.5, it can be concluded that the laser-induced surface stress in fused silica plates is impermanent but the glass annealing process must to be carried out very carefully. Since most of the samples (> 60%) were observed to be flat following annealing, it is reasonable to affirm that the residual surface stress induced by CO_2 laser polishing results from the increase of fictive temperature within the laser-irradiated area. This means that the conventional

explanation of the appearance of stresses at the glass surface when treated by a moving laser beam (see Section 7.2 for more details) is not entirely correct in terms of fused silica since it does not take into account the fictive temperature effect.

Finally, the results covered in this chapter did not confirm whether the stress produced by laser beam raster scanning is anisotropic or isotropic. Although the curvatures of the glass plates were observed to be different in value along the X and Y directions, thereby suggesting that this stress is anisotropic, this interpretation may not be entirely correct since the asymmetry in bending may also result from the geometry of the laser-irradiated area and the size of the laser-untreated frame, as found in Section 7.3.3. This suggests that more experiments related to the surface stress induced by CO_2 laser polishing are required in the future.

Chapter 8
CO_2 laser machinability study of Borofloat®33 and lead-silicate glasses

8.1 Introduction

Currently, CO_2 laser-based techniques for the fabrication of refractive micro-optical components are mainly restricted to the use of fused silica substrates. The aim of this chapter is to explore new types of glasses, from the borosilicate and lead-silicate glass family, which show some promise of suitability for the manufacture of micro-optics using a CO_2 laser beam.

The glasses investigated in this chapter were not chosen randomly. As already mentioned in Chapter 5, Borofloat®33 glass as a representative of non-alkaline-earth borosilicate glass family was selected because the optical properties of this material (e.g. refractive index and transmission spectrum) are similar to those of fused silica but its cost is lower, making this glass interesting from the economical point of view. Moreover, the thermal expansion coefficient of Borofloat®33 is the lowest of all commercially-available non-silica optical glasses. The *CTE* of this glass is only 5 times larger than that of silica. This means that Borofloat®33 may be a good candidate for efficient and "non-cracking" CO_2 laser machining (micro-cutting) at room temperature. Finally, preliminary results on single line laser scanning of Borofloat®33 described in

Section 5.3 have shown that this material may be successfully polished using a CO_2 laser beam.

The second group of glasses investigated in this chapter are lead-silicate glasses, which are characterized by high refractive index, as already mentioned in Section 2.3.2. These glasses were chosen for study because effective laser machining of these materials may lead to the fabrication of refractive micro-optics with better optical properties. In comparison to fused silica, the high-refractive-index glass used as a workpiece will allow the production of micro-optical components with a shorter focal length, fewer aberrations, and possibly thinner substrates. All these properties, in turn, are key factors in making optical systems more compact.

From among tens of lead-silicate glasses available on the market, three of them were chosen to be studied. They are as follows: SF57®, LAFN7®, and N-SF66® (Schott AG, Germany). Based on the physical properties listed in Table 8.1, the refractive index of these glasses is higher than 1.7, whilst their *CTE* is at least twice that of Borofloat®33. This means that there is an increased risk of material cracking during laser treatment of these glasses.

Table 8.1: Physical properties of Borofloat®33 and lead silicate glasses studied in this chapter. Data are valid at room temperature, based on [26, 31].

Properties	Borofloat®33	Lead-silicate glasses		
		SF 57®	N-SF66®	LAFN7®
Refractive index, n	1.47	1.85	1.92	1.75
Density, ρ (g/cm^3)	2.2	5.51	4.00	4.38
CTE (ppm/K)	3.2	9.2	6.8	6.4
Thermal cond., k (W/m·K)	1.20	0.62	0.80	0.77
Specific heat, C_p (J/kg·K)	830	360	540	-
Annealing point, T_A (°C)	560	391	711	481
Softening point, T_S (°C)	820	519	806	573

Finally, it should be acknowledged that laser machining experiments on Borofloat®33 and lead-silicate glasses were carried out using facilities provided by PowerPhotonic Ltd., a high-tech spin-out company from Heriot-Watt University.

8.2 Experimental procedure

To provide fast and extensive information with regard to CO_2 laser machinability of glass in one processing step, the laser system described in Section 3.2 was programmed to generate a matrix of single-shot laser-irradiated sites at the glass surface. Laser-irradiated sites were produced by progressive increase of axial peak irradiance (peak power per unit area) along one axis and laser pulse duration in the other, thereby generating a characteristic pattern of "dots" or "craters" at the glass surface. Such a pattern is referred to as a calibration map [1].

Prior to laser treatment, the glass samples were carefully washed using isopropanol and wiped using lens tissues, in order to remove dust and residual contamination from the glass surface. The cleaning and laser processing were carried out in a cleanroom. The calibration maps were performed using a 50 µm diameter laser beam (measured at $1/e^2$ of its maximum intensity). The axial peak irradiance delivered to the samples (I_{ax}) was changed from 25 - 600 kW/cm^2 with a 25 kW/cm^2 step, whilst the laser pulse duration (PD) was varied from 25 to 100 µs with a 12.5 µs step. The separation distance between the laser-irradiated sites was chosen to be 200 µm, and thus the laser shots did not disturb the neighbouring sites. The calibration maps were generated at a 10.59 µm wavelength. Following laser treatment, the laser-irradiated sites were investigated using an optical microscope (Leica Microsystems, Germany) and a non-contact surface measurement instrument Proscan 1000 (Scantron Industrial Products Ltd, UK). The profilometer enabled the laser-irradiated sites to be measured with a 1 µm spatial resolution. To reduce the noise produced by Proscan, the surface profile data were processed in Matlab® using an averaging method (see Section 5.2.1 for more details).

8.3 Examination of Borofloat®33

This section is focused on a detailed examination of the laser-irradiated sites generated on the surface of Borofloat®33 glass. The aim of the work covered in this section is to determine potential CO_2 laser machining conditions for this material.

8.3.1 Qualitative analysis of laser-irradiated areas

Figure 8.1 shows a selected fragment of the calibration map performed for a 1.1 mm thick Borofloat®33 sample. This map was constructed from the separate micrographs which contained the laser irradiated sites that had been produced at constant values of axial irradiance. The images were taken using a ×5 zoom microscope objective. In order to enhance details in the laser-irradiated sites, the micrographs were additionally processes in MS PowerPoint using brightness, contrast, and colour adjusters.

Examination of the laser-irradiated sites with the aid of the optical microscope and the Proscan 1000 profilometer allowed four characteristic regions of the calibration map to be distinguished, as can be seen in Figure 8.1. They are as follows:

REGION I – in which no surface effect is observed at the glass surface.
REGION II – single laser pulse produces a bump.
REGION III – single laser pulse produces a clean crater surrounded by a bumpy rim.
REGION IV – single laser pulse produces a crater surrounded by a cracked rim.

Surface deformations located near the lower boundary of REGION II are observed to be in the form of dome-shaped bumps. As explained in Section 5.3.3, these bumps result from a local increase of fictive temperature within the laser-irradiated area and also are caused by the Marangoni effect. As found experimentally in Section 5.3, the dome-shaped bumps occur at the glass surface when the temperature exceeds 720°C.

Once the axial fluence (energy per unit area) is increased, the dome-shaped bumps reach a V-shaped dimple in the central region, as can be seen in Figure 8.2 (a). As explained in Section 5.3.6, the dimples are possibly produced by vaporization of Borofloat®33 because this material begins to evaporate at relatively low temperatures ($T \approx 1000$°C), as found in Section 5.3.6.

Clean craters without any fractures are produced at the surface of Borofloat®33 when the axial peak irradiance and laser pulse duration are in the range defined by the boundary of REGION III. Generally, this region defines potential laser machining conditions for this material. As can be seen in Figure 8.2 (b), a crater produced in REGION III has a smooth quasi-Gaussian-shaped profile. Since Borofloat®33 has a tendency to bulge, this crater has a small bulge in the middle and a quite pronounced bumpy rim. As discussed in Section 5.3.3, the central bulge and the bumpy rim result from the appearance of surface tension gradient at the glass surface and the increase of fictive temperature with the laser-affected area. It is quite likely that the bumpy rim can be partially removed by annealing, as suggested by the results of Section 5.3.5.

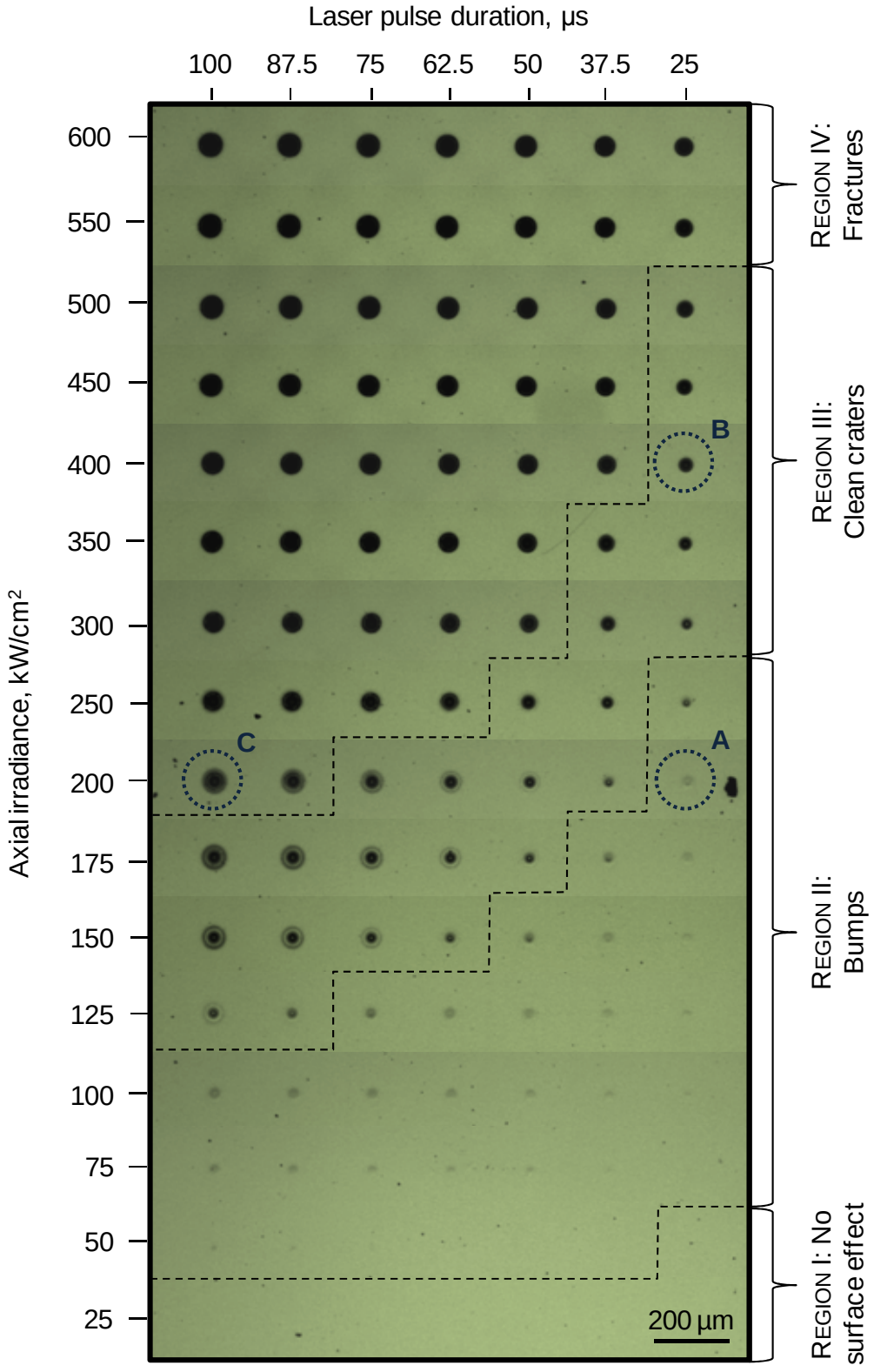

Figure 8.1: Calibration map carried out for Borofloat®33. The map was produced by using a 50 µm diameter laser beam. The dashed lines indicates characteristic region, whilst the dotted circles indicate the laser-irradiated areas which are enlarged in Figure 8.2.

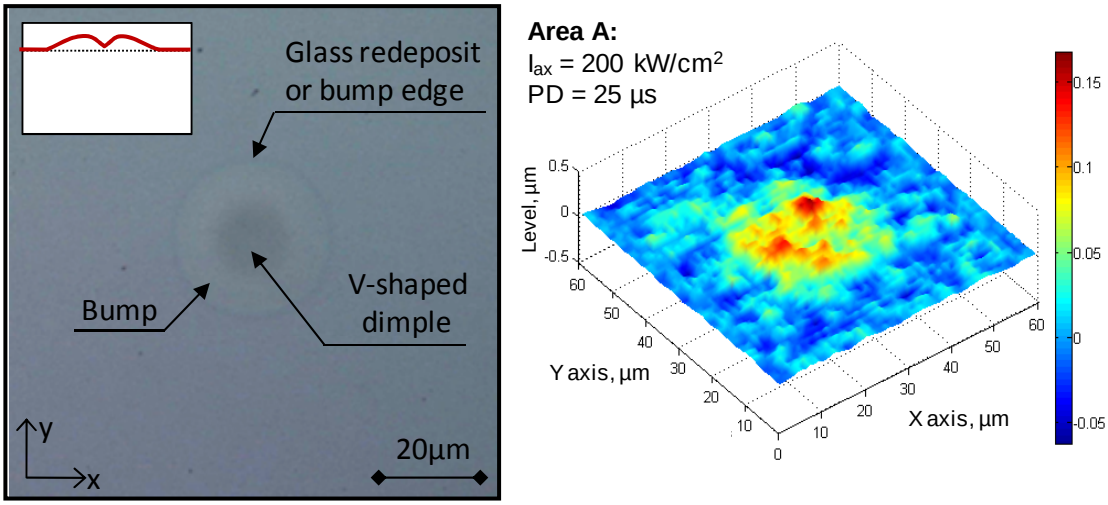

(a)

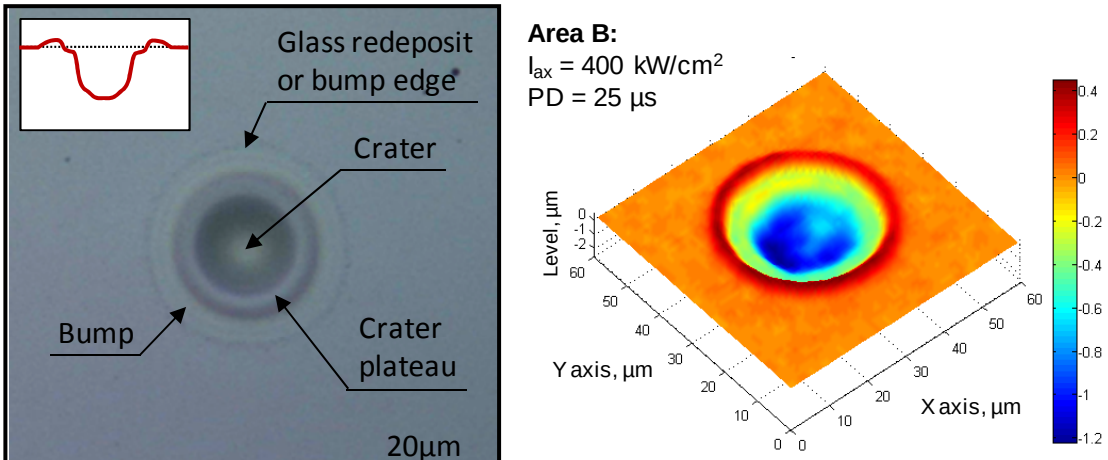

(b)

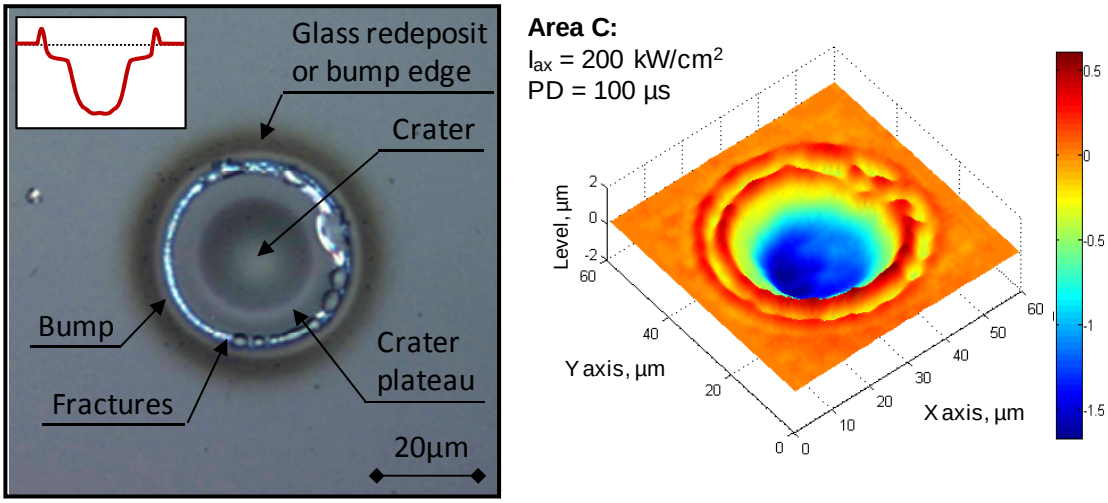

(c)

Figure 8.2: Microscope image and 3D surface profile of the laser-irradiated areas selected in Figure 8.1.

Based on the calibration map shown in Figure 8.1, the laser-irradiated sites are affected by cracking if the laser energy has a value within REGION IV. As shown in Figure 8.2 (c), fractures are apparent only inside the region of the bumpy rim. This means that stress within this region exceeded the fracture strength of Borofloat®33, the magnitude of which is not currently known. Here, it should be noted that fractures within the bumpy region were also observed in Borofloat®33, when treated by a moving CO_2 laser beam with a diameter of about 1 mm (see Section 5.3).

Finally, the laser-irradiated sites produced by short laser pulses were found to have less surface contaminants around the bumpy rim, as shown in Figure 8.3. This means that laser pulses as short as 25 µs seem to be optimal for laser micromachining of Borofloat®33.

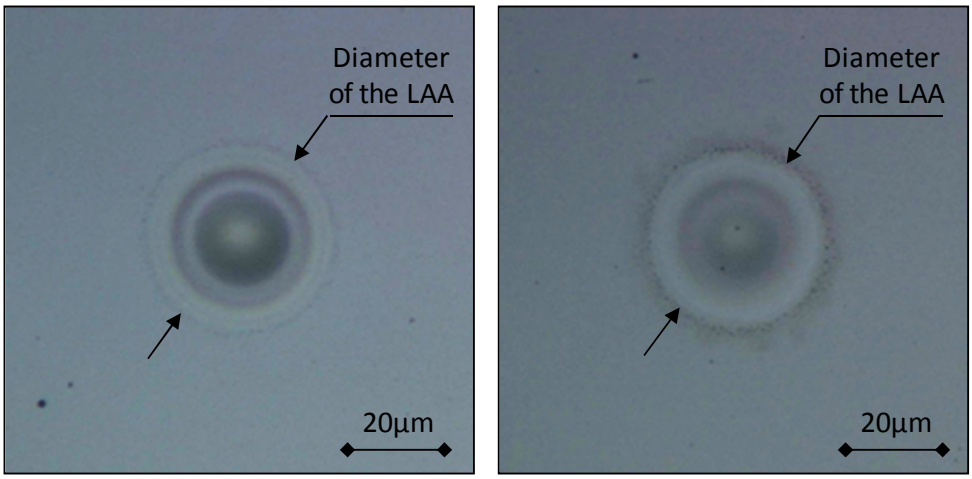

Figure 8.3: Micrographs of clean craters produced at: (a) 400 kW/cm^2 axial irradiance and 25 µs pulse duration and (b) 200 kW/cm^2 axial irradiance and 50 µs pulse duration. The LAA abbreviation stands for the laser-affected area.

8.3.2 Quantitative analysis of laser-irradiated areas

Based on the results shown in the previous section, Borofloat®33 seems to be a suitable candidate for CO_2 laser micromachining. Therefore, in this section the objective is to perform a quantitative analysis of the laser-irradiated sites depicted in Figure 8.1. Within this section, the following machining parameters are taken into account: the size of the laser-affected areas, the depth of the ablated craters, the height of the bumpy rims, and also the volumetric removal rate of the glass.

Figure 8.4 shows the diameter of the laser-affected area as a function of the axial peak irradiance for four values of laser pulse duration: 25, 50, 75, and 100 µs. This measurement was carried out using an optical microscope equipped with a ×50 zoom objective. The laser-affected area (LAA) was measured up to the edge of the bumpy rim, as can be seen in Figure 8.3.

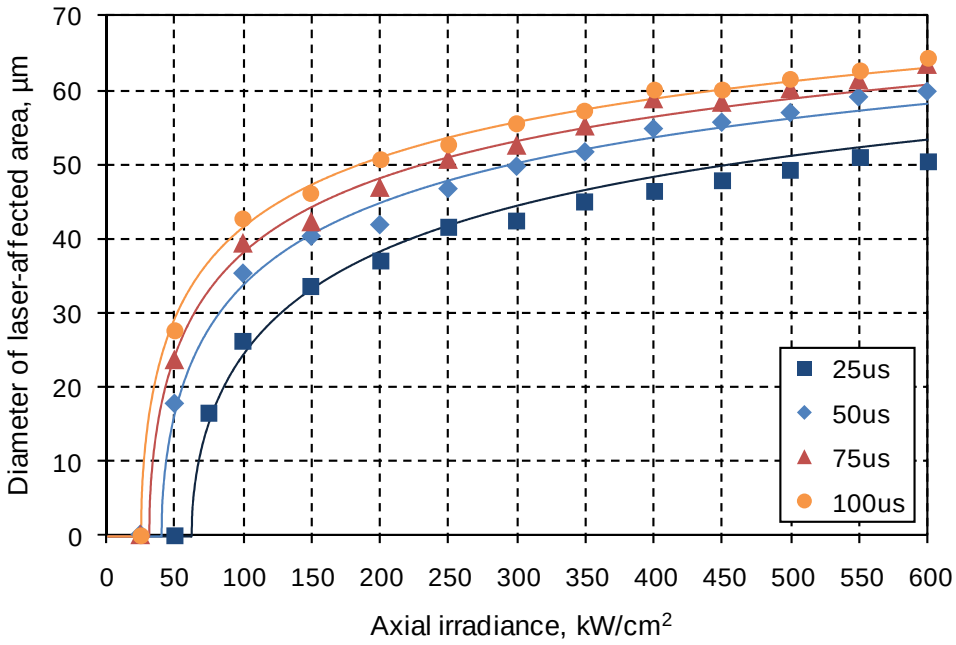

Figure 8.4: Diameter of the laser-affected area as a function of axial peak irradiance. Results presented for an about 50 µm diameter laser beam.

Based on the results presented in Figure 8.4, the laser-induced surface effect in Borofloat®33 begins to occur when the axial peak irradiance is in the range of 25 -70 kW/cm^2. This value is dependent on the value of the laser pulse width.

Figure 8.5 and Figure 8.6 show, respectively, the depth of the ablated craters and the height of the bumpy rims as a function of axial irradiance for four different values of laser pulse duration. These measurements were performed with the aid of the Proscan 1000 profilometer, utilizing the 3D surface profiles of the laser-irradiated sites, such as those shown in Figure 8.2. The height of the bumps was defined to be the maximum value within the 60 µm^2 scanned area which circumscribes the laser-induced deformation in the centre. The crater depth, in turn, corresponded to the difference in levels between the bumpy rim and the depression occurring within the laser-irradiated area.

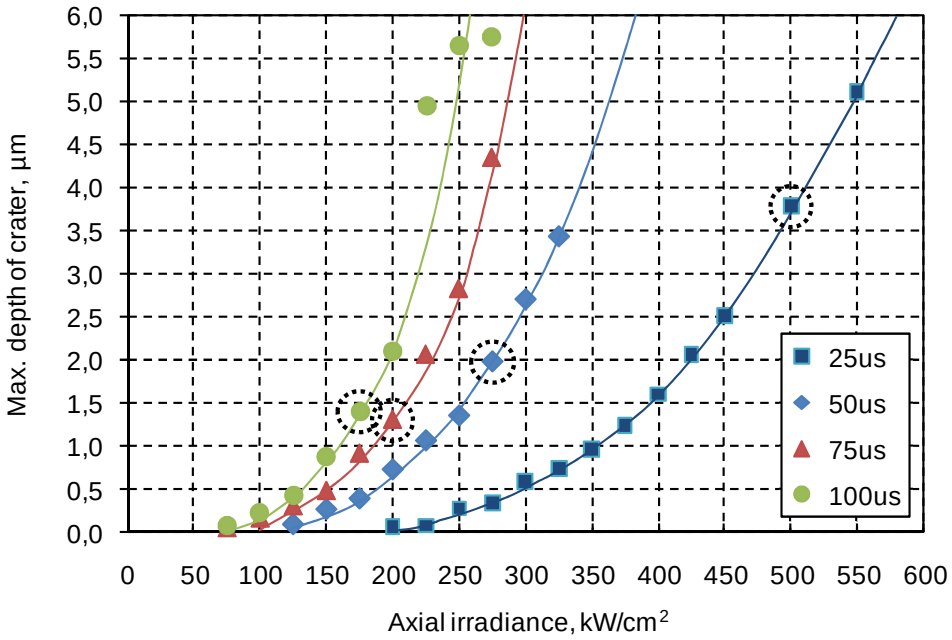

Figure 8.5: Depth of the craters as a function of the axial peak irradiance. Measurements were taken for four values of laser pulse duration: 25, 50, 75, and 100 µs. The points inside the dotted circle indicate the laser-irradiated areas above which the glass was affected by micro-cracking. Results presented for an about 50 µm diameter laser beam.

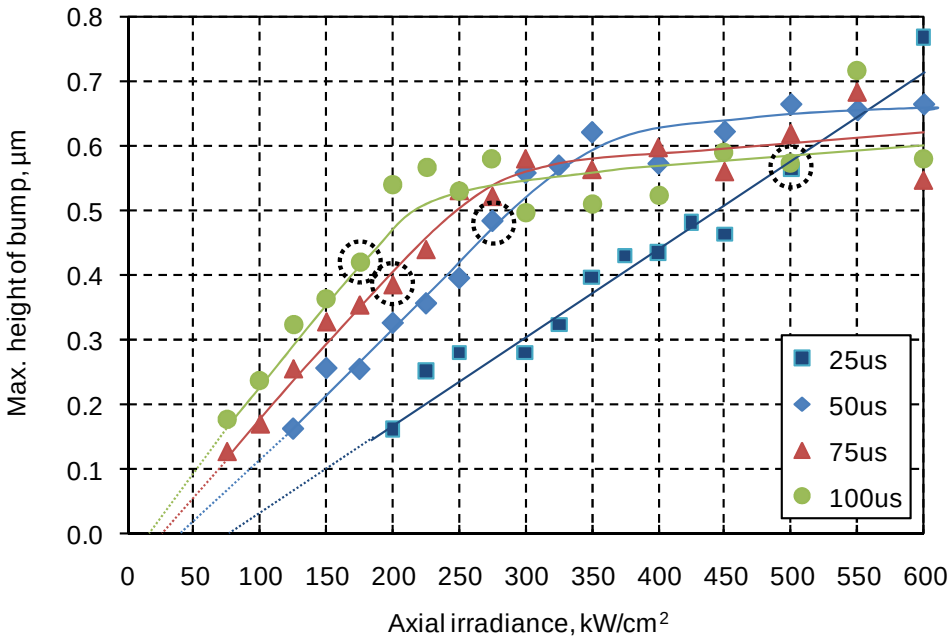

Figure 8.6: Maximum height of the bumpy rims as a function of axial peak irradiance. Measurements were taken for four values of laser pulse duration: 25, 50, 75, and 100 µs. The points inside the dotted circle indicate the laser-irradiated areas above which the glass was affected by micro-cracking. Results presented for an about 50 µm diameter laser beam.

Based on the results presented in Figure 8.5, it can be concluded that the widest machining range is achieved for the 25 µs long laser pulses. For this value of laser pulse duration, it was possible to produce clean craters as deep as 4 µm. Here, it should be noted that this depth is about 5 times smaller than that achievable in fused silica [146].

The results shown in Figure 8.6 reveal that the height of the bumpy rims increases linearly with increasing axial irradiance. This linear dependency, however, is only valid to the point at which fractures appear. Based on work reported by Bennett *et al.* [64], the linear growth of the bumps is caused by the local increase of fictive temperature within the laser-irradiated area. Since the elevated fictive temperature causes an increase in the glass volume, this region is almost certainly affected by the surface stress. Once the surface stress exceeds the fracture strength, the bumpy rim undergoes tearing and visible cracks become apparent. Then, the growth rate of the bumpy rims is observed to be less pronounced, as can be seen in Figure 8.6.

Based on the 3D surface scans of the laser-irradiated sites (see Figure 8.2), it was also possible to determine a change in the volume of Borofloat®33, when affected by a single laser pulse. The volumetric change (ΔV) within the laser-irradiated area was calculated using the following formula:

$$\Delta V = \sum_{i=1}^{M} \left(\sum_{j=1}^{N} \Delta x \cdot \Delta y \cdot f(i \cdot \Delta x, j \cdot \Delta y) \right) \tag{8.1}$$

where M and N define a number of points measured along the X and Y axis, respectively, Δx and Δy correspond to the scan step in the specific direction, and the f function determines the value of the surface level at specific scan position.

The change in the glass volume as a function of axial peak irradiance for four different values of laser pulse duration is shown in Figure 8.7. The volume change is expressed in picolitre units. Since the profilometer cannot measure steep sidewalls (acceptance angle less than 20 degrees), the glass volume was not determined for the laser-irradiated sites containing deep craters.

According to the results shown in Figure 8.7, the highest machining rate for this glass is achieved for the laser pulses as short as 25 µs. Such short laser pulses can remove approximately 1.5 picolitres of the glass per pulse, without material cracking.

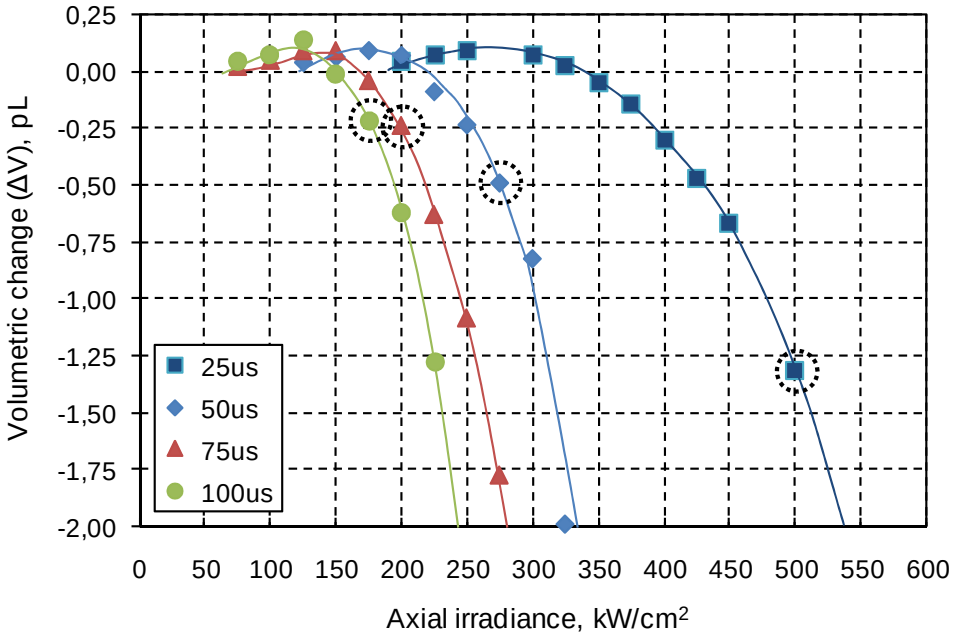

Figure 8.7: Volumetric change (in picolitres units) vs. axial peak irradiance. Measurement was taken for four values of laser pulse duration: 25, 50, 75, and 100 µs. Points inside the dotted circles indicate the laser-irradiated areas above which the glass was affected by micro-cracking. Results presented for an about 50 µm diameter laser beam.

Based on work reported in [9, 61, 108], it can be concluded that the removal rate of Borofloat®33 is an order of magnitude lower than that achieved in fused silica. The higher removal rate in fused silica is related to the fact that this glass is significantly more resistant to material cracking than Borofloat®33, and thus it can be machined at higher values of axial fluence (energy per unit area). In addition, fused silica does not undergo positive bumping, which most likely is responsible for the appearance of fractures (see results of Section 5.3).

Although Borofloat®33 is a less efficient material for CO_2 laser processing, in comparison to fused silica, the machining rate of this glass is still significantly higher than that achieved by other laser-based machining techniques covered in Section 2.6. For instance, if we assume that Borofloat®33 is treated by CO_2 laser pulses repeated with a (say) 5 kHz frequency, the removal rate of this material can be as high as 30 µlitres per hour.

In conclusion, Borofloat®33 glass seems to be an attractive material for CO_2 laser micro-machining. It is believed that the promising results shown in this section will encourage researchers to continue work on this subject.

8.4 Investigation of lead-silicate glasses

This section presents preliminary results concerning CO_2 laser machinability of high refractive index glasses, such as SF57®, N-SF66®, and LAFN7® manufactured by Schott AG (Germany). The results are presented in the form of calibrations maps, which were performed according to the experimental procedure described in Section 8.2. The calibration maps and typical deformations generated on the surface of each glass are shown in Sections 8.4.1 - 8.4.3. Since the deformations were observed to be complex in shape, quantitative analysis of the laser-irradiated sites was limited.

8.4.1 SF57® glass

The calibration map performed for the SF57® glass is shown in Figure 8.8. Based on these results, it can be concluded that the threshold above which the glass surface undergoes deformations is lower than that determined for Borofloat®33. The lower surface damage threshold is related to the fact that SF57® glass has a softening point at a temperature of 519°C rather than 820°C (see Table 8.1).

Deformations observed at the surface of SF57® glass, when treated by a single laser pulse using a fixed value of axial irradiance (I_{ax} = 100 kW/cm^2) and different values of laser pulse duration, are shown in Figure 8.9. Based on these results, it can be concluded that SF57® glass responses differently to CO_2 laser radiation than Borofloat®33 when treated under similar laser machining conditions. Generally, these laser-irradiated areas are in the form of concentric bumpy rims, which develop when the glass surface is affected by longer laser pulses.

For the glass treated at high values of axial irradiance (see Figure 8.10), laser irradiated sites are observed to be in the form of either pools or craters containing a wheel-shaped pattern in the centre. Here, it should be noted that the craters are also surrounded by quite pronounced contamination coming from the glass vapour.

Based on the results shown in Figures 8.9 - 8.10, it can be concluded that SF57® glass most likely is not suitable for making micro-optics since this material undergoes strong texturing when treated by a CO_2 laser beam, using an axial irradiance between 25 and 600 kW/cm^2 and laser pulse widths in the range of 25 - 100 µs.

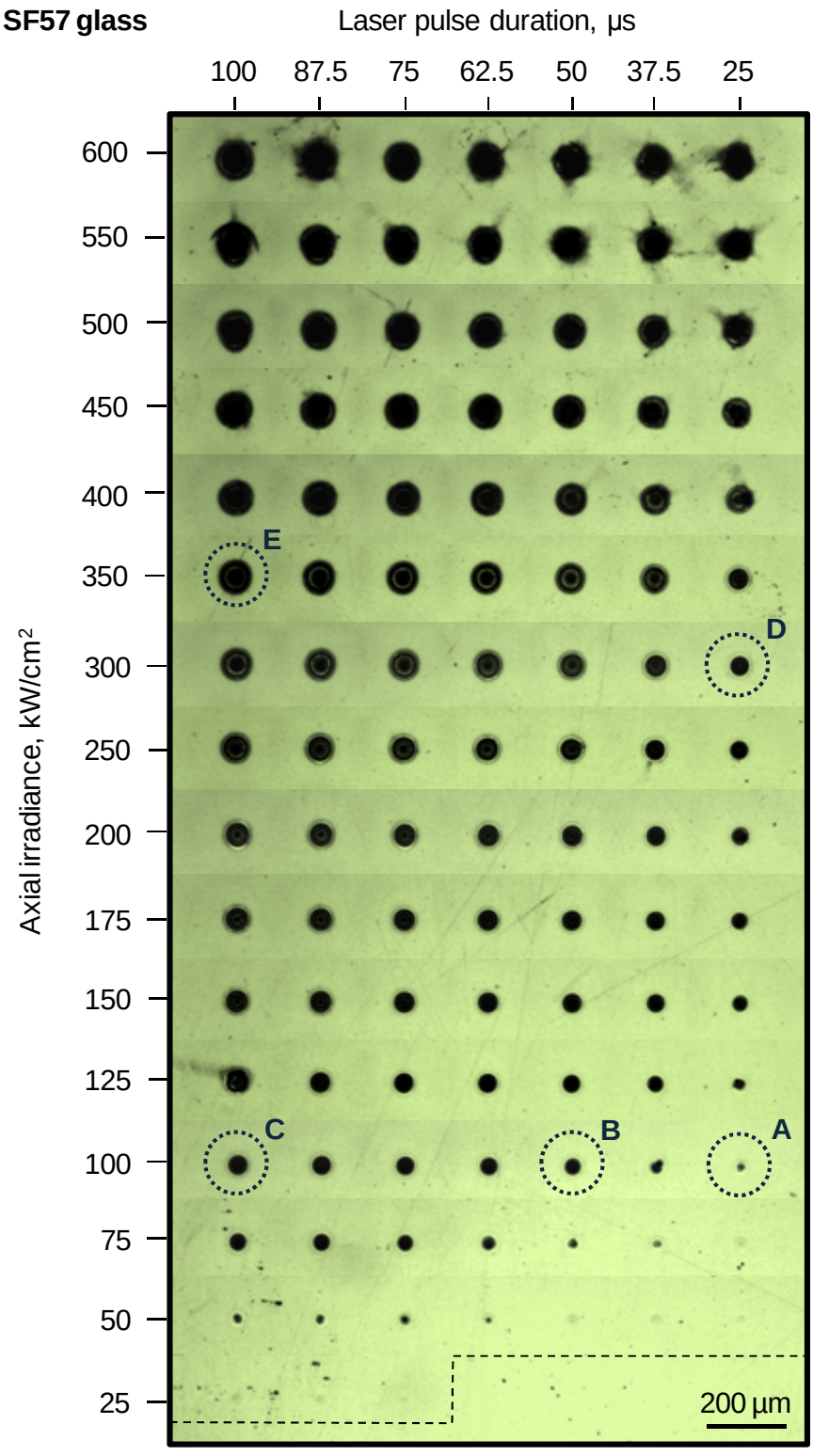

Figure 8.8: Calibration map generated for SF57® glass. The craters are produced by using a 50 µm diameter laser beam (measured at $1/e^2$ of its maximum intensity). Dashed line indicates the onset of surface effects, whilst the dotted circles indicate the laser-irradiated areas which are enlarged in Figure 8.9 and Figure 8.10.

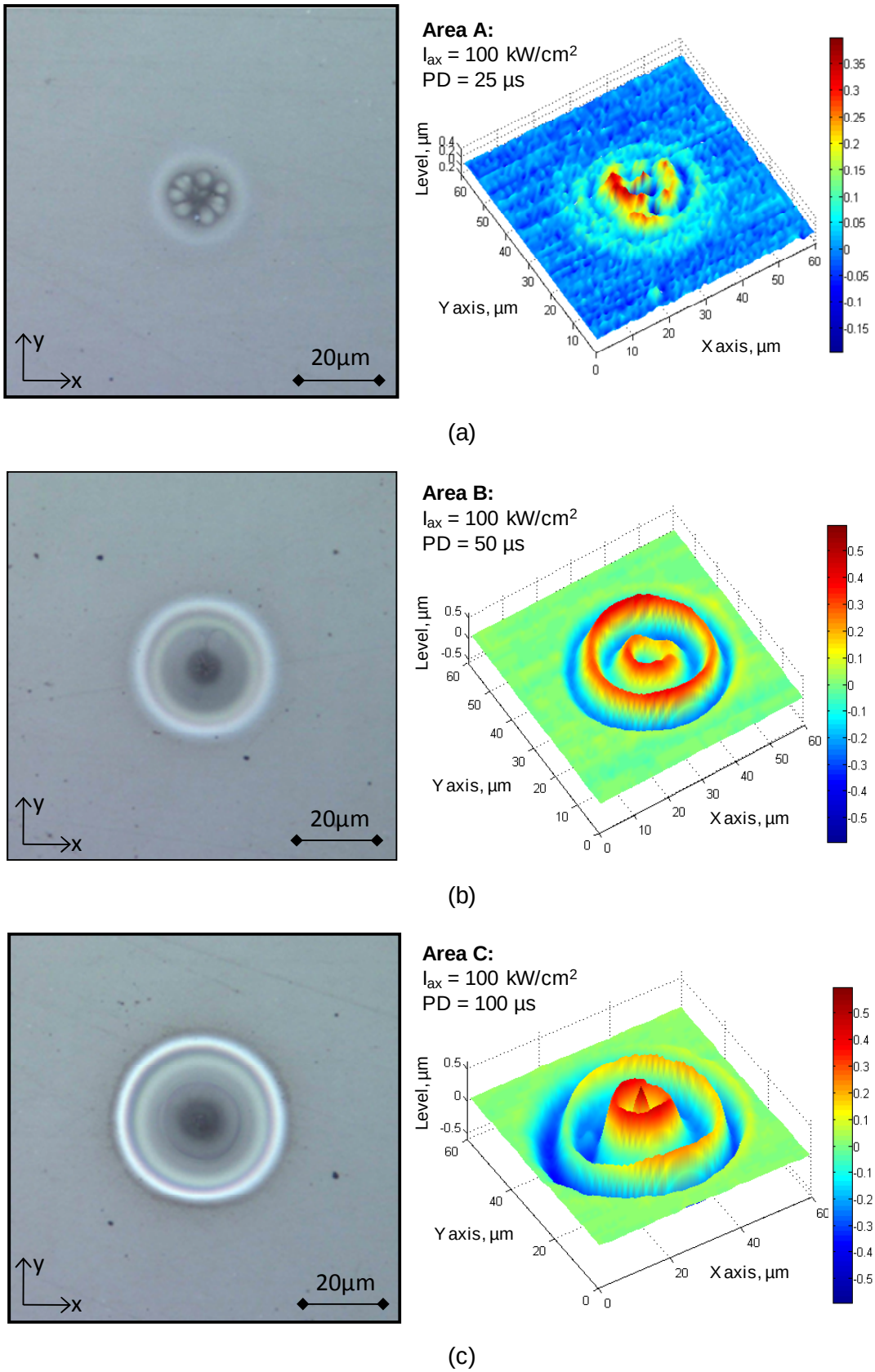

Figure 8.9: Surface deformations produced at the surface of SF57® glass by using single laser pulse with a 100 kW/cm^2 axial irradiance and pulse duration of: (a) 25 µs, (b) 50 µs, and (c) 100 µs.

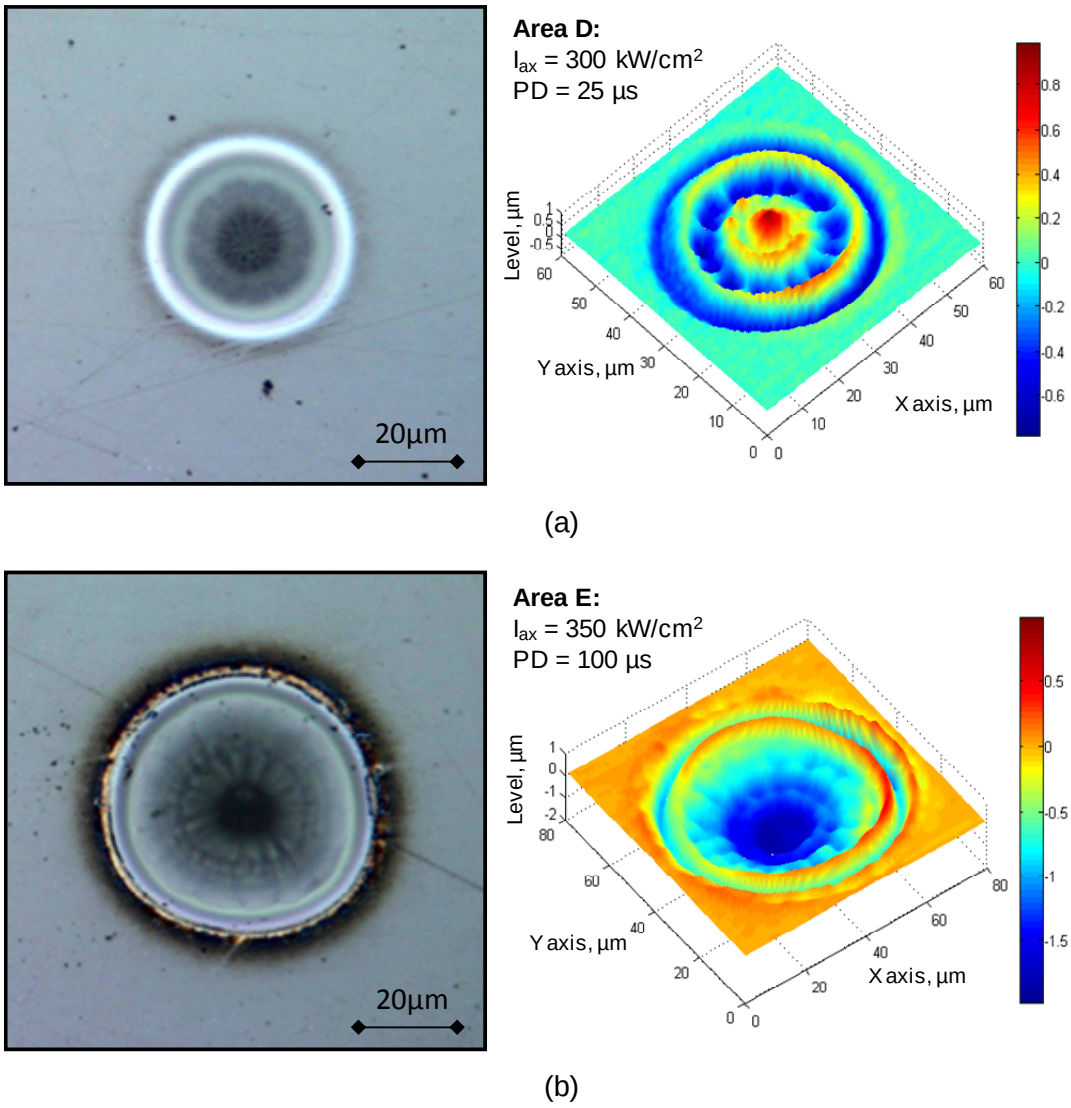

Figure 8.10: Surface deformations produced at the surface of SF57® glass by using single laser pulses with: (a) 300 kW/cm^2 axial irradiance and 25 µs pulse duration and (b) 350 kW/cm^2 axial irradiance and 100 µs pulse duration.

8.4.2 N-SF66® glass

The calibration map performed for N-SF66® glass is shown in Figure 8.11. The surface damage threshold for this material is determined to be in the range of axial irradiance of 25 - 75 kW/cm^2, thus it is similar to that determined for Borofloat®33 glass. The characteristic features observed at the surface of N-SF66® are shown in Figure 8.12. At this point, it should to be noted that deformations produced by short (25 µs) and long (100 µs) laser pulses were found to be similar in shape. Therefore, it can be concluded that this glass interacts quite 'badly' with a CO_2 laser beam, and most likely this glass is not suitable to be used as a substrate for CO_2 laser micro-machining.

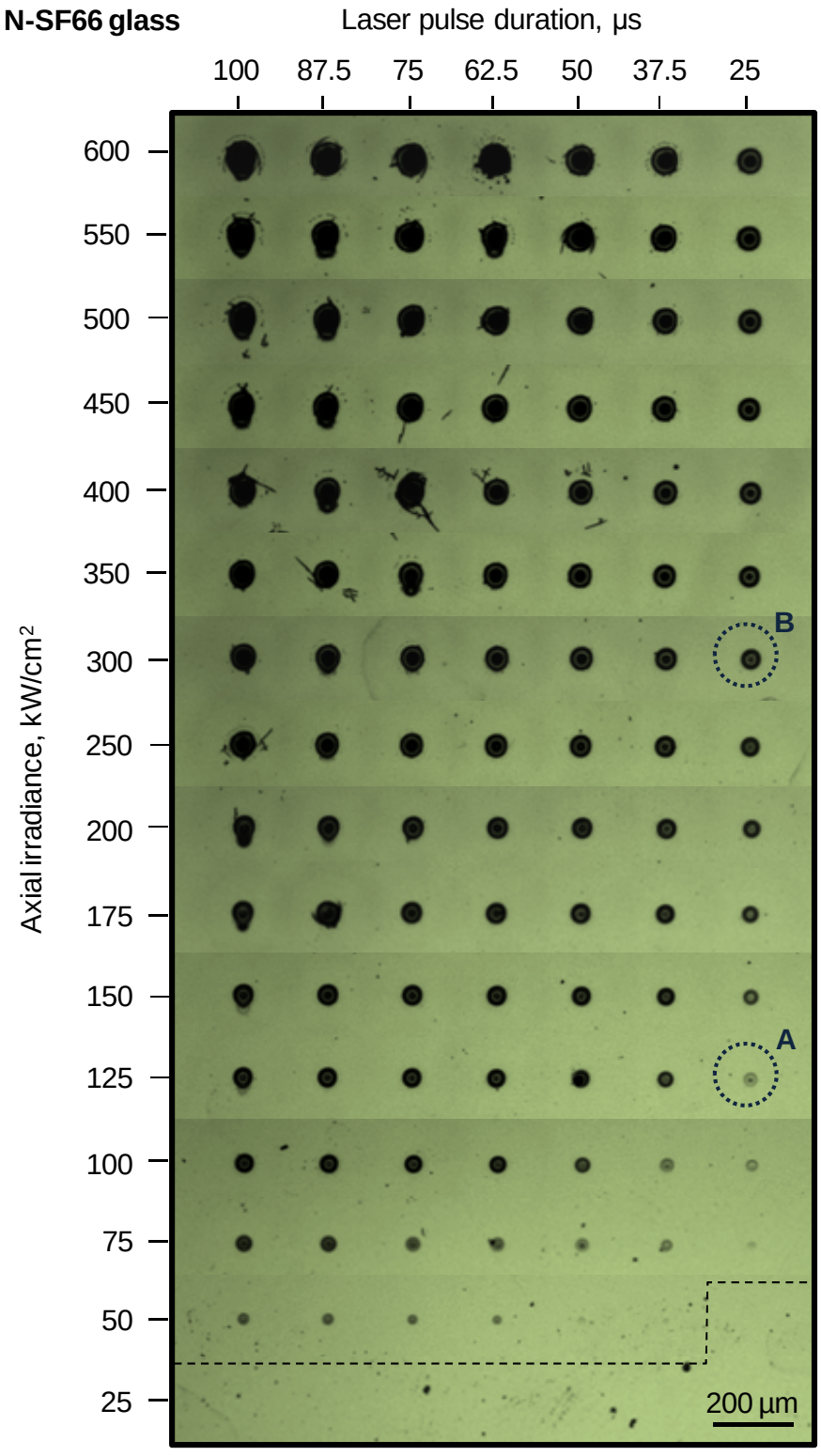

Figure 8.11: Calibration map for N-SF66® glass. The craters are produced by using a 50 µm diameter laser beam (measured at $1/e^2$ of its maximum intensity). Dashed line indicates the onset of surface effects, whilst the dotted circles indicate the laser-irradiated areas which are enlarged in Figure 8.12.

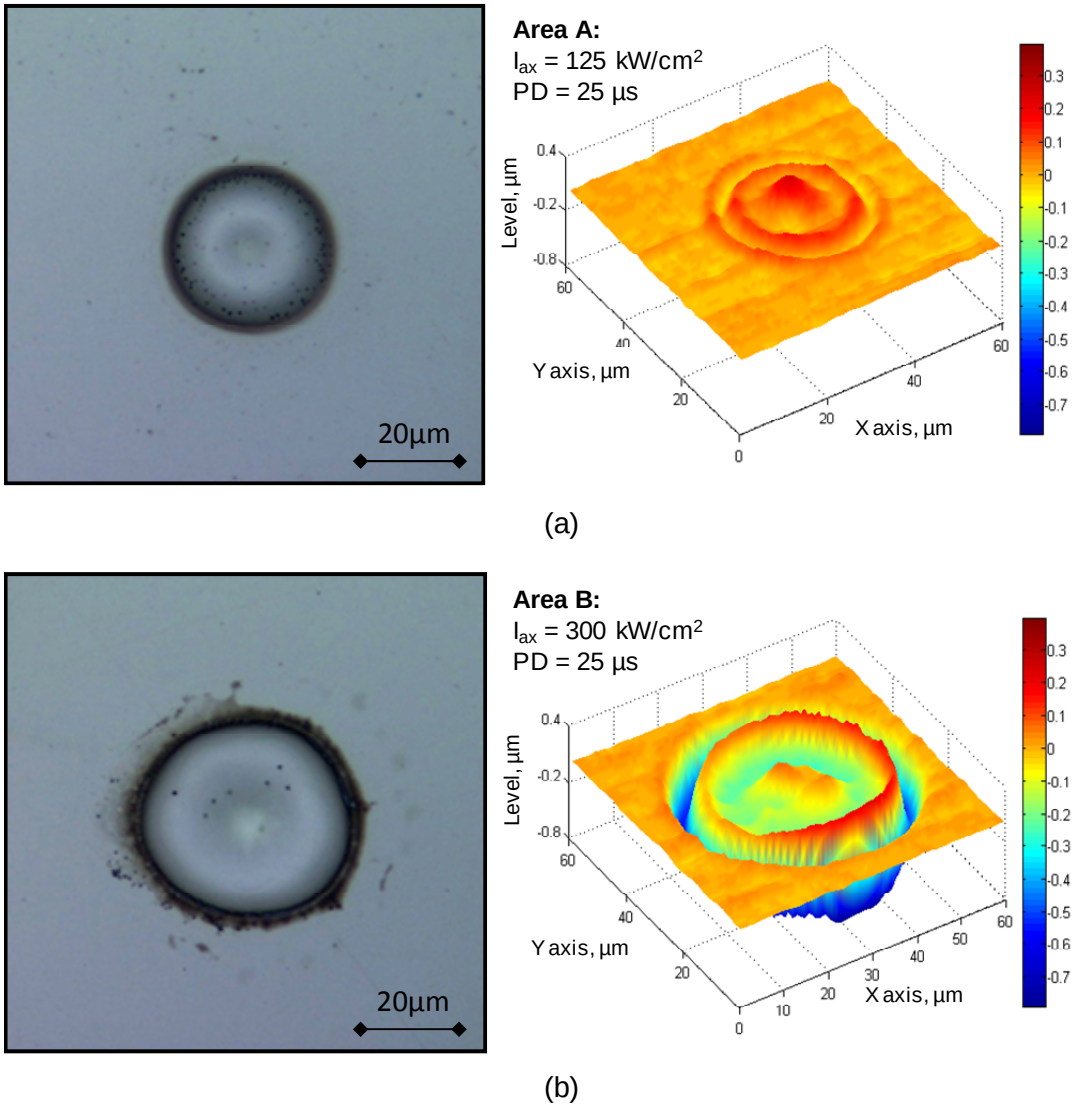

Figure 8.12: Surface deformations produced at the surface of N-SF66® glass by using single 25 µs long laser pulse and axial peak irradiance of: (a) 125 kW/cm^2 and (b) 300 kW/cm^2. Note: deformations produced by 100 µs long laser pulses were found to be similar in shape to those presented above.

8.4.3 LAFN7® glass

The calibration map performed for the LAFN7® glass is presented in Figure 8.13. For this material, the laser-induced deformations begin to occur at the surface when treated using axial irradiance values between 25 and 75 kW/cm^2. Thus, it can be concluded that the surface damage threshold for this material is similar in value to that determined for SF57® glass. This coincidence is caused by the fact that the softening point of both glasses occurs at similar values of temperature (see Table 8.1).

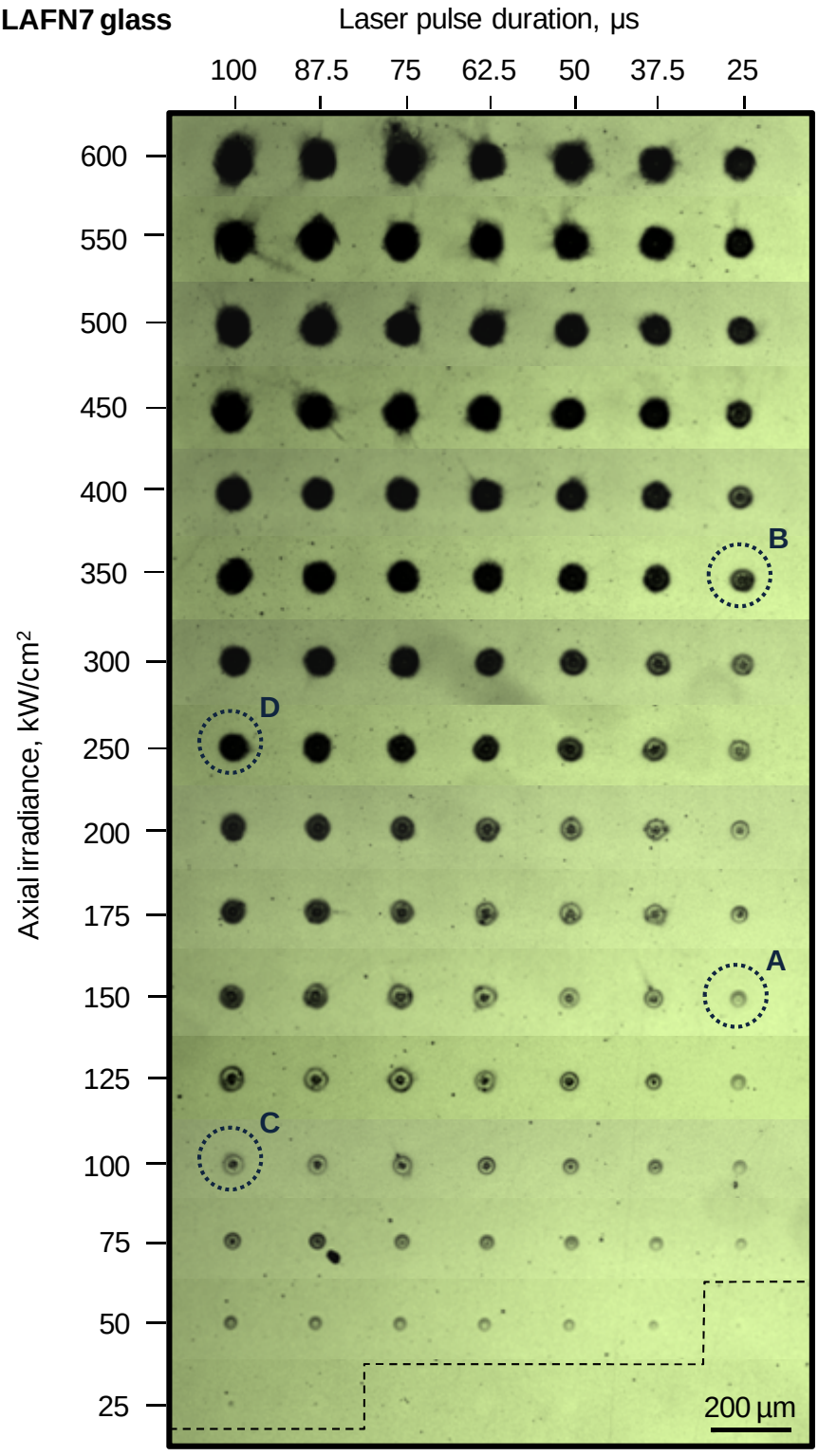

Figure 8.13: Calibration map for LAFN7® glass. The craters are produced by using a 50 µm diameter laser beam (measured at $1/e^2$ of its maximum intensity). Dashed line indicates the onset of surface effects, whilst the dotted circles indicate the laser-irradiated areas which are enlarged in Figure 8.14 and Figure 8.15.

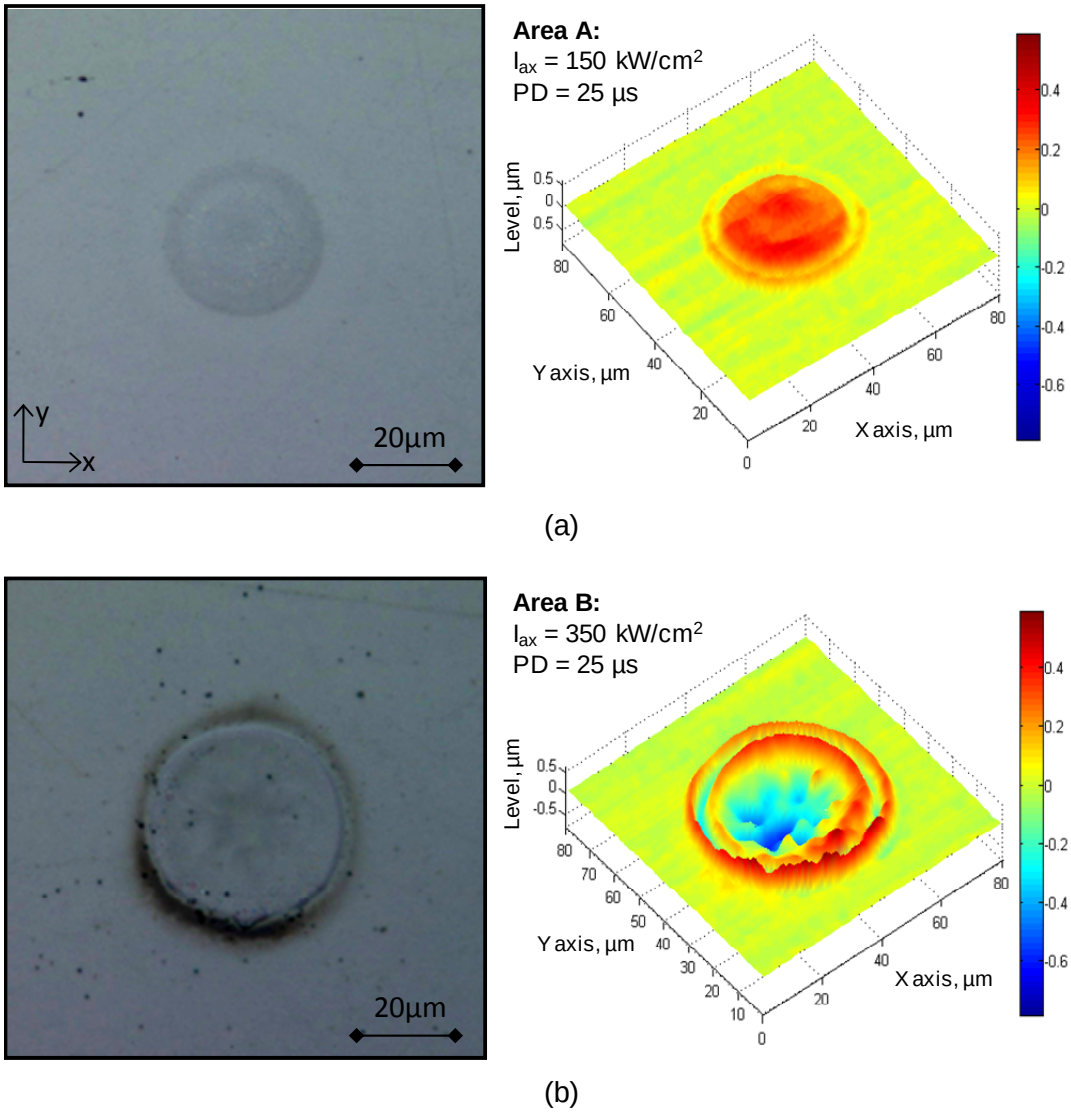

Figure 8.14: Surface deformations produced at the surface of LAFN7® glass by using single 25 µs long laser pulse and axial peak irradiance of: (a) 150 kW/cm^2 and (b) 350 kW/cm^2.

As can be seen in Figure 8.14, short laser pulses (*PD* = 25 µs) are not capable of producing smooth craters at the glass surface. At low values of axial irradiance, deformations are observed to be in the form of bumps, which are similar in shape to those observed at the surface of Borofloat®33. Once the axial irradiance exceeds the value of 300 kW/cm^2, the CO_2 laser pulse can produce a crater at the glass surface. This crater, however, contains a highly rough texture in the centre and is surrounded by the glass vapour redeposit, as can be seen in Figure 8.14 (b). Therefore, it can be concluded that 25 µs long CO_2 laser pulses most likely are not appropriate to produce a smooth laser-ablated surface in this material.

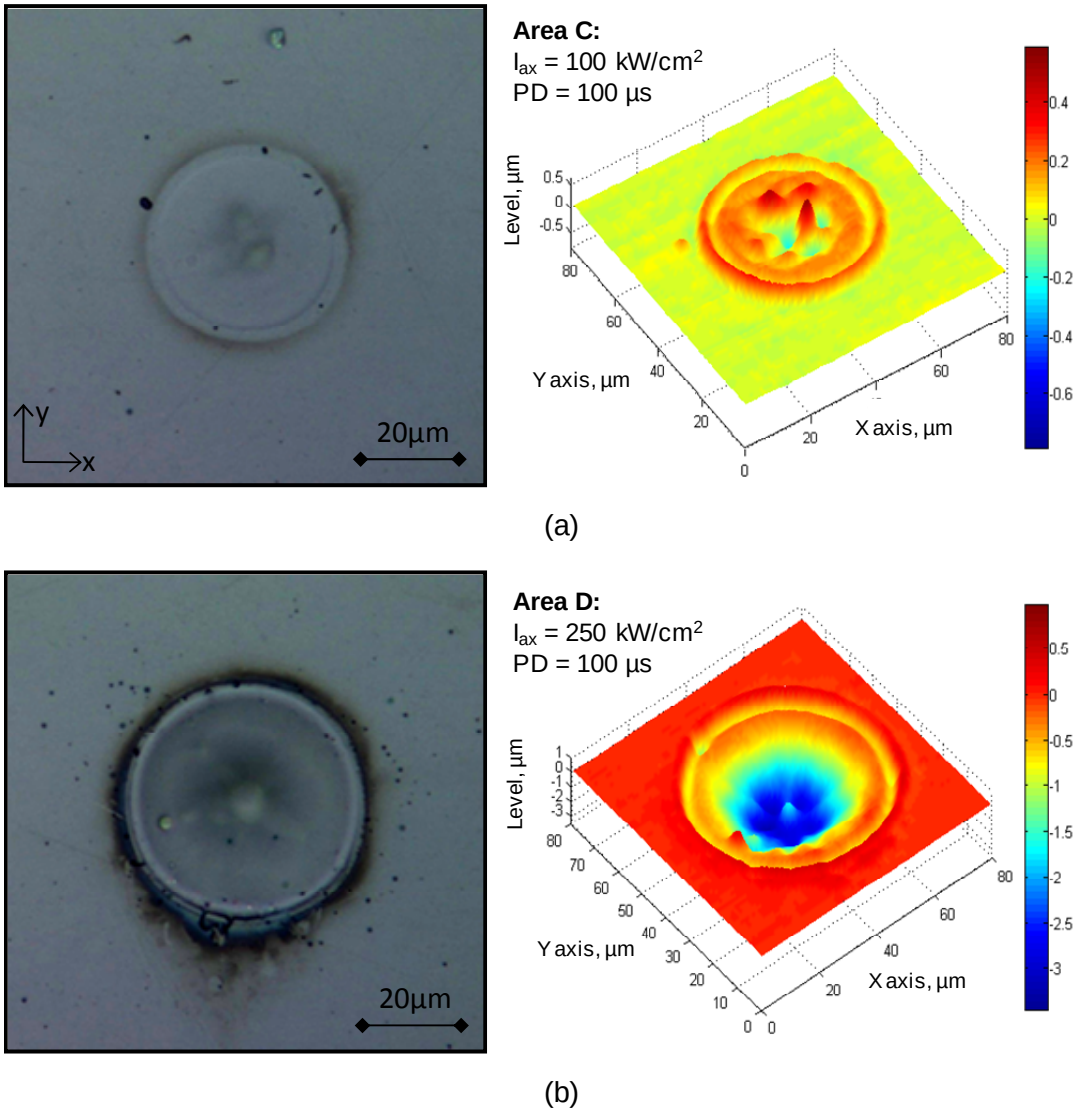

Figure 8.15: Surface deformations produced at the surface of LAFN7® glass by using single 100 µs long laser pulse and axial peak irradiance of: (a) 100 kW/cm^2 and (b) 250 kW/cm^2.

Figure 8.15 shows laser-induced surface deformations, when LAFN7® glass is affected by single 100 µs long laser pulses. For the low values of axial irradiance (I_{ax} < 150 kW/cm^2), the surface deformations are observed to be in the form of frozen splashes. This may mean that glass undergoes some metastable transformations.

On the other hand, for the high values of axial irradiance (I_{ax} > 150 kW/cm^2), the CO_2 laser pulse is able to produce a crater containing a small tip in the centre, as shown Figure 8.15 (b). Generally, this glass seems to be the most suitable material for CO_2 laser micro-machining. Nevertheless, at this stage of study it is difficult to affirm whether this glass can be used as a substrate for making micro-optics or not.

8.5 Summary and conclusions

To the author's knowledge, the work covered in this chapter demonstrated pioneering results in terms of CO_2 laser micro-machining of Borofloat®33 and lead-silicate glasses (SF57®, LAFN7®, and N-SF66®).

As shown in Section 8.3, a CO_2 laser pulse is able to produce smooth craters at the surface of Borofloat®33 glass when treated using machining conditions defined by the boundary of REGION III shown in Figure 8.2. Therefore, it is reasonable to believe that this material is appropriate to be used as a substrate for the fabrication of micro-optics, using a CO_2 laser beam as a sole machining tool. In the future, however, it is necessary to perform additional experiments in which the glass should be treated using laser beam raster scanning since these results may provide information whether this material can be machined without cracking when a large area of the glass is laser-treated.

In regard to the lead-silicate glasses, it can be concluded that these materials are not suitable for the manufacture of micro-optics, using CO_2 laser beam machining. As shown in Section 8.4, a single CO_2 laser pulse produces unusual surface deformations within the laser-irradiated area. Although craters can be produced at the surface of SF57® and LAFN7® glass, they contain a "wheel-shaped" pattern in the centre, which may lead to the appearance of significant roughness at the glass surface when treated using laser beam raster scanning. Since the lead-silicate glasses are prone to bumping and texturing, there is a high probability that these materials are also not suitable for CO_2 laser polishing. Additional experiments are required to investigate this issue in more detail in the future.

Chapter 9
Final conclusions and future work

9.1 Conclusions

The work presented in this thesis addresses important issues related to CO_2 laser polishing and micromachining of optical glasses, thereby providing valuable information to the scientific researchers and technical community working on laser processing of these brittle materials. Within this thesis, some important advances have been made in the following areas:

- CO_2 laser smoothing of binary and multi-level etched structures in fused silica.
- Laser-induced deformations produced on the surface of fused silica (HPFS 7980® Corning), Borofloat®33, and some selected lead-silicate glasses.
- Stresses in fused silica plates when treated by laser beam raster scanning.
- New possible applications for CO_2 laser polishing.

With regard to CO_2 laser smoothing of fused silica etched structures, it has been found that an approximately 1 mm diameter laser beam allows the sharp step edges to be relaxed over a distance from submicron to about 30 µm, depending on the value of laser power used. The submicrometer resolution in smoothing means that this process may be applied for fine relaxation of the etch steps of diffractive optics, in order to increase the diffraction efficiency of these optical components, as well as for polishing nano-

structures fabricated in fused silica. On the other hand, a large surface relaxation of the etched steps seems to be a promising result that may be used for the fabrication of micro-optics, as a viable alternative to the thermal reflow process. Here, it must be noted that all aforementioned findings show a new potential direction for CO_2 laser polishing.

In this thesis, an optical method based on analysis of light scatter from binary gratings has been introduced, allowing complete characterization of the CO_2 laser polishing process. Using this method, it is now possible to measure quickly the surface relaxation which begins at the submicron scale, corresponding to a temperature of approximately 1600°C for fused silica, and ends at the point where polishing causes evaporation of the glass. Since the optical method covers the whole range of temperatures at which the smoothing effect may occur, this method is proposed to be a standard tool for calibrating CO_2 laser polishing systems.

With regard to the laser-induced surface deformations in optical glasses, it has been found that they are produced by the well-known Marangoni effect, which causes a displacement of the molten glass, as well as by the fictive temperature since the laser-induced deformations have been observed to be reduced in size (or disappear) when annealed.

In the case of fused silica (HPFS 7980® Corning), it has been found that an increase of the fictive temperature causes densification of the material, thereby leading to the formation of shallow (approximately 200 µm deep) depressions within the laser-irradiated area. As shown in Section 5.2.3, the depressions in fused silica are completely removable by annealing. Here, it should be noted that this observation has been found to be consistent with the recent results reported by Feit *et al.* in [129].

Based on the experimental results presented in Chapter 7, it has been concluded that the fictive temperature has a significant influence on the value of stress produced by CO_2 laser polishing. Although the laser-induced stresses in the range of 10 - 30 MPa are produced at the surface of fused silica (see Section 7.4), causing noticeable bending of the glass plates towards the laser-treated area, they have been found to be relieved by annealing, thereby providing strong evidence that the fictive temperature is involved in the creation process of stresses. This means that the conventional explanation of the appearance of stresses in glasses under treatment by a moving laser beam, as

covered in Section 7.2, is not entirely correct when applied to fused silica, since it does not take into account the fictive temperature effect. Finally, it should be noted that the experimental results described in Section 7.3 suggest that stress induced by laser beam raster scanning is anisotropic since the glass plates were observed to be bent differently in two orthogonal directions. To confirm this suggestion, however, more experimental work is required to be done in the future.

The second glass studied in this thesis was Borofloat®33 manufactured by Schott AG (Germany). As shown in Chapter 5, this material interacts with a CO_2 laser beam in a completely different way to fused silica, and as a consequence of that, it is a more demanding material in terms of its capacity to be processed using a CO_2 laser source. Since Borofloat®33 is classified as normal (see Section 2.4.5), the laser radiation leads to the appearance of bumps at the glass surface due to a local increase of the fictive temperature within the laser-irradiated area, which *decreases* the glass density in this region, combined with the Marangoni effect. Generally, the bumps were found to grow with increasing laser power, up to the point at which the laser-induced stresses in the material are so high that bumps simply crack, suggesting that an elevated fictive temperature causes fractures. Here, it should be noted that laser treatment of the glass preheated to 350°C does not reduce the size of the bumps, indicating that 'hot' laser machining may not prevent the glass from cracking.

Although Borofloat®33 undergoes fractures when treated at high values of axial fluence (lased power), the potential machining and polishing conditions for non-cracking treatment of this material have been successfully established. This achievement, therefore, opens finally the possibility of using the CO_2 laser-based processes for manufacturing micro-optical components in Borofloat®33.

The third group of glasses studied in this thesis were lead-silicate glasses. This study revealed that these materials react 'badly' when heated by the beam at a 10.6 µm wavelength. As shown in Section 8.4, a single laser pulse produces unusual surface deformations within the laser-irradiated area (e.g. multiple rims, "wheel-shaped" pools, "frozen" splashes, and bumps). Although these glasses are most likely unsuitable for the manufacture of micro-optics, they seem to be appropriate materials for surface bumping and texturing.

Finally, this thesis presents a pioneering approach for the rapid prototyping (fabrication) of fused silica toroidal mirrors with a high ratio of the two principle radii of curvature ($RoC_1/RoC_2 > 10$). As presented in Section 6.5, these mirrors may be successfully applied in mode-selective resonator configurations to improve the laser beam quality of planar waveguide lasers. It is believed that lasers with these mirrors may begin to compete, for instance, with high power fibre lasers in which the beam quality (M^2) factor is typically close to the Gaussian diffraction limit.

9.2 Future work

In terms of CO_2 laser polishing of fused silica

a) Since it is still unknown whether the stress produced by CO_2 laser polishing is anisotropic or isotropic, in the future it is necessary to perform an experiment in which a 25.4 mm square plate will be polished by a moving beam, covering only a 22×22 mm^2 area, whilst the untreated region will be removed by sawing.
b) Build a model for simulating the stress distribution in CO_2 laser polished glasses. This possibly can be done using the COMSOL® Multiphysics package.
c) Develop the novel method for characterization CO_2 laser polishing, which is based on measurement of light-scatter from binary gratings, to provide automation of the calibration process.

In terms of CO_2 laser smoothing of etched structures in fused silica

a) Since laser smoothing was demonstrated only on two multi-level etched samples, more experiments are still required to provide more data with regard to the surface relaxation of etched steps.
b) Study of subwavelength interactions between a CO_2 laser beam and under-etched surface features, to establish technical limitations of the CO_2 laser-based reflow technique for the fabrication of micro-optics.
c) Design of a ‘digital’ structure dedicated specially for CO_2 laser treatment, to fully prove the fabrication concept of micro-optics given in Section 4.7.

In terms of rapid prototyping of toroidal mirrors

a) Testing of the laser-fabricated toroidal mirrors in a mode-selective confocal unstable resonator configuration for a 150 µm core Yb:YAG planar waveguide laser [130, 132].
b) Improvement of CO_2 laser power stability in the existing laser system, in order to achieve better surface quality of the toroidal mirrors. Discussion on possible improvements of the laser system has been provided in Section 6.6.4.

In terms of CO_2 laser treatment of Borofloat®33

a) Apply the laser machining conditions at which Borofloat®33 does not crack (referred to as Region III – see Section 8.3), in order to generate a micro-structure or a micro-optical component.
b) Perform CO_2 laser polishing of highly-scattered surfaces of binary structures made of Borofloat®33, in order to determine the extent of surface features which can be smoothed without material cracking.

In terms of CO_2 laser micro-machining of lead-silicate glasses

a) Further investigation of surface deformations produced by single laser pulses and understanding mechanisms which are responsible for the formation of such complex surface features.
b) Generate calibration maps for SF57®, N-SF66®, and LAFN7® glasses, using different laser machining conditions than those used in Chapter 8. These results may define conditions at which the laser ablation of glass would be achieved, whilst the complex bumping would be less pronounced.

Appendix: Derivation of formulas on the principle curvatures

Let's consider a two-dimensional surface given as follows:

$$f(x,y) = \mathrm{A}\,\mathrm{x}^2 + \mathrm{B}\,\mathrm{x}\,\mathrm{y} + \mathrm{C}\,\mathrm{y}^2 \tag{1}$$

The second (partial) derivatives of this function with respect to *x* and *y* are expresses as:

$$\frac{\partial^2 \mathrm{f}}{\partial \mathrm{x}^2} = 2\,\mathrm{A} \tag{2}$$

$$\frac{\partial^2 \mathrm{f}}{\partial \mathrm{y}^2} = 2\,\mathrm{C} \tag{3}$$

Unfortunately, equations (2) and (3) give us only information about the curvature of the surface along the X and Y axes. To evaluate the surface curvature in any direction, it is necessary, for instance, to substitute *y* in equation (1) for the *k*·*x*, where *k* is any constant. Now, the equation of the surface is given by:

$$f(x,kx) = (\mathrm{A} + \mathrm{B}\,\mathrm{k} + \mathrm{C}\,\mathrm{k}^2)\,\mathrm{x}^2 \tag{4}$$

On the other hand, the distance along the tangent plane in the $y = k \cdot x$ direction is expressed as:

$$s^2 = \mathrm{x}^2 + \mathrm{y}^2 = (1 + \mathrm{k}^2)\,\mathrm{x}^2 \tag{5}$$

Substituting x^2 in equation (4) for the parameter *s*, which defines the distance of some point from the origin, the surface as a function of *s* is given as follows:

$$f(s) = \frac{(\mathrm{A} + \mathrm{B}\,\mathrm{k} + \mathrm{C}\,\mathrm{k}^2)}{1 + \mathrm{k}^2}\,\mathrm{s}^2 \tag{6}$$

The second derivative of this function gives the surface curvature, *c*, in the *k* direction. This curvature is given by:

$$c(k) = 2\,\frac{(\mathrm{A} + \mathrm{B}\,\mathrm{k} + \mathrm{C}\,\mathrm{k}^2)}{1 + \mathrm{k}^2} \tag{7}$$

Since we want to know the direction of the principle curvatures for the point at which the function *f(x, y)* is either minimum or maximum, we have to equate the derivative of the *c(k)* to zero:

$$(\mathrm{B} + 2\,\mathrm{C}\,\mathrm{k})\,(1 + \mathrm{k}^2) - 2\,(\mathrm{A} + \mathrm{B}\,\mathrm{k} + \mathrm{C}\,\mathrm{k}^2)\,\mathrm{k} = 0 \tag{8}$$

$$\mathrm{k}^2 - 2\left(\frac{\mathrm{C} - \mathrm{A}}{\mathrm{B}}\right)\mathrm{k} - 1 = 0 \tag{9}$$

and then, calculate the roots of this quadratic function. The roots are given as follows:

$$\mathrm{k}_1 = \mathrm{q} + \sqrt{\mathrm{q}^2 + 1} \tag{10}$$

$$\mathrm{k}_2 = \mathrm{q} - \sqrt{\mathrm{q}^2 + 1} \tag{11}$$

where $q = (C - A) / B$. The angles between the principle curvatures and the X axis are:

$$\theta_1 = \mathrm{atan}(\mathrm{k}_1) \tag{12}$$

$$\theta_2 = \mathrm{atan}(\mathrm{k}_2) \tag{13}$$

In order to evaluate the values of the principle curvatures, it is necessary to substitute k_1 and k_2 values for *k* in equation (7). The final formulas of the principle curvatures are given as follows:

$$\mathrm{C}_1 = \mathrm{A} + \mathrm{C} + \sqrt{(\mathrm{C} - \mathrm{A})^2 + \mathrm{B}^2} \tag{14}$$

$$\mathrm{C}_2 = \mathrm{A} + \mathrm{C} - \sqrt{(\mathrm{C} - \mathrm{A})^2 + \mathrm{B}^2} \tag{15}$$

Since the constant term of equation (9) is – 1, it follows that the product of the two roots of this equation is also – 1. This means that the directions of the principle curvatures are perpendicular each other.

References

[1] E. Mendez, K. M. Nowak, H. J. Baker, F. J. Villarreal, and D. R. Hall, "Localized CO_2 laser damage repair of fused silica optics," Applied Optics **45**, 5358-5367 (2006).

[2] E. Mendez, H. J. Baker, K. M. Nowak, F. J. Villarreal, and D. R. Hall, "Highly localized CO_2 laser cleaning and damage repair of silica optical surfaces," in Proceedings of SPIE **5647**, 165 (2005).

[3] K. M. Nowak, H. J. Baker, and D. R. Hall, "Efficient laser polishing of silica micro-optic components," Applied Optics **45**, 162-171 (2006).

[4] K. M. Nowak, H. J. Baker, and D. R. Hall, "Pulsed-laser machining and polishing of silica micro-optical components using a CO_2 laser and an acousto-optic modulator," in Proceedings of SPIE **4941**, 107-112 (2003).

[5] J. F. Monjardin, K. M. Nowak, H. J. Baker, and D. R. Hall, "Correction of beam errors in high power laser diode bars and stacks," Optics Express **14**, 8178-8183 (2006).

[6] N. Trela, H. J. Baker, J. J. Wendland, and D. R. Hall, "Dual-axis beam correction for an array of single-mode diode laser emitters using a laser-written custom phase-plate," Optics Express **17**, 23576-23581 (2009).

[7] H. J. Baker, C. Ott, R. M. McBride, J. J. Wendland, and D. R. Hall, "Beam shapers for high power lasers, fabricated by laser micro-machining," in *Conference on Lasers and Electro-Optics,* (Baltimore, US, 2009).

[8] U. Brauch, P. Loosen, and H. Opower, "High-power diode lasers for direct applications," in *High-Power Diode Lasers*, R. Diehl, ed. (Springer-Verlag Berlin Heidelberg, 2000), pp. 303-368.

[9] G. A. J. Markillie, H. J. Baker, F. J. Villarreal, and D. R. Hall, "Effect of vaporization and melt ejection on laser machining of silica glass micro-optical components," Applied Optics **41**, 5660-5667 (2002).

[10] E. Mendez Fernandez de Cordoba, "Laser micro-polishing of silica optics," PhD dissertation (Heriot-Watt University, Edinburgh, 2007).

[11] R. M. Brusasco, B. M. Penetrante, J. A. Butler, S. M. Maricle, and J. E. Peterson, "CO_2-Laser Polishing for Reduction of 351-nm Surface Damage Initiation in Fused Silica," in *Laser-Induced Damage in Optical Materials*, G. J. Exarhos, R. H. Guenther, K. L. Lewis, M. J. Soileau, and C. J. Stolz, eds., Proceedings of SPIE **4679**, 34-39 (2001).

[12] P. A. Temple, W. H. Lowdermilk, and D. Milam, "Carbon dioxide laser polishing of fused silica surfaces for increased laser-damage resistance at 1064 nm," Applied Optics **21**, 3249-3255 (1982).

[13] M. D. Feit and A. M. Rubenchik, "Mechanisms of CO_2 laser mitigation of laser damage growth in fused silica," in Proceedings of SPIE **4932**, 91 (2003).

[14] F. Laguarta, N. B. Lupon, F. Vega, and J. Armengol, "Laser application for optical glass polishing," in Proceedings of SPIE **2775**, 603 (1996).

[15] A. Kuhn, P. French, D. P. Hand, I. J. Blewett, M. Richmond, and J. D. C. Jones, "Preparation of fiber optics for the delivery of high-energy high-beam-quality Nd: YAG laser pulses," Applied Optics **39**, 6136-6143 (2000).

[16] M. Udrea, H. Orun, and A. Alacakir, "Laser polishing of optical fiber end surface," Optical Engineering **40**, 2026 (2001).

[17] H. P. Herzig, *Micro-optics: Elements, systems and applications* (CRC, 1997).

[18] J. F. Bacon and A. A. Hasapis, "Viscosity of Molten Silica," Journal of Applied Physics **30**, 1470-1471 (1959).

[19] D. G. Holloway, *Physical Properties of Glass* (Wykeham Publicatons Ltd., London, 1973).

[20] R. Brückner, "Properties and structure of vitreous silica. I," Journal of Non-Crystalline Solids **5**, 123-175 (1970).

[21] R. Le Parc, C. Levelut, J. Pelous, V. Martinez, and B. Champagnon, "Influence of fictive temperature and composition of silica glass on anomalous elastic behaviour," Journal of Physics: Condensed Matter **18**, 7507-7527 (2006).

[22] N. Shen, M. J. Matthews, J. E. Fair, J. A. Britten, H. T. Nguyen, D. Cooke, S. Elhadj, and S. T. Yang, "Laser smoothing of sub-micron grooves in hydroxyl-rich fused silica," Applied Surface Science **256**, 4031-4037 (2010).

[23] Y. M. Xiao and M. Bass, "Thermal stress limitations to laser fire polishing of glasses," Applied Optics **22**, 2933-2936 (1983).

[24] C. Kittel, "Interpretation of the thermal conductivity of glasses," Physical Review **75**, 972-974 (1949).

[25] K. L. Wray and T. J. Connolly, "Thermal conductivity of clear fused silica at high temperatures," Journal of Applied Physics **30**, 1702 (1959).

[26] http://www.schott.com/borofloat/english/download/borofloat_33_e.pdf, (accessed in February 2010).

[27] A. Paul, *Chemistry of glasses* (Chapman and Hall Ltd., London, 1990).

[28] http://www.gequartz.com/en/thermal.htm, (accessed in February 2010).

[29] N. P. Bansal and R. H. Doremus, *Handbook of glass properties* (Academic press New York, 1986).

[30] http://www.valleydesign.com/7940.htm, (accessed in February 2010).

[31] "Schott Optical Glass Catalogue," (accessed in February 2010 from http://www.schott.com/advanced_optics/english/download/datasheet_all_english.pdf).

[32] D. W. Lane, "The optical properties and laser irradiation of some common glasses," Journal of Physics D: Applied Physics **23**, 1727-1734 (1990).

[33] J. E. Shelby, *Introduction to glass science and technology* (Royal Society of Chemistry, 2005).

[34] A. D. McLachlan and F. P. Meyer, "Temperature dependence of the extinction coefficient of fused silica for CO_2 laser wavelengths," Applied Optics **26**, 1728-1731 (1987).

[35] T. R. Steyer, K. L. Day, and D. R. Huffman, "Infrared absorption by small amorphous quartz spheres," Applied Optics **13**, 1586-1590 (1974).

[36] A. Fluegel, "Glass viscosity calculation based on a global statistical modelling approach," Glass Technology-European Journal of Glass Science and Technology Part A **48**, 13-30 (2007).

[37] G. Hetherington, K. H. Jack, and J. C. Kennedy, "The viscosity of vitreous silica," Physics and Chemistry of Glasses **5**, 130–136 (1964).

[38] G. Urbain, Y. Bottinga, and P. Richet, "Viscosity of liquid silica, silicates and alumino-silicates," Geochimica et Cosmochimica Acta **46**, 1061-1072 (1982).

[39] R. H. Doremus, "Viscosity of silica," Journal of Applied Physics **92**, 7619 (2002).

[40] "SciGlass - Glass Property Information System" (April 2010), retrieved http://www.sciglass.info.

[41] "Standard Reference Material 717A, Borosilicate Glass," (National Institute of Standards & Technology (NIST), Gaithersburg, MD, 20899, USA, September 18, 1996).

[42] "Standard Reference Material 710A, Soda-Lime-Silica Glass," (National Institute of Standards & Technology (NIST), Gaithersburg, MD, 20899, USA, March 20, 1991).

[43] "Standard Sample No. 711, Certificate of Viscosity Values, Lead-Silica Glass," (National Bureau of Standards, U.S. Department of Commerce, Washington, D.C., 20235, USA, July 1, 1964).

[44] G. O. Jones, "Viscosity and related properties in glass," Reports on Progress in Physics **12**, 133-162 (1949).

[45] A. Q. Tool, "Relation between inelastic deformability and thermal expansion of glass in its annealing range," Journal of the American Ceramic Society **29**, 240-253 (1946).

[46] V. Uhl, K. O. Greulich, and S. Thomas, "Comparison of the influence of the fictive and the annealing temperature on the UV-transmission properties of

synthetic fused silica," Applied Physics A: Materials Science & Processing **65**, 457-462 (1997).

[47] J. E. Shelby, "Density of vitreous silica," Journal of Non-Crystalline Solids **349**, 331-336 (2004).

[48] R. Le Parc, B. Champagnon, P. Guenot, and S. Dubois, "Thermal annealing and density fluctuations in silica glass," Journal of Non-Crystalline Solids **293**, 366-369 (2001).

[49] S. Sen, R. L. Andrus, D. E. Baker, and M. T. Murtagh, "Observation of an anomalous density minimum in vitreous silica," Physical Review Letters **93**, 125902 (2004).

[50] H. Kakiuchida, K. Saito, and A. J. Ikushima, "Precise determination of fictive temperature of silica glass by infrared absorption spectrum," Journal of Applied Physics **93**, 777 (2003).

[51] T. M. Gross and M. Tomozawa, "Fictive temperature-independent density and minimum indentation size effect in calcium aluminosilicate glass," Journal of Applied Physics **104**, 063529-063529-063510 (2008).

[52] U. Haken, O. Humbach, S. Ortner, and H. Fabian, "Refractive index of silica glass: influence of fictive temperature," Journal of Non-Crystalline Solids **265**, 9-18 (2000).

[53] I. Matthew and M. Tomozawa, "Effect of fictive temperature on the polishing rate of thermally grown silicon dioxide," Journal of the Electrochemical Society **148**, F98 (2001).

[54] D. B. Fraser, "Factors influencing the acoustic properties of vitreous silica," Journal of Applied Physics **39**, 5868-5878 (1968).

[55] M. Bertoldi and V. M. Sglavo, "Soda-borosilicate glass: normal or anomalous behavior under Vickers indentation?," Journal of Non-Crystalline Solids **344**, 51-59 (2004).

[56] A. Koike and M. Tomozawa, "Fictive temperature dependence of subcritical crack growth rate of normal glass and anomalous glass," Journal of Non-Crystalline Solids **352**, 5522-5530 (2006).

[57] B. Varughese, Y. K. Lee, and M. Tomozawa, "Effect of fictive temperature on mechanical strength of soda-lime glasses," Journal of Non-Crystalline Solids **241**, 134-139 (1998).

[58] T. R. Shiu, C. P. Grigoropoulos, D. G. Cahill, and R. Greif, "Mechanism of bump formation on glass substrates during laser texturing," Journal of Applied Physics **86**, 1311 (1999).

[59] J. Sullivan, J. Zhao, and T. D. Bennett, "Measurement of thermally induced changes in the refractive index of glass caused by laser processing," Applied Optics **44**, 7173-7180 (2005).

[60] M. Von Allmen and A. Blatter, *Laser-beam interactions with materials: physical principles and applications* (Springer Verlag, 1995).

[61] K. M. Nowak, "Rapid prototyping of micro-optics for brightness restoration of diode lasers," PhD dissertation (Heriot-Watt University, Edinburgh, 2003).

[62] M. Von Allmen, W. Lüthy, and K. Affolter, "Anisotropic melting and epitaxial regrowth of laser irradiated silicon," Applied Physics Letters **33**, 824 (1978).

[63] D. Bäuerle, *Laser Processing and Chemistry* (Springer, 1996).

[64] T. D. Bennett, D. J. Krajnovich, L. Li, and D. Wan, "Mechanism of topography formation during CO_2 laser texturing of silicate glasses," Journal of Applied Physics **84**, 2897-2905 (1998).

[65] D. Kuo, S. D. Vierk, O. Rauch, and D. Polensky, "Laser zone texturing on glass and glass-ceramic substrates," IEEE Transactions on Magnetics **33**, 944-949 (1997).

[66] A. C. Tam, J. Brannon, P. Baumgart, and I. K. Pour, "Laser texturing of glass disk substrates," IEEE Transactions on Magnetics **33**, 3181-3183 (1997).

[67] T. D. Bennett, D. J. Krajnovich, and L. Li, "Thermophysical modeling of bump formation during CO_2 laser texturing of silicate glasses," Journal of Applied Physics **85**, 153 (1999).

[68] T. D. Bennett and L. Li, "Modeling laser texturing of silicate glass," Journal of Applied Physics **89**, 942 (2001).

[69] J. Zhao, J. Sullivan, J. Zayac, and T. D. Bennett, "Structural modification of silica glass by laser scanning," Journal of Applied Physics **95**, 5475 (2004).

[70] D. Wu, Q. Zhang, G. Ma, Y. Guo, and D. Guo, "Laser bending of brittle materials," Optics and Lasers in Engineering **48**, 405-410 (2010).

[71] D. Wu, G. Ma, F. Niu, and D. Guo, "Temperature Gradient Mechanism on Laser Bending of Borosilicate Glass Sheet," Journal of Manufacturing Science and Engineering **132**, 011013 (2010).

[72] J. Lawrence, M. J. J. Schmidt, and L. Li, "The forming of mild steel plates with a 2.5 kW high power diode laser," International Journal of Machine Tools and Manufacture **41**, 967-977 (2001).

[73] G. Allcock, P. E. Dyer, G. Elliner, and H. V. Snelling, "Experimental observations and analysis of CO2 laser induced microcracking of glass," Journal of Applied Physics **78**, 7295-7303 (1995).

[74] F. Laguarta, N. Lupon, and J. Armengol, "Optical glass polishing by controlled laser surface-heat treatment," Applied Optics **33**, 6508-6513 (1994).

[75] R. G. Mace, "Annealing of fused quartz" (GE Quartz Inc., 2000), retrieved June 2010, http://www.gequartz.com/en/pdfs/annealing.pdf.

[76] R. R. Gattass and E. Mazur, "Femtosecond laser micromachining in transparent materials," Nature Photonics **2**, 219-225 (2008).

[77] X. Liu, D. Du, and G. Mourou, "Laser ablation and micromachining with ultrashort laser pulses," IEEE Journal of Quantum Electronics **33**, 1706-1716 (1997).

[78] D. Du, X. Liu, G. Korn, J. Squier, and G. Mourou, "Laser-induced breakdown by impact ionization in SiO_2 with pulse widths from 7 ns to 150 fs," Applied Physics Letters **64**, 3071-3073 (1994).

[79] M. S. Giridhar, K. Seong, A. Schülzgen, P. Khulbe, N. Peyghambarian, and M. Mansuripur, "Femtosecond pulsed laser micromachining of glass substrates with application to microfluidic devices," Applied Optics **43**, 4584-4589 (2004).

[80] A. Ben-Yakar and R. L. Byer, "Femtosecond laser ablation properties of borosilicate glass," Journal of Applied Physics **96**, 5316 (2004).

[81] Y. Li, K. Itoh, W. Watanabe, K. Yamada, D. Kuroda, J. Nishii, and Y. Jiang, "Three-dimensional hole drilling of silica glass from the rear surface with femtosecond laser pulses," Optics Letters **26**, 1912-1914 (2001).

[82] A. Marcinkevicius, S. Juodkazis, M. Watanabe, M. Miwa, S. Matsuo, H. Misawa, and J. Nishii, "Femtosecond laser-assisted three-dimensional microfabrication in silica," Optics Letters **26**, 277-279 (2001).

[83] H. Varel, D. Ashkenasi, A. Rosenfeld, M. Wähmer, and E. E. B. Campbell, "Micromachining of quartz with ultrashort laser pulses," Applied Physics A: Materials Science & Processing **65**, 367-373 (1997).

[84] K. M. Davis, K. Miura, N. Sugimoto, and K. Hirao, "Writing waveguides in glass with a femtosecond laser," Optics Letters **21**, 1729-1731 (1996).

[85] K. Miura, J. Qiu, H. Inouye, T. Mitsuyu, and K. Hirao, "Photowritten optical waveguides in various glasses with ultrashort pulse laser," Applied Physics Letters **71**, 3329 (1997).

[86] J. W. Chan, T. R. Huser, S. H. Risbud, J. S. Hayden, and D. M. Krol, "Waveguide fabrication in phosphate glasses using femtosecond laser pulses," Applied Physics Letters **82**, 2371 (2003).

[87] O. M. Efimov, L. B. Glebov, K. A. Richardson, E. Van Stryland, T. Cardinal, S. H. Park, M. Couzi, and J. L. Bruneel, "Waveguide writing in chalcogenide glasses by a train of femtosecond laser pulses," Optical Materials **17**, 379-386 (2001).

[88] G. D. Marshall, M. Ams, and M. J. Withford, "Direct laser written waveguide-Bragg gratings in bulk fused silica," Optics Letters **31**, 2690-2691 (2006).

[89] K. Minoshima, A. Kowalevicz, E. Ippen, and J. Fujimoto, "Fabrication of coupled mode photonic devices in glass by nonlinear femtosecond laser materials processing," Optics Express **10**, 645-652 (2002).

[90] R. R. Thomson, H. T. Bookey, N. D. Psaila, A. Fender, S. Campbell, W. N. Macpherson, J. S. Barton, D. T. Reid, and A. K. Kar, "Ultrafast-laser inscription of a three dimensional fan-out device for multicore fiber coupling applications," Optics Express **15**, 11691-11697 (2007).

[91] S. Taccheo, G. Della Valle, R. Osellame, G. Cerullo, N. Chiodo, P. Laporta, O. Svelto, A. Killi, U. Morgner, and M. Lederer, "Er: Yb-doped waveguide laser fabricated by femtosecond laser pulses," Optics Letters **29**, 2626-2628 (2004).

[92] P. R. Herman, R. S. Marjoribanks, A. Oettl, K. Chen, I. Konovalov, and S. Ness, "Laser shaping of photonic materials: deep-ultraviolet and ultrafast lasers," Applied Surface Science **154**, 577-586 (2000).

[93] P. E. Dyer, C. D. Walton, and K. A. Akeel, "Coherence effects in surface roughness induced by vacuum ultraviolet F2 laser ablation," Optics Letters **30**, 1336-1338 (2005).

[94] J. Ihlemann, S. Müller, S. Puschmann, D. Schäfer, M. Wei, J. Li, and P. R. Herman, "Fabrication of submicron gratings in fused silica by F_2-laser ablation," Applied Physics A: Materials Science & Processing **76**, 751-753 (2003).

[95] M. L. Ng, P. R. Herman, A. H. Nejadmalayeri, and J. Li, "F_2-laser microfabrication of multilevel diffractive optical elements," in Journal of Physics: Conference Series **59**, 696-699 (2007).

[96] P. R. Herman, J. Yang, K. Kurosawa, and T. Yamanishi, "Laser machining of single-mode rib waveguides on germanosilicate slabs," in Proceedings of SPIE **2991**, 170 (1997).

[97] A. A. Tseng, Y. T. Chen, C. L. Chao, K. J. Ma, and T. P. Chen, "Recent developments on microablation of glass materials using excimer lasers," Optics and Lasers in Engineering **45**, 975-992 (2007).

[98] J. Dou, J. Li, P. R. Herman, J. S. Aitchison, T. Fricke-Begemann, J. Ihlemann, and G. Marowsky, "Laser machining of micro-lenses on the end face of single-mode optical fibers," Applied Physics A: Materials Science & Processing **91**, 591-594 (2008).

[99] H. M. Presby, A. F. Benner, and C. A. Edwards, "Laser micromachining of efficient fiber microlenses," Applied Optics **29**, 2692-2695 (1990).

[100] U. C. Paek and A. L. Weaver, "Formation of a spherical lens at optical fiber ends with a CO_2 laser," Applied Optics **14**, 294-298 (1975).

[101] S. Calixto, M. Rosete-Aguilar, F. J. Sanchez-Marin, and L. Castañeda-Escobar, "Rod and spherical silica microlenses fabricated by CO_2 laser melting," Applied Optics **44**, 4547-4556 (2005).

[102] A. Malki, R. Bachelot, and F. Van Lauwe, "Two-step process for micro-lens-fibre fabrication using a continuous CO_2 laser source," Journal of Optics A: Pure and Applied Optics **3**, 291-295 (2001).

[103] M. Wakaki, Y. Komachi, and G. Kanai, "Microlenses and microlens arrays formed on a glass plate by use of a CO_2 laser," Applied Optics **37**, 627-631 (1998).

[104] H. Yokota, E. Sugai, and Y. Sasaki, "Optical irradiation method for fiber coupler fabrications," Optical Review **4**, 104-107 (1997).

[105] T. E. Dimmick, G. Kakarantzas, T. A. Birks, and P. S. J. Russell, "Carbon dioxide laser fabrication of fused-fiber couplers and tapers," Applied Optics **38**, 6845-6848 (1999).

[106] G. Kakarantzas, T. A. Birks, and P. S. J. Russell, "Structural long-period gratings in photonic crystal fibers," Optics Letters **27**, 1013-1015 (2002).

[107] H. W. Lee and K. S. Chiang, "CO_2 laser writing of long-period fiber grating in photonic crystal fiber under tension," Optics Express **17**, 4533-4539 (2009).

[108] H. J. Baker, G. A. J. Markillie, P. Field, Q. Cao, C. Janke, and D. R. Hall, "Precision laser processing of optical microstructures with slab waveguide CO_2 lasers," in *High Power Lasers in Manufacturing*, X. Chen, T. Fujioka, and A. Matsunawa, eds., Proceedings of SPIE **3888**, 625-634 (2000).

[109] P. P. Vitruk, H. J. Baker, and D. R. Hall, "The characteristics and stability of high power transverse radio frequency discharges for waveguide CO_2 slab laser excitation," Journal of Physics D: Applied Physics **25**, 1767 (1992).

[110] F. Träger, *Springer handbook of lasers and optics* (Springer Verlag, 2007).

[111] "Operating manual. Germanium acousto-optic modulator model 37027-3" (Neos technologies, accessed in January 2011), retrieved http://www.neostech.com/pdfs/Asize/51/51A06185.pdf.

[112] K. L. Wlodarczyk, E. Mendez, H. J. Baker, R. McBride, and D. R. Hall, "Laser smoothing of binary gratings and multilevel etched structures in fused silica," Applied Optics **49**, 1997-2005 (2010).

[113] H. L. Schick, "A Thermodynamic Analysis of the High-temperature Vaporization Properties of Silica," Chemical Reviews **60**, 331-362 (1960).

[114] J. L. Ocaña, A. García-Beltrán, F. Laguarta, J. Armengol, N. Lupón, and F. Vega, "Laser heat treatments driven by integrated beams: role of irradiation nonuniformities," Applied Optics **38**, 4570-4576 (1999).

[115] L. K. White, N. A. Miszkowski, W. A. Kurylo, and J. M. Shaw, "Flow properties and contour modeling of fusible borophosphosilicate glasses," Journal of the Electrochemical Society **139**, 822 (1992).

[116] Y. Chen, A. Y. Yi, D. Yao, F. Klocke, and G. Pongs, "A reflow process for glass microlens array fabrication by use of precision compression molding," Journal of Micromechanics and Microengineering **18**, 055022 (2008).

[117] N. S. Kapany, J. J. J. Burke, and K. Frame, "Diffraction by Apertures of Wavelength Dimensions," Applied Optics **4**, 1229-1238 (1965).

[118] M. Mansuripur, A. R. Zakharian, and J. V. Moloney, "The interaction of light with subwavelength structures," Optics and Photonics News **14**, 56-61 (2003).

[119] H. Lamb, *Hydrodynamics* (Dover Publications, New York, 1945), pp. 624-626.

[120] C. Oh and M. J. Escuti, "Time-domain analysis of periodic anisotropic media at oblique incidence: an efficient FDTD implementation," Optics Express **14**, 11870-11884 (2006).

[121] R. Gordon, A. G. Brolo, A. McKinnon, A. Rajora, B. Leathem, and K. L. Kavanagh, "Strong Polarization in the Optical Transmission through Elliptical Nanohole Arrays," Physical Review Letters **92**, 037401 (2004).

[122] M. J. Matthews, R. M. Vignes, D. Cooke, S. T. Yang, and J. S. Stolken, "Analysis of microstructural relaxation phenomena in laser-modified fused silica using confocal Raman microscopy," Optics Letters **35**, 1311-1313 (2010).

[123] S. T. Yang, M. J. Matthews, S. Elhadj, V. G. Draggoo, and S. E. Bisson, "Thermal transport in CO_2 laser irradiated fused silica: In situ measurements and analysis," Journal of Applied Physics **106**, 103106 (2009).

[124] S. S. Cole and N. W. Taylor, "The System Na_2O-B_2O_3, IV Vapor Pressures of Boric Oxide, Sodium Metaborate, and Sodium Diborate between 1150°C and 1400°C," Journal of the American Ceramic Society **18**, 82-85 (1935).

[125] W. B. Pietenpol, "Surface Tension of Molten Glass," Journal of Applied Physics **7**, 26-31 (1936).

[126] W. D. Kingery, "Surface Tension of Some Liquid Oxides and Their Temperature Coefficients," Journal of the American Ceramic Society **42**, 6-10 (1959).

[127] S. Fujino, C. Hwang, and K. Morinaga, "Surface tension of PbO-B_2O_3 and Bi_2O_3-B_2O_3 glass melts," Journal of Materials Science, 40 **9**, 2207-2212 (2005).

[128] "Annealing schedule, Borosilicate glass 3.3" (accessed in December 2010), retrieved http://www.robuglas.com/fileadmin/user_upload/download_documents/temperverlauf2002_e.pdf.

[129] M. D. Feit, M. J. Matthews, T. F. Soules, J. S. Stolken, R. M. Vignes, S. T. Yang, and J. D. Cooke, "Densification and residual stress induced by CO_2 laser-based mitigation of SiO_2 surfaces," in Proceedings of SPIE **7842**, 78420O-78421 (2010).

[130] I. J. Thomson, H. J. Baker, K. Wlodarczyk, N. Trela, and D. R. Hall, "400W Yb: YAG planar waveguide laser using novel unstable resonators," in Proceedings of SPIE **7578**, 75780K (2010).

[131] J. J. Degnan and D. R. Hall, "Finite-aperture waveguide laser resonators," IEEE Journal of Quantum Electronics **QE-9**, 901–910 (1973).

[132] I. J. Thomson, "Efficient, high-power operation of CW Yb:YAG and Q-switched Nd:YAG planar waveguide lasers," PhD dissertation (Heriot-Watt University, Edinburgh, 2010).

[133] "UV Cylindrical Lenses " (Thorlabs, Ltd., accessed in January 2011), retrieved http://www.thorlabs.de/NewGroupPage9.cfm?ObjectGroup_ID=260.

[134] "Hellma Optik" (accessed in December 2010), retrieved http://www.hellma-optics.com/text/1001/en/torische-optiken.html.

[135] N. B. Dahotre and S. P. Harimkar, *Laser fabrication and machining of materials* (Springer Verlag, 2008).

[136] J. Magee, K. G. Watkins, and W. M. Steen, "Advances in laser forming," Journal of Laser Applications **10**, 235-246 (1998).

[137] W. Dai, X. Xiang, Y. Jiang, H. J. Wang, X. B. Li, X. D. Yuan, W. G. Zheng, H. B. Lv, and X. T. Zu, "Surface evolution and laser damage resistance of CO_2 laser irradiated area of fused silica," Optics and Lasers in Engineering **49**, 273-280 (2011).

[138] Z. Hu, R. Kovacevic, and M. Labudovic, "Experimental and numerical modeling of buckling instability of laser sheet forming," International Journal of Machine Tools and Manufacture **42**, 1427-1439 (2002).

[139] M. J. Matthews, J. S. Stolken, R. M. Vignes, M. A. Norton, S. Yang, J. D. Cooke, G. M. Guss, and J. J. Adams, "Residual stress and damage-induced critical fracture on CO_2 laser treated fused silica," in Proceedings of SPIE **7504**, 750410 (2009).

[140] G. Dearden, C. Taylor, K. Bartkowiak, S. P. Edwardson, and K. G. Watkins, "An experimental study of laser micro-forming using a pulsed Nd: YAG laser and scanning optics," in Proceedings of the 22nd International Congress on

Applications of Laser & Electro-Optics (ICALEO 2003), Jacksonville, Florida, USA, October, 13-16 (2003).

[141] J. Kumar and M. S. Shunmugam, "Fitting of Reference Surfaces for Engineering Surfaces by Nonlinear Least-Squares Technique," Journal of Computing and Information Science in Engineering **6**, 349-354 (2006).

[142] C. A. Klein, "How accurate are Stoney's equation and recent modifications," Journal of Applied Physics **88**, 5487 (2000).

[143] C. H. Hsueh, "Modeling of elastic deformation of multilayers due to residual stresses and external bending," Journal of Applied Physics **91**, 9652 (2002).

[144] G. G. Stoney, "The tension of metallic films deposited by electrolysis," Proceedings of the Royal Society of London. Series A, Containing Papers of a Mathematical and Physical Character, 172-175 (1909).

[145] N. Schwarzer and F. Richter, *On the Determination of Film Stress from Substrate Bending: STONEY's Formula and Its Limits* (Techn. Univ. Chemnitz, Fakultät für Naturwissenschaften, 2006).

[146] H. J. Baker, Private communication (2010).